
University of Potsdam

Institute of Earth and Environmental Sciences
Section of Geoecology

Soil Parameter Retrieval under Vegetation Cover Using SAR Polarimetry

Dissertation submitted to the Faculty of Mathematics and Natural
Sciences at the University of Potsdam for the Degree of “doctor
rerum naturalium” (Dr. rer. nat.) in Hydrology

by

Thomas Jagdhuber

Supervisors:

Prof. Dr. Axel Bronstert (University of Potsdam)

Prof. Dr. Irena Hajsek (ETH Zurich)

Potsdam, 14/03/2012

This work is licensed under a Creative Commons License:
Attribution - Noncommercial - Share Alike 3.0 Germany
To view a copy of this license visit
<http://creativecommons.org/licenses/by-nc-sa/3.0/de/>

Published online at the
Institutional Repository of the University of Potsdam:
URL <http://opus.kobv.de/ubp/volltexte/2012/6051/>
URN <urn:nbn:de:kobv:517-opus-60519>
<http://nbn-resolving.de/urn:nbn:de:kobv:517-opus-60519>

Dedicated to my wife Franziska,
my parents Rosi and Herbert,
and my brothers Christoph and Stefan.

Preface

Maybe the period from my first steps into this research topic until the submission of my PhD thesis can be compared with an exciting journey. I was privileged to meet a lot of interesting people with even more interesting and creative ideas in two research hot spots: The Microwaves and Radar Institute of DLR and the Institute of Earth and Environmental Sciences of the University of Potsdam.

For sure, it was one of the most enriching periods in my young life. Therefore many persons have contributed to the joy and the success of this journey, and I want to sincerely thank...

...my supervisor at DLR Irena Hajnsek for her creative guidance, her continuous support and her scientific advice throughout all stages of my PhD research, which was and is a rare privilege that I enjoy to this day. Her encouraging nature and passion for science and research, but also for family, provided me a guiding example that there is a possibility to exceed boundaries and to unify tasks, which seem to be not feasible. Truly visionary.

...my supervisor at the University of Potsdam Axel Bronstert for academic supervision of my PhD thesis including his great scientific support and fruitful discussions even from a more remote situation.

...Konstantinos P. Papathanassiou for his scientific input, his hundred percent commitment to support his research colleagues, his great enthusiasm for science and his dedication to research.

I also cordially thank him as well as Irena for their friendship, for several private impulses enriching my life and endless discussions about the performance of FC Bayern München and if they will ever succeed to win the Champions League again.

...Alberto Moreira and Gerhard Krieger for the possibility to research in the very motivating and innovative environment of their institute and their department, being one of the cutting-edge hot spots for innovation in RADAR remote sensing. In addition, I want to thank Alberto Moreira for evaluating this PhD work.

...Ralf Ludwig for fostering the first research interests back in time, when I was a student at the LMU Munich, and for evaluating this PhD work.

...the past and present members of our research groups ‘Pol-InSAR’ and ‘SAR Information retrieval’ for creating the very pleasant and stimulating research atmosphere including a wonderful plurality of nationalities and professions, especially Helmut Schön, Jayanti Sharma, Ludovic Villard, Francesco De Zan, Giuseppe Parrella, Stefan Sauer, Sibylle Radzuweit, Gabi Hager, SeungKuk Lee, JunSu Kim, Michelangelo Villano, Florian Kugler, Thomas Busche, Maria-José Sanjuan-Ferrer, Matteo Pardini, Astor Toraño Caicoya, Noora Al-Kahachi and Raphael Zandonaschneider. Thank you also for proof-reading of the thesis, mostly on short notice. In addition, I also want to thank Maxim Neumann for several discussions on polarimetric modeling, Matteo Nannini for assistance with formatting and Björn Döring as well as Dirk Schrank for keeping me in shape with the DLR running crew.

...my internship and master students Miguel Kohling, Michele Martone, Iole Pisciotano, GianPaolo Massaroli and Malin Friese. It was a true pleasure to work with you. Hopefully, I could arise a bit the interest for science and research in you, at least I tried my best.

...my colleagues at the University of Potsdam for helping me and always treating me as an integrated member, though I could only be there short periods of time. A special thanks goes to the OPAQUE-team members: Thomas Gräff, Sibylle Itzerott, Dominik Reusser, Maik Heistermann, Andreas Bauer and David Kneis.

...the processing and flight crew of DLR for providing the data sets of several campaigns, especially Ralf Horn, Jens Fischer, Martin Keller and Marc Jäger.

...my friends since childhood days Michi, Christoph, Markus, Basti, Felix, Jan and Tim for almost everything besides my research.

...my family being the most unconditional and strongest supporting force throughout all my years of education. I will never forget, what you did for me and I will always try to give it back.

Finally, I want to thank my wife Franziska for her everlasting encouragement, her understanding for a researcher’s life and her refreshing sense of humor. It is her unconditional support and her patience during all the years that founded the success of my efforts. You are far more than I can express in words.

Contents

Table of contents	I
List of figures	V
List of tables	XIII
List of acronyms.	XV
List of symbols	XVII
Abstract	XXV
ZusammenfassungXXVII
1 Introduction	1
1.1. Motivation	1
1.2. State-of-the-art	3
1.3. Scope and organization of thesis	5
2 Characterization of agricultural media with respect to electro-magnetic scattering	9
2.1. Soil characteristics	9
2.1.1. Soil moisture	10
2.1.2. Soil roughness	13
2.2. Agricultural vegetation characteristics	15
3 SAR principles and polarimetry	23
3.1. SAR principles	23
3.1.1. Imaging geometry	23
3.1.2. Imaging resolution	25
3.1.3. Impulse response.	27
3.1.4. Backscattering coefficient	28
3.1.5. Speckle reduction	29
3.2. Polarimetry	30
3.2.1. Scattering matrix.	33
3.2.2. Coherent and distributed scatterers	34
3.2.2.1. Scattering vectors	34
3.2.2.2. Coherency and covariance matrix.	36
3.2.3. Symmetry properties	37

3.2.4. Decomposition theorems	38
3.2.4.1. Eigen-based decomposition	38
3.2.4.2. Model-based decomposition	43

4 Methodology of soil parameter retrieval using SAR polarimetry 47

4.1. Scattering models for bare soil.	48
4.1.1. Empirical models	48
4.1.2. Semi-empirical models	48
4.1.3. Theoretical models	48
4.1.4. Polarimetric soil moisture inversion	50
4.1.5. Polarimetric soil roughness inversion	52
4.2. Scattering and decomposition models for vegetated soils.	54
4.2.1. Modifications of model-based decompositions	55
4.2.1.1. Modification of the surface component	56
4.2.1.2. Modification of the dihedral component	56
4.2.1.3. Modification of the volume component	65
4.2.2. Separation of volume from ground components.	77
4.2.3. Separation of ground components using a scattering dominance criterion	81
4.2.4. Calculus of ground components	86
4.2.5. Inversion for soil moisture under vegetation cover	87
4.2.5.1. Inversion of surface component	87
4.2.5.2. Inversion of dihedral component	88
4.2.5.3. Inversion of surface and dihedral components using <i>Pauli</i> -based ground-to-volume ratios	89
4.2.6. Hybrid decomposition and inversion for soil moisture under vegetation cover	91
4.2.6.1. Physically constrained volume component	93
4.2.6.2. Inversion for soil moisture	94
4.2.7. Multi-angular model-based decomposition and inversion for soil moisture under vegetation cover	94
4.2.7.1. Inversion for soil moisture using a sum of absolute differences.	95

4.2.8. Inversion of soil roughness under vegetation cover	98
4.2.8.1. Modified <i>X-Bragg</i> ratio using <i>Pauli</i> -based ground- to-volume ratios	98
5 Experimental data	101
5.1. Study areas.	101
5.1.1. AgriSAR campaign	101
5.1.2. OPAQUE campaigns	110
5.1.3. SARTEO campaign	115
5.2. Polarimetric SAR data	117
5.2.1. Acquisition	117
5.2.2. Processing.	119
6 Results and validation of soil parameter retrieval with experimental data	123
6.1. Results for soil moisture	123
6.1.1. Results for soil moisture retrieval on bare soil	124
6.1.2. Results for soil moisture retrieval under vegetation cover .	131
6.1.2.1. Model-based decomposition	132
6.1.2.2. Inversion and validation of surface and dihedral components	137
6.1.2.3. Inversion and validation of surface and dihedral components using <i>Pauli</i> -based ground-to-volume ratios	145
6.1.2.4. Hybrid decomposition and inversion	150
6.1.2.5. Multi-angular model-based decomposition and in- version	158
6.1.3. Best approach for soil moisture retrieval under vegetation cover	166
6.2. Results for soil roughness	167
6.2.1. Results for soil roughness retrieval on bare soil	167
6.2.2. Results for soil roughness retrieval under vegetation cover .	170
6.2.2.1. Inversion and validation of the modified <i>X-Bragg</i> ratio approach	170

6.2.3. Best approach for soil roughness retrieval under vegetation cover	172
7 Summary and conclusions	175
7.1. Summary	175
7.2. Contributions	182
7.3. Outlook	183
Bibliography	187
Appendix	223
A Eigen-based noise correction	223
B Growth stages of plants	224
C Volume modeling with spheroidal particles.	226
D Meteorological data from the AgriSAR campaign.	227
E Intensive measurement campaigns for soil moisture within AgriSAR campaign	230
F Normalized <i>Pauli</i> -based ground-to-volume ratios.	231
G Surface and dihedral scattering mechanisms of the hybrid decomposition	234

List of Figures

1	Simplified soil model	9
2	Relation between soil moisture and soil matrix suction depending on different grain size	11
3	Different soil roughness levels	15
4	Phenology of cereal plants	17
5	Three vegetation volumes with different plant inclusions for the two-phase dielectric mixture model	19
6	Synthetic Aperture Radar (SAR) imaging geometry	24
7	Imaging geometry in range direction	24
8	Acquisition geometry involving terrain slopes for local incidence .	25
9	Formation of synthetic aperture	26
10	Conceptual, two dimensional representation of a <i>polarization ellipse</i>	31
11	Physical interpretation of the alpha scattering angle	40
12	Scattering plane of polarimetric entropy - mean scattering alpha angle	41
13	Volume over ground scattering model according to <i>Born approximation</i>	47
14	Behavior of T_{XB} -components with respect to the incidence angle θ_l , $\epsilon_s = 20$, $\psi_l = 30^\circ$	51
15	Behavior of T_{XB} -components with respect to the incidence angle θ_l , $\epsilon_s = 20$, $\psi_l = 55^\circ$	52
16	Roughness term of coherency matrix elements depending only on the rotation angle ψ_l	54
17	General work flow of soil parameter retrieval from polarimetric SAR data using polarimetric decomposition techniques	55
18	Schematical representation of ground and vegetation volume components of model-based decompositions	55
19	Behavior of the $m_{d_{g/e}}^2$ -component with respect to the local incidence angle (θ_l)	57
20	Behavior of the $m_{d_{g/e}}^2$ -component with respect to the vertical surface roughness (s)	57
21	Sensitivity of the ground-to-volume ratio difference ($\mu_{max} - \mu_{min}$) to the height of the vegetation	58
22	Sensitivity of the $m_{d_v}^2$ -component and the $m_{d_{v\theta_l}}^2$ -component to the eigenvalue difference $\mu_{max} - \mu_{min}$	59

23	Behavior of the coherency matrix elements T_{XD11} , T_{XD12} , T_{XD22} , T_{XD33} with respect to the rotation angle accounting for soil roughness	61
24	Behavior of the coherency matrix elements T_{XD11} , T_{XD12} , T_{XD22} , T_{XD33} with respect to the local incidence angle	61
25	Behavior of the coherency matrix combination $T_{XD33} + T_{XD22}$ with respect to the rotation angle accounting for soil roughness ($\epsilon_s = 20, \epsilon_t = 10, \theta_l = 30^\circ$)	62
26	Behavior of the coherency matrix combination $T_{XD33} + T_{XD22}$ with respect to the rotation angle accounting for soil roughness ($\epsilon_s = 20, \epsilon_t = 10, \theta_l = 50^\circ$)	62
27	Behavior of the coherency matrix combination $T_{XD33} + T_{XD22}$ with respect to the dielectric constant of the soil	63
28	Behavior of the coherency matrix combination $T_{XD33} + T_{XD22}$ with respect to the dielectric constant of the trunk	63
29	Behavior of the coherency matrix combination $(T_{XD22} - T_{XD33}) / (T_{XD22} + T_{XD33})$ with respect to the rotation angle accounting for soil roughness ($\epsilon_s = 20, \epsilon_t = 10, \theta_l = 30^\circ$)	64
30	Behavior of the coherency matrix combination $(T_{XD22} - T_{XD33}) / (T_{XD22} + T_{XD33})$ with respect to the rotation angle accounting for soil roughness ($\epsilon_s = 20, \epsilon_t = 10, \theta_l = 60^\circ$)	64
31	Behavior of the coherency matrix combination $(T_{XD22} - T_{XD33}) / (T_{XD22} + T_{XD33})$ with respect to the rotation angle accounting for soil roughness ($\epsilon_s = 20, \epsilon_t = 30, \theta_l = 30^\circ$)	65
32	Orientation of a spheroid in three dimensional observation space	67
33	Model of a prolate and a oblate spheroid with principal and minor axes in the particle reference frame	68
34	Particle scattering anisotropy	69
35	Behavior of the normalized vegetation volume component T_{VGH} with respect to the orientation angle width $\Delta\psi$ around $\bar{\psi} = 0^\circ$. .	71
36	Degree of orientation for the vegetation volume component . . .	72
37	Normalized volume coherency matrix component T_{VGD} with orientation angle width $\Delta\psi$	75
38	Split of the cross-component $\langle S_{XX} ^2 \rangle$	79
39	Scattering dominance criterion using the real part and imaginary part of $\langle S_{HH} S_{VV}^* \rangle$ for 19 th of April 2006 within the AgriSAR campaign	82

40	Degree of orthogonality for surface and dihedral scattering mechanisms with the local incidence angle θ_l	84
41	Degree of orthogonality of ground and volume scattering mechanisms with the local incidence angle θ_l	85
42	β_S as function of the soil dielectric constant ϵ_s for different local incidence angles θ_l as well as depolarization with increasing roughness angle ϕ_l	88
43	Sensitivity of the dihedral scattering components α_D and f_D on the dielectric constants (ϵ_s, ϵ_t) for different local incidence angles θ_l .	90
44	Processing scheme of multi-angular polarimetric decomposition and inversion procedure	95
45	Maximum $ \beta_S $ difference along the local incidence angle θ_l for different levels of the soil dielectric constant ϵ_s	96
46	Variation of the dihedral scattering intensity f_D as function of the dielectric constant of the soil ϵ_s and of the trunk ϵ_t	97
47	Variation of the dihedral scattering mechanism α_D as function of the dielectric constant of the soil ϵ_s and of the trunk ϵ_t	97
48	Sensitivity of the modified <i>X-Bragg</i> ratio ζ on the normalized <i>Pauli</i> -based ground-to-volume ratio Pa_D	99
49	Location of study areas in Germany	101
50	Local incidence angle for the AgriSAR 2006 campaign	103
51	Overview of the DEMMIN test site within the AgriSAR 2006 campaign	104
52	Data of a continuously recording soil moisture station covering the entire vegetation growth period	105
53	Weekly soil moisture measurements by ZALF/DLR covering the entire vegetation growth period	105
54	Weekly soil moisture measurements by CAU covering the entire vegetation growth period	106
55	Vegetation height measurements covering the entire vegetation growth period	106
56	Wet biomass measurements covering the entire vegetation growth period	107
57	CESBIO-ESA LASER profiler with field campaign settings	107
58	Exemplary roughness profile of the soil surface derived with CESBIO-ESA LASER profiler within the AgriSAR campaign	108

59	Measurement setup for soil roughness retrieval with a digital photogrammetric approach	108
60	Bird view on three dimensional soil roughness measurement the from AgriSAR campaign	109
61	Time series of soil roughness measurements covering the entire vegetation growth period	109
62	Topography of OPAQUE study area	110
63	Overview of study area for the OPAQUE 2007 campaign	111
64	RGB-composite of the three flight headings in HH-polarization for L-band	112
65	Local incidence angle of the multi-angular data set of the OPAQUE 2008 campaign	113
66	Overview of study area for the OPAQUE 2008 campaign	114
67	Flight tracks of the SARTEO campaign in the Rur catchment	116
68	Local incidence angle for the SARTEO campaign	117
69	DLR's airborne E-SAR system on board a Dornier Do 228-212 aircraft	118
70	Normalized <i>Pauli</i> RGB-images of the SARTEO, OPAQUE and AgriSAR campaign	120
71	Processing scheme for soil moisture inversion on bare soils	124
72	Two dimensional histograms of the $H-\bar{\alpha}$ scattering plane for the AgriSAR 2006, SARTEO 2008 and OPAQUE data with <i>X-Bragg</i> model boundaries	127
73	Two dimensional histograms of the $H-\bar{\alpha}$ scattering plane for different types of scatterers with <i>X-Bragg</i> model boundaries	128
74	Results of soil moisture inversion using the <i>X-Bragg</i> model for the AgriSAR, the OPAQUE and the SARTEO campaign	129
75	Sampling scheme on test fields for the bare soil inversion using the <i>X-Bragg</i> model	130
76	Validation of soil moisture inversion on bare soils using the <i>X-Bragg</i> model for AgriSAR, SARTEO and OPAQUE data with field measurements	130
77	A selection of test fields indicating the diversity of agricultural scattering scenarios for soil moisture inversion under vegetation cover	131
78	Scheme of model-based polarimetric decomposition technique and inversion algorithm for soil moisture	132

79	Results of the model-based polarimetric decomposition for the OPAQUE 2007 campaign	134
80	Results of the model-based polarimetric decomposition for the AgriSAR 2006 campaign	135
81	Results of the model-based decomposition for the OPAQUE 2008 and SARTEO campaign	136
82	Estimated soil moisture on bare and vegetated soils for the OPAQUE 2007 campaign	139
83	Estimated soil moisture on bare and vegetated soils for the AgriSAR 2006 campaign	140
84	Estimated soil moisture on bare and vegetated soils for the OPAQUE 2008 and SARTEO campaigns	141
85	Comparison between measured and estimated soil moisture values from the model-based approach for the OPAQUE 2007 campaign	143
86	Comparison between measured and estimated soil moisture values from the model-based approach for the AgriSAR 2006, the OPAQUE 2008 and the SARTEO 2008 campaign	144
87	Normalized <i>Pauli</i> -based ground-to-volume ratios for 19 th of April 2006 of the AgriSAR campaign	146
88	Inverted soil moisture for the AgriSAR 2006 campaign applying the model-based approach with normalized <i>Pauli</i> -based ground-to-volume ratios for the entire vegetation growth period	147
89	Inverted soil moisture for OPAQUE and SARTEO campaigns applying the model-based approach with normalized <i>Pauli</i> -based ground-to-volume ratios	148
90	Sampling scheme on the test fields for the inversion approach incorporating normalized <i>Pauli</i> -based ground-to-volume ratios	148
91	Comparison of measured and estimated soil moisture for AgriSAR, OPAQUE and SARTEO campaigns applying the model-based approach with normalized <i>Pauli</i> -based ground-to-volume ratios	149
92	Scheme of the hybrid three component decomposition and inversion algorithm for soil moisture	151
93	Land use map as well as surface and dihedral scattering mechanisms for the AgriSAR 2006 campaign	152
94	Results for soil moisture inversion under vegetation cover using a hybrid decomposition and inversion approach	154

95	Sampling scheme on the test fields for validation of the hybrid decomposition and inversion algorithm	155
96	Scatter plots of measured soil moisture values from TDR, FDR and gravimetric probes against estimated soil moisture values using the hybrid decomposition and inversion algorithm	156
97	Processing scheme of the multi-angular polarimetric decomposition and inversion procedure for soil moisture	159
98	Local incidence angle, power contributions of the three component model-based decomposition, single-angular soil moisture estimates, bi-angular soil moisture estimates, tri-angular soil moisture estimates and land use map of OPAQUE 2008 campaign	161
99	Scatter plots of measured against estimated soil moisture values for the different incidence angle configurations including all investigated fields	163
100	Roughness parameter ks inverted from anisotropy and from circular coherence magnitude for 19 th /20 th of April 2006 of the AgriSAR campaign	168
101	Validation of measured against estimated soil roughness values (ks) using anisotropy, circular coherence and the modified <i>X-Bragg</i> ratio for ‘E-W’-track and ‘N-S’-track of the AgriSAR campaign on 19 th /20 th of April 2006	169
102	Estimated soil roughness (ks) using the modified <i>X-Bragg</i> ratio for the AgriSAR 2006 campaign covering an entire vegetation growth period	171
103	Validation of mean measured against mean estimated soil roughness (ks) for the AgriSAR 2006 campaign covering an entire vegetation growth period	172
104	Phenology of rape plants	224
105	Phenology of beet plants	224
106	Phenology of maize plants	225
107	Meteorological measurements for April 2006 of the AgriSAR campaign	227
108	Meteorological measurements for May 2006 of the AgriSAR campaign	228
109	Meteorological measurements for June 2006 of the AgriSAR campaign	228

110	Meteorological measurements for July 2006 of the AgriSAR campaign	229
111	Normalized <i>Pauli</i> -based ground-to-volume ratios for the AgriSAR campaign on 7 th of June 2006	231
112	Normalized <i>Pauli</i> -based ground-to-volume ratios for the AgriSAR campaign on 5 th of July 2006	232
113	Normalized <i>Pauli</i> -based ground-to-volume ratios for the OPAQUE 2007 campaign in May	232
114	Normalized <i>Pauli</i> -based ground-to-volume ratios for the OPAQUE 2008 campaign in May	233
115	Normalized <i>Pauli</i> -based ground-to-volume ratios for the SARTEO 2008 campaign in May	233
116	Land use as well as alpha scattering angles of the surface and the dihedral component for AgriSAR 2006 campaign	234
117	Land use as well as alpha scattering angles of the surface and the dihedral component for AgriSAR 2006 campaign	235
118	Land use as well as alpha scattering angles of the surface and the dihedral component for OPAQUE 2007 campaign	235
119	Land use as well as alpha scattering angles of the surface and the dihedral component for OPAQUE 2008 campaign	236
120	Land use as well as alpha scattering angles of the surface and the dihedral component for SARTEO campaign	236

List of Tables

1	Validity range of theoretical surface scattering models for bare soil	49
2	Scattering dominance criteria after volume subtraction	81
3	<i>in situ</i> measurements of vegetation and soil moisture for May 2007 of the OPAQUE campaign	112
4	Local incidence angle of different flight headings	113
5	<i>in situ</i> measurements of soil moisture and vegetation for the OPAQUE 2008 campaign	115
6	<i>in situ</i> measurements of soil moisture for May 2008 of the SARTEO campaign	116
7	Technical specifications of the Experimental airborne SAR system (E-SAR) instrument and parameters of the acquisition geometry .	118
8	Specifications of fully polarimetric E-SAR L-band data after processing	119
9	Summary of selected fully polarimetric E-SAR L-Band acquisitions for experimental data analyses	121
10	Inversion results of the <i>X-Bragg</i> bare soil approach for different crop types	126
11	Inversion rates of the <i>X-Bragg</i> bare soil approach	126
12	Vegetation characterization and inversion results for the OPAQUE 2007 campaign	142
13	Quality assessment of inversion results with the model-based approach including all investigated crop types for the AgriSAR 2006, OPAQUE 2008 and SARTEO 2008 campaign	145
14	Quality assessment of inversion results for the AgriSAR 2006, OPAQUE 2008 and SARTEO 2008 campaign applying the model-based approach with normalized <i>Pauli</i> -based ground-to-volume ratios .	150
15	Estimated dielectric level from the α_1 -criterion	153
16	Inversion rate, RMSE, STDDEV and maximum of vegetation height for the hybrid decomposition and inversion with physically constrained volume power	157
17	Inversion rate of the different incidence angle configurations for multi-angular model-based decomposition on the OPAQUE 2008 data	162

18	Root Mean Square Error (RMSE) in vol.% of inversion for the different incidence angle configurations using the multi-angular model-based decomposition on OPAQUE 2008 data	164
19	Mean field value of Standard Deviation (STDDEV) of soil moisture within the sampling boxes in vol.% of the inversion with the multi-angular model-based decomposition on OPAQUE 2008 data . . .	164
20	RMSE, STDDEV and inversion rate of all applied decomposition and inversion algorithms for soil moisture retrieval including all study areas	166
21	Intensive soil moisture measurements of the AgriSAR campaign .	230

List of acronyms

ACF	Auto Correlation Function
AIEM	Advanced Integral Equation Method
ALOS	Advanced Land Observing Satellite
AMI	Active Microwave Instrument
ASAR	Advanced Synthetic Aperture Radar
BBCH	Biologische Bundesanstalt, Bundessortenamt und Chemische Industrie
BMBF	Federal Ministry of Education and Research
CAU	Christian-Albrechts-Universität Kiel
CESBIO	Centre d'Etude Spatiale de la BIOSphère
DEM	Digital Elevation Model
DEMMIN	Durable Environmental Multidisciplinary Monitoring Information Network
DERD	Dihedral Eigenvalue Relative Difference
DGPS	Differential Global Positioning System
DLR	German Aerospace Center
DSM	Digital Surface Model
E-SAR	Experimental airborne SAR system
EFA	Effective Field Approximation
EM	Electro-Magnetic
ENVISAT	Environmental Satellite
ERS	European Remote Sensing
ESA	European Space Agency
FC	Field Capacity
FDR	Frequency Domain Reflectometry
FM	Frequency Modulated
GANS	Ground Albedo Neutron Sensing
GCP	Ground Control Point
GO	Geometric Optics
GPR	Ground Penetrating Radar
IEM	Integral Equation Method
INS	Inertial Navigation System
ISSIA	Istituto di Studi sui Sistemi Intelligenti per l'Automazione
LASER	Light Amplification by Stimulated Emission of Radiation
LIA	Local Incidence Angle
LMU	Ludwig Maximilians Universität München
LoS	Line of Sight

MIMICS Michigan Microwave Canopy Scattering Model
MIRAS Microwave Imaging Radiometer with Aperture Synthesis
NESZ Noise Equivalent Sigma Zero
PALSAR Phased Array type L-band Synthetic Aperture Radar
PDF Probability Density Function
PO Physical Optics
PoI-InSAR Polarimetric Synthetic Aperture Radar Interferometry
PoISAR Polarimetric Synthetic Aperture Radar
PWP Permanent Wilting Point
RADAR RAdio Detection And Ranging
RAR Real Aperture Radar
RCS Radar Cross Section
RLA Radar Look Angle
RMS Root Mean Square
RMSE Root Mean Square Error
SAR Synthetic Aperture Radar
SERD Surface Eigenvalue Relative Difference
SMAP Soil Moisture Active Passive
SMOS Soil Moisture and Ocean Salinity
SNR Signal to Noise Ratio
SPM Small Perturbation Model
SSA Small Slope Approximation
STDDEV Standard Deviation
STDR Spatial Time Domain Reflectometry
SVAT Soil Vegetation Atmosphere Transfer
TDR Time Domain Reflectometry
UHF Ultra High Frequency
VHF Very High Frequency
VRT Vector Radiative Transfer
WCM Water Cloud Model
ZALF Leibniz Centre for Agricultural Landscape Research

List of symbols

a	Coordinate in <i>azimuth</i> direction
A	Polarimetric scattering anisotropy
A_e	Amplitude of polarization ellipse
A_{gr}	Unit ground area [m ²]
A_p	Particle anisotropy
A_r	Effective aperture of receiving antenna
\underline{B}	Magnetic induction [T]
B_w	System bandwidth [Hz]
$B_{w_{max}}$	Maximum system bandwidth [Hz]
$[C]$	Covariance matrix
\underline{D}	Electric induction [C/m ²]
D_{az}	<i>Azimuth</i> -dimension of antenna [m]
$[E]$	Matrix of concatenated eigenvectors
\underline{E}	Electric field [V/m]
\underline{E}_i	Incident electric field [V/m]
\underline{E}_s	Scattered electric field [V/m]
\underline{e}_x	x^{th} eigenvector of a matrix
f	Frequency [Hz]
f_0	Carrier frequency [Hz]
f_a	<i>Azimuth</i> frequency of the SAR system [Hz]
f_{ca}	Chirp rate in <i>azimuth</i> direction [Hz/s]
f_{cr}	Chirp rate in <i>range</i> direction [Hz/s]
f_D	Intensity of dihedral scattering component for the model-based decomposition
f_{D_h}	Intensity of dihedral scattering component for the hybrid decomposition
f_{rg}	Frequency of <i>range</i> sampling [Hz]
f_S	Intensity of surface scattering component for the model-based decomposition
f_{S_h}	Intensity of surface scattering component for the hybrid decomposition
f_V	Intensity of volume scattering component for the model-based decomposition
f_{V_c}	Intensity of physically constrained volume scattering component for decompositions
$f_{V_{c_h}}$	Intensity of physically constrained volume scattering component for the hybrid decomposition

f_{V_h}	Intensity of volume scattering component for the hybrid decomposition
G_t	Gain of transmitting antenna
H	Polarimetric scattering entropy
H_F	Flight height [m]
\underline{H}_i	Incident magnetic field [A/m]
h_{rms}	Root mean square height [m]
h_v	Vegetation height [m]
\underline{J}	Total current density [A/m ²]
J	Discharge or volumetric water flow [m/s]
k	Wave number in free space $k = 2\pi/\lambda_c$ [m ⁻¹]
K	Hydraulic conductivity [m/s]
k_c	Complex wave number or complex propagation constant [m ⁻¹]
kl	Effective horizontal soil roughness
ko	Degree of orthogonality
\underline{k}_{pr}	Wave propagation vector
ks	Effective vertical soil roughness
\underline{k}_x	Scattering vector of basis x
l	Correlation length [m]
L_i	Particle shape function along i^{th} dimension
L_n	Number of looks
L_{ne}	Number of effective looks
L_r	Ratio of spheroidal axis
l_s	Swath width
L_{sa}	Length of synthetic aperture [m]
m_d	Scattering loss of dihedral intensity component
\underline{m}_{di}	Magnetic dipole moment [J·T ⁻¹]
m_g	Gravimetric soil moisture content
m_s	Scattering loss of surface intensity component
m_{so}	Mass of dry soil [kg]
m_v	Volumetric soil moisture content [vol.%]
m_w	Mass of water [kg]
n	Complex refractive index
N_e	Number of particles per unit volume
nf_R	Receiver noise figure
P	Pseudo-probability
Pa	Normalized <i>Pauli</i> -based ground-to-volume ratio
P_D	Power of dihedral component of model-based decomposition

\underline{p}_{di}	Electric dipole moment [C·m]
$[P_{\xi}]$	Matrix of propagation effects
P_r	Received power
P_{rv}	Co-polarization power ratio
p_s	Scattering particle
P_S	Power of surface component of model-based decomposition
P_t	Transmitted power
P_{Tmax}	Transmitted peak power
P_V	Power of volume component of model-based decomposition
R	Range distance [m]
$[R]$	Rotation matrix
R_0	Range distance within the line of sight plane [m]
R_p	Range distance to the point scatterer [m]
R_x	<i>Bragg</i> scattering coefficient of polarization x
R_{xy}	<i>Fresnel</i> scattering coefficient of scattering plane x with polarization y
$[S]$	Scattering matrix for monostatic acquisition
s_{comp}	Compressed signal
s_{im}	SAR image
s_{re}	Received signal
s_{reb}	Received baseband signal
s_{rep}	Chirp replica of signal
s_{tr}	Transmitted pulse
S_{XX}	Scattering matrix element of polarimetric channel XX
$[T]$	Coherency matrix
t_a	Time at the beam center in <i>azimuth</i> direction [s]
t_r	Time delay of signal in <i>range</i> direction [s]
t_t	Total illumination time of a target in <i>azimuth</i> direction = target exposure time [s]
T_{XY}	Coherency matrix element of row X and column Y
$[U]$	Special unitary matrix
V	Particle volume [m ³]
v_i	Volume fraction of particles in a two-phase mixture
v_p	Velocity of platform [m/s]
v_t	Total volume of soil [m ³]
v_w	Volume of water [m ³]
w_a	Envelope of the antenna pattern in <i>azimuth</i> direction
w_r	Pulse envelope in <i>range</i> direction

x_1	Major axis of spheroid [m]
x_2	Minor axis of spheroid [m]
x_i	Axis of particle along i^{th} dimension [m]
z_0	Position of the ground [m]

Greek symbols:

α	Polarimetric scattering alpha angle [°]
α_1	Dominant polarimetric scattering alpha angle [°]
α_d	Dihedral scattering mechanism of hybrid decomposition [°]
α_D	Scattering mechanism of dihedral component for model-based decomposition
α_s	Surface scattering mechanism of hybrid decomposition [°]
α_{sl}	Angle of terrain slope [°]
α_v	Volume particle shape [°]
β	Polarimetric scattering beta angle [°]
β_{az}	Opening angle of antenna in <i>azimuth</i> direction [°]
β_{el}	Opening angle of antenna in <i>elevation</i> direction [°]
β_S	Scattering mechanism of surface component for model-based decomposition
γ	Polarimetric scattering differential phase [°]
γ_{XXYY}	Polarimetric coherence of polarizations XX and YY
Γ	Rotation angle between (H,V)-basis and eigen-basis (A,B) [°]
δ	Polarimetric scattering differential phase [°]
δ_a	Effective particle scattering anisotropy
δ_{az}	Resolution in <i>azimuth</i> direction [m]
δ_{azRAR}	Resolution in <i>azimuth</i> direction of a RAR system [m]
δ_{azSAR}	Resolution in <i>azimuth</i> direction of a SAR system [m]
δ_{pen}	Penetration depth into the soil [m]
δ_{rg}	Resolution in <i>range</i> direction [m]
δ_{rgRAR}	Resolution in <i>range</i> direction of a RAR system [m]
δ_{rgSAR}	Resolution in <i>range</i> direction of a SAR system [m]
Δ_{az}	Pixel spacing in <i>azimuth</i> direction [m]
Δ_{rg}	Pixel spacing in <i>range</i> direction [m]
Δv	Differential refractivity
$\Delta \sigma$	Differential two-way extinction
ϵ_c	Absolute complex permittivity or absolute complex dielectric constant [F/m]

ε_h	Relative complex dielectric constant of the host material in a two-phase mixture
ε_i	Relative complex dielectric constant of the inclusions in a two-phase mixture
ε_m	Relative complex dielectric constant of a two-phase mixture
ε_r	Relative complex permittivity or relative complex dielectric constant
ε_s	Real part of relative complex dielectric constant of the soil
ε_t	Real part of relative complex dielectric constant of the trunk
ζ	Modified <i>X-Bragg</i> ratio for soil roughness retrieval
θ	Incidence angle [°]
θ_l	Local incidence angle [°]
θ_r	Radar look angle [°]
λ_c	Radiation wavelength [m]
λ_x	x^{th} eigenvalue of a matrix
μ_c	Absolute complex permeability [H/m]
μ_{max}	Maximum polarimetric ground-to-volume ratio
μ_{min}	Minimum polarimetric ground-to-volume ratio
ν	Mean refractivity
ξ	Differential propagation effects in an oriented volume
Ξ	Set of 2x2 complex basis matrices
ρ	Shape parameter of volume component
ρ_b	Bulk density [kg/m ³]
ρ_{corr}	Surface correlation function of the soil = Auto Correlation Function (ACF) of the soil surface
$[\rho_{ee}]$	Polarizability tensor from incident to scattered electric field
ρ_f	Volume density of free charges [C/m ²]
$[\rho_{mm}]$	Polarizability tensor from incident to scattered magnetic field
ρ_w	Density of free water [kg/m ³]
$[\Sigma]$	Diagonal matrix of eigenvalues
σ	Mean two-way extinction
σ^0	Sigma nought or normalized backscattering coefficient
σ_{RCS}	Radar cross section of scatterer [m ²]
τ	Tilt angle of <i>Euler</i> rotations [°]
τ_e	Ellipticity angle of polarization ellipse [°]
τ_p	Pulse duration or pulse length [s]
τ_w	Distribution width of tilt angle [°]
Υ	Complex reflectivity of scatterer

ϕ	Absolute phase of electromagnetic wave [°]
ϕ_a	Phase along the <i>azimuth</i> direction [°]
ϕ_{ci}	Helicity scattering phase [°]
ϕ_d	Differential phase of dihedral component [°]
ϕ_e	Orientation angle of polarization ellipse [°]
ϕ_{li}	Linear scattering phase [°]
ϕ_{XX}	Absolute phase of polarimetric channel XX [°]
φ_x	x^{th} absolute phase of eigenvector [°]
χ	Spin angle of <i>Euler</i> rotations [°]
ψ	Depolarization angle or canting angle of <i>Euler</i> rotations [°]
ψ_h	Hydraulic potential
ψ_l	Distribution width of depolarization angle [°]
ψ_w	Distribution width of canting angle [°]
ω	Phase of transmitted signal [°]
ω_f	Angular frequency $\omega_f = 2\pi f$ [rad·s ⁻¹]
Ω	Conductivity [S·m ⁻¹]

Mathematical symbols:

$\arccos(x)$	Arccosine function
$\arcsin(x)$	Arcsine function
$\arcsinc(x)$	Arcsinc function
$\arctan(x)$	Arctangent function
$\cos(x)$	Cosine function
$\cosh(x)$	Hyperbolic cosine function
$\cot(x)$	Cotangent function = $1/\tan(x)$
$\csc(x)$	Cosecant function = $1/\sin(x)$
$eigenv(x)$	Eigenvalue operator
$eigenvec(x)$	Eigenvector operator
$exp(x)$	Exponential function
$diag(x)$	Diagonal matrix operator
$\ln(x)$	Natural logarithm function
$pdf(x)$	Probability density function
$rect(x)$	Rectangular window function
$sec(x)$	Secant function = $1/\cos(x)$
$\sin(x)$	Sine function
$sinc(x)$	Cardinal sine function = $\sin(x)/x$
$\sinh(x)$	Hyperbolic sine function

$span(x)$	Span operator
$tan(x)$	Tangent function
$Tr(x)$	Trace of a matrix x
$[x]$	Matrix of x
\underline{x}	Vector of x
$\langle x \rangle$	Expectation operator
\bar{x}	Mean value of x
$ x $	Absolute value of x
$\angle x$	Phase of x
$\Re[x]$	Real part of x
x'	Real part of x
$\Im[x]$	Imaginary part of x
x''	Imaginary part of x
Σ	Sum operator
\int	Integral operator
$ _{x=0}$	Insertion operator using x=0
*	Complex conjugate operator
\otimes	Convolution operator
$\otimes\otimes$	Two dimensional convolution operator
\simeq	Approximate value
T	Transpose operator
\circ	Element-wise multiplication operator (Hadamard operator)
$*T$	Hermitian operator
$\frac{\partial}{\partial x}$	Partial derivation of x
$\nabla \underline{v}$	$\text{Grad } \underline{v} = \frac{\partial v_x}{\partial x} \underline{x} + \frac{\partial v_y}{\partial y} \underline{y} + \frac{\partial v_z}{\partial z} \underline{z}$
$\nabla \cdot \underline{v}$	$\text{Div } \underline{v} = \frac{\partial v_x}{\partial x} + \frac{\partial v_y}{\partial y} + \frac{\partial v_z}{\partial z}$
$\nabla \times \underline{v}$	$\text{Curl } \underline{v} = \left(\frac{\partial v_z}{\partial y} - \frac{\partial v_y}{\partial z} \right) \underline{x} + \left(\frac{\partial v_x}{\partial z} - \frac{\partial v_z}{\partial x} \right) \underline{y} + \left(\frac{\partial v_y}{\partial x} - \frac{\partial v_x}{\partial y} \right) \underline{z}$
$\Delta \underline{v}$	$\text{Vector Laplacian } \nabla \cdot \nabla \underline{v} = \frac{\partial^2 v_x}{\partial x^2} \underline{x} + \frac{\partial^2 v_y}{\partial y^2} \underline{y} + \frac{\partial^2 v_z}{\partial z^2} \underline{z}$

Mathematical and physical constants:

c	Speed of light in vacuum $c = 1/\sqrt{\epsilon_0 \mu_0} = 2.997925 \cdot 10^8$ [m/s]
e	Euler's number $e \simeq 2,71828$
ϵ_0	Free space permittivity $\epsilon_0 = 8.854 \cdot 10^{-12}$ [F/m]
i	Imaginary number $i = \sqrt{-1}$
μ_0	Free space permeability $\mu_0 = 4\pi \cdot 10^{-7}$ [H/m]
π	Pi $\pi \simeq 3.141592$

Abstract

Soil conditions under vegetation cover and their spatial and temporal variations from point to catchment scale are crucial for understanding hydrological processes within the vadose zone, for managing irrigation and consequently maximizing yield by precision farming.

Soil moisture and soil roughness are the key parameters that characterize the soil status. In order to monitor their spatial and temporal variability on large scales, remote sensing techniques are required. Therefore the determination of soil parameters under vegetation cover was approached in this thesis by means of (multi-angular) polarimetric SAR acquisitions at a longer wavelength (L-band, $\lambda_c=23\text{cm}$). In this thesis, the penetration capabilities of L-band are combined with newly developed (multi-angular) polarimetric decomposition techniques to separate the different scattering contributions, which are occurring in vegetation and on ground. Subsequently the ground components are inverted to estimate the soil characteristics.

The novel (multi-angular) polarimetric decomposition techniques for soil parameter retrieval are physically-based, computationally inexpensive and can be solved analytically without any *a priori* knowledge. Therefore they can be applied without test site calibration directly to agricultural areas.

The developed algorithms are validated with fully polarimetric SAR data acquired by the airborne E-SAR sensor of the German Aerospace Center (DLR) for three different study areas in Germany. The achieved results reveal inversion rates up to 99% for the soil moisture and soil roughness retrieval in agricultural areas. However, in forested areas the inversion rate drops significantly for most of the algorithms, because the inversion in forests is invalid for the applied scattering models at L-band.

The validation against simultaneously acquired field measurements indicates an estimation accuracy (root mean square error) of 5-10vol.% for the soil moisture (range of *in situ* values: 1-46vol.%) and of 0.37-0.45cm for the soil roughness (range of *in situ* values: 0.5-4.0cm) within the catchment. Hence, a continuous monitoring of soil parameters with the obtained precision, excluding frozen and snow covered conditions, is possible.

Especially future, fully polarimetric, space-borne, long wavelength SAR missions can profit distinctively from the developed polarimetric decomposition techniques for separation of ground and volume contributions as well as for soil parameter retrieval on large spatial scales.

Zusammenfassung

Zur Verbesserung der hydrologischen Abflussmodellierung, der Flutvorhersage, der gezielten Bewässerung von landwirtschaftlichen Nutzflächen und zum Schutz vor Ernteaussfällen ist die Bestimmung der Bodenfeuchte und der Bodenrauhigkeit von grosser Bedeutung. Aufgrund der hohen zeitlichen sowie räumlichen Dynamik dieser Bodenparameter ist eine flächenhafte Erfassung mit hoher Auflösung und in kurzen zeitlichen Abständen notwendig. *In situ* Messtechniken stellen eine sehr zeit- und personalaufwändige Alternative dar, deshalb werden innovative Fernerkundungsverfahren mit aktivem Radar erprobt. Diese Aufnahmetechniken sind von Wetter- und Beleuchtungsverhältnissen unabhängig und besitzen zudem die Möglichkeit, abhängig von der Wellenlänge, in Medien einzudringen. Mit dem in dieser Arbeit verwendeten polarimetrischen Radar mit synthetischer Apertur (PolSAR) werden die Veränderungen der Polarisationen ausgewertet, da diese aufgrund der physikalischen Eigenschaften der reflektierenden Medien objektspezifisch verändert und gestreut werden. Es kann dadurch ein Bezug zwischen der empfangenen Radarwelle und den dielektrischen Eigenschaften (Feuchtegehalt) sowie der Oberflächengeometrie (Rauhigkeit) des Bodens hergestellt werden.

Da vor allem in den gemässigten Klimazonen die landwirtschaftlichen Nutzflächen die meiste Zeit des Jahres mit Vegetation bestanden sind, wurden in dieser Dissertation Verfahren entwickelt, um die Bodenfeuchte und die Bodenrauhigkeit unter der Vegetation erfassen zu können. Um die einzelnen Rückstreubeiträge der Vegetation und des Bodens voneinander zu trennen, wurde die Eindringfähigkeit von längeren Wellenlängen (L-band, $\lambda_c = 23\text{cm}$) mit neu entwickelten (multi-angularen) polarimetrischen Dekompositionstechniken kombiniert, um die Komponente des Bodens zu extrahieren und auszuwerten. Für die Auswertung wurden polarimetrische Streumodelle benutzt, um die Bodenkomponente zu modellieren und dann mit der extrahierten Bodenkomponente der aufgenommenen Daten zu vergleichen. Die beste Übereinstimmung von Modell und Daten wurde als die gegebene Bodencharakteristik gewertet und dementsprechend invertiert. Die neu entwickelten, polarimetrischen Dekompositionstechniken für langwelliges polarimetrisches SAR basieren auf physikalischen Prinzipien, benötigen wenig Rechenzeit, erfordern keine Kalibrierung und sind ohne Verwendung von *a priori* Wissen analytisch lösbar.

Um die entwickelten Algorithmen zu testen, wurden in drei verschiedenen Untersuchungsgebieten in Deutschland mit dem flugzeuggetragenen E-SAR Sensor des Deutschen Zentrums für Luft- und Raumfahrt (DLR) polarimetrische SAR Daten

aufgenommen. Die Auswertungen der PolSAR Daten haben bestätigt, dass die besten Invertierungsergebnisse mit langen Wellenlängen erzielt werden können (L-Band). Des Weiteren konnten bei der Bestimmung der Bodenfeuchte und der Bodenrauhigkeit hohe Inversionsraten erreicht werden (bis zu 99% der Untersuchungsfläche). Es hat sich gezeigt, dass die polarimetrischen Streumodelle bei der gegebenen Wellenlänge nicht für bewaldete Gebiete geeignet sind, was die Anwendbarkeit des Verfahrens auf landwirtschaftliche Nutzflächen einschränkt.

Die Validierung mit Bodenmessungen in den Untersuchungsgebieten, die zeitgleich zu den PolSAR Aufnahmen durchgeführt wurden, hat ergeben, dass eine kontinuierliche Beobachtung des Bodenzustandes (ausgenommen in Zeiten mit gefrorenem oder Schnee bedecktem Boden) mit einer Genauigkeit (Wurzel des mittleren quadratischen Fehlers) von 5-10vol.% für die Bodenfeuchte (*in situ* Messbereich: 1-46vol.%) und von 0.37-0.45cm für die Bodenrauhigkeit (*in situ* Messbereich: 0.5-4.0cm) möglich ist.

Besonders künftige Fernerkundungsmissionen mit langwelligem, voll polarimetrischem SAR können von den entwickelten Dekompositionstechniken profitieren, um die Vegetationskomponente von der Bodenkomponente zu trennen und die Charakteristik des Oberbodens flächenhaft zu bestimmen.

Part 1

Introduction

1.1. Motivation

Within the earth system the pedosphere acts as an interface between atmosphere, biosphere, lithosphere and hydrosphere. Several hydrological processes, like surface runoff, infiltration, plant water uptake and groundwater drainage, are affected by the spatial and temporal variations of soil moisture within the pedosphere, which are caused by boundary fluxes of energy and mass [39, 169, 17]. Both fluxes are inherently connected as the energy cycle initiates phase transitions in the hydrologic cycle [53, 40]. In this way solar irradiation triggers evaporation from soil and transpiration from vegetation resulting in a change of soil moisture content [260]. These changes are still very difficult to simulate by models due to the multiple and multi-dimensional dependencies of this highly varying parameter and therefore require a continuous monitoring [206].

Monitoring of soil moisture content reveals for instance the retention capabilities of the soil to store the infiltrated precipitation for a delayed and uncritical release in the discharge system [38, 28]. In this way hazard precautions, like flood forecasting and dam management, can be supported to identify critical catchment states (high pre-event soil moisture) before flooding events [39, 212]. Besides flood prevention in humid regions also agricultural management practices in semi-arid regions, like irrigation, benefit from the incorporation of soil moisture information leading to crop yield optimization in terms of precision farming [260, 322]. Another factor for yield optimization is the conservation of agricultural soils, which is supported by erosion models to investigate wind erosion in the arid case or mud-flow in the humid case [279, 10, 109]. These models require the soil roughness as spatially distributed input variable.

In practice, soil parameters, like soil roughness and soil moisture, are mostly acquired as single point measurements [35, 336, 54, 261, 44, 260], which are combined to wireless sensor networks in the case of soil moisture in order to enlarge the monitoring to the field scale [50, 30]. In addition, soil moisture sensing on this scale can be approached by geophysical methods, like Ground Penetrating Radar (GPR) [137] and Spatial Time Domain Reflectometry (STDR) [345], or Ground Albedo Neutron Sensing (GANS) [346, 259] using cosmic-ray probes. Whereas

for soil roughness sensing, laser scanning [244, 230] and stereo-photogrammetry [288, 202] are widely applied.

As the spatial upscaling from point or field-wide measurements to large scales is highly non-linear [208, 16, 82], remote sensing extends soil information retrieval from local point or field studies to spatial investigations on sub-catchment or entire catchment areas, including also very isolated regions [335, 81, 111, 183].

Since optical remote sensing of soil properties [165, 115] relies on daylight and clear weather conditions, RADAR-based methods turn out to be weather- and illumination-independent supporting a continuous soil monitoring strategy. Therefore passive microwave sensors (radiometers) [268, 145] as well as active microwave sensors (scatterometers [329, 36, 237], Synthetic Aperture Radars (SAR) [310, 312, 311]) are used on airborne or space-borne platforms [91].

Space-borne radiometers and scatterometers, like MIRAS on SMOS [166] and AMI on ERS [328], operate with low spatial resolution in the order of kilometers and high temporal resolution in the range of one acquisition every second or third day (in mid-latitudes), which is favorable for global monitoring purposes.

In contrary, SAR sensors, like PALSAR on ALOS [262] or ASAR on ENVISAT [85], acquire data in the order of decameters with a temporal resolution in the range of one acquisition every first to second week (in mid-latitudes), which fits to regional imaging purposes [231, 330, 49]. In order to combine both spatial scales for an spatially enhanced soil moisture retrieval on a global scale, an active-passive microwave sensor will be launched within the SMAP mission [97].

However, only SAR remote sensing enables a monitoring of the soil and its variability down to the field scale due to the high spatial resolution compared to the other microwave sensors. The sensitivity of SAR for soil characteristics is based on the fact that the transmitted Electro-Magnetic (EM) wave interacts with two key parameters of the soil system: Soil moisture and soil roughness. SAR sensors, used for soil parameter retrieval, acquire in different wavelengths (λ_c) ranging from X-band ($\lambda_c \simeq 3\text{cm}$, TerraSAR-X [5]), C-band ($\lambda_c \simeq 5\text{cm}$, ENVISAT-ASAR [188]), L-band ($\lambda_c \simeq 23\text{cm}$, ALOS [168]) to P-band ($\lambda_c \simeq 75\text{cm}$, AIRSAR [215]).

Moreover, SAR remote sensing has the capability to penetrate through natural media, like vegetation layers, especially with increasing wavelength [140, 66, 141]. Hence, also agricultural regions, which are most of the year covered by vegetation, can be investigated for their soil moisture and soil roughness conditions [191, 205]. This enables a continuous soil monitoring along the whole plant growth cycle, if the increasing scattering contribution from the vegetation is considered [124].

1.2. State-of-the-art

Concerning SAR remote sensing approaches, the first soil moisture and soil roughness analyses were carried out on single polarization intensities over bare soils leading to ill-posed inversion problems, because the soil moisture and the soil roughness influence are enclosed in one acquired signal [22, 88, 318, 250, 188, 323, 254]. With the emerging establishment of fully polarimetric SAR sensors, the observation space has been enlarged allowing to separate soil roughness from soil moisture influence for an unambiguous inversion of both soil parameters [127, 3, 142].

For bare soils, three different categories of EM scattering models, which relate the natural soil conditions with the characteristics of the scattered RADAR signature, can be distinguished: Empirical models, semi-empirical models and theoretical models [119, 186, 147].

As remote sensing relies on the understanding of Electro-Magnetic (EM) scattering on ground, only theoretical models can be considered as test site independent and form the basis of this thesis. Among these models, the Integral Equation Method (IEM) is widely applied for EM scattering of bare soils because of its broad range of applicability in terms of soil roughness classes [107, 108, 57]. More specialized scattering models can be introduced (from smooth to rough surface scattering): Small Perturbation Model (SPM) [255], Physical Optics (PO) Model [308] and Geometric Optics (GO) Model [312].

So far the investigation of soil parameters, like soil moisture or soil roughness, with polarimetric SAR remote sensing was constrained on bare soil areas due to the lack of retrieval algorithms including the influence of a vegetation cover [127]. The dielectric discontinuities in vegetation volumes, which can be for example stems, branches, twigs and leaves, scatter the waves in a complex manner [315, 278, 42, 190, 65].

In order to incorporate the influence of vegetation cover, different EM models have been developed to describe vegetation scattering [175, 314, 308, 33, 99, 246, 199], whereby the level of detail varies from a simple layer of uniformly shaped spheres [9] until sophisticated three dimensional models of the vegetation volume, including cylinders, dipoles and discs with their respective orientation distributions to simulate stems, branches and leaves [164, 87, 285, 337, 66]. Especially for the latter models, the amount of required input parameters exceeds by far the potential observable space of SAR remote sensing for direct inversion. On top, some of the modeling approaches also include the scattering contributions of the underlying

ground in order to simulate the total backscattered signature measured at the receiver.

Despite the variety of approaches, vegetation scattering models are mainly separated in two classes: Vector Radiative Transfer (VRT) models [55, 298, 184, 146, 339, 74] and coherent wave models [197, 58, 302, 301, 303, 192, 15]. The first class, including the widely used Water Cloud Model (WCM) [9] and the Michigan Microwave Canopy Scattering Model (MIMICS) [313], is solely bound to the law of energy conservation and calculates the incoherent sum of the independent scattering contributions to model the backscattering signature. In contrary, the second class, including the particle scattering model of [317], considers the coherent sum of all scattering contributions in the resolution cell as the backscattering signature and therefore preserves the phase information, which enables polarimetric and interferometric investigations [143, 197, 245, 87].

Unlike traditional retrieval approaches evaluating the total backscattered signature, an innovative soil information retrieval under vegetation cover should focus on the separation of the individual scattering contributions from the soil and the vegetation in order to extract only the soil properties for inversion. Therefore not one single, but several observations are necessary for a sufficient parameterization of the scattering scenario. Thus the observation space has to be enlarged using either multi-angular, multi-temporal or multi-frequency observations in combination with the polarimetric observations to tackle this decomposition problem. This thesis focus on the multi-angular polarimetric observation spaces for decomposition analyses of the single scattering components [151].

Polarimetric decompositions represent an established technique for separation of elementary scattering processes and have quite a history in polarimetric SAR remote sensing. First theoretical approaches towards polarimetric decompositions were formulated in the PhD thesis of *Huynen* in 1970 [139]. Since then a plurality of decompositions were proposed and comprehensive reviews on polarimetric decompositions were published in [71, 65, 182]. Basically, decompositions can be divided into coherent and incoherent types. Coherent decompositions, introduced by *Pauli* [65], *Krogager* [172] and *Cameron* [48], are based on the assumption that only one dominant scatterer is present within the resolution cell, which seems quite unlikely for natural environments.

In contrary, incoherent decompositions assume more than one scatterer in the resolution cell and are therefore based on second order statistics including depolarization effects. One type of incoherent decomposition analyzes the eigen-space (eigen-based decomposition) to separate different elementary scattering

processes, like the decompositions of *Cloude* [72], *Holm* [134] and *van Zyl* [319]. The other type is based on modeling the single scattering contributions by canonical EM models (model-based decomposition). The most prominent model-based decompositions were published by *Freeman & Durden* [106] and *Yamaguchi* [342, 343]. Originally, these decomposition methods were designed for forested environments including scattering interactions with the ground, with the tree trunk and the ground as well as with the tree canopy. Recently, the description of the polarimetric vegetation volume component was considerably extended by *Freeman* [105], *Neumann* [225] and *Arii* [6] using shape parameters for the scattering components (leaves, twigs, branches) and different orientation distributions within the tree canopy to characterize the polarimetric volume scattering of various tree species in a more detailed way. Besides the polarimetric decomposition models for forests, several (multi-angular) polarimetric decomposition methods for the more complex scattering scenario of agriculture, including for instance a depolarizing surface component due to soil roughness or an oriented vegetation component due to plant structure, are under development and provide the methodical foundation of this thesis [124, 159, 155, 156].

1.3. Scope and organization of thesis

The retrieval of soil characteristics by polarimetric SAR remote sensing is investigated for agricultural areas using longer wavelength to enable a soil parameter estimation along an entire vegetation growth cycle. The separation of the vegetation from the soil information should allow a continuous monitoring of soil parameters for hydrological, agricultural and hazard warning (flood, drought) applications. The following scientific questions are addressed and answered in this thesis:

- How and under which conditions can ground and vegetation scattering be separated by fully polarimetric SAR data?
- How and with which accuracy can soil parameters be inverted from fully polarimetric SAR data?
- What acquisition configuration/observation space is required for remote sensing of soil parameters under vegetation cover?

In order to address and answer these questions systematically, the thesis is structured as follows. Agricultural media are characterized by their physical properties

and their relevance with respect to Electro-Magnetic (EM) scattering in **Part 2**. The emphasis is put on parameterization of soil moisture, soil roughness and agricultural crops.

In **Part 3** the basic principles of SAR data acquisition and image formation are described, including the definition of the backscattering coefficient and the *speckle* phenomenon. The introduction of polarimetry starts from *Maxwell's* equations and leads to the *polarization ellipse* and the *Jones vector* formalism. Afterwards the concept of *polarimetric basis transformation* is presented to reveal the potential of polarimetry to acquire data in one polarization basis and transform it by unitary transformation in any other polarimetric basis. In addition, the scattering matrix is described combining the incident with the scattered field and containing the properties of the scatterer. A classification in coherent or distributed scatterers follows. In the case of distributed scatterers, the vectorization of the scattering matrix, yielding to the covariance and coherency matrix, is explained to include the statistical effects of polarimetric scattering. In the following, eigen-based and model-based decomposition techniques are introduced to analyze the backscattered signature for its elementary scattering processes.

The methodology for soil parameter retrieval using longer wavelength polarimetric SAR is explained in **Part 4**. This part starts with a review on bare soil scattering models. The theoretically based *X-Bragg* model [127] is described in detail representing an extension of the Small Perturbation Model (SPM) [255] for rough surface scattering. Afterwards polarimetric methods for soil moisture and soil roughness inversion close the chapter about bare soil parameter extraction. The next chapter deals with polarimetric scattering and decompositions for vegetated soils, in which the canonical scattering components for surface, dihedral and vegetation scattering are extended to describe rough surface (*X-Bragg*) and rough dihedral (*X-Fresnel*) scattering on ground as well as oriented/random vegetation scattering from variously shaped particles. Afterwards the entire polarimetric decomposition process is explained, including various possibilities to separate the volume from the ground components in a first step and to split the ground components into a surface and a dihedral scattering contribution in a second step. In the following the ground components are calculated exemplarily and inversion strategies for both ground components (surface, dihedral) are proposed. In the next chapter a hybrid polarimetric decomposition is introduced combining the benefits of model-based and eigen-based decompositions for soil moisture inversion under vegetation cover. Moreover, a multi-angular, model-based decomposition is described to further extend the observable space in order to invert soil moisture

under vegetation cover using several acquisitions with different incidence angles. In the end of this part the polarimetric inversion of soil roughness under vegetation cover is presented using a technique with ground-to-volume ratios.

In order to test the presented inversion algorithms, the experimental field measurement and polarimetric SAR data from three different study areas in Germany are described in **Part 5**. The data were acquired by DLR's E-SAR system within the AgriSAR, OPAQUE and SARTEO campaigns from 2006 to 2008, including a multi-temporal (AgriSAR) and a multi-incidence (OPAQUE 2008) data set for analyses. Within this Part, also the acquisition and the processing of the polarimetric SAR acquisitions are briefly described to explain the scene characteristics.

In **Part 6** the experimental results for the soil moisture and the soil roughness retrieval as well as for the validations with *in situ* measurements are presented together with a detailed discussion about potentials and limitations of the developed algorithms. In the beginning the results for soil moisture inversion on bare soils are analyzed, followed by the results for decomposition of the scattering contributions as well as for soil moisture inversion on vegetated soils. The entire set of retrieval methods ranging from single-angular to multi-angular polarimetric decomposition and inversion algorithms is investigated and evaluated leading finally to a conclusion for a best approach to invert soil moisture under vegetation cover. Thereafter the results for soil roughness retrieval on bare and on vegetated soils are evaluated against *in situ* measurements using polarimetric inversion techniques that are based on established methods and a novel algorithm.

Part 7 starts with a synopsis of each presented retrieval method for soil moisture and soil roughness summarizing the achieved results. This subsequently leads to the conclusions of the thesis research, which are splitted in the contributions to the science field and in an outlook. The outlook deals with the data assimilation of spatially distributed soil moisture into hydrological models and further SAR acquisition techniques for soil parameter retrieval.

Part 2

Characterization of agricultural media with respect to electro-magnetic scattering

In this Part the properties of agricultural media and their relevance with respect to EM scattering are presented. The characterization is focused on the description of bare soil and agricultural crops.

2.1. Soil characteristics

In a conceptual way the pedosphere can be defined as a three component medium, containing soil particles, soil water and soil air [198]. The soil particles, which form the soil matrix, depend mainly on the mineral composition, the soil texture and the soil structure leading to different soil aggregates [267,131]. The soil water and the soil air are filling the gaps between the soil particles within the matrix, as shown in Figure 1. In general, the soil characteristics are a natural result of the

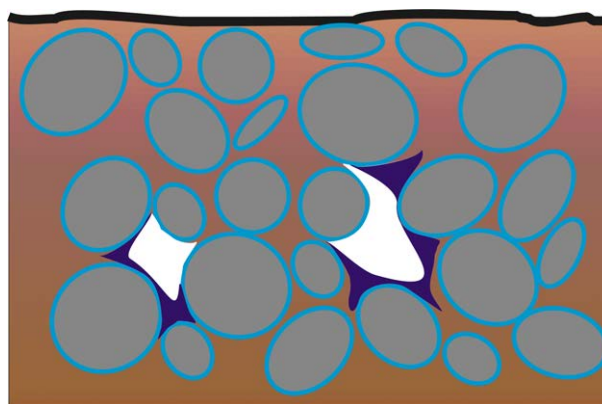


Figure 1: Simplified soil model (bright blue = adsorbed water, dark blue = water within the field capacity (FC), white = soil pores, brown = soil matrix).

different influences given by the basic rock, the topography, the climate and the vegetation [198]. All the single aspects can be incorporated to define an individual soil type with specific soil layers.

2.1.1. Soil moisture

The soil is an intermediate reservoir for storage, regulation and distribution of water guided by the saturation conditions within the soil volume, which specify the infiltration and evaporation rates. The proportion of water compared to soil particles is expressed by the soil moisture content. Depending on the consideration of the soil volume, the water fraction in the soil can be defined as volume fraction (volumetric soil moisture) m_v , using the water volume v_w divided by the total volume v_t , or as mass fraction (gravimetric soil moisture) m_g , dividing the mass of the water m_w by the mass of the dry soil m_{so} [198, 310]:

$$m_v = \frac{v_w}{v_t} \quad \text{and} \quad m_g = \frac{m_w}{m_{so}} \quad (1)$$

$$m_g = \frac{m_v \cdot \rho_w}{\rho_b}. \quad (2)$$

The volumetric and the gravimetric definitions are linked in Equation 2 by the density of the involved media: $\rho_w = m_w/v_w$ (water) and $\rho_b = m_{so}/v_t$ (bulk).

After precipitation the infiltrating water increases the moisture content of the soil. As long as the soil is not saturated by former lateral or vertical water inflow, the pore space of the soil is filled until a certain water storage capacity, which is defined as Field Capacity (FC) [267]. As soon as the moisture content exceeds the FC, percolation downwards into the ground water reservoir is observed due to saturated soil conditions. If the infiltration rates are stable over time, the water flow J can be described by *Darcy's law* along an infiltration distance s [18]

$$J = -K \cdot \frac{\partial \psi_h}{\partial s}. \quad (3)$$

K represents the hydraulic conductivity and ψ_h the hydraulic potential. If the soil medium is unsaturated, the water flow inside the porous medium can be described with the *Richards equation*, which represents the combination of the mass conservation equation with *Darcy's law* under pre-defined boundary conditions [256].

$$\frac{\partial m_v}{\partial t} = \frac{\partial}{\partial s} \left[K(m_v) \left(\frac{\partial \psi_h}{\partial s} + 1 \right) \right] \quad (4)$$

The soil water is available for plants, as long as the saturation does not drop below the Permanent Wilting Point (PWP). This point tags the minimal amount of soil water, which is necessary for plants not to wilt. Beyond this point soil water is tightly bound to the soil particles, known as adsorbed or bound water,

and is not available anymore for plants [130]. Therefore the amount of soil water between the Field Capacity (wet boundary) and the Permanent Wilting Point (dry boundary) is decisive for plant growth and plant cultivation.

Figure 2 illustrates the different stages of soil saturation (pF) as a function of soil water content and grain size [267]. Sandy, silty or clayey soils reveal a low,

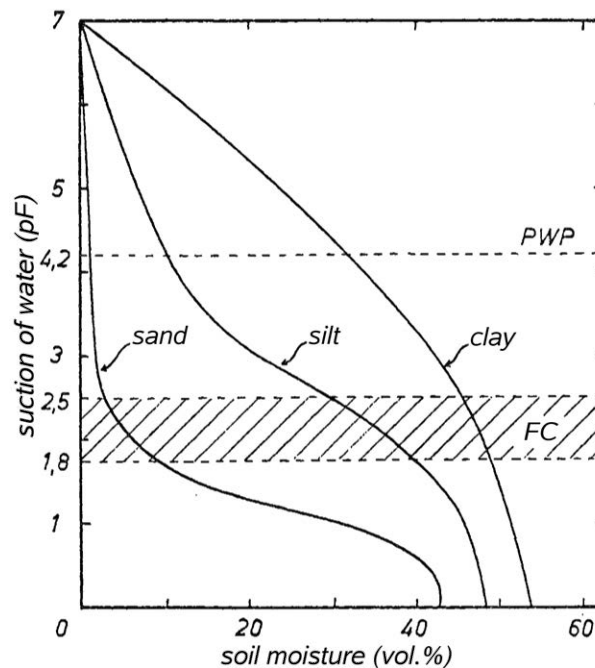


Figure 2: Relation between soil moisture and soil matrix suction depending on different grain size, (FC = field capacity, PWP = permanent wilting point) [267, p. 178].

intermediate or high water storage capacity. The increase in retention capabilities due to a stronger adsorption can be traced back to the increase of total surface area with decreasing grain diameter [267]. However, the complexity of retention capabilities in natural soils complicates simple conclusions about the behavior of water in porous media.

Nonetheless, the basis for this behavior is established by the special properties of water. The water molecule acts like a dipole due to the higher electronegativity of the oxygen atom compared to the two hydrogen atoms [198]. This difference of charge attracts water molecules to each other and other dipolar media. This attraction, known as hydrogen bonding, causes its high melting point, high surface tension, capillary action and leads to the dielectric properties of the soil [198]. The dielectric properties are described by the absolute complex dielectric constant ϵ_c ,

also called absolute complex permittivity [310]:

$$\epsilon_c = \epsilon'_c - i\epsilon''_c = \epsilon_0 (\epsilon'_r - i\epsilon''_r) \quad \text{with} \quad \epsilon_0 = 8.85 \cdot 10^{-12} [\text{F/m}]. \quad (5)$$

ϵ_c represents an absolute complex parameter, whereas ϵ_r stands for the relative complex dielectric constant. The latter describes the intrinsic properties of the medium and can be split into a real part (ϵ'_r) and an imaginary part (ϵ''_r). ϵ'_r corresponds to the relative permittivity and refers to the dielectric content of the medium. ϵ''_r is linked to the absorption capabilities of a medium and relates to its conductivity as well as its dielectric loss.

Hence, the dielectric constant of the soil represents a link between the soil moisture and the Electro-Magnetic (EM) waves of remote sensing devices. In order to transform the relative dielectric constant of the soil ϵ_r into soil moisture values, a variety of methods exists, which are grouped after *Wagner et al.* [326]:

- Empirical and semi-empirical conversion functions [296, 194, 284]
- Theoretical mixing models [130, 84, 90, 25, 263]
- Numerical mixing models [34, 306]
- Phenomenological relaxation models [327]
- Mixing models combined with phenomenological material equations [213, 243, 235]

In this thesis the empirical conversion function of *Topp et al.* is applied to convert the real part of the relative dielectric constant ϵ'_r into volumetric soil moisture using volume percent (m_v [vol.%] = $m_v \cdot 100$) as unit [296].

$$m_v = -5.3 \cdot 10^{-2} + 2.92 \cdot 10^{-2} \epsilon'_r - 5.5 \cdot 10^{-4} \epsilon'^2_r + 4.3 \cdot 10^{-6} \epsilon'^3_r. \quad (6)$$

Equation 6 represents a widely applicable polynomial for agricultural soils, because the dependence on soil texture is reduced to a minimum (only selection between organic and inorganic soils) [296]. Moreover, it does not need to be additionally parameterized, like for different soil fractions, which is favorable for inversion purposes [326].

The imaginary part of the relative dielectric constant ϵ''_r is not considered in the later analyses, in order to further reduce the parameter space and due to its minor role for longer wavelength ($f_c = 1.3\text{GHz}$) stated by the *Cole-Cole* diagram in [310, p.2024]. Focusing on the real part of the relative dielectric constant, a dry soil

sensed with microwaves of more than 5cm wavelength (λ_c) shows an ϵ_r' of 2-3, whereas a very moist soil has an ϵ_r' of 35-40 [90, 263]. This difference results in an increase of the backscattering signal with rising moisture content, in which the relation is non-linear.

Since the water is bound tightly to the matrix, as the soil is dry (bound water), the dielectric constant increases only slightly [98]. But if the content of soil moisture increases, the water dipoles will be able to move within the soil medium with relative ease (free water) compared to the bound water. The free water dipoles can be aligned stronger by the wave-induced electromagnetic field, which results in an increased backscatter signal and a shallower penetration into the soil [130]. Equation 7 defines the penetration depth δ_{pen} as [310]

$$\delta_{pen} \simeq \frac{\lambda_c \sqrt{\epsilon_r'}}{2\pi\epsilon_r''} \quad \text{assuming} \quad \epsilon_r' \gg \epsilon_r''. \quad (7)$$

In summary, the soil moisture content and the respective relative dielectric constant are a function of the fraction of bound to free water, the bulk soil density, the shape of the soil particles, the shape of the water inclusions, the salinity and the soil temperature [130]. Concerning the effect of soil temperature on ϵ_r , a significant change occurs, when the temperature drops below zero and the water in the soil starts to freeze [310]. Therefore the subsequently presented inversion algorithms for soil moisture and soil roughness are not applicable for frozen soils.

2.1.2. Soil roughness

The geometrical structure of the air-soil boundary is defined as soil roughness. For a precise description of this parameter, it would be necessary to know the exact size, shape and geometry of the single objects on the soil surface as well as their exact position to each other. Therefore the description of this component can be only a statistical approximation for natural media. Mostly two parameters are applied [80, 323]: The Root Mean Square (RMS)-height h_{rms} for the vertical roughness characterization and the correlation length l for the horizontal roughness characterization [89]. Thus the RMS-height along n samples is defined as [132, 47]:

$$h_{rms} = \sqrt{\frac{\sum_{i=1}^n (h_i - \bar{h})^2}{n-1}}, \quad (8)$$

where h_i is the vertical height at location i and \bar{h} represents the mean vertical height of the soil surface for n samples.

In order to specify the correlation length l , a surface correlation function ρ_{corr} , also known as Auto Correlation Function (ACF), has to be selected, which describes the statistical independence of two locations on a surface separated by a distance x . Regarding the shape of the surface correlation function exponential, *Gaussian* or power law distributions are commonly used [107, 47]:

$$\rho_{corr}(x) = \exp\left(-\frac{x^2}{l^2}\right) \quad \text{Gaussian} \quad (9)$$

$$\rho_{corr}(x) = \exp\left(-\sqrt{2}\frac{|x|}{l}\right) \quad \text{Exponential} \quad (10)$$

$$\rho_{corr}(x) = \exp\left(-\left(\frac{x}{l}\right)^n\right) \quad \text{Power law.} \quad (11)$$

In terms of measurements, the autocorrelation function describes the degree of correlation between the height h_i at location i and the height h_{i+x} at a horizontal distance x from i [132, 47]:

$$\rho_{corr} = \frac{\int h_i h_{i+x} di}{\int h_i^2 di}, \quad (12)$$

where the limits of integration extend over the overlapping segment of the height profiles. The horizontal displacement, at which the correlation ρ_{corr} drops below $1/e$, is defined as correlation length l [132].

With increasing soil roughness, agricultural fields can be grouped into three different tillage stages: Seedbed, harrowed and ploughed [223]. During ploughing clods are formed from the soil crumb turning the topsoil upside down. Within the harrowing process the clods are shredded. Finally the seedbed is prepared by flattening the surface using grubbers and rolls.

Due to these cultivation and tillage practices, agricultural fields have a preferential direction, which results in a superposition of different roughness components with a specific directionality and size (in decreasing sense): Topography, furrows, clods and soil aggregates [26, 323, 196]. Besides the mechanical soil tillage, also a natural change of roughness occurs along the vegetation growth period due to rain and root growth of the plants, which supports the idea of multi-temporal sensing of soil roughness [4].

Concerning remote sensing devices, it is of importance that the observable soil roughness differs with wavelength, meaning that with lower frequency the soil appears less rough. This turns for instance a smooth surface sensed in L-band

($\lambda_c=23\text{cm}$) into a rough surface in X-band ($\lambda_c=3\text{cm}$). With rising roughness, the incoherent scattering parts of the scattered wave gain importance compared to the coherent scattering part, which is sketched in Figure 3 for the three tillage stages. This process reaches its limit, when the scattering appears isotropic, like for a *Lambertian* scatterer. Therefore the remotely sensed parameter represents an

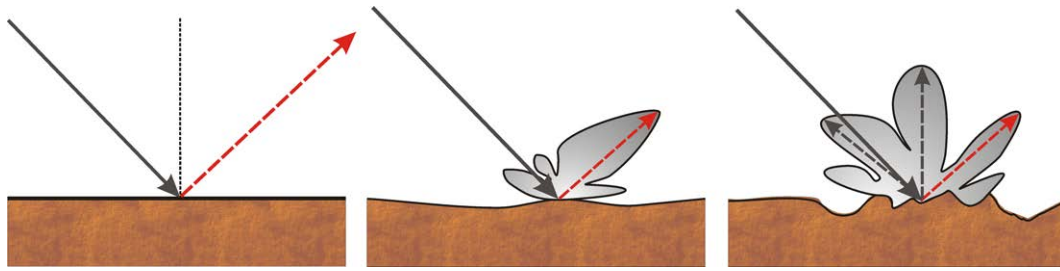


Figure 3: Different soil roughness levels (schematically); Left: Smooth surface (seedbed), middle: Semi-rough surface (harrowed field), right: Rough surface (ploughed field); Red solid arrows = coherent scattering part; Black dashed arrows = incoherent scattering parts.

‘effective’ vertical (ks) or horizontal (kl) roughness. It is expressed as a combination of the RMS-height h_{rms} or the correlation length l with the wave number k of the transmitted EM wave and therefore dimensionless:

$$ks = k \cdot h_{rms} = \frac{2\pi}{\lambda_c} \cdot h_{rms} \quad (13)$$

$$kl = k \cdot l = \frac{2\pi}{\lambda_c} \cdot l. \quad (14)$$

ks will be called ‘soil roughness’ in the course of this thesis.

2.2. Agricultural vegetation characteristics

The different agricultural crops, which are taken for field investigations and validation in this thesis, are cereals, oilseed rape, maize and sugar beet. For the cultivation of these crops some of the main influencing factors are the day light period, the light intensity, the soil temperature, the soil fertility and the water availability along the growing season [223]. The development stages of agricultural plants are characterized by the ‘BBCH’-scale of *Meier*, which represents a standard for discrimination of phenological stages along the growth period [207]:

- Germination / sprouting
- Leaf development

2.2. AGRICULTURAL VEGETATION CHARACTERISTICS

- Formation of side shoots / tillering
- Stem elongation or rosette growth / shoot development
- Development of harvestable vegetative plant parts or vegetatively propagated organs / booting
- Inflorescence emergence / heading
- Flowering
- Development of fruit
- Ripening / maturing of fruit
- Senescence / beginning of dormancy

As cereal plants represent the majority of crop types within the later investigated study areas, a visualization and a detailed description of their phenological development along the growing season are given in Figure 4 and as follows [224]:

The crop species, the seedbed preparation, the depth of seeding and the seeding time are decisive for the germination, the optimum coverage and the best density of plants per field [223]. A very dense and leaf-dominated canopy should be avoided to prevent disease development. The stem elongation is activated by special weather conditions like a cold period (vernalization) for winter cereals [223]. Within this stage the main shoot grows intensively and the head develops. Finally the flag leaf appears and indicates the finalization of this stage.

In the booting stage the head is pushed through the flag leaf and the heading follows as soon as the ears are directly visible. Flowering sets in, either before or after head emergence depending on the plant species. All plant heads flower within a few days and the grain (or fruit) development stages follow.

During the water ripe stage, kernel length and width develop and the size of the kernel increases distinctively containing mostly fluid, which turns into a milk-like fluid in the subsequent milk stage. When the consistency of the kernel content has a dough-like appearance, the soft dough stage is reached, which transforms with ongoing hardening of the kernel material to the hard dough stage. Now the kernel arrives at the maturity stage and the water content in the kernel drops to 30-40%. During the following kernel hard stage, the cereal plant becomes yellow and the water concentration lowers to 20-25%. If it drops below 13-14%, the harvest ripe stage sets in and the kernels can be stored after harvest without any additional drying.

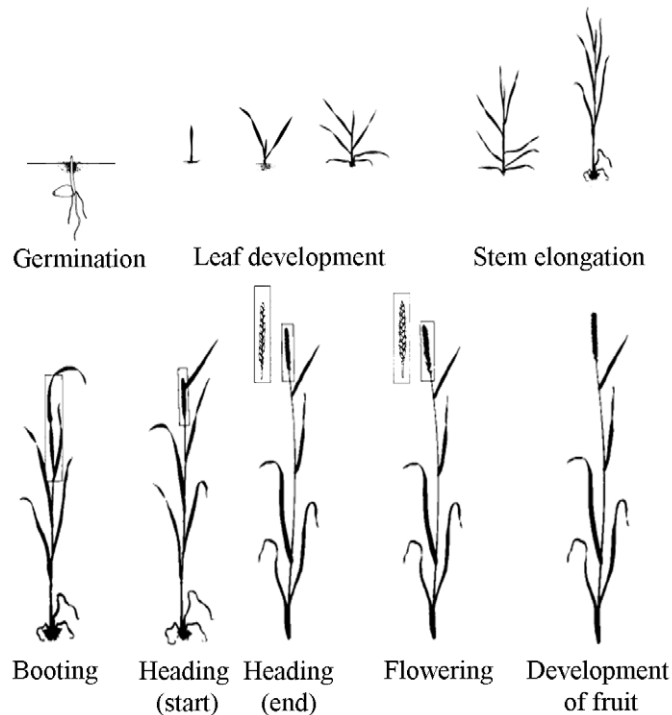


Figure 4: Phenology of cereal plants [207].

Further figures of phenological stages for oilseed rape, maize and sugar beet are attached in Appendix B. While oilseed rape develops very similar compared to cereal plants, maize and sugar beet do not have a booting stage and no side shoots are developed. Sugar beet can be grown together with wheat and barley in a crop rotation over several years, as the top leaves of the beet are serving as a natural fertilizer for the soil.

Concerning Electro-Magnetic (EM) scattering, the vegetation covers the soil surface by a certain height, density and extent, which is a function of seeding density, plant geometry and plant biomass. The geometry depends on the distribution of leaves, twigs, branches and stems. Each entity of the plant has its own shape and three dimensional orientation resulting in a distribution of orientations within the entire vegetation canopy, which has to be taken into account for EM modeling. In addition, the plant density and the moisture of plants within the field mainly determine the penetration of the EM waves into the vegetation canopy [65]. A variety of formulas is reported in literature to model the plant dielectric properties [241, 277, 78, 276, 170, 59, 307, 93, 300, 309, 289].

For reasons of space, only the two-phase dielectric mixture model of *Ulaby* is introduced exemplarily [310]. The two-phase mixture consists of a host material (i.e. air in the case of agriculture) and its inclusions (e.g. spheroidal particles). The inclusions are modeled as identically shaped particles of the same size as well as

orientation and represent the plants in the vegetation volume. The particles and the host material have the relative complex dielectric constants ε_i and ε_h , respectively. If both media are considered isotropic (uniform in all directions), ε_h and ε_i are scalars. If both media are assumed anisotropic, the relative complex dielectric constants change to positive semi-definite hermitian matrices [236, 65].

Moreover, the volume fraction v_i of the particles in the host material is defined by [310]

$$v_i = \frac{\pi \cdot x_1 \cdot x_2 \cdot x_3 \cdot N_e}{6}, \quad (15)$$

where x_1, x_2, x_3 are the particle dimensions along the x-, y- and z-axis. In addition, N_e represents the number of particles per unit volume of the mixture.

The relative complex dielectric constant of the two-phase mixture ε_m is described by the *Polder-Van Santen/de Loo*r formula [249, 83], assuming a small volume fraction ($v_i < 0.01$) and a low-frequency approach, where the particle dimensions are considerably smaller than the wavelength ($x_1, x_2, x_3 \ll \lambda_c$) [65]:

$$\varepsilon_m = \varepsilon_h + \frac{v_i(\varepsilon_i - \varepsilon_h)}{1 + L_i \left(\frac{\varepsilon_i}{\varepsilon_h} - 1 \right)}. \quad (16)$$

L_i is the particle shape function along the i^{th} dimension and is defined for the general three dimensional case as [310, 65]

$$L_1 = \int_0^\infty \frac{x_1 x_2 x_3}{16 \left(s + \left(\frac{x_1}{2} \right)^2 \right)^{\frac{3}{2}} \left(s + \left(\frac{x_2}{2} \right)^2 \right)^{\frac{1}{2}} \left(s + \left(\frac{x_3}{2} \right)^2 \right)^{\frac{1}{2}}} ds$$

$$L_2 = \int_0^\infty \frac{x_1 x_2 x_3}{16 \left(s + \left(\frac{x_1}{2} \right)^2 \right)^{\frac{1}{2}} \left(s + \left(\frac{x_2}{2} \right)^2 \right)^{\frac{3}{2}} \left(s + \left(\frac{x_3}{2} \right)^2 \right)^{\frac{1}{2}}} ds \quad (17)$$

$$L_3 = \int_0^\infty \frac{x_1 x_2 x_3}{16 \left(s + \left(\frac{x_1}{2} \right)^2 \right)^{\frac{1}{2}} \left(s + \left(\frac{x_2}{2} \right)^2 \right)^{\frac{1}{2}} \left(s + \left(\frac{x_3}{2} \right)^2 \right)^{\frac{3}{2}}} ds.$$

$$\text{General condition: } L_1 + L_2 + L_3 = 1. \quad (18)$$

A closed form of the integrals in Equation 17 exists, when spheroids (ellipsoid with two equal axes $x_1 = x_2$) are used as particles in the two-phase mixture [310]. In order to simulate different plant structures or different phenological stages of a plant, three canonical shapes are proposed:

1. Prolate spheroid ($x_1=x_2$ and $x_3>x_1$)

$$L_3 = \frac{1-e_e^2}{2e_e^3} \left(\ln \left(\frac{1+e_e}{1-e_e} \right) - 2e_e \right)$$

$$L_1 = L_2 = \frac{1-L_3}{2} \quad (19)$$

$$e_e = \sqrt{1 - \left(\frac{x_1}{x_3} \right)^2}.$$

2. Sphere ($x_1=x_2=x_3$)

$$L_1 = L_2 = L_3 = \frac{1}{3}. \quad (20)$$

3. Oblate spheroid ($x_1=x_2$ and $x_3<x_1$)

$$L_3 = \frac{1}{e_e^2} \left(1 - \frac{\sqrt{1-e_e^2}}{e_e} \arcsin(e_e) \right)$$

$$L_1 = L_2 = \frac{1-L_3}{2} \quad (21)$$

$$e_e = \sqrt{1 - \left(\frac{x_3}{x_1} \right)^2}.$$

According to Equations 19, 20 and 21 three differently shaped vegetation volumes can be formed: A volume of prolate spheroids, a volume of spheres and a volume of oblate spheroids. The three vegetation volumes are shown in Figure 5. While

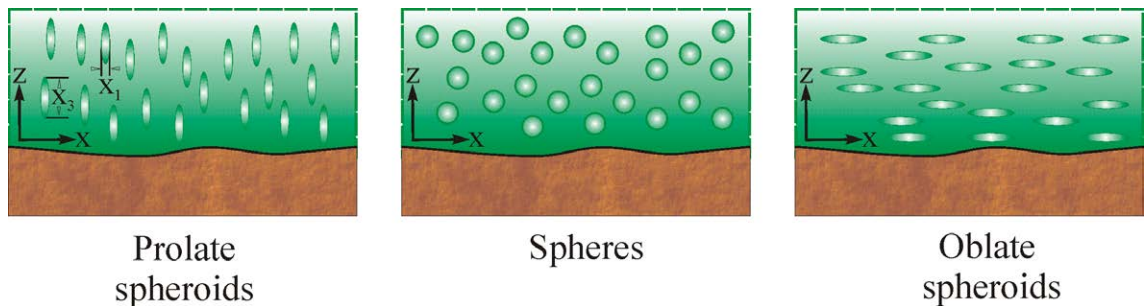


Figure 5: Three vegetation volumes with different plant inclusions for the two-phase dielectric mixture model of *Ulaby*: Prolate spheroids ('needles') modeling a thin, stalk-dominated crop (left), spheres (middle), oblate spheroids ('discs') modeling a broad, leaf-dominated crop (right) [310, 65].

the position of the single particles is random within the vegetation layer, the orientation is identical leading to strongly oriented vegetation volumes in the case of spheroids. For this case the wave propagation is anisotropic within the media and consequently the relative complex dielectric constant enlarges from a scalar ϵ_m , like in the case of spheres as particles, to a matrix $[\epsilon_m]$. In addition, it is assumed for simplicity that the coordinate systems (x, y, z) of the EM wave and of the particles coincide. Hence, the full matrix $[\epsilon_m]$ reduces to a diagonal matrix $[\epsilon_m] = \text{diag}(\epsilon_m^x, \epsilon_m^y, \epsilon_m^z)$ [65]. Equations 22 to 24 introduce the relative complex dielectric constant of the two-phase mixture ϵ_m for the three canonical vegetation volumes of Figure 5 [310, 65]:

1. Vegetation volume of prolate spheroids like ‘needles’ ($L_1=L_2=0.5$ and $L_3=0$)

$$\begin{aligned}\epsilon_m^x &= \epsilon_h \left(1 + 2v_i \frac{\epsilon_i - \epsilon_h}{\epsilon_i + \epsilon_h} \right) \\ \epsilon_m^y &= \epsilon_m^x \\ \epsilon_m^z &= \epsilon_h + v_i(\epsilon_i - \epsilon_h).\end{aligned}\tag{22}$$

2. Vegetation volume of spheres ($L_1=L_2=L_3$)

$$\epsilon_m = \epsilon_h \left(1 + 3v_i \frac{\epsilon_i - \epsilon_h}{\epsilon_i + 2\epsilon_h} \right).\tag{23}$$

3. Vegetation volume of oblate spheroids like ‘discs’ ($L_1=L_2=0$ and $L_3=1$)

$$\begin{aligned}\epsilon_m^x &= \epsilon_h + v_i(\epsilon_i - \epsilon_h) \\ \epsilon_m^y &= \epsilon_m^x \\ \epsilon_m^z &= \epsilon_h \left(1 + v_i \left(1 - \frac{\epsilon_h}{\epsilon_i} \right) \right).\end{aligned}\tag{24}$$

Totally oriented vegetation volumes, like in Equations 22 and 24, represent an exceptional case in nature. Therefore the case of a randomly oriented vegetation volume of spheroids should be also taken into account resulting in

$$\epsilon_m = \epsilon_h + \frac{v_i}{3}(\epsilon_i - \epsilon_h) \sum_{i=1,2,3} \frac{1}{1 + L_i \left(\frac{\epsilon_i}{\epsilon_h} - 1 \right)}.\tag{25}$$

Besides the general formula in Equation 25, ϵ_m for a randomly oriented volume of prolate spheroids is obtained by

$$\epsilon_m = \epsilon_h + \frac{v_i(\epsilon_i - \epsilon_h)(5\epsilon_h + \epsilon_i)}{3(\epsilon_h + \epsilon_i)} \quad (26)$$

and for a randomly oriented volume of oblate spheroids by

$$\epsilon_m = \epsilon_h + \frac{v_i}{3}(\epsilon_i - \epsilon_h) \left(2 + \frac{\epsilon_h}{\epsilon_i} \right). \quad (27)$$

In conclusion, the orientation and the shape of the inclusions (particles) characterize the dielectric properties of the vegetation layer and therefore the influence of the vegetation layer on the polarization signature. Hence, both parameters will be included in the modeling of polarimetric scattering from vegetation volumes in Chapter 4.2.1.3..

As vegetation is not static over time, it changes its phenology resulting in a growth cycle, which is mostly driven by the different seasons. The vegetation change represents a challenge for a continuous soil moisture monitoring in agricultural areas due to the non-stationarity of the scattering scenario. Thus several volume cases, presented above, might be applicable within a growth cycle of a plant. This has to be considered in the later developed EM scattering models used for parameter inversion in agricultural environments.

Part 3

SAR principles and polarimetry

In this Part the principles of SAR and the basic concepts of SAR polarimetry are introduced.

3.1. SAR principles

In the middle of last century, *Wiley* discovered the SAR principle and since then numerous airborne and space-borne SAR systems have been operated successfully [75]. SAR is an active microwave imaging technique widely weather- and illumination-independent, allowing high spatial resolution imaging of large areas. Therefore this remote sensing technique qualifies for diverse environmental applications, like monitoring agricultural regions, forests, glaciers, oceans and urban areas [312, 310, 76, 132, 94].

3.1.1. Imaging geometry

SAR is based on a coherent imaging technique and acquires two-dimensional reflectivity maps of a given scene. In a conceptual description the transmitter, mounted on a space- or airborne platform, transmits a microwave pulse in slant direction towards the ground. After interaction with the ground the scattered pulse is received by the receiver. If transmitter and receiver are co-located, the acquisition system is called monostatic, which is the case for the airborne data used in this thesis. Differently, bistatic systems have a spatially separated transmitter and receiver.

Figure 6 shows the standard imaging geometry of a SAR system. The platform moves along *azimuth* in flight direction. The microwave pulses are transmitted perpendicular to *azimuth* in Line of Sight (LoS) direction (*slant range*), under a given incidence angle θ as depicted in Figure 7. If the terrain is flat, the incidence angle θ is equal to the Radar Look Angle (RLA) θ_r . The illuminated area on the ground is known as RADAR *footprint*. As the platform moves along the *azimuth* direction, the *swath* (l_s) on ground is generated. As airborne data are exclusively used in this thesis, the earth curvature is neglected in this conceptual description. However, terrain slopes influence the imaging geometry, as shown in Figure 8. The slope angle α_{sl} and the Local Incidence Angle (LIA) θ_l are defined with respect to

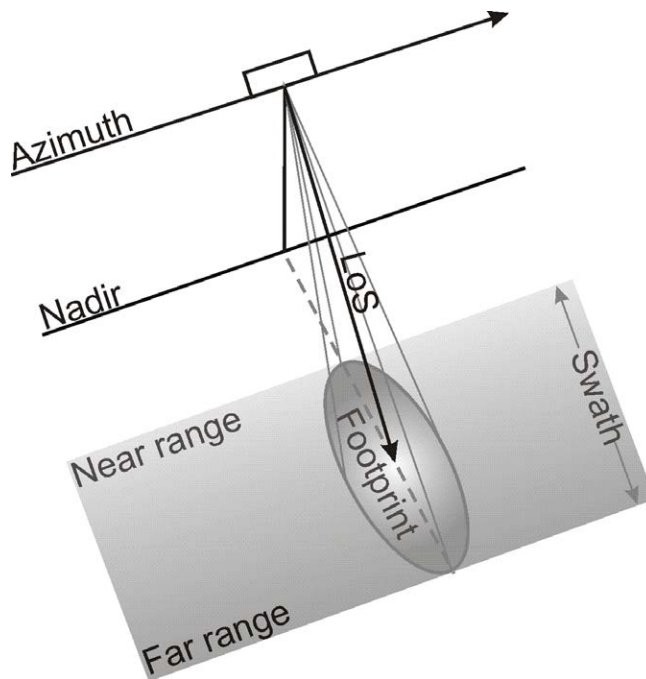


Figure 6: SAR imaging geometry; LoS=Line of Sight.

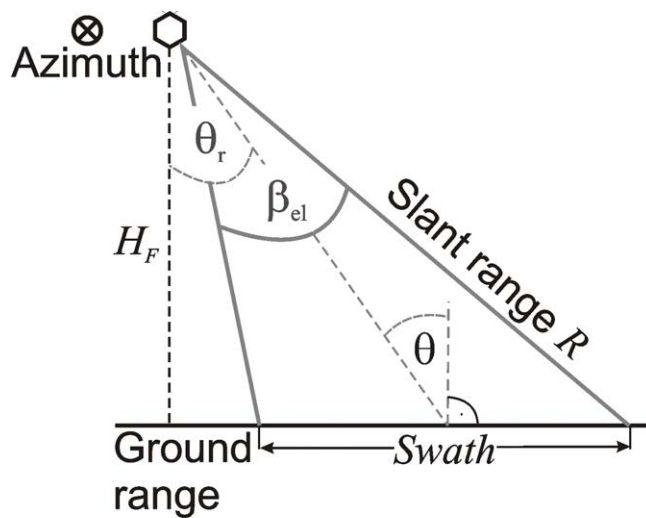


Figure 7: Imaging geometry in range direction; θ_r =Radar Look Angle, θ =incidence angle, H_F =flight altitude, β_{el} =antenna opening angle in elevation.

the surface normal

$$\theta_l = \theta_r - \alpha_{sl}. \quad (28)$$

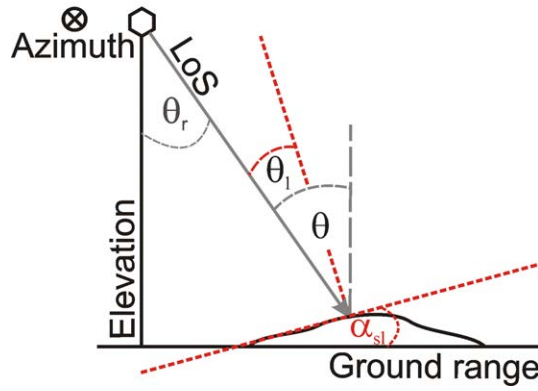


Figure 8: Acquisition geometry involving terrain slopes α_{sl} for local incidence; θ_l =Local Incidence Angle.

3.1.2. Imaging resolution

The resolution of a SAR system is defined in *slant range* and in *azimuth* direction. The pulses of the SAR system, received from different scatterers, are resolved due to their time delay. Therefore the resolution in *slant range* direction $\delta_{r_{GRAR}}$ is a function of the pulse duration (pulse length) τ_p [76]

$$\delta_{r_{GRAR}} = \frac{c \cdot \tau_p}{2}. \quad (29)$$

c is the velocity of the EM wave. As it is rather difficult to increase the *slant range* resolution by transmitting shorter pulses, the use of frequency modulated pulses has been established. Commonly, a linear Frequency Modulated (FM) pulse of the form $s(t) = \exp(i\pi f_{cr} t^2)$, called *chirp* (cf. Chapter 3.1.3.), is applied, with a bandwidth $B_w = |f_{cr}| \tau_p$ leading to the following *slant range* resolution of a SAR [76]

$$\delta_{r_{SSAR}} = \frac{c}{2B_w}. \quad (30)$$

f_{cr} is known as the range chirp rate. The *azimuth* resolution of a real antenna at a certain *slant range* distance R is given by [75]

$$\delta_{az_{RAR}} \simeq \frac{\lambda_c}{D_{az}} R \simeq \beta_{az} R, \quad (31)$$

where D_{az} represents the physical dimension of the antenna in *azimuth* direction, and λ_c the radiation wavelength. The opening angle of the antenna β_{az} in *azimuth* direction, is described as [75]

$$\beta_{az} \simeq \frac{\lambda_c}{D_{az}}. \quad (32)$$

Equation 31 describes the resolution of a Real Aperture Radar (RAR) in *azimuth* direction. In order to obtain a constantly high resolution across the whole swath, i.e. with varying *slant range* distances, *Wiley* proposed the formation of a synthetic aperture in *azimuth* direction by operating the antenna in a pulsed mode, as indicated in Figure 9. As the same scatterer is then imaged multiple times during overflight, a large antenna (with a narrow beam) can be synthesized by coherently combining the received pulses.

The antenna opening angle for the synthetic aperture is obtained from $\beta_{az_{SAR}} \simeq D_{az}/(2R)$, accounting for the two-way path length $2R$ [75]. Using this relation, the spatial resolution in *azimuth* direction of a SAR $\delta_{az_{SAR}}$ becomes independent of the *slant range* distance as well as of the wavelength λ_c and depends only on the dimension of the antenna in *azimuth* D_{az} [75]

$$\delta_{az_{SAR}} \simeq \beta_{az_{SAR}} R \simeq \frac{D_{az}}{2}. \quad (33)$$

It is important to note, that the image resolution is not the same as the image

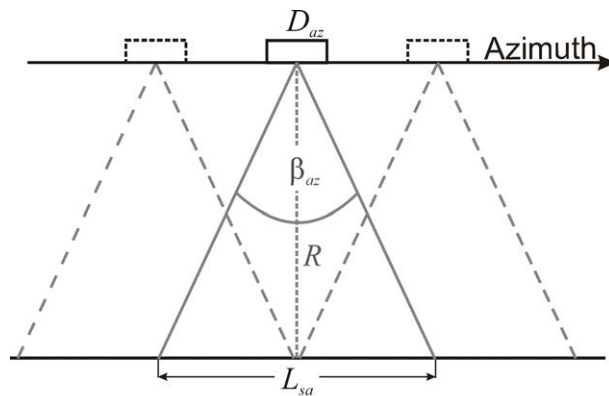


Figure 9: Formation of synthetic aperture L_{sa} .

sampling. The *range* and *azimuth* sampling (Δ_{rg} , Δ_{az}) are defined as [75]

$$\Delta_{rg} = \frac{c}{2} \cdot f_{rg}^{-1} \quad \text{and} \quad \Delta_{az} = v_p \cdot PRF^{-1}, \quad (34)$$

where f_{rg} is the *range* sampling frequency and *PRF* the Pulse Repetition Frequency in *azimuth*. v_p represents the speed of the platform.

3.1.3. Impulse response

After the definition of the acquisition geometry, the SAR image formation is addressed for the simple case of a point-like scatterer. The transmitted linearly FM pulse s_{tr} can be described by a real-valued envelope w_r , which is a *rect*-function, and a phase term including the carrier frequency f_0 and the *range* chirp rate f_{cr} [51, 222]

$$s_{tr} = w_r(t) \exp(i(2\pi f_0 t + \pi f_{cr} t^2)). \quad (35)$$

The received pulse from the point scatterer s_{re} at distance R_p from the sensor can be understood as a time delayed and attenuated replica of the transmitted pulse [51, 222]

$$s_{re}(t; R_p) = \Upsilon w_r\left(t - \frac{2R_p}{c}\right) \exp\left(i\pi\left(2f_0\left(t - \frac{2R_p}{c}\right) + f_{cr}\left(t - \frac{2R_p}{c}\right)^2\right)\right), \quad (36)$$

where the time delay of the received pulse is given by $t_r = 2R_p/c$. Υ represents the complex reflectivity of the scatterer. After demodulation, the carrier frequency is removed leading to the baseband signal [51, 222]

$$s_{reb}(t; R_p) = \Upsilon w_r\left(t - \frac{2R_p}{c}\right) \exp\left(i\pi\left(-\frac{4f_0 R_p}{c} + f_{cr}\left(t - \frac{2R_p}{c}\right)^2\right)\right). \quad (37)$$

As the platform is moving in *azimuth* direction a and consecutively transmitting pulses, the point scatterer is imaged multiple times. The received pulses correspond to different *slant range* distances R_p , which can be approximated as [77]

$$R_p(R_0; a) = \sqrt{R_0^2 + a^2} \simeq R_0 \left(1 + \frac{a^2}{2R_0^2}\right) = R_0 + \frac{a^2}{2R_0} = R_0 + \frac{(v_p(t - t_a))^2}{2R_0}, \quad (38)$$

where R_0 denotes the *slant range* distance, when the scatterer is located within the LoS-plane. t_a is the time corresponding to the beam center in *azimuth* direction. The phase derivative in the *azimuth* direction leads to the *azimuth* frequency f_a at time t

$$f_a(t) = \frac{\partial \phi_a}{2\pi \partial t} = \frac{\partial\left(\frac{-4\pi R_p}{\lambda_c}\right)}{2\pi \partial t} = \frac{-2v_p^2(t - t_a)}{\lambda_c \sqrt{R_0^2 + v_p^2(t - t_a)^2}} \approx \frac{-2v_p^2(t - t_a)}{\lambda_c R_0} = -f_{ca}(t - t_a). \quad (39)$$

f_{ca} stands for the chirp rate in *azimuth* direction. Consequently, an approximately linear frequency variation is introduced by the movement of the platform. Using

Equation 39 and considering, that $c \gg v_p$, the recorded two dimensional signal can be approximated as

$$s_{reb}(t; a) \simeq \Upsilon w_r \left(t - \frac{2R_p}{c} \right) w_a \left(\frac{t - t_a}{t_t} \right) \exp \left(-\frac{i4\pi f_0 R_p}{c} \right) \cdot \underbrace{\exp \left(i\pi f_{cr} \left(t - \frac{2R_p}{c} \right)^2 \right)}_{\text{range chirp}} \underbrace{\exp \left(-i\pi f_{ca} (t - t_a)^2 \right)}_{\text{azimuth chirp}}, \quad (40)$$

where w_a represents the envelope of the antenna pattern in *azimuth* direction, assumed to be of rectangular shape, and t_t the total illumination time of the scatterer in *azimuth* direction.

The concept of ‘matched filtering’ is applied for obtaining the desired resolution of a SAR image s_{im} , which comprises a two dimensional convolution of the recorded signal of Equation 40 with its two dimensional, time reversed and complex conjugated chirp replica $s_{rep}^*(-t_r - t, -t_a - t)$

$$s_{im}(t; a) = s_{reb}(t; a) \otimes \otimes s_{rep}^*(-t_r - t, -t_a - t). \quad (41)$$

$\otimes \otimes$ defines the two dimensional convolution and $*$ is the complex conjugate operator. The compressed signal of a point scatterer is finally obtained by

$$s_{comp}(t; a) \simeq \Upsilon \exp \left(-\frac{i4\pi f_0 R_p}{c} \right) \text{sinc}(\pi f_{cr} t_r t) \text{sinc}(\pi f_{ca} t_t), \quad (42)$$

where $\text{sinc}(x) = \sin(x)/x$. A thorough description of SAR signal processing and image formation, using several algorithms in different implementations, is given in [75, 294, 51, 104, 95, 76, 19].

3.1.4. Backscattering coefficient

The acquisition system and the scatterer are linked by the *RADAR equation*:

$$P_r = \frac{P_t G_t A_r}{(4\pi)^2 R_p^4} \sigma_{RCS}. \quad (43)$$

Assuming a point-like scatterer in the far field of a lossless medium [143, 312], the received power P_r can be written as a function of the

- P_t : Transmitted power
- G_t : Gain of transmitting antenna

- A_r : Effective aperture of receiving antenna, linked to the receiver gain G_r by $A_r = (\lambda_c^2 G_r)/(4\pi)$
- R_p : Range distance to the scatterer
- σ_{RCS} : Radar cross section of the scatterer
- $1/(16\pi^2 R_p^4)$: Two way radial spreading loss.

The Radar Cross Section (RCS) σ_{RCS} expresses the cross section of an idealized isotropic scatterer that generates the equivalent scattered power density as the observed scatterer in direction of the receiving antenna [182]. It depends on the geometry (orientation, shape, size) and properties (dielectric content, density) of the scatterer as well as on system and acquisition parameters (wavelength, local incidence).

For natural media, with distributed scatterers (cf. Chapter 3.2.), the averaged $\langle \sigma_{RCS} \rangle$ is used, which is normalized by unit ground area A_{gr} leading to the normalized backscattering coefficient σ^0 [252, 182]

$$\sigma^0 = \left\langle \frac{\sigma_{RCS}}{A_{gr}} \right\rangle \quad \text{with} \quad A_{gr} = \frac{\Delta_{rg} \Delta_{az}}{\sin(\theta_l)}. \quad (44)$$

3.1.5. Speckle reduction

Inherent of SAR image data is a granular effect, also known as *speckle*, which is caused by the interference of the signals received from differently located scatterers within the resolution cell [118]. As the detailed structure within each resolution cell is not known, the properties of the *speckle* phenomenon are described statistically [181].

Speckle can be modeled by a multiplicative noise model [182] and can be reduced by multi-looking or filtering techniques to enhance the radiometric resolution on the cost of spatial resolution [182, 180, 179].

Multi-looking is performed by an averaging operation. The averaging can be done in the spatial domain by including the neighboring pixels or in the frequency domain by splitting the synthetic aperture in several sub-apertures and add them incoherently [101, 182]. For quantization the effective number of looks L_{ne} can be approximated by the number of looks L_n using [133, 299]

$$L_{ne} = \frac{\Delta_{rg} \Delta_{az}}{\delta_{rg} \delta_{az}} \cdot L_n. \quad (45)$$

3.2. Polarimetry

SAR polarimetry is based on the different oscillation patterns of the transmitted/received pulses, known as polarizations. The polarization of the transmitted pulse is modified during the interaction with the scatterers. The modification is inherently linked to the geometry (size, shape, orientation) and the physical properties (dielectric content, density) of the scatterer. Therefore, polarimetry provides unique information for the physical interpretation of scattering processes and for physical parameter retrieval.

Basically, EM waves are described by the *Maxwell* equations [144]

$$\nabla \times \underline{E}(\underline{R}, t) = -\frac{\partial \underline{B}(\underline{R}, t)}{\partial t} \quad (46)$$

$$\nabla \times \underline{H}(\underline{R}, t) = \underline{J}(\underline{R}, t) + \frac{\partial \underline{D}(\underline{R}, t)}{\partial t} \quad (47)$$

$$\nabla \cdot \underline{D}(\underline{R}, t) = \rho_f(\underline{R}, t) \quad (48)$$

$$\nabla \cdot \underline{B}(\underline{R}, t) = 0, \quad (49)$$

where $\nabla \times \underline{E}(\underline{R}, t)$, $\nabla \times \underline{H}(\underline{R}, t)$, $\nabla \cdot \underline{D}(\underline{R}, t)$, $\underline{J}(\underline{R}, t)$, $\rho_f(\underline{R}, t)$, $\nabla \cdot \underline{B}(\underline{R}, t)$ represent the space-time variable electric field, magnetic field, electric induction, total current density, volume density of free charges and magnetic induction, respectively. Assuming a linear (free of saturation and hysteresis) and source-free medium, the wave equation can be defined as [182]

$$\Delta \underline{E}(\underline{R}, t) - \mu_c \varepsilon_c \frac{\partial^2 \underline{E}(\underline{R}, t)}{\partial t^2} - \mu_c \Omega \frac{\partial \underline{E}(\underline{R}, t)}{\partial t} = -\frac{1}{\varepsilon_c} \frac{\partial \nabla \rho_f(\underline{R}, t)}{\partial t}. \quad (50)$$

Due to the homogeneity and isotropic nature of the medium assumed, the absolute complex permittivity ε_c , the absolute complex permeability μ_c and the conductivity Ω are scalars and independent of the fields. For a solution of Equation 50, monochromatic plane waves with a constant complex amplitude $|\underline{E}_c|$ are assumed. Hence, the right side of Equation 50 becomes zero and a complex expression $\underline{E}_c(\underline{R})$ of the monochromatic time-space electric field can be defined as [182]

$$\underline{E}_c(\underline{R}, t) = \Re [|\underline{E}_c| \exp(-ik_{pr}\underline{R})] \quad \text{regarding} \quad \underline{E}_c(\underline{R}, t) \cdot \hat{k} = 0, \quad (51)$$

where \Re represents the real part of a complex number and \underline{k}_{pr} is the propagation vector defined by the direction of propagation \hat{k} and the complex wave number k_c

$$k_c = k'_c - ik''_c = \omega_f \sqrt{\mu_c \epsilon'_c} \sqrt{1 - i \frac{\epsilon''_c}{\epsilon'_c}}. \quad (52)$$

The corresponding propagation Equation can be written as [182]

$$\Delta \underline{E}(\underline{R}) + \omega_f^2 \mu_c \epsilon'_c \left(1 - i \frac{\Omega}{\epsilon'_c \omega_f}\right) \underline{E}(\underline{R}) = \Delta \underline{E}(\underline{R}) + k_c^2 \underline{E}(\underline{R}) = 0, \quad (53)$$

incorporating the absolute complex dielectric constant ϵ_c (cf. Equation 5) [182]

$$\epsilon_c = \epsilon'_c - i\epsilon''_c = \epsilon'_c - i \frac{\Omega}{\omega_f}. \quad (54)$$

If the electrical field is defined in an orthogonal basis $(\hat{x}, \hat{y}, \hat{z})$ with $\hat{k} = \hat{z}$, the electric field in the time domain, assuming a loss-free medium, can be described as [182]

$$\underline{E}(z, t) = \begin{bmatrix} E_{0x} \cos(\omega_f t - k_c z + \phi_x) \\ E_{0y} \cos(\omega_f t - k_c z + \phi_y) \\ 0 \end{bmatrix}. \quad (55)$$

Figure 10 outlines the *polarization ellipse* as a two dimensional representation of

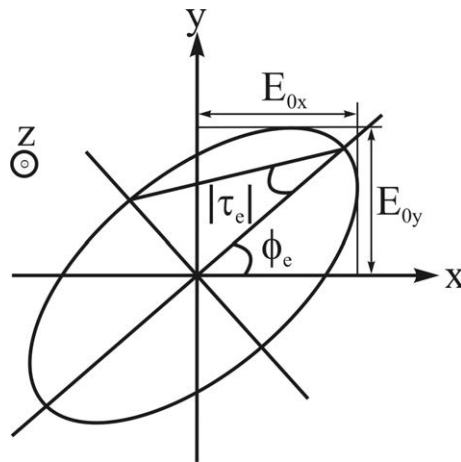


Figure 10: Conceptual, two dimensional representation of a *polarization ellipse* with orientation angle ϕ_e and ellipticity angle τ_e .

wave polarization. The ellipse is parameterized by three variables [182]:

1. The amplitude of the ellipse:

$$A_e = \sqrt{E_{0x}^2 + E_{0y}^2} \quad (56)$$

2. The ellipse orientation angle $\phi_e \in [-\pi/2, \pi/2]$:

$$\tan(2\phi_e) = 2 \frac{E_{0x}E_{0y}}{E_{0x}^2 - E_{0y}^2} \cos(\delta_e) \quad \text{and} \quad \delta_e = \phi_y - \phi_x \quad (57)$$

3. The ellipse aperture or ellipticity angle $\tau_e \in [-\pi/4, \pi/4]$:

$$|\sin(2\tau_e)| = 2 \frac{E_{0x}E_{0y}}{E_{0x}^2 + E_{0y}^2} |\sin(\delta_e)|. \quad (58)$$

The sense of rotation is determined by the sign of the ellipticity angle τ_e , while looking in the direction of propagation \hat{z} . A right hand rotation is linked to a negative sign, whereas a positive sign is connected to a left hand rotation [29].

An alternative representation of plane monochromatic waves is given by the complex *Jones vector* [182]

$$\underline{E}_j = \underline{E}_c|_{z=0} = \underline{E}_c(0) = \begin{bmatrix} E_{0x} \exp(i\phi_x) \\ E_{0y} \exp(i\phi_y) \end{bmatrix}. \quad (59)$$

The *Jones vector* is associated with the parameters of the *polarization ellipse* in the following way [182]

$$\begin{aligned} \underline{E}_j &= A_e \exp(i\phi) \begin{bmatrix} \cos(\phi_e) \cos(\tau_e) - i \sin(\phi_e) \sin(\tau_e) \\ \sin(\phi_e) \cos(\tau_e) + i \cos(\phi_e) \sin(\tau_e) \end{bmatrix}, \\ &= A_e \exp(i\phi) \begin{bmatrix} \cos(\phi_e) & -\sin(\phi_e) \\ \sin(\phi_e) & \cos(\phi_e) \end{bmatrix} \begin{bmatrix} \cos(\tau_e) \\ i \sin(\tau_e) \end{bmatrix}, \end{aligned} \quad (60)$$

while ϕ represents an absolute phase term.

The power of polarimetry reveals in the ability to transform an EM wave acquired in one polarization basis (e.g. (H,V)-basis) into any other polarization basis (e.g. (A,B)-basis) by a unitary transformation, called *basis transformation* [182]

$$\begin{aligned} \underline{E}_{j(H,V)} &= [U]_{(A,B) \rightarrow (H,V)} \underline{E}_{j(A,B)} \\ \text{with } [U]_{(A,B) \rightarrow (H,V)} &= [U](\phi_e, \tau_e, \phi)^{-1} = [U](-\phi) [U](-\tau_e) [U](-\phi_e). \end{aligned} \quad (61)$$

The special unitary transformation matrix \underline{U}_2 can be rewritten in terms of the *polarization ellipse* parameters [182]

$$\begin{aligned} [U](\phi_e, \tau_e, \varphi) &= [U](\phi_e)[U](\tau_e)[U](\varphi) & (62) \\ &= \begin{bmatrix} \cos(\phi_e) & -\sin(\phi_e) \\ \sin(\phi_e) & \cos(\phi_e) \end{bmatrix} \begin{bmatrix} \cos(\tau_e) & i\sin(\tau_e) \\ i\sin(\tau_e) & \cos(\tau_e) \end{bmatrix} \begin{bmatrix} \exp(i\phi) & 0 \\ 0 & \exp(-i\phi) \end{bmatrix}. \end{aligned}$$

3.2.1. Scattering matrix

The incident and the scattered *Jones* vectors (\underline{E}^i , \underline{E}^s) for a plane wave under far field conditions are related by a complex 2x2 scattering matrix $[S]$ [182]:

$$\underline{E}^s = \frac{\exp(-ik_c R)}{R} [S] \underline{E}^{i*}. \quad (63)$$

At first, the scattering matrix $[S_{BI}]$ for a bistatic acquisition in the (H,V)-basis is presented

$$\begin{aligned} [S_{BI}] &= \begin{bmatrix} S_{HH} & S_{HV} \\ S_{VH} & S_{VV} \end{bmatrix} & (64) \\ &= \exp(i\phi_{HH}) \begin{bmatrix} |S_{HH}| & |S_{HV}| \exp(i(\phi_{HV} - \phi_{HH})) \\ |S_{VH}| \exp(i(\phi_{VH} - \phi_{HH})) & |S_{VV}| \exp(i(\phi_{VV} - \phi_{HH})) \end{bmatrix}, \end{aligned}$$

where the first letter of the subscript in Equation 64 indicates the received polarization and the second letter the transmitted polarization [167, 182, 65]. The absolute phase term (ϕ_{HH}) is of secondary importance in polarimetric analyses. The complex scattering matrix $[S]$ consists of seven parameters: Four amplitudes and three differential phases.

In the case of a monostatic configuration the scattering matrix $[S_M]$ is obtained by the [182, 65]

$$\text{reciprocity theorem: } S_{HV} = S_{VH} = S_{XX} \quad (65)$$

$$\begin{aligned} [S_M] &= \begin{bmatrix} S_{HH} & S_{XX} \\ S_{XX} & S_{VV} \end{bmatrix} & (66) \\ &= \exp(i\phi_{HH}) \begin{bmatrix} |S_{HH}| & |S_{XX}| \exp(i(\phi_{XX} - \phi_{HH})) \\ |S_{XX}| \exp(i(\phi_{XX} - \phi_{HH})) & |S_{VV}| \exp(i(\phi_{VV} - \phi_{HH})) \end{bmatrix}. \end{aligned}$$

In this configuration the parameter space is confined to five values, three amplitudes and two differential phases, which can be used for characterization of the

scatterer. The total energy backscattered from the scatterer and recorded at the sensor can be expressed by the *span* of $[S]$ [182, 65]:

$$\text{span}([S]) = \text{Tr}([S][S]^*{}^T), \quad (67)$$

where T represents the transpose matrix operator.

3.2.2. Coherent and distributed scatterers

Assuming a single scatterer within the resolution cell A_{gr} , the scatterer can be fully described by the scattering matrix $[S]$ [182]. Hence, this deterministic scatterer is coherently imaged like a single ‘point scatterer’. In contrary, distributed scatterers consist of multiple scatterers that induce depolarization and require a complete description from a second order formulation. Therefore the scattering matrix $[S]$ is vectorized by a vector operator ($\text{Vec}\{x\}$) to generate a system vector

$$[S] \Rightarrow \underline{k} = \text{Vec}\{[S]\} = \frac{1}{2}\text{Tr}([S]\Xi), \quad (68)$$

where Ξ represents a set of 2x2 complex basis matrices [60,63]. In the field of SAR polarimetry two basis matrix sets are commonly used: The *Pauli* basis matrices (Ξ_P) and the lexicographic basis matrices (Ξ_L) [182, 65].

3.2.2.1. Scattering vectors

The set of *Pauli* basis matrices Ξ_{P_4} in the bistatic case is given by [61]

$$\Xi_{P_4} = \left\{ \sqrt{2} \begin{bmatrix} 1 & 0 \\ 0 & 1 \end{bmatrix}, \sqrt{2} \begin{bmatrix} 1 & 0 \\ 0 & -1 \end{bmatrix}, \sqrt{2} \begin{bmatrix} 0 & 1 \\ 1 & 0 \end{bmatrix}, \sqrt{2} \begin{bmatrix} 0 & -i \\ i & 0 \end{bmatrix} \right\}, \quad (69)$$

which results in the bistatic *Pauli* scattering vector \underline{k}_{P_4} :

$$\underline{k}_{P_4} = \frac{1}{\sqrt{2}} \left[\begin{array}{cccc} S_{HH} + S_{VV} & S_{HH} - S_{VV} & S_{HV} + S_{VH} & i(S_{HV} - S_{VH}) \end{array} \right]^T \quad (70)$$

The set of lexicographic basis matrices Ξ_{L_4} is given by [63]:

$$\Xi_{L_4} = \left\{ 2 \begin{bmatrix} 1 & 0 \\ 0 & 0 \end{bmatrix}, 2 \begin{bmatrix} 0 & 1 \\ 0 & 0 \end{bmatrix}, 2 \begin{bmatrix} 0 & 0 \\ 1 & 0 \end{bmatrix}, 2 \begin{bmatrix} 0 & 0 \\ 0 & 1 \end{bmatrix} \right\}. \quad (71)$$

After vectorization the bistatic lexicographic scattering vector \underline{k}_{L_4} is obtained as

$$\underline{k}_{L_4} = \begin{bmatrix} S_{HH} & S_{HV} & S_{VH} & S_{VV} \end{bmatrix}^T. \quad (72)$$

The *span* can be calculated from the scattering vectors \underline{k} by

$$\text{span}(S) = \underline{k}^{*T} \cdot \underline{k} = |\underline{k}|^2 \quad [182]. \quad (73)$$

Using a special unitary SU(4) transformation matrix the two scattering vectors (\underline{k}_{P_4} , \underline{k}_{L_4}) can be transformed into each other by [71]

$$\underline{k}_{P_4} = [U_{4T}] \underline{k}_{L_4} \quad \text{using} \quad [U_{4T}] = \frac{1}{\sqrt{2}} \begin{bmatrix} 1 & 0 & 0 & 1 \\ 1 & 0 & 0 & -1 \\ 0 & 1 & 1 & 0 \\ 0 & i & -i & 0 \end{bmatrix}. \quad (74)$$

In the monostatic case the set of *Pauli* basis matrices Ξ_{P_3} reduces to [63]

$$\Xi_{P_3} = \left\{ \sqrt{2} \begin{bmatrix} 1 & 0 \\ 0 & 1 \end{bmatrix}, \sqrt{2} \begin{bmatrix} 1 & 0 \\ 0 & -1 \end{bmatrix}, \sqrt{2} \begin{bmatrix} 0 & 1 \\ 1 & 0 \end{bmatrix} \right\}. \quad (75)$$

The three dimensional *Pauli* scattering vector \underline{k}_{P_3} is defined as

$$\underline{k}_{P_3} = \frac{1}{\sqrt{2}} \begin{bmatrix} S_{HH} + S_{VV} & S_{HH} - S_{VV} & 2S_{XX} \end{bmatrix}^T. \quad (76)$$

The set of Lexicographic basis matrices Ξ_{L_3} in the monostatic case becomes [63]

$$\Xi_{L_3} = \left\{ 2 \begin{bmatrix} 1 & 0 \\ 0 & 0 \end{bmatrix}, 2\sqrt{2} \begin{bmatrix} 0 & 1 \\ 0 & 0 \end{bmatrix}, 2 \begin{bmatrix} 0 & 0 \\ 0 & 1 \end{bmatrix} \right\}. \quad (77)$$

After vectorization the monostatic lexicographic scattering vector \underline{k}_{L_3} is

$$\underline{k}_{L_3} = \begin{bmatrix} S_{HH} & \sqrt{2}S_{XX} & S_{VV} \end{bmatrix}^T. \quad (78)$$

The transformation from *Pauli* basis to lexicographic basis can be done with the special unitary SU(4) transformation matrix [71]:

$$\underline{k}_{P_3} = [U_{3T}] \underline{k}_{L_3} \quad \text{using} \quad [U_{3T}] = \frac{1}{\sqrt{2}} \begin{bmatrix} 1 & 0 & 1 \\ 1 & 0 & -1 \\ 0 & \sqrt{2} & 0 \end{bmatrix}. \quad (79)$$

In a next step the scattering vectors are used to form the polarimetric coherency matrix and the polarimetric covariance matrix [60].

3.2.2.2. Coherency and covariance matrix

The outer product of the scattering vectors (k_{P_4} , k_{L_4}) and their adjoint vectors together with an averaging operation $\langle \dots \rangle$ leads to the coherency $\langle [T_4] \rangle$ and covariance $\langle [C_4] \rangle$ matrix in the bistatic case [182]

$$\langle [C_4] \rangle = \langle \underline{k}_{L_4} \cdot \underline{k}_{L_4}^{*T} \rangle \quad \text{and} \quad \langle [T_4] \rangle = \langle \underline{k}_{P_4} \cdot \underline{k}_{P_4}^{*T} \rangle. \quad (80)$$

The full expressions are given as [182, 65]

$$\langle [C_4] \rangle = \begin{bmatrix} \langle |S_{HH}|^2 \rangle & \langle S_{HH}S_{HV}^* \rangle & \langle S_{HH}S_{VH}^* \rangle & \langle S_{HH}S_{VV}^* \rangle \\ \langle S_{HV}S_{HH}^* \rangle & \langle |S_{HV}|^2 \rangle & \langle S_{HV}S_{VH}^* \rangle & \langle S_{HV}S_{VV}^* \rangle \\ \langle S_{VH}S_{HH}^* \rangle & \langle S_{VH}S_{HV}^* \rangle & \langle |S_{VH}|^2 \rangle & \langle S_{VH}S_{VV}^* \rangle \\ \langle S_{VV}S_{HH}^* \rangle & \langle S_{VV}S_{HV}^* \rangle & \langle S_{VV}S_{VH}^* \rangle & \langle |S_{VV}|^2 \rangle \end{bmatrix} \quad (81)$$

$$\langle [T_4] \rangle = \frac{1}{2} \begin{bmatrix} \langle |S_{HH} + S_{VV}|^2 \rangle & \langle (S_{HH} + S_{VV})(S_{HH} - S_{VV})^* \rangle \dots \\ \langle (S_{HH} - S_{VV})(S_{HH} + S_{VV})^* \rangle & \langle |S_{HH} - S_{VV}|^2 \rangle \dots \\ \langle (S_{HV} + S_{VH})(S_{HH} + S_{VV})^* \rangle & \langle (S_{HV} + S_{VH})(S_{HH} - S_{VV})^* \rangle \dots \\ \langle i(S_{HV} - S_{VH})(S_{HH} + S_{VV})^* \rangle & \langle i(S_{HV} - S_{VH})(S_{HH} - S_{VV})^* \rangle \dots \\ \langle (S_{HH} + S_{VV})(S_{HV} + S_{VH})^* \rangle & \langle -i(S_{HH} + S_{VV})(S_{HV} - S_{VH})^* \rangle \\ \langle (S_{HH} - S_{VV})(S_{HV} + S_{VH})^* \rangle & \langle -i(S_{HH} - S_{VV})(S_{HV} - S_{VH})^* \rangle \\ \langle |S_{HV} + S_{VH}|^2 \rangle & \langle -i(S_{HV} + S_{VH})(S_{HV} - S_{VH})^* \rangle \\ \langle i(S_{HV} - S_{VH})(S_{HV} + S_{VH})^* \rangle & \langle |S_{HV} - S_{VH}|^2 \rangle \end{bmatrix}. \quad (82)$$

In the monostatic case the expressions change to

$$\langle [T_3] \rangle = \langle \underline{k}_{P_3} \cdot \underline{k}_{P_3}^{*T} \rangle, \quad \langle [C_3] \rangle = \langle \underline{k}_{L_3} \cdot \underline{k}_{L_3}^{*T} \rangle \quad (83)$$

leading to [182, 65]

$$\langle [T_3] \rangle = \frac{1}{2} \begin{bmatrix} \langle |S_{HH} + S_{VV}|^2 \rangle & \langle (S_{HH} + S_{VV})(S_{HH} - S_{VV})^* \rangle & 2\langle (S_{HH} + S_{VV})S_{XX}^* \rangle \\ \langle (S_{HH} - S_{VV})(S_{HH} + S_{VV})^* \rangle & \langle |S_{HH} - S_{VV}|^2 \rangle & 2\langle (S_{HH} - S_{VV})S_{XX}^* \rangle \\ 2\langle S_{XX}(S_{HH} + S_{VV})^* \rangle & 2\langle S_{XX}(S_{HH} - S_{VV})^* \rangle & 4\langle |S_{XX}|^2 \rangle \end{bmatrix} \quad (84)$$

$$\langle [C_3] \rangle = \begin{bmatrix} \langle |S_{HH}|^2 \rangle & \sqrt{2} \langle S_{HH} S_{XX}^* \rangle & \langle S_{HH} S_{VV}^* \rangle \\ \sqrt{2} \langle S_{XX} S_{HH}^* \rangle & 2 \langle |S_{XX}|^2 \rangle & \sqrt{2} \langle S_{XX} S_{VV}^* \rangle \\ \langle S_{VV} S_{HH}^* \rangle & \sqrt{2} \langle S_{VV} S_{XX}^* \rangle & \langle |S_{VV}|^2 \rangle \end{bmatrix}. \quad (85)$$

Special unitary transformation matrices relate the two scattering vectors and also the coherency and covariance matrix with each other (cf. Equations 74 and 79) [182, 65]:

$$\text{Bistatic: } \langle [T_4] \rangle = [U_{4T}] \langle [C_4] \rangle [U_{4T}]^{-1} \quad \text{Monostatic: } \langle [T_3] \rangle = [U_{3T}] \langle [C_3] \rangle [U_{3T}]^{-1}. \quad (86)$$

From this point on, only the monostatic case ($\langle [T_3] \rangle$, $\langle [C_3] \rangle$) will be considered and the matrices will be labeled $\langle [T] \rangle$ and $\langle [C] \rangle$.

3.2.3. Symmetry properties

Symmetry properties lead to a simplified scattering problem. Various assumptions of scattering symmetries are reported in the literature [317, 229, 71, 182, 65]. In the context of the thesis only the reflection, rotation and azimuthal symmetry are of relevance and are introduced in the following for the coherency matrix $\langle [T] \rangle$.

For reflection symmetry, the scatterers are assumed to have an axis of symmetry in the plane defined by the LoS- and the nadir-vector. In this way, the correlation terms between co- and cross-polarized signals are zero ($T_{13} = T_{23} = T_{31} = T_{32} = 0$) [71]

$$\langle [T] \rangle_{ref} = \begin{bmatrix} T_{11} & T_{12} & 0 \\ T_{12}^* & T_{22} & 0 \\ 0 & 0 & T_{33} \end{bmatrix}. \quad (87)$$

A reflection symmetric coherency matrix $\langle [T] \rangle_{ref}$ is fully characterized by five parameters.

Another type of symmetry is rotation symmetry implying invariance to rotations around the LoS. It can be expressed by the eigenvalues ($\lambda_1, \lambda_2, \lambda_3$ and $\lambda_1 \geq \lambda_2 \geq \lambda_3 \geq 0$) of $\langle [T] \rangle_{ref}$ (cf. Chapter 3.2.4.1. [182, 67])

$$\langle [T] \rangle_{rot} = \begin{bmatrix} \lambda_1 & 0 & 0 \\ 0 & (\lambda_2 + \lambda_3)/2 & i(\lambda_2 - \lambda_3)/2 \\ 0 & -i(\lambda_2 - \lambda_3)/2 & (\lambda_2 + \lambda_3)/2 \end{bmatrix}. \quad (88)$$

The rotationally symmetric coherency matrix $\langle [T] \rangle_{rot}$ is fully characterized by the three eigenvalues, while the condition $T_{22} = T_{33}$ holds. In addition, the correlation terms T_{23} and T_{32} are non-zero in contrast to all other off-diagonal elements.

Assuming both previous symmetries results in azimuthal symmetry that presents the highest level of symmetry: All planes containing the LoS vector are valid symmetry planes [71]

$$\langle [T] \rangle_{azim} = \begin{bmatrix} 2\lambda_1 & 0 & 0 \\ 0 & (\lambda_2 + \lambda_3) & 0 \\ 0 & 0 & (\lambda_2 + \lambda_3) \end{bmatrix}. \quad (89)$$

The azimuthal symmetric coherency matrix $\langle [T] \rangle_{azim}$ is fully characterized by only two parameters ($T_{11}, T_{22} = T_{33}$), while all off-diagonal elements are zero.

3.2.4. Decomposition theorems

The received SAR signal of almost any natural media is a mixed response of different scattering processes occurring within the resolution cell. Therefore polarimetric decomposition techniques have been developed and used to separate the different scattering contributions [182]. Equation 90 describes a generic example of an incoherent decomposition using the coherency matrix notation

$$\langle [T] \rangle = \sum_{i=1}^N [T_i] = [T_1] + [T_2] + \dots + [T_N]. \quad (90)$$

Two different types of incoherent decompositions can be deduced for polarimetric SAR data analyses: Eigen-based decompositions and model-based decompositions.

3.2.4.1. Eigen-based decomposition

The diagonalization of the averaged coherency matrix $\langle [T] \rangle$ into real, non-negative eigenvalues and complex eigenvectors refers to the characteristics of a positive-semidefinite hermitian matrix [60, 62, 71].

$$\begin{aligned} \langle [T] \rangle &= [E_3][\Sigma][E_3]^{-1} = \begin{bmatrix} \underline{e}_1 & \underline{e}_2 & \underline{e}_3 \end{bmatrix} \begin{bmatrix} \lambda_1 & 0 & 0 \\ 0 & \lambda_2 & 0 \\ 0 & 0 & \lambda_3 \end{bmatrix} \begin{bmatrix} \underline{e}_1 & \underline{e}_2 & \underline{e}_3 \end{bmatrix}^{-1} \\ &= \sum_{i=1}^3 \lambda_i \underline{e}_i \cdot \underline{e}_i^{*T} = [T_1] + [T_2] + [T_3]. \end{aligned} \quad (91)$$

Equation 91 can be interpreted as a decomposition of the coherency matrix $\langle [T] \rangle$ in up to three statistically independent scattering components ($[T_1], [T_2], [T_3]$). Each component refers to a deterministic scatterer and is of rank one. The eigenvalues

quantify the power of each uncorrelated component and their sum expresses the total power backscattered to the sensor, known as the *span* [65]:

$$\text{span}(\langle [T] \rangle) = \lambda_1 + \lambda_2 + \lambda_3. \quad (92)$$

If only one eigenvalue of $\langle [T] \rangle$ is non-zero, a deterministic scatterer is present, which can be fully described by the scattering matrix $[S]$. In contrary, if all eigenvalues of $\langle [T] \rangle$ are non-zero, three orthogonal scattering mechanisms occur.

The normalized eigenvectors can be unitarily parameterized with the parameters α , β , γ , δ and ϕ for the i^{th} eigenvector, where $\phi = \varphi_1$, $\delta = \varphi_2 - \varphi_1$ and $\gamma = \varphi_3 - \varphi_1$ [63, 71, 182, 65]

$$\underline{e}_i = \exp(i\phi_i) \begin{bmatrix} \cos(\alpha_i) \\ \sin(\alpha_i) \cos(\beta_i) \exp(i\delta_i) \\ \sin(\alpha_i) \sin(\beta_i) \exp(i\gamma_i) \end{bmatrix} = \begin{bmatrix} e_{i1} \\ e_{i2} \\ e_{i3} \end{bmatrix} \text{ for } [E_3] = \begin{bmatrix} \underline{e}_1 & \underline{e}_2 & \underline{e}_3 \end{bmatrix}. \quad (93)$$

In a more general way, any reciprocal polarimetric backscattering mechanism can be tracked back to the identity $[1, 0, 0]^T$ by the *point reduction theorem* expressed by three matrix transformation operators [63, 65]

$$\begin{bmatrix} 1 \\ 0 \\ 0 \end{bmatrix} = e^{-i\phi} \begin{bmatrix} \cos(\alpha) & \sin(\alpha) & 0 \\ -\sin(\alpha) & \cos(\alpha) & 0 \\ 0 & 0 & 1 \end{bmatrix} \begin{bmatrix} 1 & 0 & 0 \\ 0 & \cos(\beta) & \sin(\beta) \\ 0 & -\sin(\beta) & \cos(\beta) \end{bmatrix} \begin{bmatrix} 1 & 0 & 0 \\ 0 & e^{-i\delta} & 0 \\ 0 & 0 & e^{-i\gamma} \end{bmatrix} \underline{k}_p. \quad (94)$$

The parameters α , β , δ , γ can be linked to physical parameters. The α scattering angle represents an intrinsic scattering type, which is depicted in Figure 11 and is calculated in Equation 95 [70]. If α is close to zero, surface scattering will be assumed. For α around 45° dipole scattering occurs, while dihedral scattering is characterized by α -values close to 90° .

The β angle can be related to the orientation of the scatterer in azimuth direction by $\beta/2$ and is obtained from [100]

$$\alpha_i = \text{acos}(|e_{i1}|) \quad \alpha_i \in [0^\circ, 90^\circ] \quad (95)$$

$$\beta_i = \text{atan}\left(\frac{|e_{i3}|}{|e_{i2}|}\right) \quad \beta_i \in [0^\circ, 90^\circ]. \quad (96)$$

The differential propagation between linear polarizations is represented by $\phi_{li} = -\delta = \varphi_1 - \varphi_2 =$ linear scattering phase [70]. In addition, the differential propagation between circular polarizations is allocated to $\phi_{ci} = \gamma - \delta = \varphi_3 - \varphi_2 =$ helicity

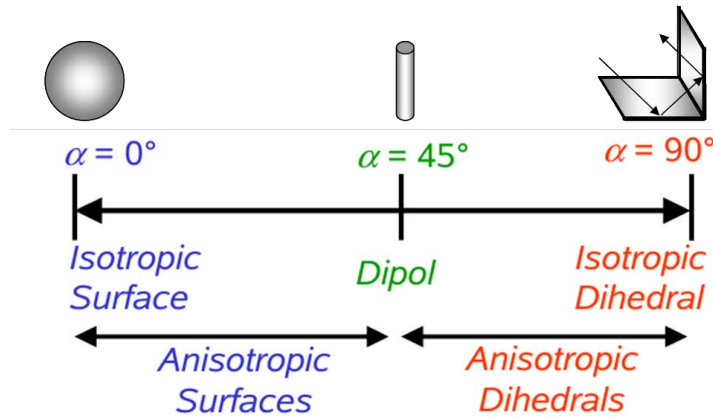


Figure 11: Physical interpretation of the alpha scattering angle (from surface scattering $\alpha=0^\circ$ to dihedral scattering $\alpha=90^\circ$).

scattering phase [70].

The eigenvector-derived parameters (i.e. $\alpha_1, \alpha_2, \alpha_3$) are not independent due to the orthogonality of the eigenvectors, which leads to a probabilistic *Bernoulli* model [65]. The scatterer is modeled as a combination of the parameterized eigenvectors and the pseudo-probabilities P_i [182]

$$P_i = \frac{\lambda_i}{\sum_{k=1}^3 \lambda_k} \quad \text{regarding} \quad \sum_{k=1}^3 P_k = 1 \quad \text{and} \quad \lambda_1 \geq \lambda_2 \geq \lambda_3 \quad (97)$$

to express an average scattering mechanism [182, 65]:

$$\bar{\alpha} = P_1 \alpha_1 + P_2 \alpha_2 + P_3 \alpha_3 \quad (98)$$

$$\bar{\beta} = P_1 \beta_1 + P_2 \beta_2 + P_3 \beta_3 \quad (99)$$

$$\bar{\delta} = P_1 \delta_1 + P_2 \delta_2 + P_3 \delta_3 \quad (100)$$

$$\bar{\gamma} = P_1 \gamma_1 + P_2 \gamma_2 + P_3 \gamma_3. \quad (101)$$

If only the dominant scattering mechanism is of importance, the parameters of the first (dominant) eigenvector (i.e. α_1) serve as a reference for analysis.

The pseudo-probabilities P_i of Equation 97 can be also used as weights to define a degree of disorder of each scattering type [60], which is represented by the polarimetric entropy after *von Neumann* [63]

$$H = - \sum_{i=1}^3 P_i \log_3 P_i \quad \text{with} \quad H = [0, 1]. \quad (102)$$

There are two extreme cases to distinguish:

$$\text{Non-depolarizing scatterers: } H = 0 \Rightarrow [T] = \begin{bmatrix} x & 0 & 0 \\ 0 & 0 & 0 \\ 0 & 0 & 0 \end{bmatrix} \quad (103)$$

$$\text{Fully-depolarizing scatterers: } H = 1 \Rightarrow [T] = \begin{bmatrix} x & 0 & 0 \\ 0 & x & 0 \\ 0 & 0 & x \end{bmatrix} \quad (104)$$

For natural media the entropy should range between the two extreme cases of Equations 103 and 104.

A physically-meaningful representation of the scatterers can be obtained by displaying the data within the so-called polarimetric entropy - mean scattering alpha angle plane, for which *Cloude* and *Pottier* defined a segmentation scheme for L-band, as indicated in Figure 12 [72].

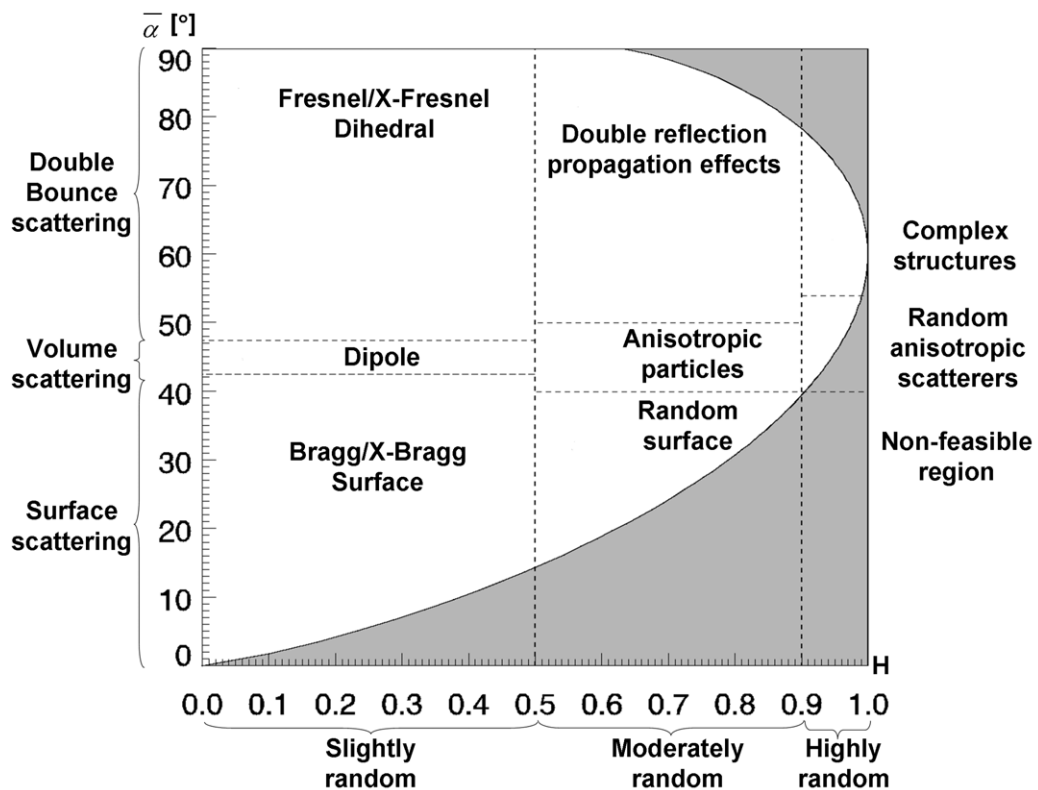


Figure 12: Scattering plane of polarimetric entropy - mean scattering alpha angle with segmentation scheme of [72] for L-band (dashed lines).

Another polarimetric parameter, which puts more emphasis on the lower order

eigenvalues and therefore on the secondary scattering mechanism, is the anisotropy A [182, 65]:

$$A = \frac{\lambda_2 - \lambda_3}{\lambda_2 + \lambda_3} = \frac{P_2 - P_3}{P_2 + P_3}. \quad (105)$$

The anisotropy gains importance in higher entropy environments (e.g. vegetation scattering) with $H > 0.7$. There are two extreme cases:

One single secondary scattering mechanism:

$$A = 1 \quad (\lambda_3 = 0) \quad \Rightarrow \quad [\Sigma] = \begin{bmatrix} \lambda_1 & 0 & 0 \\ 0 & \lambda_2 & 0 \\ 0 & 0 & 0 \end{bmatrix} \quad (106)$$

Two equal secondary scattering mechanisms:

$$A = 0 \quad (\lambda_2 = \lambda_3) \quad \Rightarrow \quad [\Sigma] = \begin{bmatrix} \lambda_1 & 0 & 0 \\ 0 & \lambda_2 & 0 \\ 0 & 0 & \lambda_2 \end{bmatrix} \quad (107)$$

In this way the anisotropy classifies as an indicator for azimuthal symmetry, where $\lambda_2 = \lambda_3$ like in densely vegetated areas.

3.2.4.1.1. Roll-invariance of eigen-based parameters

Terrain slopes cause LoS rotations and distort the measured coherency matrix $\langle [T] \rangle$. These LoS rotations can be expressed by [71]

$$[R_{2\psi}] = \begin{bmatrix} 1 & 0 & 0 \\ 0 & \cos(2\psi) & \sin(2\psi) \\ 0 & -\sin(2\psi) & \cos(2\psi) \end{bmatrix}. \quad (108)$$

If the eigen-based decomposition is rotated azimuthally by $[R_{2\psi}]$

$$\langle [T'] \rangle = [R_{2\psi}] [E_3] [\Sigma] [E_3]^{-1} [R_{2\psi}]^{-1} = [E'_3] [\Sigma] [E'_3]^{-1}, \quad (109)$$

the new unitary eigenvector-matrix $[E'_3]$ is given by [182]

$$[E'_3] = \begin{bmatrix} \cos(\alpha_1) \exp(i\phi'_1) & \cos(\alpha_2) \exp(i\phi'_2) & \cos(\alpha_3) \exp(i\phi'_3) \\ \sin(\alpha_1) \cos(\beta'_1) \exp(i(\delta'_1 + \phi'_1)) & \sin(\alpha_2) \cos(\beta'_2) \exp(i(\delta'_2 + \phi'_2)) & \sin(\alpha_3) \cos(\beta'_3) \exp(i(\delta'_3 + \phi'_3)) \\ \sin(\alpha_1) \sin(\beta'_1) \exp(i(\gamma'_1 + \phi'_1)) & \sin(\alpha_2) \sin(\beta'_2) \exp(i(\gamma'_2 + \phi'_2)) & \sin(\alpha_3) \sin(\beta'_3) \exp(i(\gamma'_3 + \phi'_3)) \end{bmatrix}. \quad (110)$$

The eigenvalues λ_i are not affected by the azimuthal rotations. Thus the eigenvalue-based parameters A , H , P_i and $span$ are independent of LoS rotations, which makes them more robust for physical parameter retrieval in hilly terrain. In addition, the scattering mechanisms α_i and the mean scattering mechanism $\bar{\alpha}$ are not compromised as well by the rotations. Consequently, the characteristics of the scattering mechanism are independent from scatterer orientations with respect to the LoS [65]. In contrary, the parameters β_i , δ_i and γ_i are roll-variant and need corrections before physical interpretation.

Unfortunately, the single components of the eigen-based decomposition ($[T_1], [T_2], [T_3]$) may not represent directly different physical scattering mechanisms, as depolarizing mechanisms can be distributed over several eigenvalues and eigenvectors inhibiting direct allocation.

3.2.4.2. Model-based decomposition

Model-based decompositions for natural scatterers use pre-defined, physical scattering models to interpret the scattering process. Compared to the eigen-based decomposition, scattering mechanisms with a rank higher than one, as for example vegetation scattering, can be included in the modeling. A simple and generic case of model-based decompositions considers a non-penetrable surface superimposed by a volume of particles [65]. This can be modeled with three components defined as surface $[T_S]$, dihedral $[T_D]$ and volume $[T_V]$ scattering [106, 343, 342]

$$\langle [T] \rangle = [T_S] + [T_D] + [T_V]. \quad (111)$$

In addition, the total power P_{tot} of all components can be retrieved by summation of the power contributions P_S , P_D , P_V , which are calculated from the trace of the single scattering component matrices

$$P_{tot} = Tr([T_S]) + Tr([T_D]) + Tr([T_V]) = P_S + P_D + P_V. \quad (112)$$

Finally, the normalized power of each scattering component can be obtained by division with P_{tot} . This provides the opportunity to compare the strength of the different scattering contributions with respect to each other.

3.2.4.2.1. Surface component

The first component in Equation 111 represents direct backscatter from a smooth surface ($k_s < 0.3$), which can be expressed by the SPM or Bragg scattering model

[65]. In [343, 124] the parameterization of the rank-1 surface component in the coherency matrix notation is given as

$$[T_S] = f_S \begin{bmatrix} 1 & \beta_S^* & 0 \\ \beta_S & |\beta_S|^2 & 0 \\ 0 & 0 & 0 \end{bmatrix}. \quad (113)$$

The surface scattering intensity f_S and the surface scattering mechanism ratio β_S are defined as

$$f_S = \frac{m_s^2}{2} |R_h + R_v|^2 \quad \text{and} \quad \beta_S = \frac{R_h - R_v}{R_h + R_v}. \quad (114)$$

The coefficients R_h and R_v are the horizontal and the vertical *Bragg* scattering coefficients and m_s represents the soil roughness influence on the intensity component f_S . Both *Bragg* scattering coefficients depend only on the dielectric constant of the soil ϵ_s and the local incidence angle θ_l . Equation 113 does not account for depolarization effects of rough soils and will be extended for this purpose in Chapter 4.2.1.1. in order to explain cross-polarized scattering on natural surfaces due to surface roughness.

3.2.4.2.2. Dihedral component

The dihedral scattering component can be modeled as a double *Fresnel* reflection on smooth dielectric media leading to the following rank-1 coherency matrix [124]

$$[T_D] = f_D \begin{bmatrix} |\alpha_D|^2 & \alpha_D & 0 \\ \alpha_D^* & 1 & 0 \\ 0 & 0 & 0 \end{bmatrix}. \quad (115)$$

The dihedral scattering intensity f_D and the dihedral scattering mechanism ratio α_D are given by

$$f_D = \frac{m_d^2}{2} |R_{sh}R_{th} + R_{sv}R_{tv} \exp(i\phi_d)|^2, \quad \alpha_D = \frac{R_{sh}R_{th} - R_{sv}R_{tv} \exp(i\phi_d)}{R_{sh}R_{th} + R_{sv}R_{tv} \exp(i\phi_d)}, \quad (116)$$

where the horizontal and vertical *Fresnel* coefficients of the soil plane (R_{sh}, R_{sv}) and of the trunk plane (R_{th}, R_{tv}) depend on the soil and trunk dielectric constant (ϵ_s and ϵ_t) and the respective incidence angle $\theta_s = \theta_l$ and $\theta_t = \pi/2 - \theta_l$ [124]. The phase ϕ_d incorporates differential propagation in the case of an orientated vegetation layer, while m_d represents the scattering loss on the intensity component f_D .

Therefore this dihedral component assumes lossy, but non-depolarizing reflections,

which are only the case for very smooth surfaces. A further development of this component is shown in Chapter 4.2.1.2. including a rough surface for the soil scattering plane to incorporate depolarization effects.

3.2.4.2.3. Volume component

The most challenging component with respect to EM modeling is the vegetation volume. A widely used approach deals with the vegetation volume as a cloud of equally shaped particles with a certain orientation distribution, as detailed in [317, 67, 342, 124, 189]. In one of the simplest ways the volume component is modeled as randomly oriented cloud of dipoles. The initial vertical dipole can be expressed with the following scattering matrix $[S_{vdi}]$:

$$[S_{vdi}] = \begin{bmatrix} 0 & 0 \\ 0 & 1 \end{bmatrix}. \quad (117)$$

After expansion to the coherency matrix, the matrix is rotated around the LoS by an angle of 2ψ to account for the orientation of the scattering particles

$$\begin{aligned} [T_{rot}] &= [R_{2\psi}] [T_{vdi}] [R_{2\psi}]^T \\ &= \begin{bmatrix} 1 & 0 & 0 \\ 0 & \cos(2\psi) & \sin(2\psi) \\ 0 & -\sin(2\psi) & \cos(2\psi) \end{bmatrix} \begin{bmatrix} 1/2 & -1/2 & 0 \\ -1/2 & 1/2 & 0 \\ 0 & 0 & 0 \end{bmatrix} \begin{bmatrix} 1 & 0 & 0 \\ 0 & \cos(2\psi) & -\sin(2\psi) \\ 0 & \sin(2\psi) & \cos(2\psi) \end{bmatrix}. \end{aligned} \quad (118)$$

In order to respect all the different orientations occurring within vegetation, the rotated coherency matrix $[T_{rot}]$ is integrated together with the specific probability density function $pdf(\psi)$ of orientations assuming a uniform angular distribution $pdf(\psi) = 1/(2\pi)$ and a distribution width $\Delta\psi = \psi_2 - \psi_1 = 2\pi$ in the case of a randomly oriented vegetation volume [343]

$$[T_V] = f_V \int_{\psi_1}^{\psi_2} pdf(\psi) [T_{rot}] d\psi = f_V \begin{bmatrix} \frac{1}{2} & 0 & 0 \\ 0 & \frac{1}{4} & 0 \\ 0 & 0 & \frac{1}{4} \end{bmatrix}. \quad (119)$$

In Chapter 4.2.1.3. the volume modeling will be extended to different orientation distributions simulating different vegetation geometries. Furthermore, investigations on the shape of the volume particles will be conducted to widen the approach for a variety of vegetation scattering scenarios in agriculture.

Part 4

Methodology of soil parameter retrieval using SAR polarimetry

In this chapter polarimetric decomposition techniques are established for the retrieval of soil moisture and soil roughness in the presence of vegetation cover. A simplified scattering scenario of a single-layered vegetation volume over a soil surface, as shown in Figure 13, is considered [305].

For this scenario the validity of the *distorted Born approximation* [174,304], including the *Foldy-Lax approximation* [176, 102] and the truncation of the *Born series* at the first order term (*Born approximation*) [32], is assumed (cf. Figure 13). The approximation supposes no interactions between the single (discrete) scatterers, neglecting multiple scattering at the expense of single scattering [32]. In a general

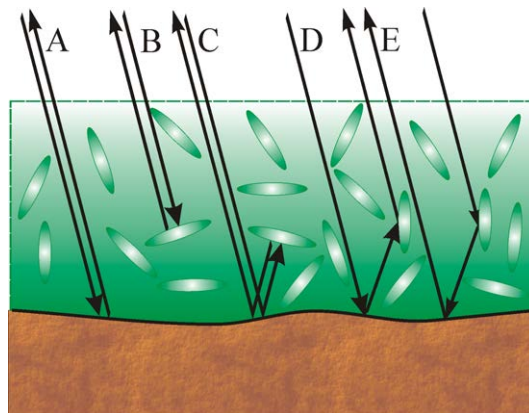


Figure 13: Volume over ground scattering model according to *Born approximation* including (A) surface scattering from the underlying ground (i.e. single bounce scattering), (B) direct volume scattering, (C) ground-volume-ground scattering (i.e. triple bounce scattering), (D,E) ground-volume scattering (i.e. double bounce or dihedral scattering) [225].

agricultural scattering scenario the polarimetric signature contains contributions from the vegetation layer and the underlying ground. In order to be able to retrieve the soil parameters, the scattering contribution of the ground has first to be isolated from the one of the vegetation. After removing the vegetation component, the contributions from soil roughness and soil moisture need to be separated in terms of the remaining ground component. This separation is also necessary in the case of bare soil scattering. In this context, the use of (simple) scattering

models for description of the individual scattering contributions is essential.

4.1. Scattering models for bare soil

Historically, the retrieval of soil moisture from SAR acquisitions started on bare soils, which represent the simplest scattering case due to the absence of the vegetation disturbance. Three different model categories, for relating the soil parameters to the scattering signature, can be distinguished: Empirical models, semi-empirical models and theoretical surface scattering models [119, 186, 147].

4.1.1. Empirical models

These models are based on empirically established relations between the scattering signature and soil parameters. The advantage lies in the simplicity of the approaches, which are set up quickly without complicated modeling of the scattering scenario. The price for this is that the derived relations are hardly transferable to other field and site conditions [349, 177, 250, 219, 331, 43, 56]. Hence, the relations have to be adapted for different soil conditions and for different seasons. Consequently, their usefulness is rather restricted.

4.1.2. Semi-empirical models

Semi-empirical models start from a theoretical basis and use regressions from experimental data to derive simplified inversion models. The most commonly used semi-empirical models are the ones, developed by *Oh et al.* and *Dubois et al.* [234, 232, 92, 238, 24]. Due to the advantage of a theoretical basis, these models are more general and transferable for different soil conditions obeying the validity criterion, under which they were developed. Their applicability is confined to bare or sparsely vegetated soils with $2.6 < kl < 19.2$, $0.1 < ks < 6.0$, $9\text{vol.}\% < mv < 31\text{vol.}\%$ as well as $10^\circ < \theta_l < 70^\circ$ for the *Oh* model and $ks < 2.5$ as well as $\theta_l > 30^\circ$ for the *Dubois* model [234, 232, 92]. Unfortunately, both are incoherent models, describing only a subset of the available observation space. Accordingly, none of the two models can explain roughness induced depolarization effects.

4.1.3. Theoretical models

For theoretical models, the roughness induced geometry is parameterized and analytical approximations of the scattering signature are derived based on Electro-

Magnetic (EM) theory. Topical reviews on numerous theoretical surface scattering models can be found in [264, 312, 305, 304, 96]. Many theoretical scattering models originate from the *Stratton-Chu Integral Equation* under the *plane wave and far field approximations* [287, 143]. As no direct solution for randomly rough surfaces exists, approximations are applied restricting each EM scattering model to a certain validity range (cf. Table 1), which is defined by the horizontal and the vertical roughness (kl, ks). If ks and kl are large, a rough surface can be approximated by

Table 1: Validity range of theoretical surface scattering models for bare soil [312, 127, 107, 325].

Scattering model	Vertical roughness	Horizontal roughness	Dielectric constant
SPM	$ks < 0.3$	$kl > \sqrt{2}/0.3 \cdot ks$	-
PO	$ks < 1/(4\sqrt{2}) \cdot kl$	$kl = 4\sqrt{2} \cdot ks$	-
SSA	$ks = \sin(\theta_l) \cdot kl$	$kl = \sin^{-1}(\theta_l) \cdot ks$	-
GO	$ks > \sqrt{10}/(2\cos(\theta_l))$	$kl > 6^*, l^2 = 2.76s\lambda_c^*$	-
IEM	$ks < 1.2\sqrt{\epsilon_s}/kl^+$	$kl < 1.2\sqrt{\epsilon_s}/ks^+$	$\epsilon_s = ks^2 \cdot kl^2/1.44^+$

*validity criterion of the *Kirchoff* model, ⁺for a *Gaussian* correlation function

the concatenation of tangential planes, known as *tangential plane approximation* or *Kirchhoff approximation* [20, 312]. Assuming only specular reflections under the *stationary phase approximation*, the Geometric Optics (GO) model can be formulated from the *Kirchhoff approximation* [308, 312]. Integrating the *Kirchhoff model* over the entire rough surface within the resolution cell (*scalar approximation*) results in the Physical Optics (PO) model for medium rough surfaces [308, 312]. In order to fill the gap between the GO model (for rough surfaces) and the PO model (for medium rough surfaces), *Voronovich* developed the Small Slope Approximation (SSA) model [325, 324] and *Fung et al.* proposed the Integral Equation Method (IEM) model. This model introduces a multiple scattering term into the *Kirchoff approximation* [107, 108, 57, 338]. Due to the broad applicability, this model and the Advanced Integral Equation Method (AIEM) are well established within the SAR community [350, 13, 274, 292, 318, 280]. In the case of very rough surface characteristics ($ks \gg 1$) the IEM model simplifies to the GO model and in the case of slightly rough surfaces ($ks \ll 1$) it turns into the Small Perturbation Model (SPM), also known as *Bragg scattering model* [255, 316]. The SPM emanates from the *Taylor series expansion* of perfectly conducting surfaces [312, 308]. Thus, depolarization effects due to rough surfaces are not taken into account, which is the same for all the aforementioned models. For this reason *Hajnsek et al.* proposed an extension of the SPM, including a roughness-induced

depolarization component to account for cross-polarized scattering ($k_s < 1$), which is called *Extended Bragg* or *X-Bragg* model [127].

4.1.4. Polarimetric soil moisture inversion

The inversion procedure for surface soil moisture in *Hajnsek et al.* is based on the comparison of the eigen-analysis of the data coherency matrix $\langle [T_{Data}] \rangle$, introduced in Chapter 3.2.4.1. [127], with the eigen-analysis of the coherency matrix from the *X-Bragg* model $[T_{XB}]$ for surface scattering, which is introduced in the following. Starting from the *Bragg* scattering matrix $[S_B]$ in Equation 120, the coherency matrix $[T_B]$ is calculated

$$[S_B] = m_s \begin{bmatrix} R_h & 0 \\ 0 & R_v \end{bmatrix} \Rightarrow [T_B] = k_{P_{3B}} \cdot k_{P_{3B}}^{*T} \Rightarrow [T_{BR}] = [R_{2\psi}] [T_B] [R_{2\psi}]^T. \quad (120)$$

Roughness can be incorporated by rotating $[T_B]$ by an angle ψ about the LoS

$$[T_{BR}] = [R_{2\psi}] \frac{m_s^2}{2} \begin{bmatrix} |R_h + R_v|^2 & (R_h + R_v)(R_h - R_v)^* & 0 \\ (R_h - R_v)(R_h + R_v)^* & |R_h - R_v|^2 & 0 \\ 0 & 0 & 0 \end{bmatrix} [R_{2\psi}]^T \quad (121)$$

and integrating ψ over a given width of a uniform Probability Density Function (PDF) ($pdf(\psi) = 1/(2\psi_l)$) depending on the surface roughness [127]:

$$\begin{aligned} [T_{XB}] &= \int_{-\psi_l}^{\psi_l} pdf(\psi) \cdot [T_{BR}] d\psi \\ &= m_s^2 \begin{bmatrix} T_{B11} & T_{B12} \cdot sinc(2\psi_l) & 0 \\ T_{B12}^* \cdot sinc(2\psi_l) & T_{B22} \cdot (1 + sinc(4\psi_l)) & 0 \\ 0 & 0 & T_{B22} \cdot (1 - sinc(4\psi_l)) \end{bmatrix} \end{aligned} \quad (122)$$

$$T_{B11} = \frac{1}{2} |R_h + R_v|^2 \quad (123)$$

$$T_{B12} = \frac{1}{2} (R_h + R_v)(R_h - R_v)^* \quad (124)$$

$$T_{B22} = \frac{1}{4} |R_h - R_v|^2. \quad (125)$$

Besides uniform, also *Gaussian* and exponential PDFs have been proposed and applied [275]. At the end, the roughness induced depolarization is incorporated in the scattering formalism and is controlled by the range of the rotation angle distribution width ψ_l .

The *X-Bragg* model can be used to replace the classical surface scattering component within the model-based decomposition (cf. Chapter 3.2.4.2.1.) and is expressed in the notation of the model-based decomposition as [124]

$$[T_{XB}] = fs \begin{bmatrix} 1 & \beta_S^* \text{sinc}(2\psi_l) & 0 \\ \beta_S \text{sinc}(2\psi_l) & \frac{1}{2} |\beta_S|^2 (1 + \text{sinc}(4\psi_l)) & 0 \\ 0 & 0 & \frac{1}{2} |\beta_S|^2 (1 - \text{sinc}(4\psi_l)) \end{bmatrix}. \quad (126)$$

In Figures 14 and 15 the behavior of the individual coherency matrix components of $[T_{XB}]$ with respect to the local incidence angle θ_l for two different soil roughness levels ($\psi_1 = [30^\circ, 55^\circ]$) is shown. The components of $[T_{XB}]$ rise with increasing local incidence angle θ_l , while T_{XB11} reveals the strongest backscattering followed by T_{XB12} and T_{XB22} . For a high soil roughness level ($\psi_1 = 55^\circ$ in Figure 15), T_{XB33} outruns the T_{XB22} -component due to the roughness induced depolarization.

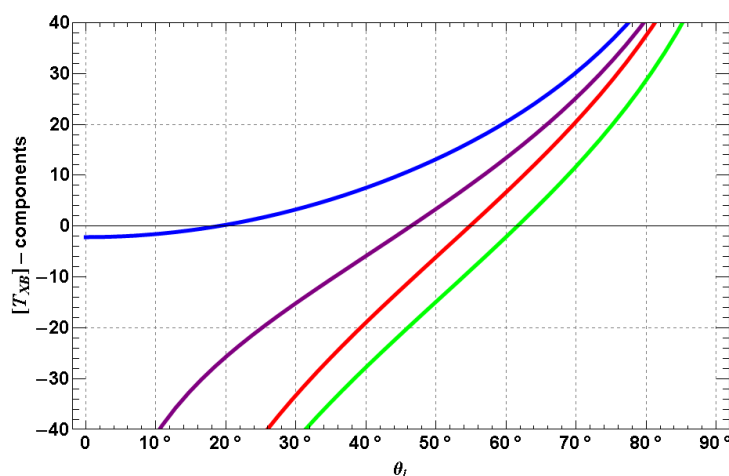


Figure 14: Behavior of $[T_{XB}]$ -components in [dB] with respect to the incidence angle θ_l , $\epsilon_s = 20$, $\psi_l = 30^\circ$: T_{XB11} (blue), T_{XB12} (purple), T_{XB22} (red), T_{XB33} (green).

Hajnsek et al. identified ratios of the coherency matrix elements that are independent of the soil dielectric content ϵ_s (cf. Equation 127) or of the soil roughness ψ_1 (cf. Equation 128) [127]

$$\text{sinc}(4\psi_1) = \frac{T_{XB22} - T_{XB33}}{T_{XB22} + T_{XB33}} \quad (127)$$

$$\frac{|R_h - R_v|^2}{|R_h + R_v|^2} = \frac{T_{XB22} + T_{XB33}}{T_{XB11}}. \quad (128)$$

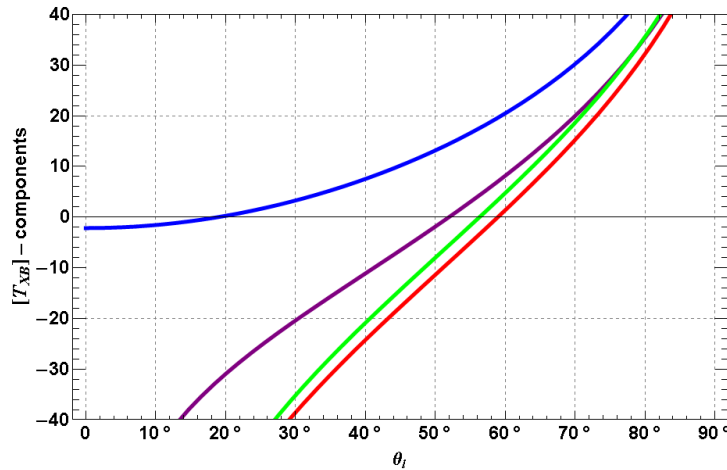


Figure 15: Behavior of $[T_{XB}]$ -components in [dB] with respect to the incidence angle θ_i , $\varepsilon_s = 20$, $\psi_i = 55^\circ$: T_{XB11} (blue), T_{XB12} (purple), T_{XB22} (red), T_{XB33} (green).

In this way, the influence of the dielectric constant (soil moisture) and of the soil roughness can be separated by using the polarimetric entropy and the mean scattering alpha angle. In order to invert for both soil parameters, the difference between the polarimetric entropy and the mean scattering alpha angle of the *X-Bragg* model and of the polarimetric SAR data is minimized. Furthermore, the use of polarimetric entropy and mean scattering scattering alpha angle has the advantage of independence on LoS rotations, as introduced in the presence of topographic terrain variations (cf. Chapter 3.2.4.1.1.).

4.1.5. Polarimetric soil roughness inversion

The second key parameter of the soil is the roughness. Over the last decades several methods for soil roughness retrieval on bare soils were developed, which can be distinguished in empirical, semi-empirical and theoretical methods. Similar as in the case of soil moisture, empirical and semi-empirical approaches compromise robustness and generality [323, 349, 348]. Theoretical models, as the IEM, allow the derivation of a more general roughness descriptions [239, 323]. As this soil scattering model needs input from both, the soil roughness and the moisture, some roughness retrieval approaches use multi-angular/multi-temporal acquisitions to calibrate the model in order to bypass the dependency on soil moisture and to estimate the soil roughness [73, 266, 11, 251].

In order to separate the roughness from the soil contribution for a subsequent derivation of the roughness parameter ks , polarimetric approaches have been pro-

ven to be effective:

- *Cloude et al.* derived a semi-empirical, linear relationships of ks and the anisotropy A [64, 68, 119]

$$ks = 1 - A. \quad (129)$$

The anisotropy is a function of the minor eigenvalues, which can be prone to noise errors [127]. Thus polarimetric noise filtering, as presented in Appendix A, improves the reliability of the roughness retrieval method.

- *Mattia et al.* proposed the modulus of the circular coherence $|\gamma_{RRLL}|$ for surface roughness [204]. This study was deepened in [270] for different incidence angles, where a decrease of $|\gamma_{RRLL}|$ was correlated with an increase of the surface roughness ks . The comparison of A and $|\gamma_{RRLL}|$ reveals an increased sensitivity of the circular coherence towards smooth surfaces ($ks < 0.5$), if compared to the anisotropy. This is due to the fact that the third eigenvalue decreases much faster than the cross-component $\langle |S_{XX}|^2 \rangle$ [126, 270]. Following [270], a simple linear relationship between ks and $|\gamma_{RRLL}|$ was defined in [126]

$$ks = 1 - |\gamma_{RRLL}| = 1 - \left| \frac{\langle S_{RR} S_{LL}^* \rangle}{\sqrt{\langle |S_{RR}|^2 \rangle \cdot \langle |S_{LL}|^2 \rangle}} \right| \quad (130)$$

$$S_{RR} = \frac{1}{2} (S_{HH} - S_{VV} + i2S_{XX}) \quad \text{and} \quad S_{LL} = \frac{1}{2} (S_{VV} - S_{HH} + i2S_{XX}). \quad (131)$$

- *Hajnsek et al.* proposed a ratio of the coherency matrix elements as shown in Equation 127, which depends only on the depolarization angle ψ_l controlling the surface roughness in the *X-Bragg* model [127]. In a second step the soil roughness parameter ks of Equation 13 can be calculated as a first approximation by $ks = 2/\pi \cdot \psi_l$ [150]

$$ks = \frac{1}{2\pi} \cdot \arcsinc \left(\frac{T_{22} - T_{33}}{T_{22} + T_{33}} \right). \quad (132)$$

Figure 16 depicts the trend of the ratio for different roughness levels, leading to negative values of the ratio for high roughness levels ($\psi_l > 45^\circ$).

Assuming reflection symmetry, the equivalence of $|\gamma_{RRLL}|$ and $\arcsinc(4\psi_l)$ can be verified underlining the similarity of the two approaches [127, 65]:

$$|\gamma_{RRLL}| = \left| \frac{T_{33} - T_{22}}{T_{22} + T_{33}} \right| = \frac{T_{22} - T_{33}}{T_{22} + T_{33}} = \arcsinc(4\psi_l). \quad (133)$$

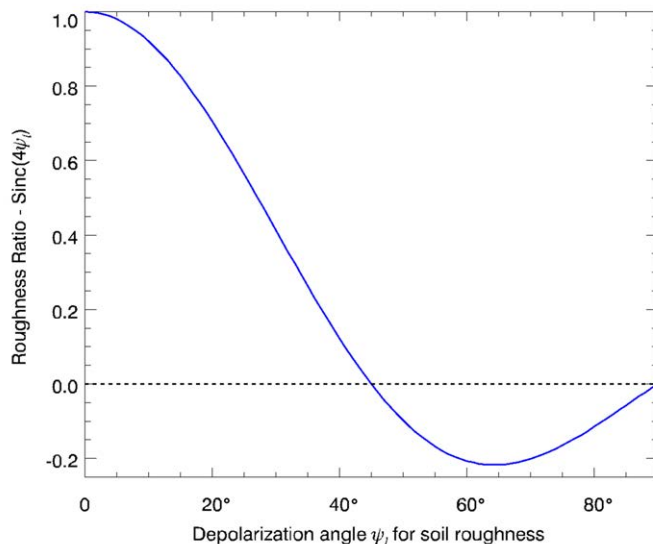


Figure 16: Roughness term of coherency matrix elements $\text{sinc}(4\psi_l) = (T_{22} - T_{33}) / (T_{22} + T_{33})$ depending only on the rotation angle ψ_l , which refers to different soil roughness induced depolarization states.

For azimuthal symmetry the calculus even simplifies to

$$|\gamma_{RRLL}| = |(\lambda_3 - \lambda_2) / (\lambda_2 + \lambda_3)|. \quad (134)$$

An overview of several polarimetric estimation approaches for soil roughness is provided by *Marzahn* and *Ludwig* in [202].

4.2. Scattering and decomposition models for vegetated soils

Instead of modeling and inverting for the total scattered signal, polarimetric scattering decompositions may allow to separate the single scattering components and to invert them individually reducing the dimensionality of the inversion problem. The general work flow for soil parameter retrieval using polarimetric decompositions, is shown in Figure 17. For the retrieval of soil information under vegetation using fully polarimetric SAR data, an inversion method using theoretically-based EM models is required, which still allows an analytical solution of the decomposition model without inclusion of *a priori* knowledge to obtain test site independence.

A fully polarimetric SAR system operated at longer wavelengths (e.g. L-band with $\lambda_c = 23\text{cm}$) is considered suitable to achieve the needed penetration through the

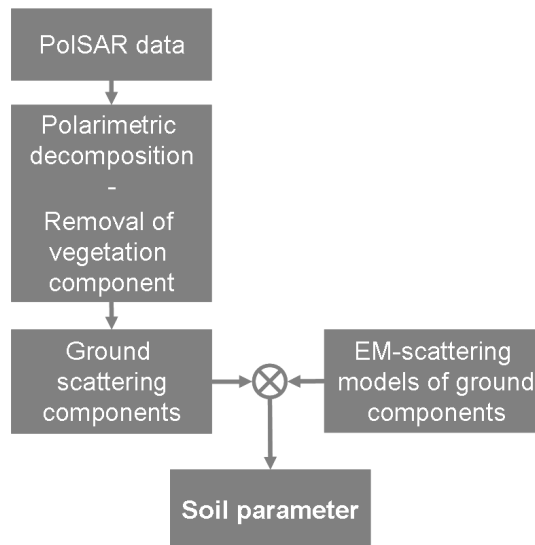


Figure 17: General work flow of soil parameter retrieval from polarimetric SAR data using polarimetric decomposition techniques.

agricultural vegetation layer and to retrieve information about the underlying soil. Thus the assumptions of the following polarimetric scattering models are adapted to fit longer wavelength SAR acquisitions.

4.2.1. Modifications of model-based decompositions

As introduced in Chapter 3.2.4.2. model-based decompositions can be used to decompose a polarimetric scattering signature into a set of (canonical) scattering contributions. Therefore the decomposition techniques can be utilized to separate the vegetation from the ground, including surface and dihedral scattering components:

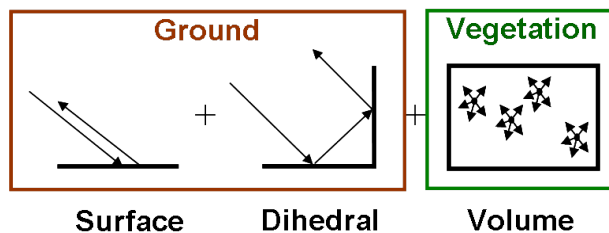


Figure 18: Schematical representation of ground (surface, dihedral) and vegetation (volume) components of model-based decompositions.

However, the canonical scattering components, used in standard decomposition approaches and described in Chapter 3.2.4.2., are not flexible enough to be able to describe a realistic agricultural scattering scenario. Therefore the scattering

components needs to be modified and enlarged with respect to Chapter 3.2.4.2. in order to be able to represent different natural scattering scenarios including depolarizing ground scattering or oriented volume scattering.

4.2.1.1. Modification of the surface component

A *Bragg* surface scattering model, like addressed in Equation 113, is applied in standard polarimetric model-based decompositions as presented in Equation 111. The validity range of this scattering model is limited to a vertical surface roughness of $ks < 0.3$, appearing in the roughness loss factor $m_s = 2\cos(\theta_l)^2 \cdot ks \cdot kl \cdot \exp(-\frac{1}{2}(klsin(\theta_l))^2)$ [312, 308]. Many natural soil scatterers are beyond the validity range of *Bragg* ($ks|s < 0.3|1.1\text{cm}$). A second key limitation is the inability of the *Bragg* surface scattering model to describe roughness induced depolarization occurring for instance on agricultural fields. The *X-Bragg* model, introduced in Chapter 4.1.4., allows to compensate both limitations at least partially ($ks|s < 1|3.7\text{cm}$) and will be used as a more realistic alternative to *Bragg* in the following. The price to pay is the increase of required parameters from two (*Bragg*) to three (*X-Bragg*).

4.2.1.2. Modification of the dihedral component

In Chapter 3.2.4.2.2. the classical dihedral component has been introduced as double *Fresnel* reflection. A first step to consider the losses due to surface roughness on f_D is done by incorporating the so called *modified Fresnel* scattering coefficients [178]. The polarization independent loss component m_d is defined as

$$\begin{aligned} m_{d_g} &= \exp(-2 \cdot k^2 \cdot s^2 \cdot \cos(\theta_l)^2) && \text{Gaussian ACF} \\ m_{d_e} &= \exp(-2 \cdot k \cdot s \cdot \cos(\theta_l)) && \text{Exponential ACF,} \end{aligned} \quad (135)$$

depending on the Auto Correlation Function (ACF) of the surface description [65, 124, 312]. The behavior of the *Gaussian* $m_{d_g}^2$ and of the exponential $m_{d_e}^2$ roughness intensity loss with respect to the local incidence angle θ_l and the vertical surface roughness s is given in Figures 19 and 20. Figure 19 indicates a decreasing loss with increasing incidence angle, which is more pronounced for a *Gaussian* surface at high roughness scenarios. In Figure 20 a rougher soil causes a bigger loss of the dihedral intensity, which is stronger for small local incidence angles. The exponential ACF induces stronger losses than the *Gaussian* ACF for low vertical roughness, while the situation is reversed in high roughness scenarios for steep local incidence angles ($\theta_l = 20^\circ$). In addition, a vegetation attenuation loss term $m_{d_{v/v\theta_l}}$ for the dihedral intensity component f_D , accounting for a two-way vegeta-

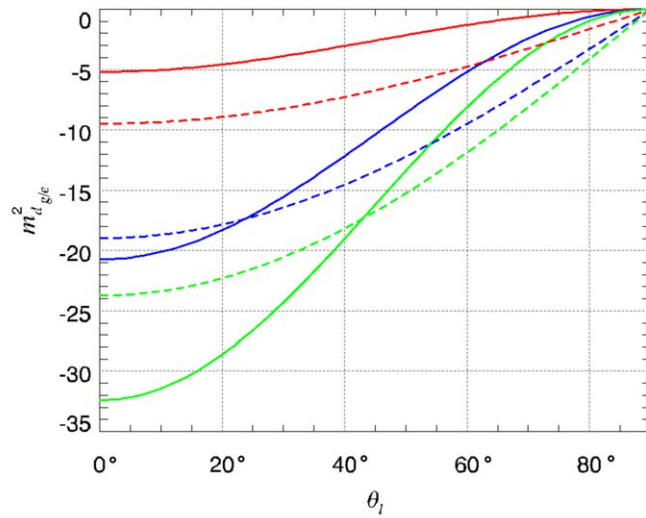


Figure 19: Behavior of the $m_{d_{g/e}}^2$ -component with respect to the local incidence angle (θ_l) in [dB] for three roughness conditions s : Red=2cm, blue=4cm, green=5cm; Dashed=exponential ACF, solid=*Gaussian* ACF.

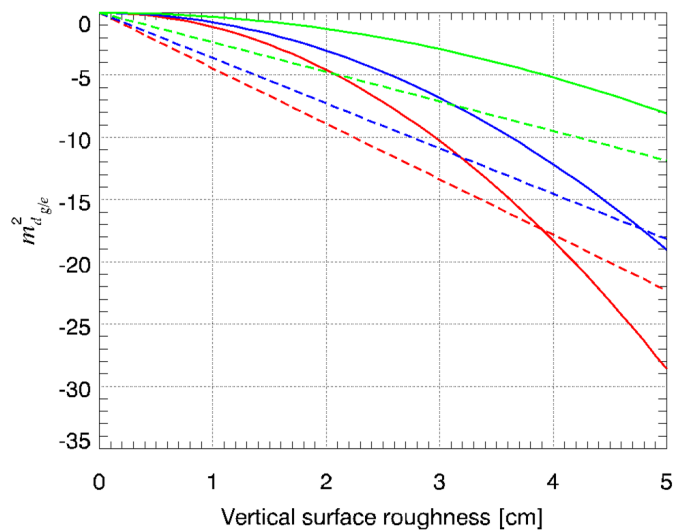


Figure 20: Behavior of the $m_{d_{g/e}}^2$ -component with respect to the vertical surface roughness (s) in [dB] for three local incidence angles θ_l : Red=20°, blue=40°, green=60°; Dashed=exponential ACF, solid=*Gaussian* ACF.

tion attenuation during the propagation through the vegetation layer [159, 129], can be defined as

$$m_{d_v} = \exp\left(\frac{-1}{2(\mu_{max} - \mu_{min})}\right), \quad \text{where } \mu_{max} = \frac{\lambda_1}{P_V} \quad \text{and} \quad \mu_{min} = \frac{\lambda_2}{P_V}, \quad (136)$$

or as function of the local incidence θ_l :

$$m_{d_v, \theta_l} = \exp\left(\frac{-\sin(\theta_l)^2}{2(\mu_{max} - \mu_{min})}\right). \quad (137)$$

In Equations 136 and 137 μ_{max} and μ_{min} are the maximum and minimum polarimetric ground-to-volume ratios, which can be calculated from the eigenvalues (λ_1 , λ_2) of the summed ground component matrix ($[T_g] = [T_S] + [T_D]$) after removal of the volume component and the power of the volume component from a model-based decomposition P_V (cf. Equation 112). Figure 21 establishes the relation between the ground-to-volume difference $\mu_{max} - \mu_{min}$ and the vegetation height with $R^2 = 0.9$, while Figure 22 displays the sensitivity of the vegetation attenuation component m_{d_v, θ_l}^2 with respect to the ground-to-volume difference. The dependence of m_{d_v, θ_l} on the local incidence leads to a decrease of the vegetation attenuation loss for shallower local incidence angles.

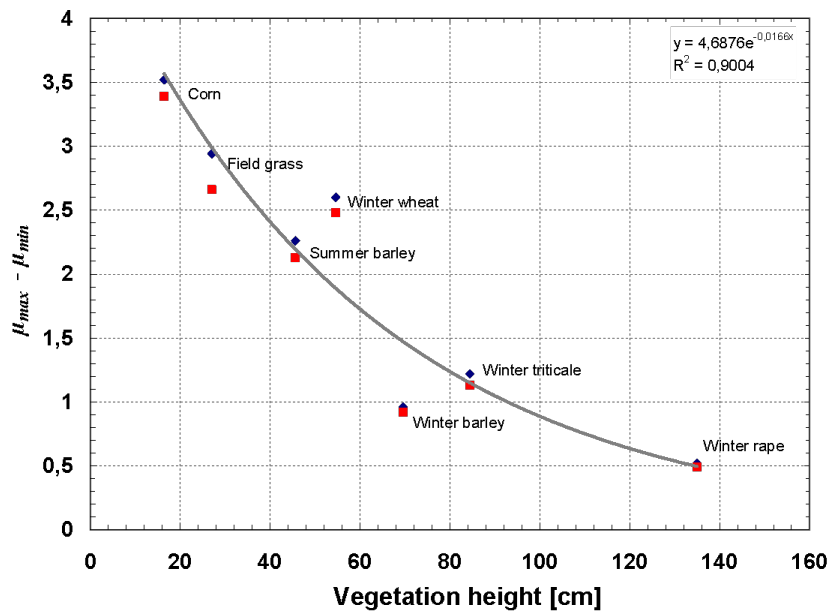


Figure 21: Sensitivity of the ground-to-volume ratio difference ($\mu_{max} - \mu_{min}$) to the height of the vegetation for OPAQUE campaign data of May 2007 in L-band (after model-based decomposition including volume power correction); Blue diamonds= mean of field, red squares= median of field, black line= regression curve.

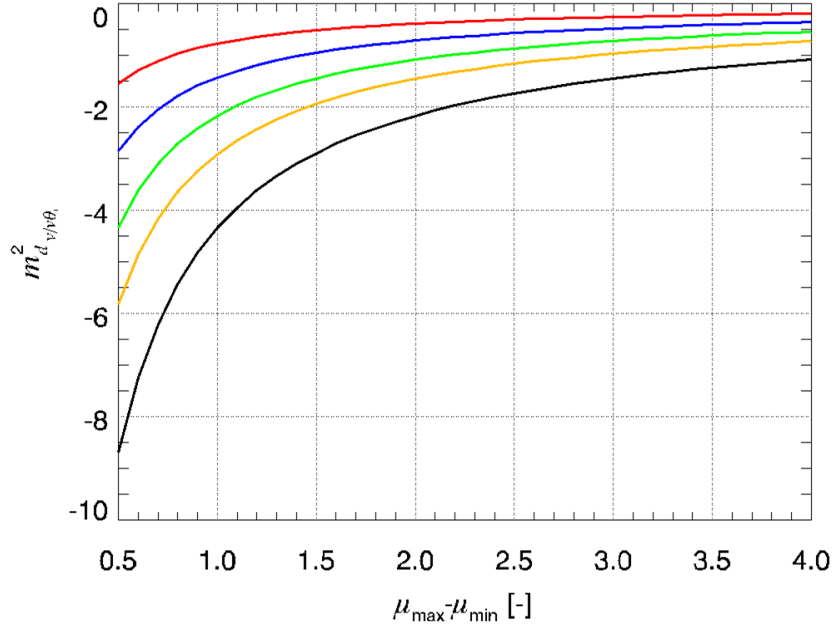


Figure 22: Sensitivity of the $m_{d_v}^2$ -component (black) and the $m_{d_{v\theta_l}}^2$ -component (colored) in [dB] to the ground-to-volume difference ($\mu_{max} - \mu_{min}$) for different local incidence angles: $m_{d_{v\theta_l=25^\circ}}^2$ (red), $m_{d_{v\theta_l=35^\circ}}^2$ (blue), $m_{d_{v\theta_l=45^\circ}}^2$ (green), $m_{d_{v\theta_l=55^\circ}}^2$ (yellow).

Despite all modifications, the m_d -component can not account for roughness induced depolarization. The following model approach with an extended dihedral scattering matrix $[S_{XD}]$ copes with this shortcoming.

Natural soil surfaces exhibit a distinct surface roughness and thus depolarize the dihedral scattering signal. This can be modeled, similar to the *X-Bragg* case, by integrating along a LoS-rotation distribution of the soil plane. The LoS-rotation of the soil plane (R_{sh}, R_{sv}) with rotation angle ψ is incorporated in Equation 138 [154]. Scattering of the vertical plane (R_{th}, R_{tv}) is still represented by a non-depolarizing *Fresnel* reflection of a vertical plant stalk/stem (cf. Equation 199) [154]:

$$[S_{XD}] = \begin{bmatrix} S_{XD11} & S_{XD12} \\ S_{XD21} & S_{XD22} \end{bmatrix} = \frac{m_{d_{e/g/v/v\theta_l}}}{2}. \quad (138)$$

$$\left(\left(\begin{bmatrix} 1 & 0 \\ 0 & -1 \end{bmatrix} \begin{bmatrix} 1 & 0 \\ 0 & \exp(i\phi_d) \end{bmatrix} \begin{bmatrix} \cos\psi & \sin\psi \\ -\sin\psi & \cos\psi \end{bmatrix} \begin{bmatrix} R_{sh} & 0 \\ 0 & R_{sv} \end{bmatrix} \begin{bmatrix} \cos\psi & -\sin\psi \\ \sin\psi & \cos\psi \end{bmatrix} \begin{bmatrix} R_{th} & 0 \\ 0 & R_{tv} \end{bmatrix} \right) + \right.$$

$$\left. \left(\begin{bmatrix} R_{th} & 0 \\ 0 & R_{tv} \end{bmatrix} \begin{bmatrix} \cos\psi & \sin\psi \\ -\sin\psi & \cos\psi \end{bmatrix} \begin{bmatrix} R_{sh} & 0 \\ 0 & R_{sv} \end{bmatrix} \begin{bmatrix} \cos\psi & -\sin\psi \\ \sin\psi & \cos\psi \end{bmatrix} \begin{bmatrix} 1 & 0 \\ 0 & \exp(i\phi_d) \end{bmatrix} \begin{bmatrix} 1 & 0 \\ 0 & -1 \end{bmatrix} \right) \right).$$

As natural media consists of distributed scatterers the scattering matrix $[S_{XD}]$ is expanded to the coherency matrix $[T_{XD}]$ using the *Pauli* scattering vector \underline{k}_{PXD} [154]:

$$\underline{k}_{PXD} = \frac{m_{d_e/g/v/v\theta_l}}{\sqrt{2}} \left[\begin{array}{ccc} S_{XD11} + S_{XD22} & S_{XD11} - S_{XD22} & S_{XD12} + S_{XD21} \end{array} \right]^T. \quad (139)$$

After rotation, the coherency matrix is integrated over ψ assuming a uniform PDF of $2\psi_l$ width. This results in a reflection symmetric coherency matrix $[T_{XD}]$ for a depolarizing dihedral scattering component with a soil roughness influence represented by ψ_l by means of an *Extended Fresnel* or *X-Fresnel* formalism [154]:

$$\begin{aligned} [T_{XD}] &= m_{d_e/g/v/v\theta_l}^2 \int_{-\psi_l}^{\psi_l} \underline{k}_{PXD} \cdot \underline{k}_{PXD}^{*T} \cdot pdf(\psi) \, d\psi \\ &= m_{d_e/g/v/v\theta_l}^2 \left[\begin{array}{ccc} T_{XD11} & T_{XD12} & 0 \\ T_{XD21} & T_{XD22} & 0 \\ 0 & 0 & T_{XD33} \end{array} \right] = f_{DXD} \left[\begin{array}{ccc} cd_{XD} & \alpha_{XD} & 0 \\ \alpha_{XD}^* & 1 & 0 \\ 0 & 0 & xd_{XD} \end{array} \right]. \end{aligned} \quad (140)$$

In this way the *X-Fresnel* components for a dihedral scattering can be defined as follows

$$f_{DXD} = m_{d_e/g/v/v\theta_l}^2 T_{XD22}, \quad \alpha_{XD} = \frac{T_{XD12}}{T_{XD22}}, \quad cd_{XD} = \frac{T_{XD11}}{T_{XD22}}, \quad xd_{XD} = \frac{T_{XD33}}{T_{XD22}}, \quad (141)$$

where α_{XD} and f_{DXD} correspond to the rank-1 *Fresnel* components α and f_D [154]. Figures 23 and 24 show the behavior of the coherency matrix elements T_{XD11} , T_{XD12} , T_{XD22} and T_{XD33} on the local incidence angle θ_l , the rotation angle accounting for soil roughness ψ_l and the dielectric constants ϵ_s, ϵ_t . The plot of Figure 23 indicates a positive trend for T_{XD33} and a negative trend for the remaining matrix elements stating the increase of roughness induced depolarization until at least $\psi_l=60^\circ$ [154].

The dependency on the local incidence angle (θ_l), shown in Figure 24, has a maximum or a minimum, depending on the coherency matrix element, at approximately 45° . Thus it rises from 0° until 45° and then decreases from 45° until 90° or vice versa. T_{XD11} and T_{XD12} decrease approximately until 45° due to decreasing odd bounce scattering and then increase again up to the starting level at almost grazing angles ($\theta_l \rightarrow 90^\circ$). T_{XD22} and T_{XD33} increase until mid-range of the local incidence angle due to increasing even bounce scattering as well as rising depolarization and then decrease to the starting level, while it depends on the depolarization level (ψ_l) which curve is superior with respect to each other [154]. The *Brewster* angles, where vertically polarized scattering (S_{VV}) drops to zero, are at

the crossing points (red dots in Figure 24), where T_{XD11} equals T_{XD22} .

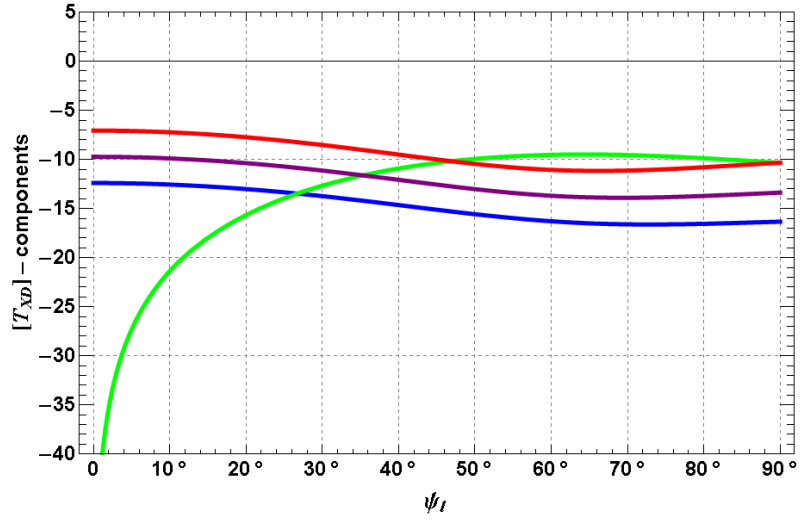


Figure 23: Behavior of the coherency matrix elements T_{XD11} (blue), T_{XD12} (purple), T_{XD22} (red), T_{XD33} (green) in [dB] with respect to the rotation angle accounting for soil roughness ψ_l , $m_d = 1$, $\phi_d = 0^\circ$, $\varepsilon_s = 20$, $\varepsilon_t = 10$, $\theta_l = 30^\circ$ [154].

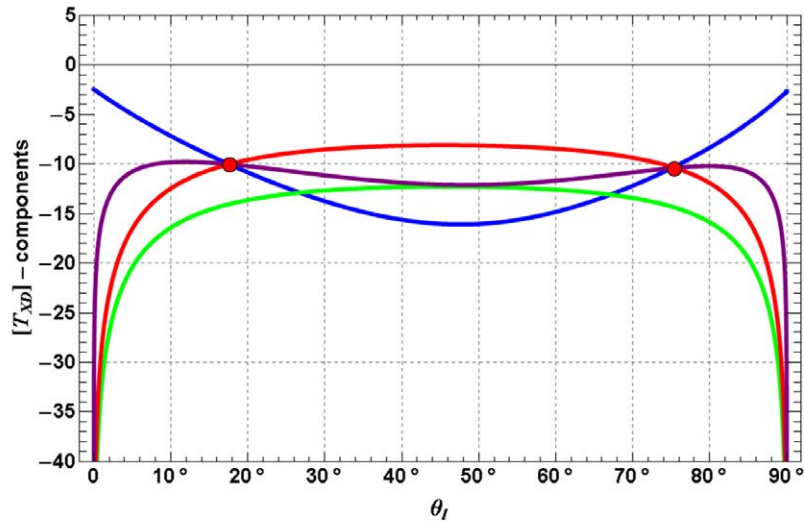


Figure 24: Behavior of the coherency matrix elements T_{XD11} (blue), T_{XD12} (purple), T_{XD22} (red), T_{XD33} (green) in [dB] with respect to the local incidence angle θ_l (red points = Brewster angle), $m_d = 1$, $\phi_d = 0^\circ$, $\varepsilon_s = 20$, $\varepsilon_t = 10$, $\psi_l = 30^\circ$ [154].

Comparing Figures 25 and 26 with Figures 27 and 28 reveals the sensitivity of $T_{XD33} + T_{XD22}$ on the dielectric constants ($\varepsilon_s, \varepsilon_t$) and its insensitivity on the surface roughness ψ_l . Therefore this term is preferable for the retrieval of the dielectric

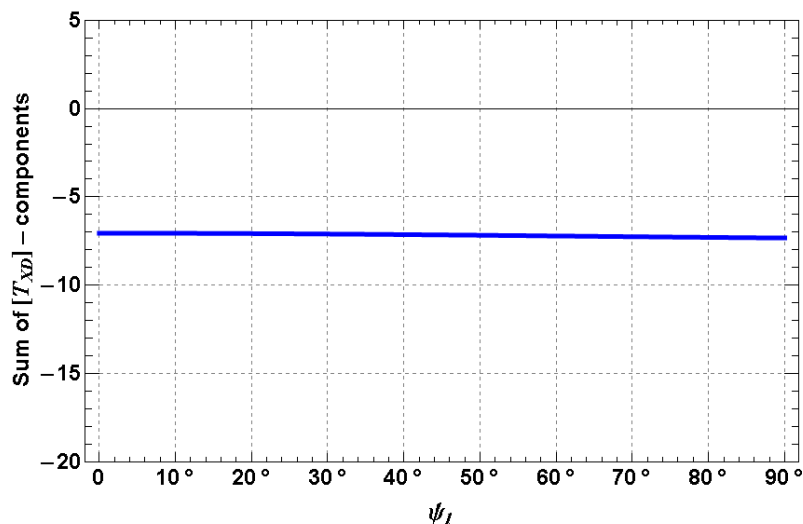


Figure 25: Behavior of the coherency matrix combination $T_{XD33} + T_{XD22}$ in [dB] with respect to the rotation angle accounting for soil roughness ψ_l , $m_d = 1$, $\phi_d = 0^\circ$, $\epsilon_s = 20$, $\epsilon_t = 10$, $\theta_l = 30^\circ$ [154].

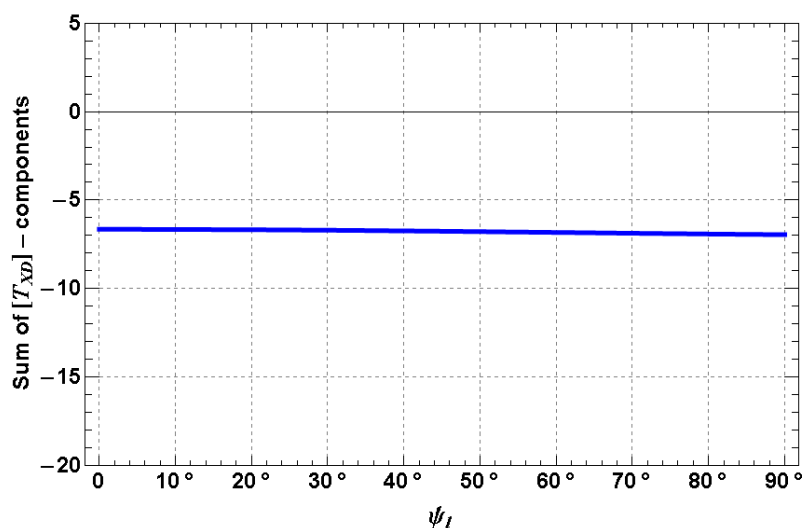


Figure 26: Behavior of the coherency matrix combination $T_{XD33} + T_{XD22}$ in [dB] with respect to the rotation angle accounting for soil roughness ψ_l , $m_d = 1$, $\phi_d = 0^\circ$, $\epsilon_s = 20$, $\epsilon_t = 10$, $\theta_l = 50^\circ$ [154].

properties of the soil ϵ_s and trunk ϵ_t , avoiding at the same time the influence of soil roughness. But due to the coupling of the two dielectric constants within the *Fresnel* coefficients, they can not be retrieved independently from each other.

Finally, Figures 29 to 31 show the behavior of the ratio $(T_{XD22} - T_{XD33}) / (T_{XD22} + T_{XD33})$ with respect to the soil roughness ψ_l . The function $\text{sinc}(4\psi_l)$ is also plot-

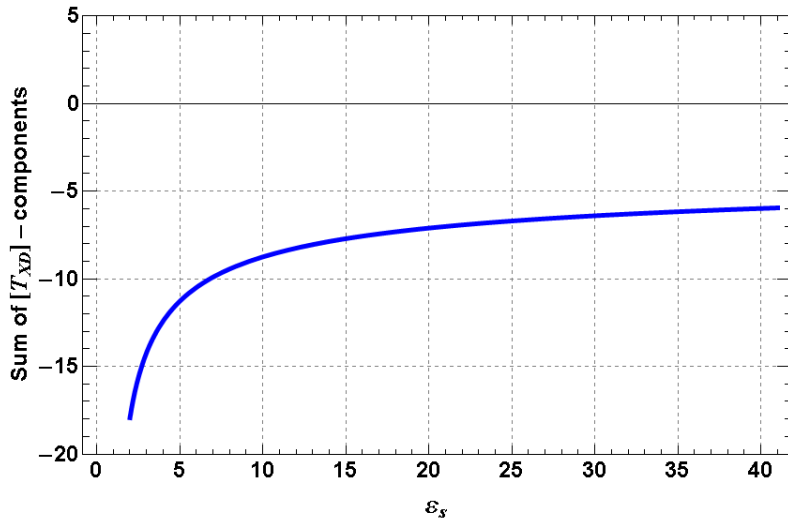


Figure 27: Behavior of the coherency matrix combination $T_{XD33} + T_{XD22}$ in [dB] with respect to the dielectric constant of the soil ε_s , $m_d = 1$, $\phi_d = 0^\circ$, $\varepsilon_t = 10$, $\theta_l = 30^\circ$, $\psi_l = 30^\circ$ [154].

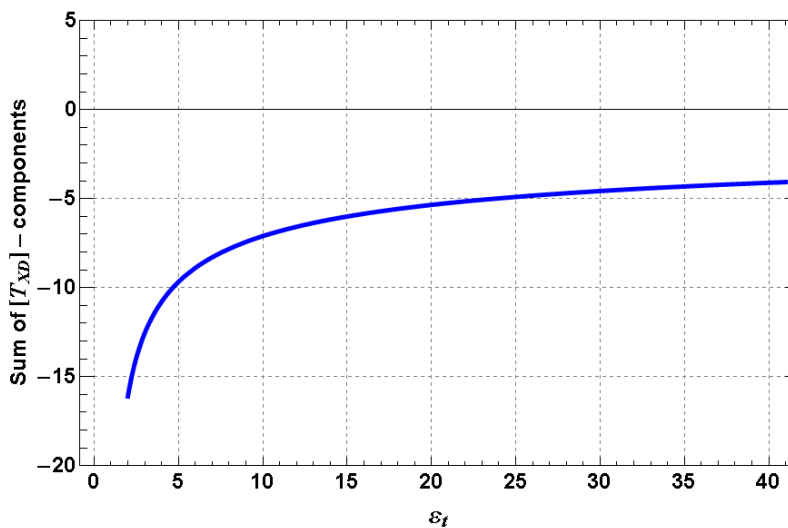


Figure 28: Behavior of the coherency matrix combination $T_{XD33} + T_{XD22}$ in [dB] with respect to the dielectric constant of the trunk ε_t , $m_d = 1$, $\phi_d = 0^\circ$, $\varepsilon_s = 20$, $\theta_l = 30^\circ$, $\psi_l = 30^\circ$ [154].

ted as a reference. The overlap of the two functions for the different ranges of local incidence θ_l and dielectric constants $(\varepsilon_s, \varepsilon_t)$ is distinct [154], indicating that the ratio only depends on the soil roughness and not on the dielectric properties of the media [154]. Furthermore, the trend with soil roughness ψ_l can be modeled by a simple $\text{sinc}(4\psi_l)$ -function [154]. It is worth noting that the ratio

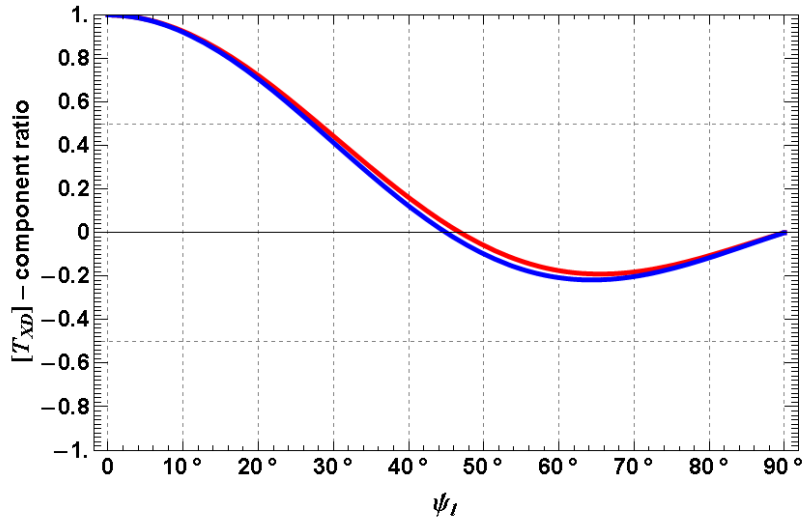


Figure 29: Behavior of the coherency matrix combination $(T_{XD22} - T_{XD33})/(T_{XD22} + T_{XD33})$ with respect to the rotation angle accounting for soil roughness ψ_l (blue) and comparison with the function $\text{sinc}(4\psi_l)$ (purple), $\phi_d = 0^\circ$, $\varepsilon_s = 20$, $\varepsilon_t = 10$, $\theta_l = 30^\circ$ [154].

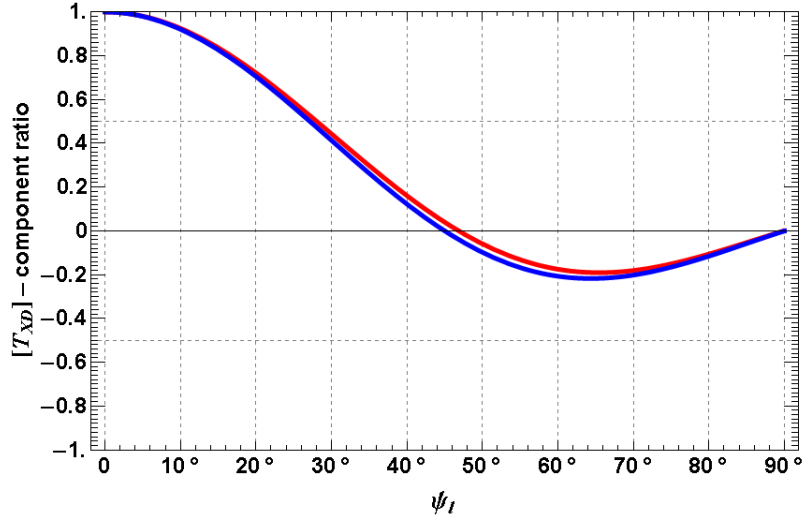


Figure 30: Behavior of the coherency matrix combination $(T_{XD22} - T_{XD33})/(T_{XD22} + T_{XD33})$ with respect to the rotation angle accounting for soil roughness ψ_l (blue) and comparison with the function $\text{sinc}(4\psi_l)$ (purple), $\phi_d = 0^\circ$, $\varepsilon_s = 20$, $\varepsilon_t = 10$, $\theta_l = 60^\circ$ [154].

$(T_{XD22} - T_{XD33})/(T_{XD22} + T_{XD33})$ is independent of the loss factor $m_{d_{e/g/v/v\theta_l}}$, unlike the term $T_{XD33} + T_{XD22}$. But both terms still include the dependency on the differential phase ϕ_d , which becomes important in the case of strongly oriented media [154].

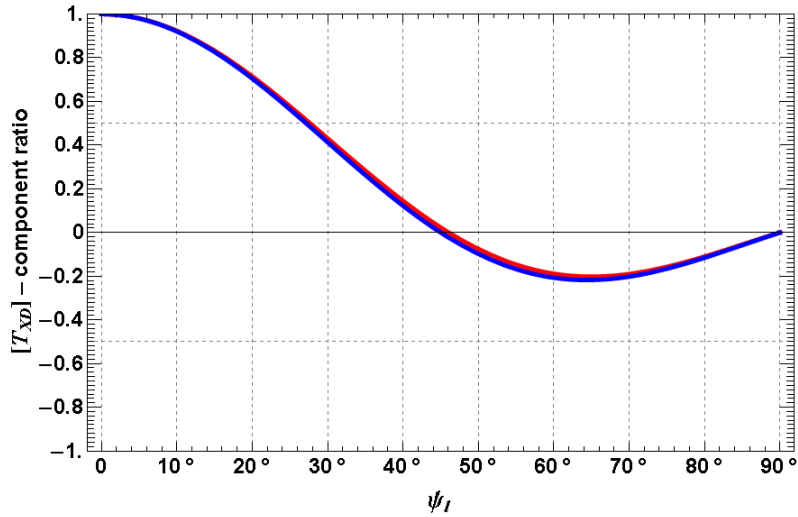


Figure 31: Behavior of the coherency matrix combination $(T_{XD22} - T_{XD33}) / (T_{XD22} + T_{XD33})$ with respect to the rotation angle accounting for soil roughness ψ_l (blue) and comparison with the function $\text{sinc}(4\psi_l)$ (purple), $\phi_d = 0^\circ$, $\varepsilon_s = 20$, $\varepsilon_t = 30$, $\theta_l = 30^\circ$ [154].

4.2.1.3. Modification of the volume component

The vegetation volume component $[T_V]$ reveals as the most complex of all model-based scattering components due to its geometrical variability in space and its phenological variability in time. Numerous scattering models for vegetation have been developed and an overview is given in Chapter 1.2.. For the present case, a coherent model approach, using small scattering particles ($p_s \ll \lambda_c$), describes the vegetation as a one-layer volume, sparsely filled with three dimensional scattering centers in a homogeneous background [317, 174, 65, 225]. For a sparsely and homogeneously distributed medium of non-interacting discrete scatterers concerning extinction and refractivity effects, the Effective Field Approximation (EFA), which considers the exciting field to be equal to an ‘effective’ field, holds [174, 305, 245]. Each of these discrete scattering centers represents a particle with a specific shape and material properties. To retrieve the scattered field a large amount of these particles is considered to provide a macroscopic description of the scattering medium [65]. Thus the scattering matrix $[S]$ of an arbitrary vegetation volume can be retrieved by the integration over a particle shape, defined with dimensions x_1 , x_2 , x_3 , and over a distribution of orientation angles multiplied by a constant factor S_{xy} [281, 65]. The orientation angles are given by the *Euler’s* rotation angles ψ , τ

and χ , including a certain Probability Density Function (PDF) for each orientation angle distribution. For a random orientation, the distribution width is set to the maximum and results in the following scattering matrix [65]

$$[S] = \int_0^\infty \int_0^\infty \int_0^\infty \int_0^{2\pi} \int_0^\pi \int_0^{2\pi} S_{xy} pdf(x_1, x_2, x_3, \chi, \tau, \psi) dx_1 dx_2 dx_3 d\chi d\tau d\psi. \quad (142)$$

Hence, the vegetation volume becomes a function of the shape and orientation of the particles in the three dimensional space including their orientation distribution means, PDFs and widths.

However, the starting point for the volume modeling is the single particle of arbitrary shape, which is supposed to be small compared to the wavelength implying *Rayleigh scattering* [317, 32]. The incident field induces an electric dipole moment \underline{p}_{di} and a magnetic dipole moment \underline{m}_{di} [317]. The relation between the incident fields and the induced moments is established by diagonal 3x3 polarizability tensors, like for example $[\rho_{ee}] = \text{diag}(\rho_{ee1}, \rho_{ee2}, \rho_{ee3})$ [2, 65, 1]

$$\begin{bmatrix} \underline{p}_{di} \\ \underline{m}_{di} \end{bmatrix} = \begin{bmatrix} [\rho_{ee}] & [\rho_{em}] \\ [-\rho_{em}] & [\rho_{mm}] \end{bmatrix} \begin{bmatrix} \underline{E}^i \\ \underline{H}^i \end{bmatrix}, \quad \text{where} \quad (143)$$

$$\underline{E}^i = \begin{bmatrix} E_H^i & E_V^i & 0 \end{bmatrix}^T \quad \text{and} \quad \underline{H}^i = \sqrt{\epsilon_0/\mu_0} \begin{bmatrix} -E_V^i & E_H^i & 0 \end{bmatrix}^T. \quad (144)$$

ϵ_0 and μ_0 are the permittivity and the permeability of the free space. The polarization tensors have to be transformed from their local coordinate system into the coordinate system of the observer to calculate the moments in the three dimensional space (cf. Figure 32). This is carried out by the *Euler* rotation angles (spin χ , tilt τ , canting ψ), which can be integrated into a single general rotation matrix $[R_g]$ [281, 65]

$$[R_g] = \begin{bmatrix} \cos(\chi) & \sin(\chi) & 0 \\ -\sin(\chi) & \cos(\chi) & 0 \\ 0 & 0 & 1 \end{bmatrix} \begin{bmatrix} \cos(\tau) & 0 & -\sin(\tau) \\ 0 & 1 & 0 \\ \sin(\tau) & 0 & \cos(\tau) \end{bmatrix} \begin{bmatrix} \cos(\psi) & \sin(\psi) & 0 \\ -\sin(\psi) & \cos(\psi) & 0 \\ 0 & 0 & 1 \end{bmatrix} = \quad (145)$$

$$\begin{bmatrix} \cos(\psi)\cos(\tau)\cos(\chi) - \sin(\psi)\sin(\chi) & \cos(\psi)\sin(\chi) + \sin(\psi)\cos(\tau)\cos(\chi) - \sin(\tau)\cos(\chi) \\ -\cos(\psi)\cos(\tau)\sin(\chi) - \sin(\psi)\cos(\chi) & \cos(\psi)\cos(\chi) - \sin(\psi)\cos(\tau)\sin(\chi) & \sin(\tau)\sin(\chi) \\ \cos(\psi)\sin(\tau) & \sin(\psi)\sin(\tau) & \cos(\tau) \end{bmatrix}.$$

Hence, the general expression of Equation 143 can be rewritten for the three dimensional case [65]

$$\begin{bmatrix} \underline{p}_{di}^{real} \\ \underline{m}_{di}^{real} \end{bmatrix} = \begin{bmatrix} [R_g^{-1}] [\rho_{ee}] [R_g] & [R_g^{-1}] [\rho_{em}] [R_g] \\ [R_g^{-1}] [-\rho_{em}] [R_g] & [R_g^{-1}] [\rho_{mm}] [R_g] \end{bmatrix} \begin{bmatrix} \underline{E}^i \\ \underline{H}^i \end{bmatrix} \quad (146)$$

Instead of evaluating Equation 146 and estimate the scattering matrix $[S]$ for a

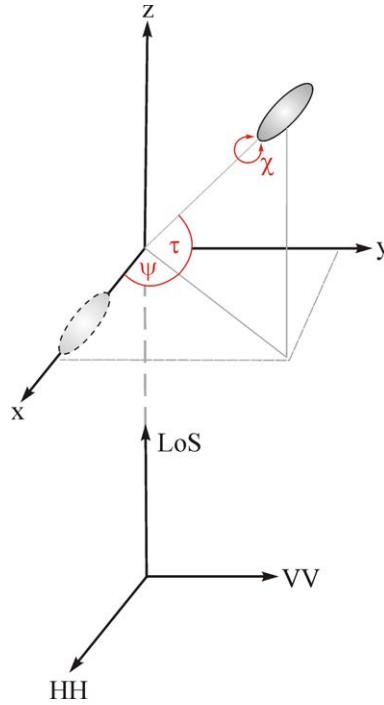


Figure 32: Orientation of a spheroid in three dimensional observation space in terms of the *Euler* rotation angles for canting ψ , tilt τ and spin χ and the geometry of the SAR acquisition.

particle with arbitrary shape, it makes sense to concentrate on scattering from natural environments described by non-chiral particles of canonical shape. For an appropriate particle shape, spheroids with major axis (x_1) and two equally long minor axes ($x_2 = x_3$) are a realistic assumption for agricultural vegetation that simplify Equation 142 [162, 67, 189] (cf. Figure 33). Depending on the ratio of the particle axes $L_r = x_1/x_2$, the shape of spheroids can vary from thin dipoles via discs with prolate or oblate shape to spheres [1]. The polarizabilities along the major ρ_{ee1} and minor axes ρ_{ee2} are then defined as [67]

$$\rho_{ee1} = \frac{V}{4\pi(L_1 + 1/(\epsilon_r - 1))} \quad \text{and} \quad \rho_{ee2} = \frac{V}{4\pi(L_2 + 1/(\epsilon_r - 1))}, \quad (147)$$

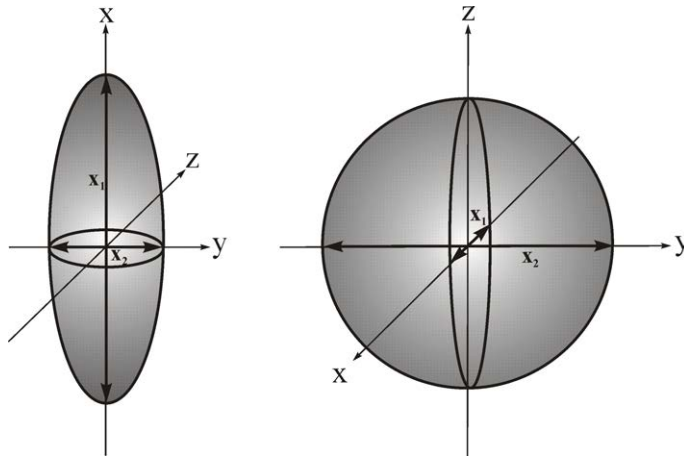


Figure 33: Model of a prolate (left) and oblate (right) spheroid with principal (x_1) and minor axes ($x_2 = x_3$) in the particle reference frame.

where ϵ_r stands for the complex relative dielectric constant of the particle. V is the particle volume (e.g. $V = \pi/6x_1x_2^2$) and L_1 , L_2 and L_3 are particle shape functions, defined for the general case in Equation 17, which for the special case of spheroids (cf. Figure 33) simplify to [317, 31, 225]

$$L_1 = \begin{cases} \text{prolate: } \frac{1-e^2}{e^2} \left(-1 + \frac{1}{2e} \ln \frac{1+e}{1-e} \right) & x_1 > x_2 = x_3 \quad e^2 = 1 - \frac{x_2^2}{x_1^2} \\ \text{oblate: } \frac{1+f^2}{f^2} \left(1 - \frac{1}{f} \arctan(f) \right) & x_1 < x_2 = x_3 \quad f^2 = \frac{x_2^2}{x_1^2} - 1 \end{cases} \quad (148)$$

$$L_2 = L_3 = \frac{1}{2}(1 - L_1).$$

Under the assumption of non-chiral spheroids for Equation 146, the polarizability tensors $[\rho_{em}]$ and $[\rho_{mm}]$ become zero, so that the induced magnetic dipole moment vanishes ($m_{di} = 0$). Moreover, the assumption of the two equal minor axes simplifies the polarizability tensor further to $[\rho_{ee}] = \text{diag}(\rho_{ee1}, \rho_{ee2}, \rho_{ee2})$ [65]. For this reason, the rotation about the spin angle χ becomes obsolete ($\chi = 0$) [189] and Equation 146 turns out as follows

$$\begin{bmatrix} p_{di}^{real} \end{bmatrix} = \begin{bmatrix} \cos(\tau)\cos(\psi) & -\sin(\psi) & \sin(\tau)\cos(\psi) \\ \cos(\tau)\sin(\psi) & \cos(\psi) & \sin(\tau)\sin(\psi) \\ -\sin(\tau) & 0 & \cos(\tau) \end{bmatrix} \begin{bmatrix} \rho_{ee1} & 0 & 0 \\ 0 & \rho_{ee2} & 0 \\ 0 & 0 & \rho_{ee2} \end{bmatrix}$$

$$\begin{bmatrix} \cos(\tau)\cos(\psi) & \cos(\tau)\sin(\psi) & -\sin(\tau) \\ -\sin(\psi) & \cos(\psi) & 0 \\ \sin(\tau)\cos(\psi) & \sin(\tau)\sin(\psi) & \cos(\tau) \end{bmatrix} \begin{bmatrix} E_H^i \\ E_V^i \\ 0 \end{bmatrix}. \quad (149)$$

The particle anisotropy A_p can be defined as the ratio of the principle polarizabilities (cf. Figure 34) [65]

$$A_p = \frac{\rho_{ee1}}{\rho_{ee2}} = \frac{L_2 + 1/(\epsilon_r - 1)}{L_1 + 1/(\epsilon_r - 1)} \begin{cases} A_p < 1 & \text{oblate spheroids} \\ A_p = 1 & \text{spheres} \\ A_p > 1 & \text{prolate spheroids} \end{cases} \quad (150)$$

It reveals that A_p can be used to a certain degree a reference for the particle shape. The dielectric constant of the particle confines the range of possible values for A_p stronger with decreasing dielectric content, degrading the quality of A_p as a shape indicator [65]. This means, the higher the plant moisture, the easier the particle shape can be obtained.

A_p is also related to the effective particle scattering anisotropy δ_a of *Neumann et al.* by using $\delta_a = (A_p - 1)/(1 + A_p + 2A_p \cot(\tau)^2)$ [225, 227], to the alpha scattering angle of *Cloude and Pottier* by using $\alpha = \arctan(|A_p - 1|/(A_p + 1))$ [226, 227] and to the shape parameter of *Freeman* via $\rho = (1 + 3A_p)/(3 + A_p)$ for oblate spheroids and via $\rho = (3 + A_p)/(1 + 3A_p)$ for prolate spheroids [105, 129]. Hence, the rotated polarizability tensor $[\rho_{ee\text{rot}}] = [R_g^{-1}] [\rho_{ee}] [R_g]$ in Equation 149 can be further simplified with $[\rho_{ee}] = \text{diag}(A_p, 1, 1)$ resulting in [65]

$$[\rho_{ee\text{rot}}] = \begin{bmatrix} \rho_{ee\text{rot}11} & \rho_{ee\text{rot}12} & \rho_{ee\text{rot}13} \\ \rho_{ee\text{rot}21} & \rho_{ee\text{rot}22} & \rho_{ee\text{rot}23} \\ \rho_{ee\text{rot}31} & \rho_{ee\text{rot}32} & \rho_{ee\text{rot}33} \end{bmatrix} = \quad (151)$$

$$\begin{bmatrix} 1 + (A_p - 1)\cos(\tau)^2\cos(\psi)^2 & (A_p - 1)\cos(\tau)^2\sin(\psi)\cos(\psi)(1 - A_p)\cos(\tau)\sin(\tau)\cos(\psi) & \\ (A_p - 1)\cos(\tau)^2\sin(\psi)\cos(\psi) & 1 + (A_p - 1)\cos(\tau)^2\sin(\psi)^2 & (1 - A_p)\cos(\tau)\sin(\tau)\sin(\psi) \\ -(A_p - 1)\cos(\tau)\sin(\tau)\cos(\psi) - (A_p - 1)\cos(\tau)\sin(\tau)\sin(\psi) & & A_p\sin(\tau)^2 + \cos(\tau)^2 \end{bmatrix}.$$

The monostatic scattering matrix $[S_{MV}]$ of a spheroidal particle is given by [189,

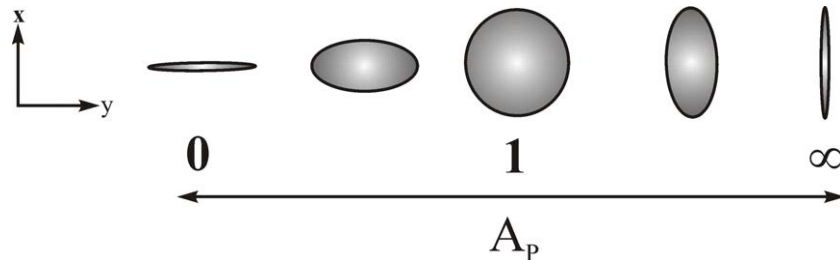


Figure 34: Particle scattering anisotropy A_p , ranging from a oblate spheroid $A_p = 0$ to a prolate spheroid $A_p \rightarrow \infty$ in the x-y plane.

317, 65]

$$\begin{aligned}
 [S_{MV}] &= \begin{bmatrix} \rho_{ee_{rot11}} & \rho_{ee_{rot12}} \\ \rho_{ee_{rot12}} & \rho_{ee_{rot22}} \end{bmatrix} \\
 &= \begin{bmatrix} (A_p - 1)\cos(\tau)^2\cos(\psi)^2 + 1 & (A_p - 1)\cos(\tau)^2\sin(\psi)\cos(\psi) \\ (A_p - 1)\cos(\tau)^2\sin(\psi)\cos(\psi) & (A_p - 1)\cos(\tau)^2\sin(\psi)^2 + 1 \end{bmatrix}
 \end{aligned} \quad (152)$$

and can be decomposed into a LoS rotation about ψ and a matrix of the tilted spheroidal particle [65]

$$[S_V] = \begin{bmatrix} \cos(\psi) & \sin(\psi) \\ -\sin(\psi) & \cos(\psi) \end{bmatrix} \begin{bmatrix} \sin(\tau)^2 + A_p \cos(\tau)^2 & 0 \\ 0 & 1 \end{bmatrix} \begin{bmatrix} \cos(\psi) & \sin(\psi) \\ -\sin(\psi) & \cos(\psi) \end{bmatrix}^T. \quad (153)$$

The corresponding coherency matrix $[T_{VS}]$ is

$$\begin{aligned}
 [T_{VS}] &= \quad (154) \\
 \frac{1}{2} &\begin{bmatrix} (2+N\cos(\tau)^2)^2 & (2+N\cos(\tau)^2)N^*\cos(\tau)^2\cos(2\psi) & (2+N\cos(\tau)^2)N^*\cos(\tau)^2\sin(2\psi) \\ (2+N^*\cos(\tau)^2)N\cos(\tau)^2\cos(2\psi) & (N\cos(\tau)^2\cos(2\psi))^2 & N^2\cos(\tau)^4\cos(2\psi)\sin(2\psi) \\ (2+N^*\cos(\tau)^2)N\cos(\tau)^2\sin(2\psi) & N^2\cos(\tau)^4\cos(2\psi)\sin(2\psi) & (N\cos(\tau)^2\sin(2\psi))^2 \end{bmatrix},
 \end{aligned}$$

where $N = A_p - 1$ is applied [65].

So far, only one single particle with orientation τ, ψ in the three dimensional space is considered. In order to model a cloud of uniformly shaped particles, a uniform PDF of canting angles ($pdf(\psi) = 1/(2\Delta\psi)$) and tilt angles ($pdf(\tau) = \cos(\tau)/(2\cos(\bar{\tau})\sin(\Delta\tau))$) with mean orientation distribution angles ($\bar{\psi}, \bar{\tau}$) and given orientation distribution widths ($\psi_w = 2\Delta\psi, \tau_w = 2\Delta\tau$) are assumed.

The representative volume coherency matrix $[T_{VG}]$ after element-wise integration is given in Equation 155 for the respective case of mean angles $\bar{\psi}$ and $\bar{\tau}$ (detailed solution in Appendix C):

$$[T_{VG}] = \int_{\bar{\psi}-\Delta\psi}^{\bar{\psi}+\Delta\psi} \int_{\bar{\tau}-\Delta\tau}^{\bar{\tau}+\Delta\tau} [T_{VS}] pdf(\tau) pdf(\psi) d\tau d\psi. \quad (155)$$

The special case with mean orientation around zero $\bar{\psi} = 0$ and $\bar{\tau} = 0$ (horizontal mean orientation) is given as follows (detailed solution in Appendix C):

$$[T_{VGH}] = \int_{-\Delta\psi}^{+\Delta\psi} \int_{-\Delta\tau}^{+\Delta\tau} [T_{VS}] pdf(\tau) pdf(\psi) d\tau d\psi. \quad (156)$$

In Figure 35 two different tilt distributions widths ($\Delta\tau = 45^\circ$ and $\Delta\tau = 90^\circ$) are incorporated in the volume modeling of $[T_{VGH}]$. For prolate spheroids, the coherency

matrix elements are independent of the tilt angle width τ_w centered around zero. The absolute values do not change, despite $\Delta\tau$ changes from 45° to 90° . This can be explained by the fact that the major particle axis overlaps with the LoS-axis, which is congruent with the plane of tilt rotations. For oblate spheroids the T_{VGH11} -component decreases with decreasing tilt distribution width $\Delta\tau$, whereas the T_{VGH12} -, T_{VGH22} - and T_{VGH33} -components behave in the opposite way. The sensitivity of the volume matrix $[T_{VGH}]$ with varying canting angle distribution $\Delta\psi$ is explained later in Figure 37.

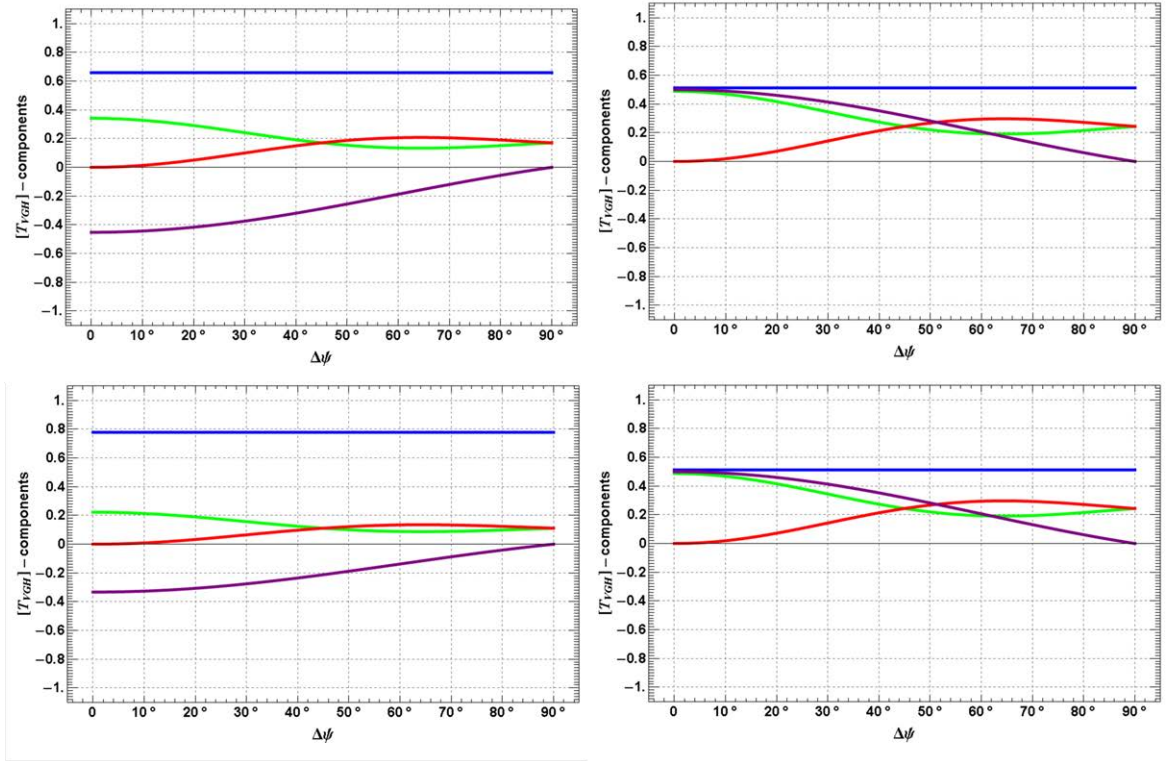


Figure 35: Normalized volume coherency matrix components T_{VGH11} (blue), T_{VGH12} (purple), T_{VGH22} (green), T_{VGH33} (red) as function of the orientation angle width $\Delta\psi$ around $\bar{\psi} = 0^\circ$; From left to right: Oblate spheroids ($A_p = 0$), prolate spheroids ($A_p = 100$); From top to bottom: $\Delta\tau = 45^\circ$ and $\Delta\tau = 90^\circ$ centered around $\bar{\tau} = 0^\circ$.

Hence, a vegetation volume of spheroidal particles allows the variation of particle shape ($N = A_p - 1$), of orientation angle PDFs ($pdf(\psi), pdf(\tau)$), of mean orientation angles ($\bar{\psi}, \bar{\tau}$) and of orientation angle widths (ψ_w, τ_w). This enables a flexible modeling of a variety of agricultural crops from thin stalk-dominated to broad leaf-dominated geometries with different orientation distributions. In Equations 155 and 156 uniform PDFs are assumed. However, a variety of orientation angle PDFs, including uniform [67, 189, 124], trigonometric [342, 158, 123, 159, 7], *Gaussian* [225] and *von Mises* [227] functions, have been proposed and used in

the literature.

Figure 36 describes the influence of the distribution width of the orientation angles (ψ_w, τ_w) on the modeling of the vegetation orientation, ranging from strongly oriented to randomly oriented vegetation volumes.

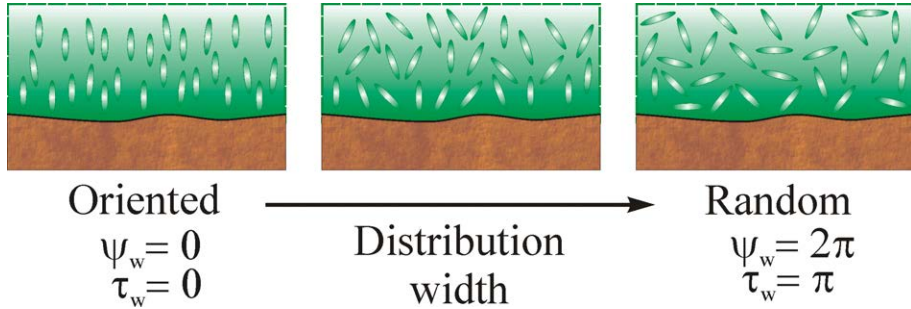


Figure 36: Degree of orientation for the vegetation volume component as a function of the distribution width of the orientation angles (ψ_w, τ_w).

For a further simplification of the volume modeling, the tilt rotation can be assumed to follow a uniformly random distribution ($\Delta\tau = \frac{\pi}{2}$) resulting in $\tau_w = \pi$ and a PDF of $pdf(\tau) = \frac{\cos(\tau)}{2}$. Thus only the azimuthal rotation (ψ) can vary uniformly and a simplified vegetation volume $[T_{VGS}]$ is obtained [65]

$$[T_{VGS}] = \begin{bmatrix} 2 + \frac{4}{3}N + \frac{4}{15}N^2 & (\frac{2}{3}N + \frac{4}{15}N^2) \text{sinc}(2\Delta\psi) & 0 \\ (\frac{2}{3}N + \frac{4}{15}N^2) \text{sinc}(2\Delta\psi) & \frac{2}{15}N^2 (1 + \text{sinc}(4\Delta\psi)) & 0 \\ 0 & 0 & \frac{2}{15}N^2 (1 - \text{sinc}(4\Delta\psi)) \end{bmatrix}. \quad (157)$$

So far, only the *Born approximation* was considered leading to a polarization independent attenuation and refraction due to the random orientation of the volume particles. Consequently, the mean extinction σ and the mean refraction ν are included in the intensity component of the volume f_V (cf. Chapter 3.2.4.2.).

If the vegetation volume has a preferred orientation (i.e. $\psi_w \ll 2\pi$ or $\tau_w \ll \pi$), a differential extinction $\Delta\sigma$ and a differential refractivity $\Delta\nu$ occur [301, 65]. In this case the *distorted Born approximation* applies for anisotropic volume scattering [15].

In the presence of differential extinction and refraction the polarization state of the wave changes constantly during propagation through the vegetation volume [301, 69]. Only the so-called eigen-polarization states (A, B) of the volume, that are orthogonal to each other for homogeneous volumes, propagate undistorted through the volume [193, 41]. The general volume matrix $[T_{VG}]$ can be trans-

formed from the measured (H, V) -basis to the (A, B) -eigen-basis

$$\left[T_{VG}^{A,B} \right] = [R_{2\Gamma}] \left[T_{VG}^{H,V} \right] [R_{2\Gamma}]^T. \quad (158)$$

Subsequently, the volume coherency matrix in its eigen-basis $\left[T_{VG}^{A,B} \right]$ can be taken to correct for differential propagation effects ξ inside the oriented volume by a LoS-rotation, as defined in Equations 159-161 [301,69,65]. The differential propagation effects ξ are calculated as [65]

$$\xi = (\nu_B - \nu_A - ik(\sigma_A - \sigma_B))z = (\Delta\nu + ik(\Delta\sigma)) \frac{h_v - z_0}{\cos(\theta_l)}, \quad (159)$$

where k is the wave number in free space. z represents the local incidence-dependent (θ_l) path length through the vegetation layer with upper boundary h_v (vegetation height) and lower boundary z_0 (position of the ground) [314, 15]. The matrix accounting for propagation effects $[P_\xi]$ is [65]

$$[P_\xi] = \exp(-i(k_{c_A} + k_{c_B})z) \begin{bmatrix} \cosh(i\xi) & \sinh(i\xi) & 0 \\ \sinh(i\xi) & \cosh(i\xi) & 0 \\ 0 & 0 & 1 \end{bmatrix} \quad (160)$$

and can be used to correct the volume matrix $\left[T_{VG}^{A,B} \right]$ for differential propagation effects [65]

$$\left[T_{VGP}^{A,B} \right] = \int_0^{h_v} \exp\left(-\frac{2(\nu_B + \nu_A)(h_v - z_0)}{\cos(\theta)}\right) [P_\xi] \left[T_{VG}^{A,B} \right] [P_{\xi^*}] dz. \quad (161)$$

In order to work again in the measured (H, V) -basis, the corrected volume matrix $\left[T_{VGP}^{A,B} \right]$ is rotated back using the inverse transformation of Equation 158. It becomes clear, that the inversion of the general volume case including anisotropic propagation effects is beyond the potential provided by conventional polarimetric acquisitions. In order to obtain a balanced inversion problem, the parameter space has to be reduced. Following assumptions can be made for a simplified volume scattering model:

- Differential propagation effects are neglected ($\xi = 0$), and an isotropic mean refraction ν and mean extinction σ are considered.
- The spheroidal particles are non-chiral ($[\rho_{em}] = [\rho_{mm}] = 0$), untilted ($\tau = 0$) and spin-symmetric ($\chi = 0$).
- The orientation variation is limited to an azimuthal LoS-rotation around the

canting angle (ψ).

- The PDF of the canting angle (ψ) is of sine, cosine or uniform shape.
- The distribution width (ψ_w) is confined between 0 and π or 0 and 2π , which represents moderately oriented or randomly oriented volumes.

Under these assumptions the scattering matrix $[S_{VG}]$ can be expressed as [65]

$$[S_{VG}] = \int_{\psi} \begin{bmatrix} \cos(\psi) & \sin(\psi) \\ -\sin(\psi) & \cos(\psi) \end{bmatrix} \begin{bmatrix} A_p & 0 \\ 0 & 1 \end{bmatrix} \begin{bmatrix} \cos(\psi) & \sin(\psi) \\ -\sin(\psi) & \cos(\psi) \end{bmatrix}^T pdf(\psi) d\psi. \quad (162)$$

The volume is normalized with respect to the total power ($Span([S_{VG}]) = Tr([T_{VG}])$) [342, 343] and the corresponding volume coherency matrix $[T_{VGD}]$ is obtained by using a uniform PDF

$$[T_{VGD}] = \frac{1}{1+A_p^2} \cdot \begin{bmatrix} \frac{1}{2}(A_p+1)^2 & \frac{1}{2}(A_p^2-1)\text{sinc}(2\Delta\psi) & 0 \\ \frac{1}{2}(A_p^2-1)\text{sinc}(2\Delta\psi) & \frac{1}{4}(A_p-1)^2(1+\text{sinc}(4\Delta\psi)) & 0 \\ 0 & 0 & \frac{1}{4}(A_p-1)^2(1-\text{sinc}(4\Delta\psi)) \end{bmatrix}. \quad (163)$$

Figure 37 shows the behavior for the single coherency matrix elements of $[T_{VGD}]$ varying the particle anisotropy A_p and canting angle distributions $\Delta\psi$. Figure 37 demonstrates that for a spherical particle ($A_p = 1$) only the T_{11} -element is different from zero. For ($A_p \neq 1$) the behavior of oblate ($A_p = 0$) and prolate ($A_p = 100$) particles as a function of the canting angle width $\Delta\psi$ is identical except for the T_{12} -element, where the sign changes. For absolutely oriented volumes ($\Delta\psi = 0^\circ$), T_{33} is zero and $|T_{11}| = |T_{22}| = |T_{12}| = 0.5$. In addition, the coherence of T_{12} ($\gamma_{T_{12}} = T_{12}/\sqrt{T_{11} \cdot T_{22}}$) is one. For randomly oriented oblate ($A_p = 0$) and prolate ($A_p = 100$) spheroids ($\Delta\psi = 90^\circ$), the T_{11} -element is still 0.5, while the other two diagonal elements of the coherency matrix (T_{22} , T_{33}) have the same level of 0.25. Hence, there are no oriented features in the volume any more ($T_{12} = 0$).

In order to predefine certain parameters of the vegetation model, *Yamaguchi et al.* proposed the copolarization power ratio P_{rv}

$$P_{rv} = 10 \log \frac{\langle |S_{VV}|^2 \rangle}{\langle |S_{HH}|^2 \rangle} \quad (164)$$

to distinguish between the three canonical orientation cases in natural media: Horizontally oriented, vertically oriented and randomly oriented vegetation [342, 341, 124]

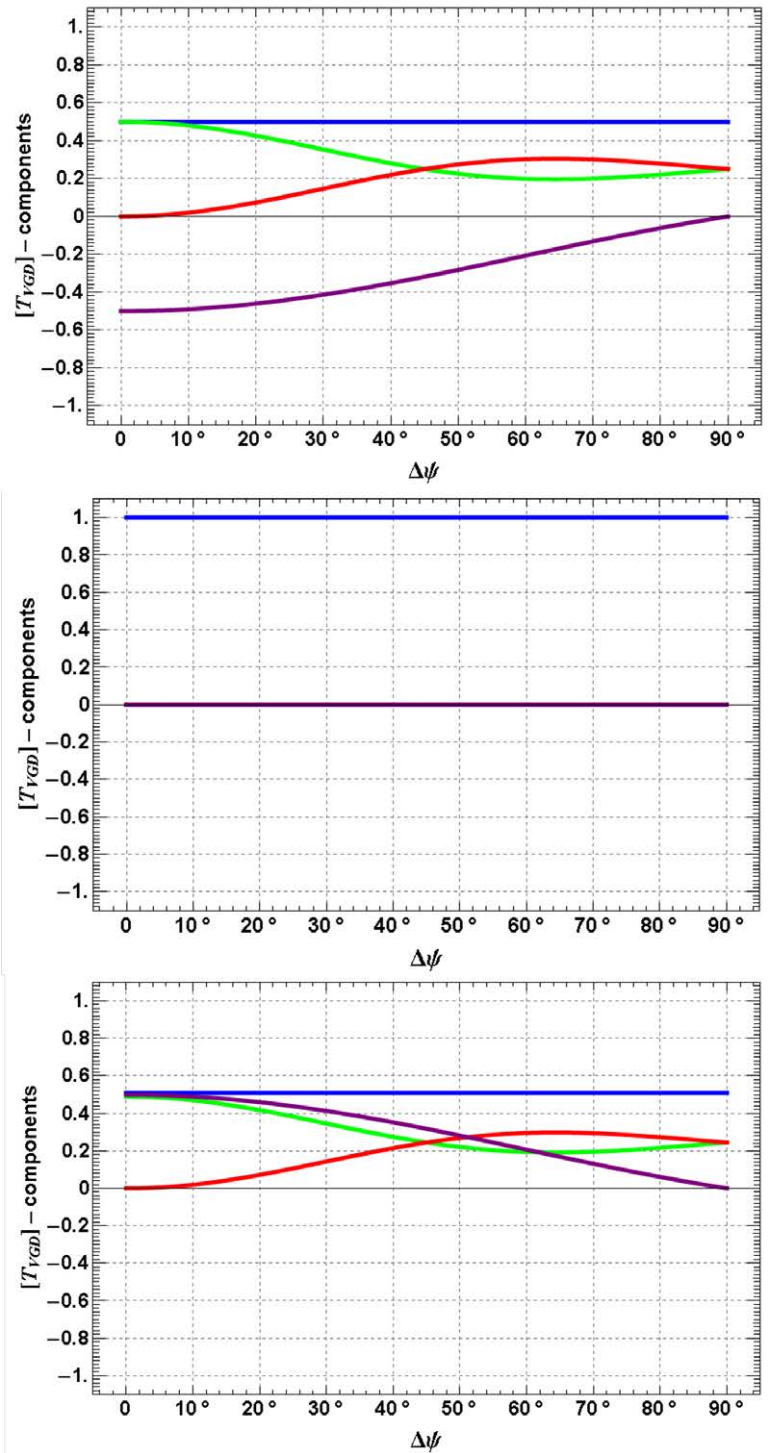


Figure 37: Normalized volume coherency matrix component T_{VGD11} (blue), T_{VGD12} (purple), T_{VGD22} (green), T_{VGD33} (red) as function of the orientation angle width $\Delta\psi$; From top to bottom: Oblate spheroids ($A_p = 0$), spheres ($A_p = 1$) and prolate spheroids ($A_p = 100$).

- Random volume: $-2\text{dB} < P_{rv} < 2\text{dB}$, $\Delta\psi=2\pi$, $pdf(\psi)=\frac{1}{2\pi}$, $0 < \psi < 2\pi$
- Vertical volume: $P_{rv} < -2\text{dB}$, $\Delta\psi=\pi$, $pdf(\psi)=\frac{1}{2}\sin(\psi)$, $0 < \psi < \pi$
- Horizontal volume: $P_{rv} > 2\text{dB}$, $\Delta\psi=\pi$, $pdf(\psi)=\frac{1}{2}\cos(\psi)$, $-\pi/2 < \psi < \pi/2$

The corresponding volume coherency matrices for oblate ($A_p \rightarrow 0$) or prolate spheroids ($A_p \rightarrow \infty$) result in the randomly oriented volume $[T_{VR}]$ [124]

$$[T_{VR}] = \frac{1}{4} \begin{bmatrix} 2 & 0 & 0 \\ 0 & 1 & 0 \\ 0 & 0 & 1 \end{bmatrix}, \quad (165)$$

the horizontally oriented volume $[T_{VH}]$

$$[T_{VH}] = \frac{1}{30} \begin{bmatrix} 15 & -5 & 0 \\ -5 & 7 & 0 \\ 0 & 0 & 8 \end{bmatrix} \quad (166)$$

and the vertically oriented volume $[T_{VV}]$

$$[T_{VV}] = \frac{1}{30} \begin{bmatrix} 15 & 5 & 0 \\ 5 & 7 & 0 \\ 0 & 0 & 8 \end{bmatrix}. \quad (167)$$

For the strongly oriented cases, *Hajnssek et al.* also introduced volume coherency matrices with a stronger orientation using PDFs of $\frac{1}{\sqrt{2}}\cos(\psi)$ (horizontal) as well as of $\frac{1}{\sqrt{2}}\sin(\psi)$ (vertical) and a distribution width of $\psi_w = \frac{\pi}{2}$, which are presented in detail in [124].

While dipoles are widely used as volume particles, they are not sufficient to describe the wide variety of agricultural volumes [106, 105, 343]. Instead of keeping the particle shape constant, the particle orientation within the volume can be fixed using a uniform PDF ($\Delta\psi = 2\pi$, $pdf(\psi) = \frac{1}{2\pi}$, $0 < \psi < 2\pi$) and the particle shape can be varied by the shape parameter ρ leading to the following volume coherency

matrices [128, 123, 124]

$$\begin{aligned}
 [T_{VSh}] &= \begin{bmatrix} 1+\rho & 0 & 0 \\ 0 & 1-\rho & 0 \\ 0 & 0 & 1-\rho \end{bmatrix}, & [T_{VA_{poblake}}] &= \frac{2}{3+A_p} \begin{bmatrix} 2(1+A_p) & 0 & 0 \\ 0 & 1-A_p & 0 \\ 0 & 0 & 1-A_p \end{bmatrix}, \\
 [T_{VA_{pprolate}}] &= \frac{2}{1+3A_p} \begin{bmatrix} 2(A_p+1) & 0 & 0 \\ 0 & A_p-1 & 0 \\ 0 & 0 & A_p-1 \end{bmatrix}.
 \end{aligned} \tag{168}$$

ρ is another representation of the particle anisotropy A_p , given by $\rho = (1+3A_p)/(3+A_p)$ for oblate spheroids and $\rho = (3+A_p)/(1+3A_p)$ for prolate spheroids [105, 129]. Thus, different particle shapes from (oblate/prolate) spheroids to spheres can be included in the vegetation volume modeling and linked to a variable or a fixed orientation scenario.

In this thesis both, three component and two component model-based decompositions were examined for agriculture [128]. However, both ground components, surface and dihedral, are highly probable to occur in agricultural vegetation scattering (cf. Chapter 6.1.2.1.). Therefore, the results in Part 6 focus on three component model-based decompositions.

4.2.2. Separation of volume from ground components

The separation of the volume $[T_V]$ and the ground $[T_G]$ component is accomplished by subtracting the modeled vegetation volume component with its volume intensity f_V from the measured Polarimetric Synthetic Aperture Radar (PolSAR) data $\langle [T_{Data}] \rangle$. For a volume component with reflection symmetry this can be written in a general way as

$$[T_G] = \langle [T_{Data}] \rangle - f_V [T_V] = \begin{bmatrix} T_{11} & T_{12} & 0 \\ T_{12}^* & T_{22} & 0 \\ 0 & 0 & T_{33} \end{bmatrix} - f_V \begin{bmatrix} V_{11} & V_{12} & 0 \\ V_{12} & V_{22} & 0 \\ 0 & 0 & V_{33} \end{bmatrix}. \tag{169}$$

In the ideal case, where the vegetation volume model fits perfectly to the reality, the remaining ground component is unbiased. However, if the volume modeling is inappropriate, Equation 169 leads to biased or even non-physical results for the ground component $[T_G]$. To avoid this, several methods were proposed introducing mathematical and/or physical constraints:

- Positive-semidefiniteness of *Hermitian* ground matrix $[T_G]$

The real eigenvalues of the *Hermitian* ground matrix $[T_G]$ must be greater or equal zero. If this is not the case, the volume intensity f_V is modified accordingly [320, 321]. The eigenvalues of the ground matrix are calculated, confined to zero and solved for the volume intensity components f_{V1} , f_{V2} and f_{V3} :

$$\text{eigen}([T_G]) = \{\lambda_1, \lambda_2, \lambda_3\} = 0 \Rightarrow \text{Solve for the three solutions of } f_V \quad (170)$$

$$f_{V1} = \frac{T_{12}^* - T_{22}V_{11} + T_{12}V_{12}^* - T_{11}V_{22} - \sqrt{AT}}{2(|V_{12}|^2 - V_{11}V_{22})} \quad (171)$$

$$f_{V2} = \frac{T_{12}^* - T_{22}V_{11} + T_{12}V_{12}^* - T_{11}V_{22} + \sqrt{AT}}{2(|V_{12}|^2 - V_{11}V_{22})} \quad (172)$$

$$AT = (T_{22}V_{11} - T_{12}^*V_{12} - T_{12}V_{12}^* + T_{11}V_{22})^2 - 4(|T_{12}|^2 - T_{11}T_{22}) \cdot (|V_{12}|^2 - V_{11}V_{22})$$

$$f_{V3} = \frac{T_{33}}{V_{33}} \quad (173)$$

Finally the minimum volume intensity $f_{V_{min}}$ is estimated

$$f_{V_{min}} = \min(f_{V1}, f_{V2}, f_{V3}). \quad (174)$$

In this way, the volume intensity f_V is corrected, but the assumed volume type $[T_V]$ itself is not changed.

- Positive-semidefiniteness of *Hermitian* ground matrix $[T_G]$ and minimization of a remainder matrix $[T_{Re}]$

In this case not only the criterion of non-negative eigenvalues is applied for correction, but also a remainder matrix $[T_{Re}]$ is introduced and minimized by varying the shape and/or the particle orientation.

$$\begin{aligned} \langle [T_{Data}] \rangle - [T_V] &= [T_G] + [T_{Re}] \Rightarrow \begin{bmatrix} T_{11} & T_{12} & 0 \\ T_{12}^* & T_{22} & 0 \\ 0 & 0 & T_{33} \end{bmatrix} - f_V \begin{bmatrix} V_{11} & V_{12} & 0 \\ V_{12} & V_{22} & 0 \\ 0 & 0 & V_{33} \end{bmatrix} \\ &= \begin{bmatrix} T_{G11} & T_{G12} & 0 \\ T_{G12}^* & T_{G22} & 0 \\ 0 & 0 & T_{G33} \end{bmatrix} + \begin{bmatrix} T_{R11} & T_{R12} & T_{R13} \\ T_{R21} & T_{R22} & T_{R23} \\ T_{R31} & T_{R32} & T_{R33} \end{bmatrix}. \end{aligned} \quad (175)$$

Arii and *van Zyl* developed this constraint and generated a so called *adaptive non-negative eigenvalue decomposition*, which included an adaptive vegetation volume model [7, 8]. It should be noted, that this decomposition is not unique. Multiple solutions can occur, when iterating through the search space of the volume model.

- Weighting of volume component with normalized *Pauli*-based ground-to-volume ratios (Pa_S, Pa_D, Pa_G)

This more physical constraint uses ground/volume intensity ratios to weight the influence of the volume component on the co-polarized $\langle [T_{Data}] \rangle$ -elements [150]. Figure 38 indicates the separation of the cross-component $T_{33} = x \cdot \langle |S_{XX}|^2 \rangle$ into a part coming from the vegetation (volume) and another part coming from the soil (roughness). Accordingly, each coherency matrix element T_{XY} can be

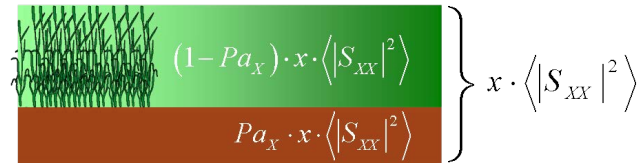


Figure 38: Split of the cross-component $x \cdot \langle |S_{XX}|^2 \rangle$ into a vegetation ($(1 - Pa_X) \cdot x \cdot \langle |S_{XX}|^2 \rangle$) and a soil roughness ($Pa_X \cdot x \cdot \langle |S_{XX}|^2 \rangle$) part by normalized *Pauli*-based ground-to-volume ratios Pa_X [150].

corrected for roughness and/or vegetation using the normalized *Pauli*-based ground-to-volume ratios Pa in the following way:

$$\text{Surface-to-volume ratio: } Pa_S = \frac{T_{11} - T_{33}}{T_{11} + T_{33}} \quad (176)$$

$$\text{Dihedral-to-volume ratio: } Pa_D = \frac{T_{22} - T_{33}}{T_{22} + T_{33}} \quad (177)$$

$$\text{Combined ratio: } Pa_G = \frac{T_{11} + T_{22} - 2T_{33}}{T_{11} + T_{22} + 2T_{33}} \quad (178)$$

Correction of roughness influence:

$$T_{XYcr} = T_{XY} - Pa_X \cdot x \cdot \langle |S_{XX}|^2 \rangle = T_{XY} - Pa_X \cdot V_{XY} \cdot f_V \quad (179)$$

Correction of vegetation influence:

$$T_{XYcv} = T_{XY} - (1 - Pa_X) \cdot x \cdot \langle |S_{XX}|^2 \rangle = T_{XY} - (1 - Pa_X) \cdot V_{XY} \cdot f_V. \quad (180)$$

A weighted matrix of the vegetation volume $[T_{V_{wei}}]$ is subtracted from the measured coherence matrix $\langle [T_{Data}] \rangle$. In this way, the ratio of the ground and the volume scattering components results in a physically meaningful estimate of the occurring ground and volume components and their relative dominance

$$\begin{aligned} [T_{G_{cv}}] &= \langle [T_{Data}] \rangle - f_V [T_{V_{wei}}] \\ &= \begin{bmatrix} T_{11} & T_{12} & 0 \\ T_{12}^* & T_{22} & 0 \\ 0 & 0 & T_{33} \end{bmatrix} - f_V \begin{bmatrix} (1 - Pa_S)V_{11} & (1 - Pa_G)V_{12} & 0 \\ (1 - Pa_G)V_{12} & (1 - Pa_D)V_{22} & 0 \\ 0 & 0 & V_{33} \end{bmatrix}. \end{aligned} \quad (181)$$

It is worth mentioning, that the Surface Eigenvalue Relative Difference (SERD) and the Dihedral Eigenvalue Relative Difference (DERD) defined by *Allain* as relative measurements of ground compared to volume scattering, are very similar to the proposed ratios Pa_S and Pa_D [3]. The implementation of the normalized *Pauli*-based ground-to-volume ratios Pa in the retrieval of soil moisture is described in Chapter 4.2.5.3. and of soil roughness in Chapter 4.2.8.1..

- Physically constrained volume component including *Bragg* surface scattering α_b or *Fresnel* dihedral scattering α_f

The volume intensity component f_V is constrained by a *Bragg* surface or *Fresnel* dihedral scattering component [152, 153, 65]. The constrained volume intensity f_{Vc} is obtained from Equation 182, using a best estimate of the expected *Bragg* surface or *Fresnel* dihedral scattering $\alpha_{b/f}$ and solving for f_V

$$\alpha = \arccos \left(\frac{1}{\sqrt{1 + 4 \left| \frac{T_{12}^* - f_V V_{12}}{T_{11} - T_{22} - f_V V_{11} + f_V V_{22} \pm RT} \right|^2}} \right). \quad (182)$$

$$RT = \frac{\sqrt{T_{11}^2 + (T_{22} + f_V V_{11})^2 + 4(T_{12} - f_V V_{12})(T_{12}^* - f_V V_{12}) - 2T_{11}(T_{22} + f_V(V_{11} - V_{22})) \dots}{\dots - 2f_V(T_{22} + f_V V_{11})V_{22} + f_V^2 V_{22}^2}}. \quad (183)$$

In this way, the former volume intensity f_V component is physically constrained by the expected *Bragg* surface or *Fresnel* dihedral scattering to obtain f_{Vc}

$$f_{Vc} = \frac{4V_{12} \cos(2\alpha_{b/f})(T_{12}^* - T_{12} + (T_{12} + T_{12}^*) \cos(2\alpha_{b/f})) + 2(T_{11} - T_{22})(V_{22} - V_{11}) \sin(2\alpha_{b/f})^2}{(4V_{12}^2 - (V_{11} - V_{22})^2 + (4V_{12}^2 + (V_{11} - V_{22})^2) \cos(4\alpha_{b/f}))} \pm \frac{2\sqrt{((T_{12} - T_{12}^*)(V_{11} - V_{22}) + (2(T_{11} - T_{22})V_{12} - (T_{12} + T_{12}^*)(V_{11} - V_{22})) \cos(2\alpha_{b/f}))^2 \sin(2\alpha_{b/f})^2}}{(4V_{12}^2 - (V_{11} - V_{22})^2 + (4V_{12}^2 + (V_{11} - V_{22})^2) \cos(4\alpha_{b/f}))}. \quad (184)$$

Further details of this approach will be given in Chapter 4.2.6.1.. Whereas more complex ground scattering models, like *X-Bragg* or *X-Fresnel*, can also be included in the formalism, but require a higher parameterization that is unfavorable for inversion purposes.

4.2.3. Separation of ground components using a scattering dominance criterion

The subtraction of the volume scattering component from the measured polarimetric SAR data represents the first step of a polarimetric decomposition process resulting in the retrieval of the ground components.

In a second step, the two ground components (surface, dihedral) have to be separated from each other, whereby a difference in the co-polarization phase $\angle\langle S_{HH}S_{VV}^*\rangle$ is used as indicator. Dominant dihedral scattering exhibits a $\angle\langle S_{HH}S_{VV}^*\rangle$ close to π , whereas dominant surface scattering causes a $\angle\langle S_{HH}S_{VV}^*\rangle$ close to zero due to the different backscattering geometry [71]. Table 2 summarizes the scattering dominance criteria. In Figure 39 two images of the occurring dominant

Table 2: Scattering dominance criteria after volume subtraction [106, 319, 6, 65, 157].

Dominance criterion	Surface dominant	Dihedral dominant	References
Real part of $\langle S_{HH}S_{VV}^*\rangle$	$\Re[\langle S_{HH}S_{VV}^*\rangle] > 0$	$\Re[\langle S_{HH}S_{VV}^*\rangle] < 0$	Freeman, 1998; Yamaguchi, 2006
Alpha scattering angle α	$\alpha < 45^\circ$	$\alpha > 45^\circ$	van Zyl, 1992; Arii, 2009; Cloude, 2010
Phase of T_{12} (no volume subtraction)	$\phi_{T_{12}} < 0^\circ$	$\phi_{T_{12}} > 0^\circ$	Cloude, 2010
Imaginary part of $\langle S_{HH}S_{VV}^*\rangle$	$\Im[\langle S_{HH}S_{VV}^*\rangle] > 0$	$\Im[\langle S_{HH}S_{VV}^*\rangle] < 0$	Jagdhuber, 2012

scattering together with the land use map of the AgriSAR campaign and a *Pauli*-RGB image for the 19th of April 2006 are shown. Red color represents surface dominance and blue color dihedral dominance. A frame in the images highlights the dihedral dominance for the $\Re[\langle S_{HH}S_{VV}^*\rangle]$ -criterion (3rd image) and the surface dominance for the $\Im[\langle S_{HH}S_{VV}^*\rangle]$ -criterion (4th image). The land use indicates a winter wheat field (orange). The *Pauli*-image indicates a double bounce (dihedral) signature. But field survey reports the absence of any vertically oriented vegetation component (e.g. stalk) at that time, because the plants had only developed their leaves, covering the soil. Therefore the criterion using the imaginary part of $\langle S_{HH}S_{VV}^*\rangle$ might be a valid alternative to the well known $\Re[\langle S_{HH}S_{VV}^*\rangle]$ -criterion of [106]. The soil moisture level of 20-30vol.%, as reported by the field measurements in Figures 53 and 54, makes penetration into the soil unlikely.

The orthogonality of the *Bragg* (surface) and the *Fresnel* (dihedral) component is

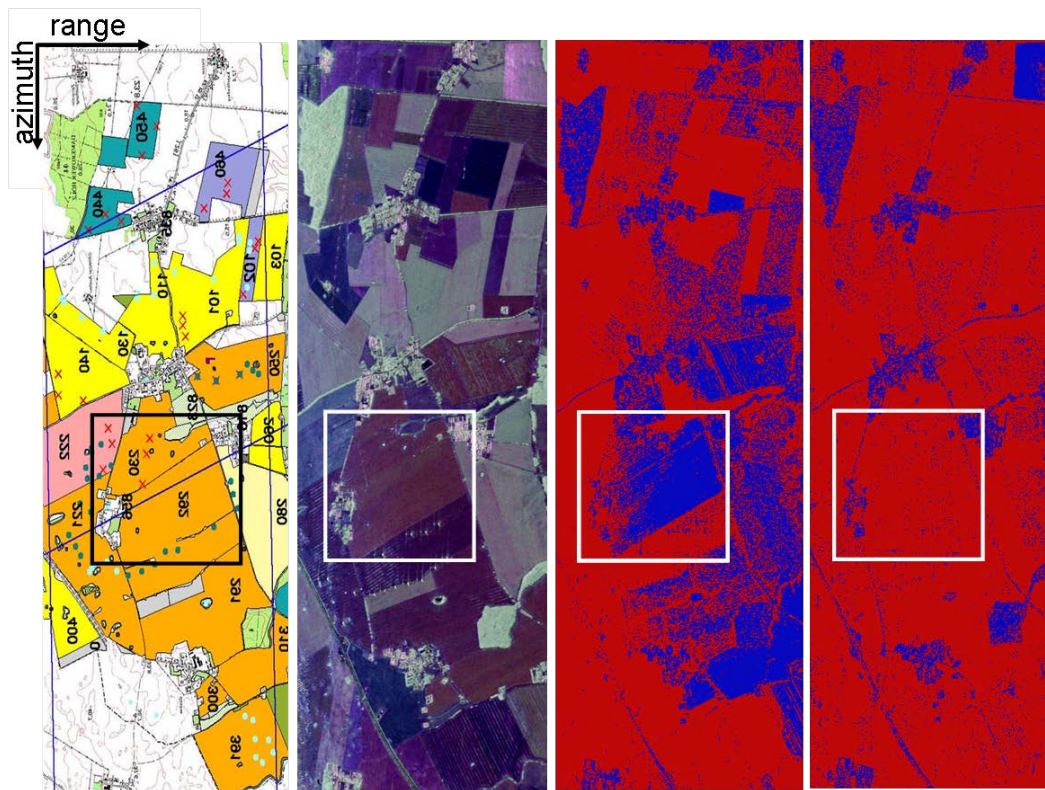


Figure 39: Scattering dominance criterion using the real part and imaginary part of $\langle S_{HH}S_{VV}^* \rangle$ for 19th of April 2006 within the AgriSAR campaign (from left to right): Land use map, RGB-composite of *Pauli* power components (R: even bounce, G: volume, B: odd bounce), dominance criterion $\Re[\langle S_{HH}S_{VV}^* \rangle]$ and dominance criterion $\Im[\langle S_{HH}S_{VV}^* \rangle]$; Surface (dihedral) dominance refers to red (blue) areas. The frame indicates a winter wheat area.

favorable for the well separation of the two components within the decomposition [71]. In Figure 40 the degree of orthogonality $Ko_{comp1-comp2}$ given for rank-1 mechanisms by the scalar product of the two *Pauli*-vectors (cf. Chapter 3.2.2.) and for rank-2 and higher mechanisms by the trace of the matrix product of the coherency matrices for a given range of local incidence angles θ_l [228, 65]:

$$\text{Rank} = 1: Ko_{rank1} = 20 \cdot \log \left(\left| \underline{k}_{P_{comp1}}^{*T} \cdot \underline{k}_{P_{comp2}} \right| \right) \quad (185)$$

$$\text{Bragg: } \underline{k}_{P_{Bragg}} = m_s / \sqrt{2} \begin{bmatrix} R_h + R_v & R_h - R_v & 0 \end{bmatrix}^T$$

$$\text{Fresnel: } \underline{k}_{P_{Fresnel}} = m_d / \sqrt{2} \begin{bmatrix} R_{sh}R_{tv} - R_{sv}R_{tv} \exp(i\phi_d) & R_{sh}R_{tv} + R_{sv}R_{tv} \exp(i\phi_d) & 0 \end{bmatrix}^T$$

$$\text{Rank} > 1: Ko_{rank>1} = 10 \cdot \log \left(\left| \text{Tr} \left([T_{comp1}] \cdot [T_{comp2}]^{*T} \right) \right| \right) \quad (186)$$

$$\text{X-Bragg: } [T_{X-Bragg}] = [T_{XB}] \quad (\text{cf. Equation 126})$$

$$\text{X-Fresnel: } [T_{X-Fresnel}] = [T_{XD}] \quad (\text{cf. Equation 140})$$

$$\text{Randomly oriented volume: } [T_{Volume}] = [T_{VGS}] \quad (\text{cf. Equation 157})$$

The lower the degree of orthogonality Ko becomes, the higher is the orthogonality and the easier a possible separation of the two scattering mechanisms. The two ground mechanisms remain orthogonal over a wide range of soil ϵ_s and trunk moisture states ϵ_t as well as roughness stages ψ_l (not shown, cf. [65] p.188-189). For local incidence angles below $\sim 20^\circ$ as well as above $\sim 70^\circ$, the orthogonality for the ground mechanisms already declines significantly ($Ko > -10\text{dB}$) in Figure 40, if a distinct soil moisture ($\epsilon_s = 20$), a moderate trunk moisture ($\epsilon_t = 10$), a moderate surface roughness ($\psi_l = 30^\circ$), no scattering losses ($m_d = m_s = 1$) and no differential propagation ($\phi_d = 0^\circ$) are assumed. Therefore, the separation of the two ground components gets difficult at very steep as well as grazing incidence.

In addition, the separation of the ground components shows a minimum of Ko around a local incidence of $\theta_l \approx 50^\circ$ for $\epsilon_s = 20$, $\epsilon_t = 10$ and $\psi_l = 30^\circ$, which encourages a soil moisture inversion under shallow local incidence angle conditions. Moreover, different dielectric constants of soil and of trunk do not significantly influence the orthogonality of the ground scattering mechanisms. However, the change in dielectric constants affects for instance the position of the minima for $Ko_{Bragg-Fresnel}$ due to the shift of the *Brewster* angles.

Figure 41 demonstrates the degree of orthogonality Ko between ground ($[T_G]$) and volume ($[T_V]$) scattering for a range of local incidence angles θ_l . As the vegetation volume is assumed randomly oriented ($\Delta\psi = 180^\circ$, $\Delta\tau = 90^\circ$), the influence of the soil roughness ($\psi_l = 30^\circ$) vanishes, which explains the similarity of the orthogonality of *Extend Bragg* (*Extended Fresnel*) scattering to volume scattering compared

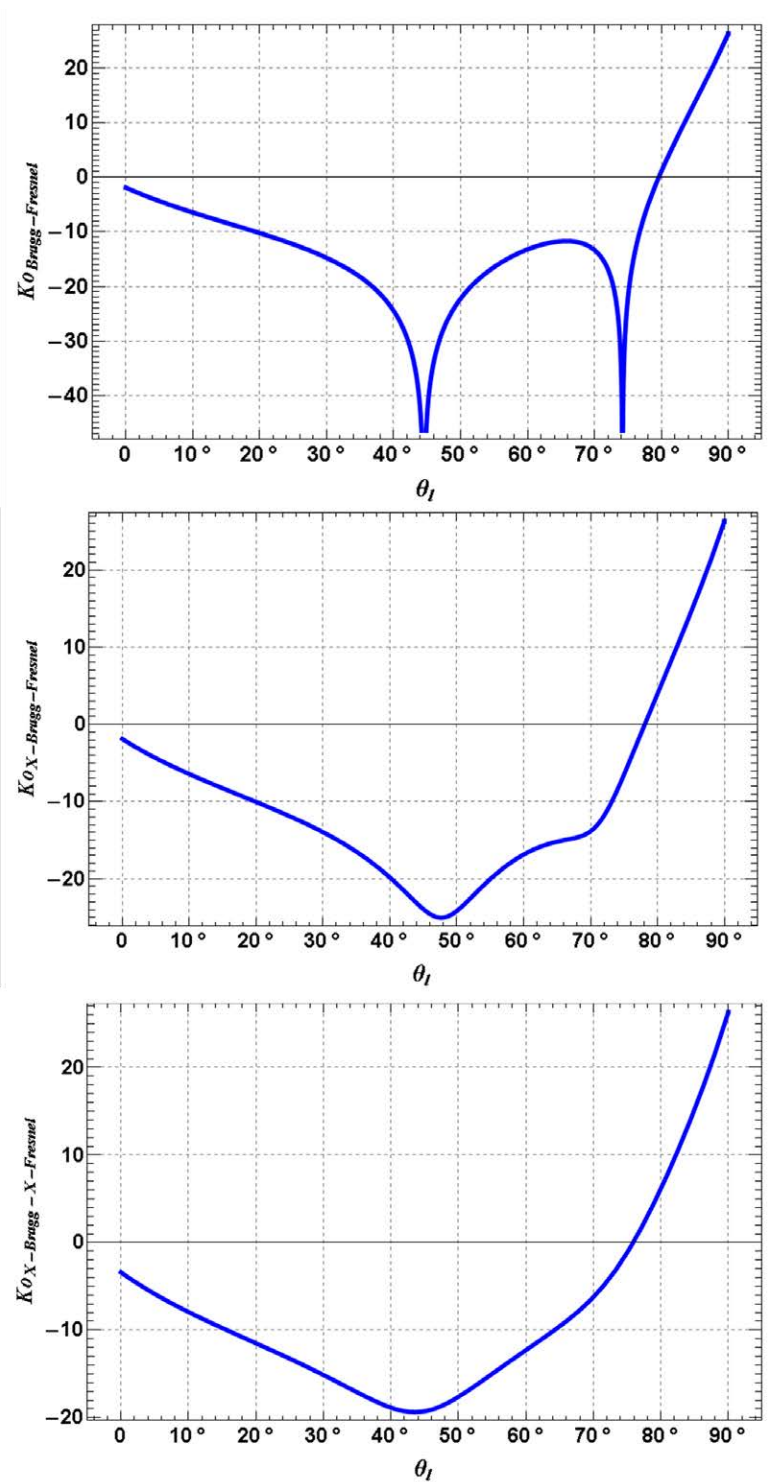


Figure 40: Degree of orthogonality Ko of surface and dihedral scattering mechanisms with local incidence angle θ_l in [dB] (from top to bottom): $KO_{Bragg-Fresnel}$, $KO_{X-Bragg-Fresnel}$, $KO_{X-Bragg-X-Fresnel}$, (using no scattering loss for both ground components: $m_d = m_s = 1$, no differential phase: $\phi_d = 0^\circ$, a distinct soil moisture: $\epsilon_s = 20$, a moderate plant moisture: $\epsilon_t = 10$ and a moderate soil roughness: $\psi_l = 30^\circ$).

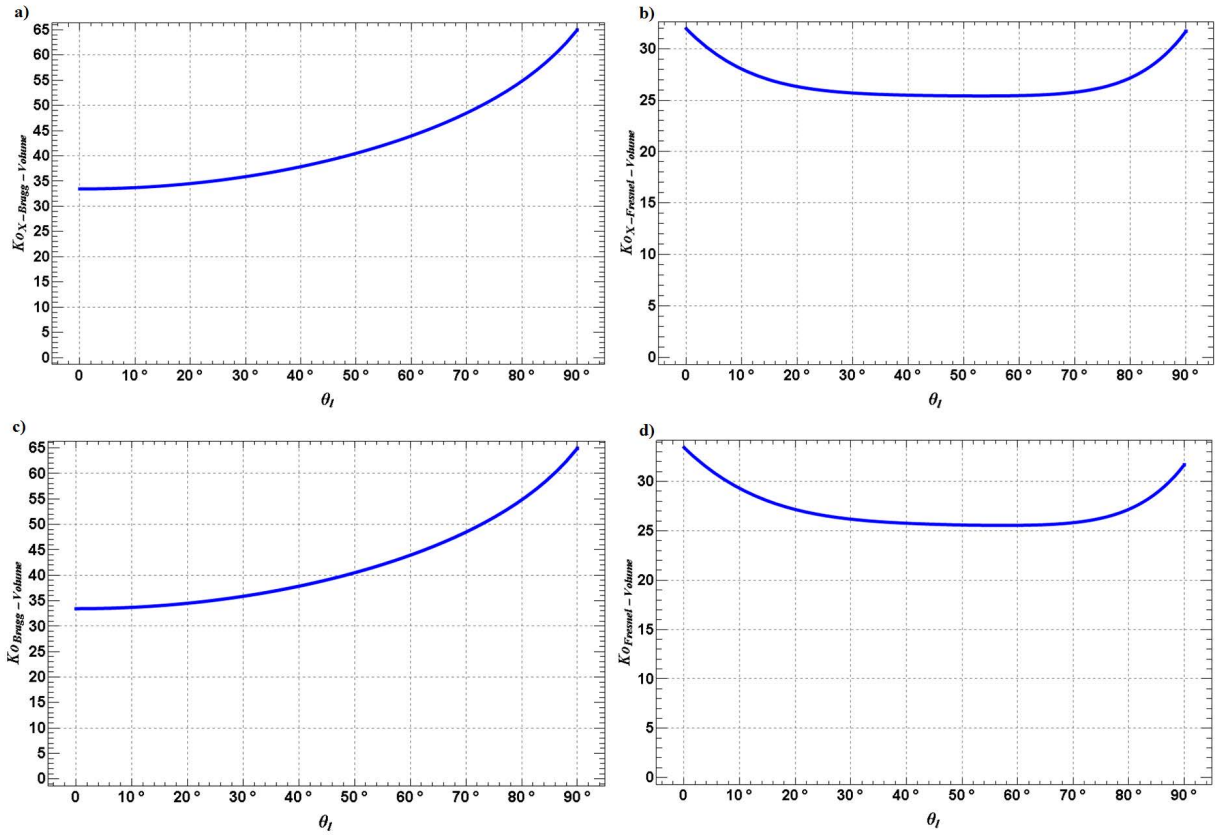


Figure 41: Degree of orthogonality Ko of ground and volume scattering mechanisms with local incidence angle θ_l in [dB]; a) $Ko_{X-Bragg-Volume}$, b) $Ko_{X-Fresnel-Volume}$, c) $Ko_{Bragg-Volume}$, d) $Ko_{Fresnel-Volume}$, (using no scattering loss for both ground components: $m_d = m_s = 1$, no differential phase: $\phi_d = 0^\circ$, a distinct soil moisture: $\epsilon_s = 20$, a moderate plant moisture: $\epsilon_t = 10$, a moderate soil roughness: $\psi_l = 30^\circ$, and a random volume of untilted prolate spheroids: $A_p = 100$, $\Delta\psi = 180^\circ$, $\Delta\tau = 90^\circ$).

with the orthogonality of *Bragg* (*Fresnel*) scattering to volume scattering. For *X-Fresnel* and *Fresnel* a slightly higher change in orthogonality behavior with respect to volume scattering can be noticed (cf. Figure 41). In addition, it is clearly visible for all local incidence angles, that the dihedral and the surface scattering mechanisms exhibits no orthogonality ($K_o > 25\text{dB}$) to volume scattering of randomly oriented dipoles. In this case the scattering contributions of the vegetation component are spread over several eigenvectors and a model-based decomposition is necessary for separation of the volume and surface scattering components.

4.2.4. Calculus of ground components

First, a criterion for ground scattering dominance is selected (cf. Table 2) to set the non-dominant ground scattering mechanism (α_D or β_S) to zero [343]. In this way, the under-determined problem (e.g. in [106, 343]) becomes balanced and the remaining ground components (α_D or β_S , f_S , f_D , f_V) can be calculated from the polarimetric observables ($T_{11}, T_{22}, T_{33}, T_{12}$).

In Equations 187-194 an exemplary calculus of the ground components for a model-based coherency matrix including *Bragg* surface scattering (cf. Equation 113), *Fresnel* dihedral scattering (cf. Equation 115) and a reflection-symmetric rank-3 volume scattering is performed, assuming a real dielectric constant.

$$\begin{bmatrix} T_{11} & T_{12} & 0 \\ T_{12}^* & T_{22} & 0 \\ 0 & 0 & T_{33} \end{bmatrix} = f_S \begin{bmatrix} 1 & \beta_S^* & 0 \\ \beta_S & |\beta_S|^2 & 0 \\ 0 & 0 & 0 \end{bmatrix} + f_D \begin{bmatrix} |\alpha_D|^2 & \alpha_D & 0 \\ \alpha_D^* & 1 & 0 \\ 0 & 0 & 0 \end{bmatrix} + f_V \begin{bmatrix} V_{11} & V_{12} & 0 \\ V_{12} & V_{22} & 0 \\ 0 & 0 & V_{33} \end{bmatrix} \quad (187)$$

$$f_V = \frac{1}{V_{33}} T_{33} \quad (188)$$

Dominant surface scattering ($\alpha_D = 0$):

$$f_S = T_{11} - V_{11} f_V \quad (189)$$

$$\beta_S = \frac{-|T_{12}| - V_{12} f_V}{T_{11} - V_{11} f_V} \quad (190)$$

$$f_D = T_{22} - V_{22} f_V - |\beta_S|^2 \cdot f_S \quad (191)$$

Dominant dihedral scattering ($\beta_S = 0$):

$$f_D = T_{22} - V_{22} f_V \quad (192)$$

$$\alpha_D = \frac{|T_{12}| - V_{12} f_V}{T_{22} - V_{22} f_V} \quad (193)$$

$$f_S = T_{11} - V_{11} f_V - |\alpha_D|^2 \cdot f_D. \quad (194)$$

This decomposition incorporates a variable vegetation component substitutable with the volume cases proposed in Equations 165 to 167 within Chapter 4.2.1.3.. In addition, more complex ground scattering components like *X-Bragg* (cf. Equation 126) or *X-Fresnel* (cf. Equation 140) can be included to account for depolarizing ground scattering.

Furthermore the separation of the volume and the ground scattering components can be modified (cf. Chapter 4.2.2.) to improve the removal of the volume component.

4.2.5. Inversion for soil moisture under vegetation cover

After the polarimetric decomposition, the surface and dihedral components are inverted to retrieve soil moisture under vegetation cover.

An alternative inversion of the ground components is presented that includes the *Pauli*-based ground-to-volume ratios and therefore incorporates a separation of volume and roughness contributions within the involved cross-polarized component.

4.2.5.1. Inversion of surface component

The surface scattering components f_S and β_S of $[T_S]$ are functions of the horizontal and vertical *Bragg* scattering coefficients (R_h , R_v) as well as m_s (cf. Chapter 3.2.4.2.1.)

$$R_h = \frac{\cos(\theta_l) - \sqrt{\epsilon_s - \sin(\theta_l)^2}}{\cos(\theta_l) + \sqrt{\epsilon_s - \sin(\theta_l)^2}}, \quad R_v = \frac{(\epsilon_s - 1)(\sin(\theta_l)^2 - \epsilon_s(1 + \sin(\theta_l)^2))}{(\epsilon_s \cos(\theta_l) + \sqrt{\epsilon_s - \sin(\theta_l)^2})^2}, \quad (195)$$

defined by the dielectric constant of the soil ϵ_s and the local incidence angle θ_l . Additionally, f_S depends on the surface scattering loss m_s (cf. Equation 114). Therefore β_S is employed for inversion, as it allows to bypass the dependency on m_s . The scattering mechanism ratio β_S for *Bragg* and *X-Bragg* scattering can be calculated as

$$\text{Bragg: } \beta_S = \frac{R_h - R_v}{R_h + R_v} \quad \text{X-Bragg: } \beta_S = \frac{R_h - R_v}{R_h + R_v} \cdot \text{sinc}(2\psi_l). \quad (196)$$

The left plot of Figure 42 presents the variation of β_S with dielectric constant of the soil ϵ_s and local incidence angles θ_l for *Bragg* scattering. An increasing sensitivity of β_S towards lower soil moistures and shallower incidence angles is visible. The depolarization-term ($\text{sinc}(\psi_l)$) acts as a diminishing factor leading to higher moisture estimates due to the smaller β_S -value with increasing surface

roughness (cf. Figure 42 right). The dielectric constant of the soil ϵ_s is obtained

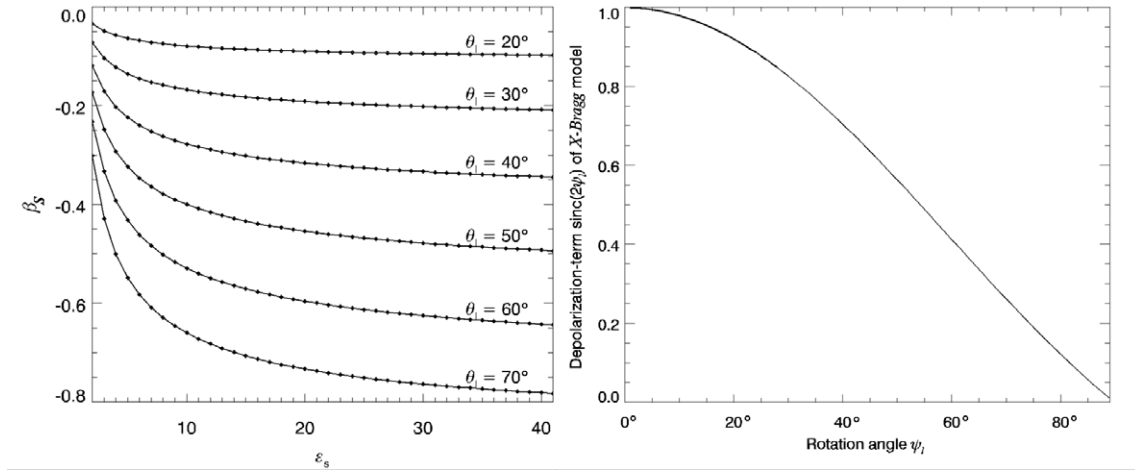


Figure 42: β_S as function of the soil dielectric constant ϵ_s for different local incidence angles θ_l (left); Depolarization (i.e. $\text{sinc}(2\psi_l)$) as function of the rotation angle ψ_l representing the soil roughness influence (right).

by minimizing the difference between the modeled β_S -values, which are function of the local incidence angle and the dielectric constant of the soil, and the beta values β_{S_d} from the data decomposition:

$$\min_{\epsilon_s} (|\beta_S(\theta_l|\epsilon_s) - \beta_{S_d}|). \quad (197)$$

The universal transformation function of *Topp et al.*, given in Equation 6, is finally used to convert the dielectric constant into volumetric soil moisture [vol.%].

4.2.5.2. Inversion of dihedral component

As discussed in Chapter 3.2.4.2.2., the dihedral scattering components f_D and α_D of $[T_D]$ are functions of the dihedral loss factor $m_{d_{e/g/v/v\theta_l}}$, the differential phase ϕ_d as well as the horizontal and vertical *Fresnel* coefficients of the soil (R_{sh}, R_{sv}) and of the trunk (R_{th}, R_{tv})

$$f_D = \frac{m_{d_{e/g/v/v\theta_l}}^2}{2} |R_{sh}R_{th} + R_{sv}R_{tv} \exp(i\phi_d)|^2, \quad \alpha_D = \frac{R_{sh}R_{th} - R_{sv}R_{tv} \exp(i\phi_d)}{R_{sh}R_{th} + R_{sv}R_{tv} \exp(i\phi_d)}. \quad (198)$$

The horizontal and vertical *Fresnel* coefficients of the soil and of the trunk depend on the soil and trunk dielectric constant (ϵ_s, ϵ_t) and the respective incidence angles

$\theta_s = \theta_l$ and $\theta_t = \pi/2 - \theta_l$.

$$R_{ih} = \frac{\cos(\theta_i) - \sqrt{\varepsilon_i - \sin(\theta_i)^2}}{\cos(\theta_i) + \sqrt{\varepsilon_i - \sin(\theta_i)^2}}, \quad R_{iv} = \frac{\varepsilon_i \cos(\theta_i) - \sqrt{\varepsilon_i - \sin(\theta_i)^2}}{\varepsilon_i \cos(\theta_i) + \sqrt{\varepsilon_i - \sin(\theta_i)^2}}, \quad (199)$$

where $i \in \{t, s\}$. The inversion of the dihedral component has a twofold dependency on the dielectric constant of the soil ε_s and of the trunk ε_t . For this reason f_D and α_D are used jointly to estimate ε_t and ε_s for a given local incidence θ_l .

Figure 43 depicts the sensitivity of f_D and α_D on the dielectric constants ($\varepsilon_s, \varepsilon_t$) for different local incidence angles θ_l . For steep local incidence ($\theta_l=25^\circ$), the sensitivity to the dielectric constant of the trunk ε_t is pronounced compared to the dielectric constant of the soil ε_s . The situation is reversed for shallow local incidence ($\theta_l=55^\circ$), whereas at $\theta_l=45^\circ$ the sensitivity to both dielectric constants is balanced. The different m_d -factors in Equations 135-137, which account for the roughness $m_{d_{g/e}}$ or vegetation attenuation loss $m_{d_{v/\theta_l}}$, cause a decline of the f_D -component, which leads to higher moistures estimates. The dielectric constant of the soil ε_s and the trunk ε_t are obtained by minimizing the difference between the modeled α_D - and f_D -values and the α_{D_d} - and f_{D_d} -values obtained from the decomposition

$$\min_{\varepsilon_s, \varepsilon_t} \left(\begin{array}{l} |f_D(\theta_l | \varepsilon_s, \varepsilon_t) - f_{D_d}| \\ |\alpha_D(\theta_l | \varepsilon_s, \varepsilon_t) - \alpha_{D_d}| \end{array} \right). \quad (200)$$

Finally the transformation function of *Topp et al.* is used to obtain the volumetric soil moisture [vol.%].

4.2.5.3. Inversion of surface and dihedral components using *Pauli*-based ground-to-volume ratios

The cross-polarized scattering component S_{XX} is characterized by a mixed scattering response of the vegetation cover and the underlying soil. Hence, a data derived criterion for splitting the cross-polarized component into a roughness and vegetation contribution is highly desirable [150]. The normalized *Pauli*-based ground-to-volume ratios already introduced in Equation 176 are a possible option to approach this problem [150]. *Hajnsek et al.* [127] derived a polarimetric ratio from the *X-Bragg* model for bare soils, which is sensitive to soil moisture and independent of soil roughness induced depolarization. The presence of vegetation requires an adapted T_{33} -element accounting for the influence of the vegetation leading to a modified polarimetric ratio, which is only sensitive to soil moisture

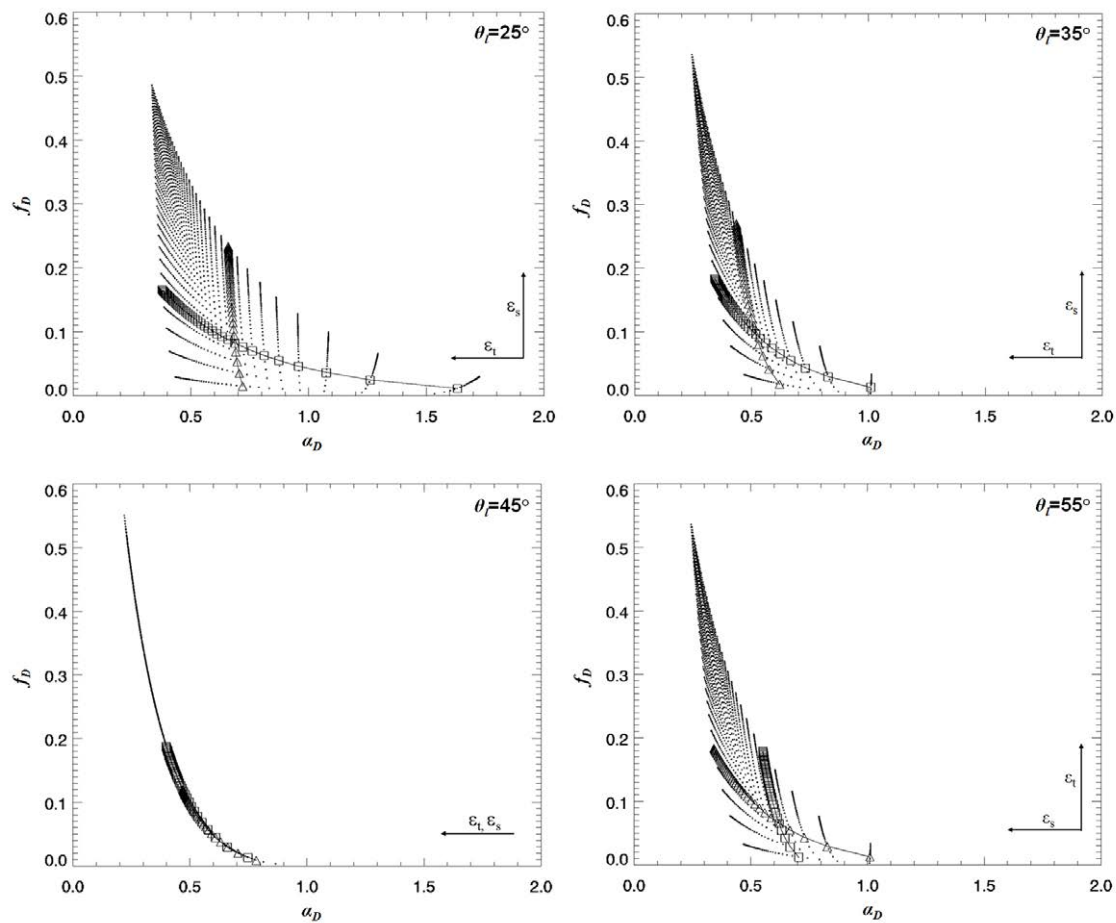


Figure 43: Sensitivity of the dihedral scattering components α_D and f_D on the dielectric constants (ϵ_s , ϵ_t) for different local incidence angles, $\theta_l=25^\circ$ (upper left), $\theta_l=35^\circ$ (upper right), $\theta_l=45^\circ$ (lower left), $\theta_l=55^\circ$ (lower right); $\epsilon_s=\epsilon_t=[2, 41]$, (example line of triangles=difference of ϵ_s by ± 1 , example line of squares=difference of ϵ_t by ± 1 , black arrows show main direction of increase of ϵ_s and ϵ_t).

under vegetation:

$$\text{Bare soil: } \frac{|R_h - R_v|^2}{|R_h + R_v|^2} = \frac{T_{22} + T_{33}}{T_{11}} \quad \text{Vegetated soil: } \frac{|R_h - R_v|^2}{|R_h + R_v|^2} = \frac{T_{22cv} + Pa_G \cdot T_{33}}{T_{11cv}}. \quad (201)$$

A second type of ratios for soil moisture estimation can be derived from the ground component of the model-based decomposition, as presented in Chapters 4.2.2.-4.2.5.. In Equations 187-194 volume scattering ($C_{xy} \cdot f_v$) is already considered by the three component model-based decomposition, but the f_v -element is not explicitly separated into a vegetation and soil roughness contribution. This can be done as in Equation 202, where only the vegetation part of f_v is subtracted from the coherency matrix elements using the normalized *Pauli*-based ground-to-volume ratios of Equations 176-179.

Surface inversion from *X-Bragg* scattering:

$$\frac{R_h - R_v}{R_h + R_v} \cdot \text{sinc}(2\psi_l) = \frac{T_{12cv}}{T_{11cv}} = \frac{T_{12} - (1 - Pa_G) \cdot V_{12} \cdot f_v}{T_{11} - (1 - Pa_S) \cdot V_{11} \cdot f_v}. \quad (202)$$

Dihedral inversion from modified *Fresnel* scattering:

$$\frac{m_{d_{e/g/v/v\theta_l}}^2}{2} |R_{sh}R_{th} + R_{sv}R_{tv} \exp(i\phi_d)|^2 = T_{22cv} = T_{22} - (1 - Pa_D) \cdot V_{22} \cdot f_v \quad (203)$$

$$\frac{R_{sh}R_{th} - R_{sv}R_{tv} \exp(i\phi_d)}{R_{sh}R_{th} + R_{sv}R_{tv} \exp(i\phi_d)} = \frac{T_{12cv}}{T_{22cv}} = \frac{T_{12} - (1 - Pa_G) \cdot V_{12} \cdot f_v}{T_{22} - (1 - Pa_D) \cdot V_{22} \cdot f_v}. \quad (204)$$

This way, all ground components for the soil moisture retrieval are calculated by using only the vegetation contribution of the cross-polarized component for the separation of vegetation and ground. Finally the retrieval of soil moisture from the surface and dihedral scattering components is performed as discussed in the previous Chapters 4.2.5.1. and 4.2.5.2..

4.2.6. Hybrid decomposition and inversion for soil moisture under vegetation cover

The term ‘hybrid decomposition’ implies the combination of a model-based decomposition, used to separate a depolarizing vegetation from the ground components (as introduced in Chapter 4.2.2.), with an eigen-based decomposition, used to separate the ground component into a surface and a dihedral contribution (cf. in Chapter 4.2.3.) [152, 153, 156]. Equation 205 represents a hybrid decomposition

of $\langle [T_{data}] \rangle$ into surface $[T_S] = f(f_{S_h}, \alpha_s)$, dihedral $[T_D] = f(f_{D_h}, \alpha_d)$, and random volume scattering $[T_V] = f(f_{V_h}, \alpha_v)$ [156]:

$$\langle [T_{data}] \rangle = [T_S] + [T_D] + [T_V] \quad (205)$$

$$= f_{S_h} \begin{bmatrix} \cos(\alpha_s)^2 & -\cos(\alpha_s)\sin(\alpha_s) & 0 \\ -\cos(\alpha_s)\sin(\alpha_s) & \sin(\alpha_s)^2 & 0 \\ 0 & 0 & 0 \end{bmatrix} + f_{D_h} \begin{bmatrix} \sin(\alpha_d)^2 & \cos(\alpha_d)\sin(\alpha_d) & 0 \\ \cos(\alpha_d)\sin(\alpha_d) & \cos(\alpha_d)^2 & 0 \\ 0 & 0 & 0 \end{bmatrix} \\ \dots + f_{V_h} \begin{bmatrix} \cos(\alpha_v)^2 & 0 & 0 \\ 0 & \frac{1}{2}\sin(\alpha_v)^2 & 0 \\ 0 & 0 & \frac{1}{2}\sin(\alpha_v)^2 \end{bmatrix}. \quad (206)$$

The randomly oriented volume component includes a particle shape α_v variable ranging from spheres ($\alpha_v = 0$) to dipoles ($\alpha_v = 45^\circ$). In a first step, the volume intensity component f_{V_h} is calculated [156]

$$f_{V_h} = 2T_{33} \csc(\alpha_v)^2 = \frac{2T_{33}}{\sin(\alpha_v)^2} \quad (207)$$

and the volume coherency matrix $[T_V]$ is subtracted from $\langle [T_{data}] \rangle$ to obtain the ground component ($[T_S] + [T_D]$) as [156]

$$[T_S] + [T_D] = \begin{bmatrix} T_{11} & T_{12} & 0 \\ T_{12}^* & T_{22} & 0 \\ 0 & 0 & T_{33} \end{bmatrix} - f_{V_h} \begin{bmatrix} \cos(\alpha_v)^2 & 0 & 0 \\ 0 & \frac{1}{2}\sin(\alpha_v)^2 & 0 \\ 0 & 0 & \frac{1}{2}\sin(\alpha_v)^2 \end{bmatrix}. \quad (208)$$

In a second step the eigen-based decomposition of ($[T_S] + [T_D]$) leads to the corresponding eigenvalues (f_{D_h}, f_{S_h}) and eigenvector elements (α_s, α_d) [156]

$$f_{D_h, S_h} = \frac{1}{16} \left(8T_{11} + 8T_{22} - f_V(6 + 2\cos(2\alpha_v)) \pm \sqrt{22f_V^2 + 64(4|T_{12}|^2 + (T_{11} - T_{22})^2) + 32f_V(T_{22} - T_{11}) + 6f_V((f_V - 4T_{11} + 4T_{22})4\cos(2\alpha_v) + 3f_V\cos(4\alpha_v))} \right) \quad (209)$$

$$\alpha_{d,s} = \arccos \left(\left(1 + 256 \left| \frac{T_{12}^*}{2f_V - 8T_{11} + 8T_{22} + 6f_V\cos(2\alpha_v) \pm \sqrt{AR}} \right| \right)^{-\frac{1}{2}} \right) \quad (210)$$

$$AR = 22f_V^2 + 64(|T_{12}|^2 + (T_{11} - T_{22})^2) + 32f_V(T_{22} - T_{11}) + 6f_V((f_V - 4T_{11} + 4T_{22}) \cdot 4\cos(2\alpha_v) + 3f_V\cos(4\alpha_v)).$$

The eigenvalues (f_{D_h}, f_{S_h}) represent the intensity of the two different ground components (surface, dihedral). The components α_s and α_d symbolize the ground (surface, dihedral) scattering mechanisms. Due to their orthogonality the relation

$\alpha_d = \pi/2 - \alpha_s$ applies resulting in a physical separation between surface and dihedral scattering [65, 152]. According to Figure 11, alpha angles between 0° and 45° are assigned to surface scattering, whereas the orthogonal alpha angles, ranging between 45° and 90° , are classified as dihedral scattering. f_{D_h} and f_{S_h} are allocated according to the corresponding alpha angles.

4.2.6.1. Physically constrained volume component

The principle of a physically constrained volume intensity component f_{V_c} was already established in Chapter 4.2.2.. In this approach a *Bragg* surface scattering component (introduced in Chapter 3.2.4.2.1.) is employed in the f_{V_h} -calculus to derive a physically constrained volume intensity component $f_{V_{c_h}}$. The *Bragg* model is chosen, because of the reduced number of parameters required, compared to the higher parameterized *X-Bragg*, *Fresnel* or *X-Fresnel* models.

The f_{V_h} -component is reformulated including the *Bragg* surface scattering angle α_b obtained from the eigen-decomposition of Equation 113 [153, 156]

$$f_{V_{c_h}} = \frac{4(T_{11} - T_{22} + \csc(2\alpha_b))^2 \sqrt{|(-T_{12} + T_{12}^* + (T_{12} + T_{12}^*)\cos(2\alpha_b))^2 \sin(2\alpha_b)^2|}}{1 + 3\cos(2\alpha_b)}. \quad (211)$$

In order to run the *Bragg* model in a forward sense to obtain α_b , the local incidence angle θ_l and the mean dielectric level ϵ_{est} must be known.

In order to estimate ϵ_{est} the dominant alpha angle α_1 [65, p.98] is calculated and only the dominant surface scattering areas ($\alpha_1 < 25^\circ$) are considered. This intends to narrow the analysis down to the areas, which are dominated by surface scattering (cf. Figure 11) and should be less biased by vegetation scattering.

Afterwards Equation 211 is solved for a variety of possible ϵ_{est} -levels ($\epsilon_{est} = [5, 40]$), which might occur within the study area, leading to a set of α_s -layers with different dielectric level ($\alpha_s(f_{V_{c_h}}(\epsilon_{est}))$).

The selection of the relevant ϵ_{est} -level is then based on minimizing the mean value of the difference between α_1 and the different α_s -layers. The procedure is defined as α_1 -criterion in Equation 212 and obtains additionally the fitting α_b , the fitting $f_{V_{c_h}}$ and the fitting surface scattering mechanism α_s for subsequent soil moisture inversion.

α_1 -criterion [153, 156]:

$$\{mean(\alpha_1 - \alpha_{s_{f_{V_{c_h}}(\epsilon_{est})}})\}_{\alpha_1 < 25^\circ} \rightarrow 0 \Rightarrow \epsilon_{est} \Rightarrow \alpha_b \Rightarrow f_{V_{c_h}} \Rightarrow \alpha_s. \quad (212)$$

If the physically constrained volume component f_{Vch} is applied to Equations 209-210, the influence of α_v cancels out within the soil moisture inversion procedure [153]. Consequently, the soil moisture inversion is by definition independent of the particle shape [153, 156].

4.2.6.2. Inversion for soil moisture

The inversion procedure of the hybrid decomposition is developed from the inversion procedures described in Chapter 4.2.5.. In order to convert from the notation of the hybrid decomposition to the notation used in Chapter 4.2.5., the following Equations are employed [156]:

$$\text{Surface component: } \beta_S = -\tan(\alpha_s) \quad (213)$$

$$\text{Dihedral components: } \alpha_D = \tan(\alpha_d), f_D = f_{Dh} \cdot \cos(\alpha_d). \quad (214)$$

After conversion the inversion schemes as well as the sensitivities of the inversions are equivalent to Chapter 4.2.5..

4.2.7. Multi-angular model-based decomposition and inversion for soil moisture under vegetation cover

During the thesis studies it revealed that the soil moisture inversion seems to be practically confined between a local incidence angle of $\sim 25^\circ$ and $\sim 65^\circ$ (cf. [159, 151, 39] and Chapter 4.2.3.) and performs better for shallow incidence angles [155] (cf. Chapter 4.2.3., 4.2.5.1. and 4.2.5.2.). This is of importance for soil moisture inversion in study areas with distinct topographic variations. A possible solution is to combine data acquired at different flight headings (cf. Figure 64) and use them in a multi-angular inversion scheme.

Using multi-angular data for soil information retrieval is not a novel idea. Multi-angular inversion approaches for soil moisture have been proposed in [347, 12, 251, 265, 282, 283, 334] for C-band single-polarimetric and for fully-polarimetric data [114]. However, the change of soil (moisture/roughness) and vegetation (plant moisture/phenology) conditions in time between the acquisitions limits drastically the approach and restricts a rigorous soil moisture retrieval.

Here, polarimetric decomposition techniques are applied on quasi-simultaneously acquired, multi-angular data to develop a multi-angular polarimetric decomposition for soil moisture inversion over bare and vegetated soils. In this way the polarimetric and the multi-incidence observable space are combined for soil mois-

ture retrieval.

After removal of the vegetation component, using one of the methods presented in Chapter 4.2.2. for each of the different scenes n , the surface and dihedral components are estimated as introduced in Chapter 4.2.4.. Figure 44 shows the processing scheme of the multi-angular polarimetric decomposition.

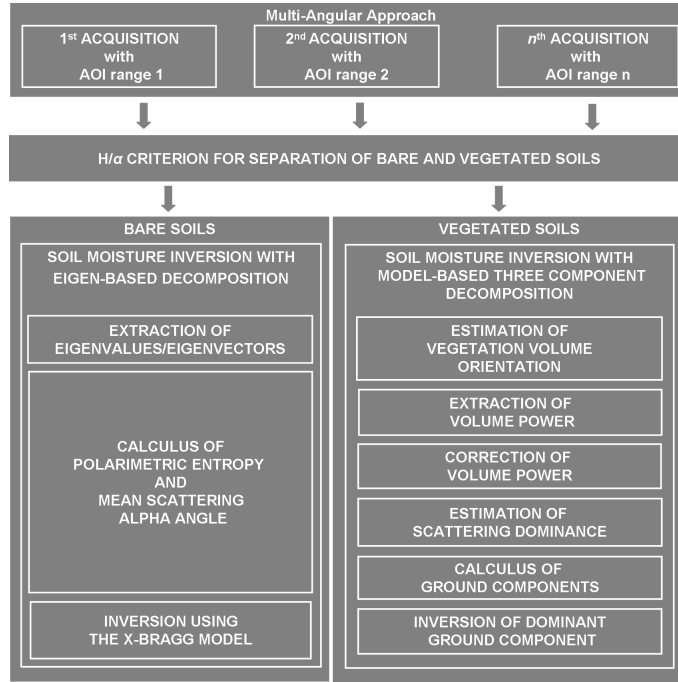


Figure 44: Processing scheme of multi-angular polarimetric decomposition and inversion procedure from bare and vegetated soils.

4.2.7.1. Inversion for soil moisture using a sum of absolute differences

For the single acquisition case, the inversion of the surface and dihedral components is already established in Chapter 4.2.5.. Within these inversions the absolute of the difference between the model and the data is minimized. This principle can be extended introducing the p-norm for $p=1$, which yields to a sum of absolute differences for up to k acquisitions.

Starting with the surface scattering case, the absolute of the difference between the modeled β_S and the data derived β_{S_d} is minimized for all k acquisitions by varying the soil dielectric constant ϵ_s

$$\min_{\epsilon_s} \left(\sum_{n=1}^k |\beta_{S_n}(\theta_{t_n} | \epsilon_s) - \beta_{S_{d_n}}| \right). \quad (215)$$

To underline the effect of multi-angularity and the sensitivity of the β_S -component to different ranges of local incidence, Figure 45 depicts the maximum beta difference $|\beta_S|_{max}$ ($|\beta_S|_{max} = \left| \beta_{S_{\theta_l}} - \beta_{S_{\theta_l=0}} \right|_{\epsilon_s}$) varying with the local incidence angle θ_l for different levels of the soil dielectric constant ϵ_s . For local incidence angles larger

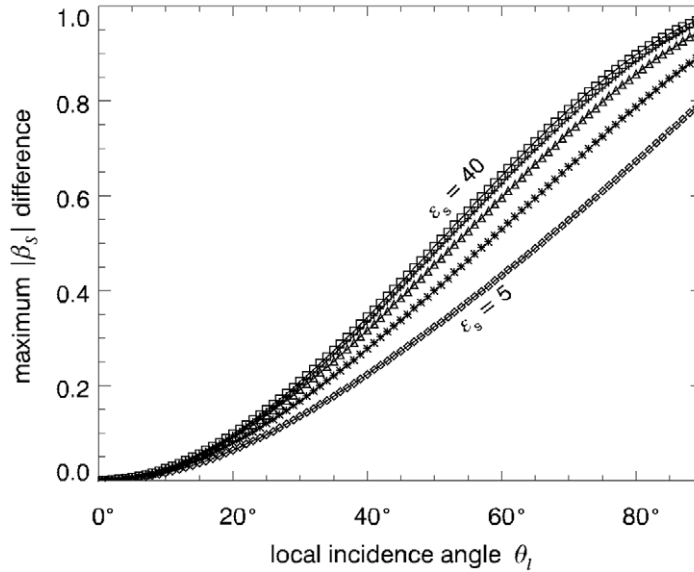


Figure 45: Maximum $|\beta_S|$ difference ($|\beta_S|_{max} = \left| \beta_{S_{\theta_l}} - \beta_{S_{\theta_l=0}} \right|_{\epsilon_s}$) along the local incidence angle θ_l for different levels of the soil dielectric constant ϵ_s [155].

than 20° , $|\beta_S|_{max}$ is rising strongly and continuously for all levels of dielectric constant, which indicates an increasing sensitivity at shallower local incidence. This is especially evident for wet soils with high values of dielectric constant.

Turning now to the dihedral scattering, the absolute difference between the modeled α_D , f_D and the data derived α_{D_d} , f_{D_d} values is minimized for the soil ϵ_s and the trunk ϵ_t dielectric constants across all k acquisitions

$$\min_{\epsilon_s, \epsilon_t} \left(\begin{array}{l} \sum_{n=1}^k |f_{D_n}(\theta_{l_n} | \epsilon_s, \epsilon_t) - f_{D_{d_n}}| \\ \sum_{n=1}^k |\alpha_{D_n}(\theta_{l_n} | \epsilon_s, \epsilon_t) - \alpha_{D_{d_n}}| \end{array} \right). \quad (216)$$

It is of special interest to have a closer look to the behavior of α_D and f_D at steep ($\theta_l = 30^\circ$) and shallow ($\theta_l = 60^\circ$) local incidence angles as shown in Figures 46 and 47.

While the dihedral intensity parameter f_D does not vary considerably with local incidence angle θ_l , the dihedral scattering mechanism α_D reveals a distinct variation. Small angles of local incidence evince a strong dependence of α_D on the dielectric constant of the trunk ϵ_t (left plot in Figure 47), whereas large angles of

4.2. SCATTERING AND DECOMPOSITION MODELS FOR VEGETATED SOILS

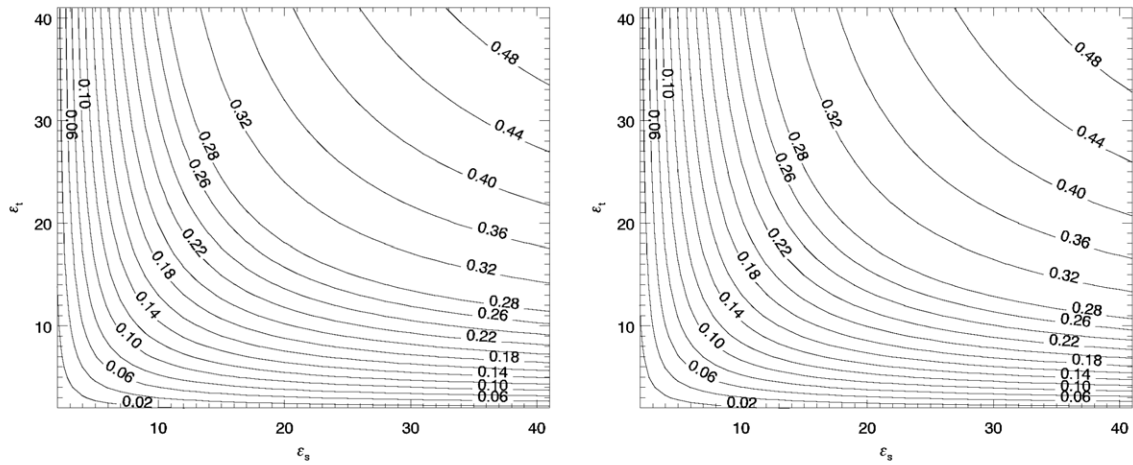


Figure 46: Variation of the dihedral scattering intensity f_D as function of the dielectric constant of the soil ϵ_s and of the trunk ϵ_t for local incidence angle $\theta_l=30^\circ$ (left) and $\theta_l=60^\circ$ (right).

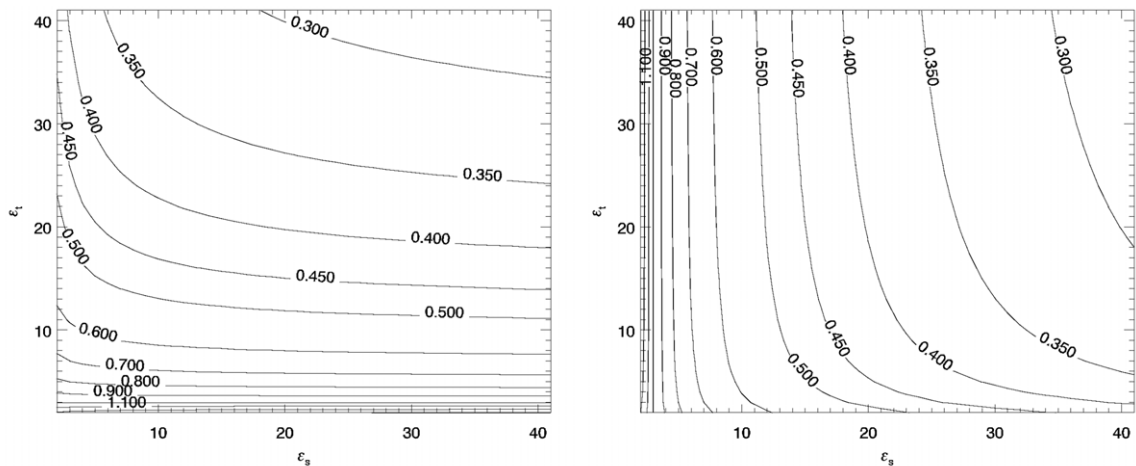


Figure 47: Variation of the dihedral scattering mechanism α_D as function of the dielectric constant of the soil ϵ_s and of the trunk ϵ_t for local incidence angle $\theta_l=30^\circ$ (left) and $\theta_l=60^\circ$ (right) [155].

local incidence cause a strong variation of α_D dominated by the dielectric constant of the soil ϵ_s (right plot in Figure 47).

4.2.8. Inversion of soil roughness under vegetation cover

Both, the vegetation cover and the soil roughness, influence the cross-polarized scattering component S_{xx} and the T_{33} -component respectively due to their intricate structure. Hence, it is a challenge to separate the scattering contribution of the soil roughness from the scattering contribution of the vegetation geometry using only polarimetric SAR data. The question arises, how much of the scattering energy in the cross-polarized scattering component originates from each of the two contributions. In the following, physically-based weights are applied on the T_{33} -component to separate both scattering contributions.

4.2.8.1. Modified X-Bragg ratio using Pauli-based ground-to-volume ratios

The ratio of the coherency matrix elements introduced in Equation 132 assigns the T_{33} -component to the roughness contribution of the soil. In the presence of vegetation cover, this assumption is questionable. Therefore the normalized Pauli-based ground-to-volume ratios Pa , introduced in Equations 176 to 179, are used to split the T_{33} -component into a soil and a vegetation contribution [150].

The ratio of Equation 132 was modified in Equation 217 incorporating the normalized Pauli-based ground-to-volume ratio of the dihedral component Pa_D and the vegetation corrected coherency matrix element (T_{22cv}) of Equation 180. Thus only the contributions attributed to soil roughness ($Pa_D \cdot T_{33}$) are considered [150].

$$\zeta = \text{sinc}(4\psi_l) = \frac{T_{22cv} - Pa_D \cdot T_{33}}{T_{22cv} + Pa_D \cdot T_{33}} \quad (217)$$

$$ks = \frac{1}{2\pi} * \text{arcsinc} \left(\frac{T_{22cv} - Pa_D \cdot T_{33}}{T_{22cv} + Pa_D \cdot T_{33}} \right). \quad (218)$$

In Figure 48 the influence of the vegetation and of the soil roughness on ζ is shown by the increase (more roughness influence/less vegetation influence) or decrease (more vegetation influence/less roughness influence) of the normalized Pauli-based ground-to-volume ratio Pa_D . For high depolarization levels ($T_{33} = 80\% T_{22}$), the change in ζ can be between 0 and almost 0.9 depending on Pa_D . In a final step the soil roughness parameter ks can be calculated from Equation 218.

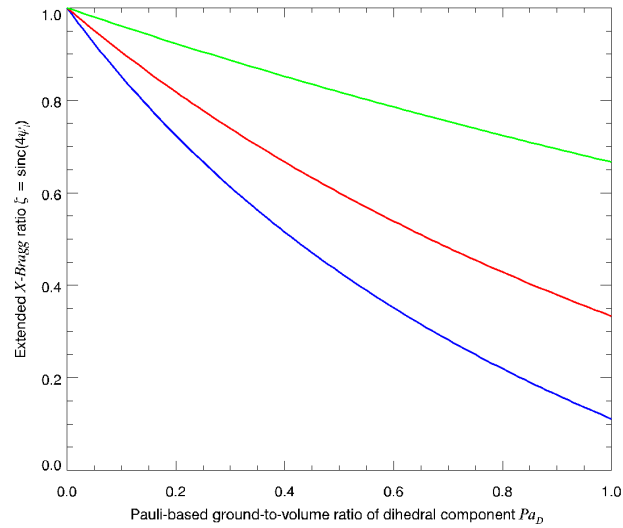


Figure 48: Sensitivity of the modified *X-Bragg* ratio ζ on the normalized *Pauli*-based ground-to-volume ratio Pa_D , $T_{22}=1$, $T_{33}=80\%T_{22}$ (blue), $T_{33}=50\%T_{22}$ (red), $T_{33}=20\%T_{22}$ (green). The higher the ground contribution with rising Pa_D , the bigger is the influence on the retrieval of soil roughness with ζ .

Part 5

Experimental data

In this Part the *in situ* measurements and the simultaneously acquired, fully polarimetric SAR data are introduced for the different study areas.

5.1. Study areas

The *in situ* measurements and the airborne polarimetric SAR data were collected within the AgriSAR, OPAQUE and SARTEO campaigns, which were conducted within 2006 and 2008 in three different study areas located in Germany.

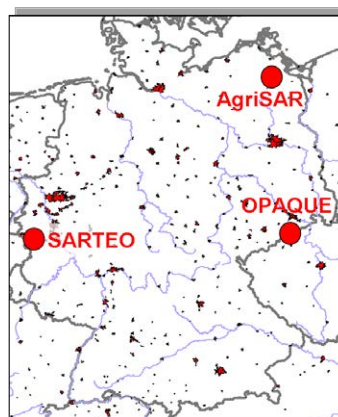


Figure 49: Location of study areas in Germany.

5.1.1. AgriSAR campaign

AgriSAR stands for Agricultural bio/geophysical retrieval from frequent repeat pass SAR and optical imaging. The campaign was funded by the European Space Agency (ESA) and includes a variety of field measurements and sensor overflights conducted in 2006. As main goal of the campaign *in-situ*, airborne SAR and optical remote sensing data were collected over an entire vegetation growth period, involving an European team of 16 institutions [23, 120, 124]. The study area is situated in Mecklenburg- Western Pomerania (cf. Figure 49) close to the town of Goermin (53° 59' 30" N, 13° 16' 20" E), where also the agricultural research facility Durable Environmental Multidisciplinary Monitoring Information Network (DEM-MIN) is located.

The fields have an average size of $\sim 200\text{-}250\text{ha}$ within the 25.000ha of the DEM-MIN study area [23]. In this region of intensive farming, the main crop types on the fields are winter wheat, winter barley, winter rape, summer corn and sugar beet.

The altitudinal range of the smooth local topography within the study area is around 50m and drops gently from North towards the Penne River in the South [113]. Figure 50 shows the local incidence angle for the different flight tracks varying predominantly between 25° and 55° , which corresponds to the Radar Look Angle (RLA) of the E-SAR system (cf. Table 7) and underlines the small topographic variations of the test site within the Northern German lowland. The agricultural site is located in a moraine area, formed during the last Pleistocene, with highly productive soils of loamy sand and sandy loam texture [202]. The mean annual temperature ranges between 7.6°C and 8.2°C and the annual sum of precipitation varies between 500mm and 650mm [113, 138].

Figure 51 contains the study area with the different test fields, the sampling locations and the two flight strips of the E-SAR sensor. Over four months, every one- to two-weeks *in situ* measurements were acquired, establishing a field database of detailed plant and soil measurements. Simultaneously, DLR's Experimental airborne SAR system (E-SAR) acquired (single-, dual-, fully polarimetric, interferometric and polarimetric interferometric) SAR data at X-, C- and L-Band.

A total amount of twelve flights were conducted for an East-West ('E-W') flight heading along the main growing season from April to July 2006. This provides the frequent repeat coverage, which is an important feature to understand soil parameter retrieval under growing vegetation cover [23]. On some campaign dates also a North-South ('N-S') flight heading was acquired (cf. Figure 51). Focusing on the field measurements, Figure 52 presents the soil moisture at two different depth from a continuously recording measurement station for the entire vegetation growth period. A decreasing trend in soil moisture is recorded, which gets more monotonous with increase of measuring depth due to the smaller influence of the fast varying processes at the soil-atmosphere boundary layer. This trend can be traced back to several dry periods apparent in the meteorological data of Appendix D.

Additionally, weekly soil moisture measurements were conducted by mobile Frequency Domain Reflectometry (FDR) [211, 261, 260] and Time Domain Reflectometry (TDR) [297, 295, 195, 336] probes from Leibniz Centre for Agricultural Landscape Research (ZALF), Christian-Albrechts-Universität Kiel (CAU) and DLR [23]. A comprehensive overview on measurement techniques for soil moisture is given

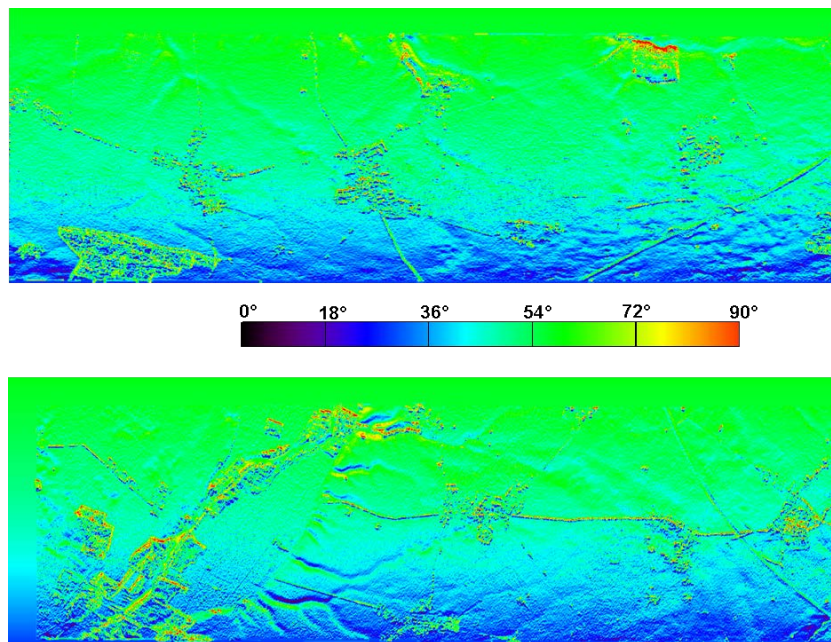


Figure 50: Local incidence angle of the two flight headings (top: ‘E-W’-track, bottom: ‘N-S’-track) for the AgriSAR 2006 campaign, (cf. LIA variation for flat terrain: 25°-55°).

in [260, 272, 268].

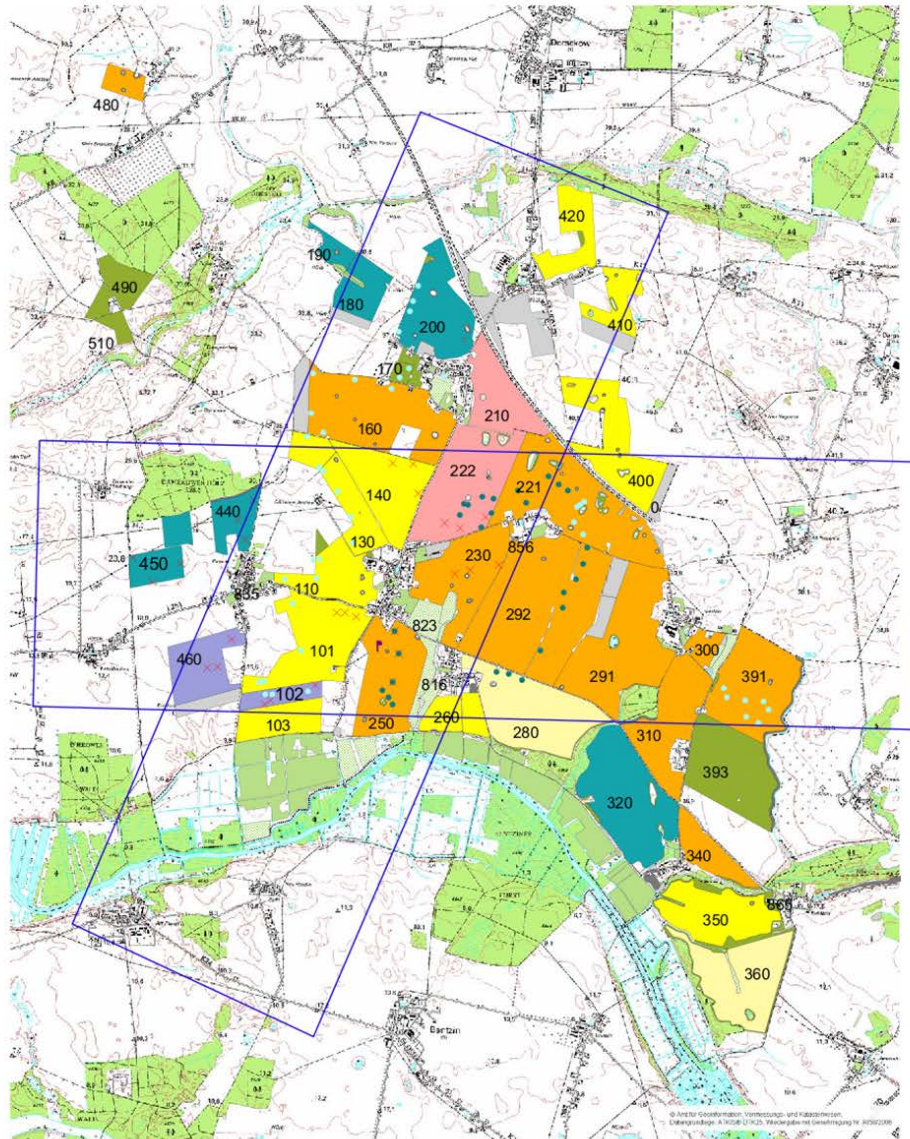
The measurements depicted in Figures 53 and 54 confirm the decreasing soil moisture trend along the growth cycle for the AgriSAR study area in 2006. Furthermore three intensive campaigns were launched in the beginning (19th/20th of April), in the middle (6th/7th of June) and in the end (5th/6th of July) of the vegetation growth period. An overview of the soil moisture measurements for these campaigns is given in Appendix E. Figures 55 and 56 present the development of the vegetation along the agricultural growth cycle from April to July for a variety of crop types, where a distinct vegetation canopy can be stated for instance in July 2006 with a maximum height of 215cm on the summer maize field and a maximum wet biomass of 8.0kg/m² on the winter rape field.

Apart from the vegetation measurements, laser-profiling [47, 112] and digital photogrammetry [288, 202, 258, 257, 286] were used to measure soil roughness. A general overview on roughness measurement techniques is given in [203, 161].

The utilized Centre d’Etude Spatiale de la BIOSphère (CESBIO)-ESA LASER profiler is capable to acquire roughness profiles up to 25m length in steps of 5m, while the spatial resolution is 5mm and the vertical precision is specified with $\pm 1.5\text{mm}$ [80] (cf. Figure 57). During the campaign the LASER had some acquisition failures due to linkage problems between the LASER and the laptop [23]. Therefore only profiles of reduced length with 3-15m were produced for

5.1. STUDY AREAS

AGRISAR 2006 Sampling locations



Scale: 1 0 1 2 Kilometers

Legend

Sampling locations

- LMU, TDR measurements 1st intensive campaign
- LMU, TDR measurements 2nd intensive campaign
- × Sampling locations of weekly measurements
- Bowen ratio station and TDR station
- Flight tracks

Field crops

- field grass
- grassland
- cutting pasture
- set aside
- set aside: rape
- sugar beet
- no crop currently
- winter wheat
- winter barley
- maize
- rape

Figure 51: Overview of the DEMMIN test site within the AgriSAR 2006 campaign containing test fields, sampling locations for ground measurements and the two flight strips of the E-SAR sensor [23].

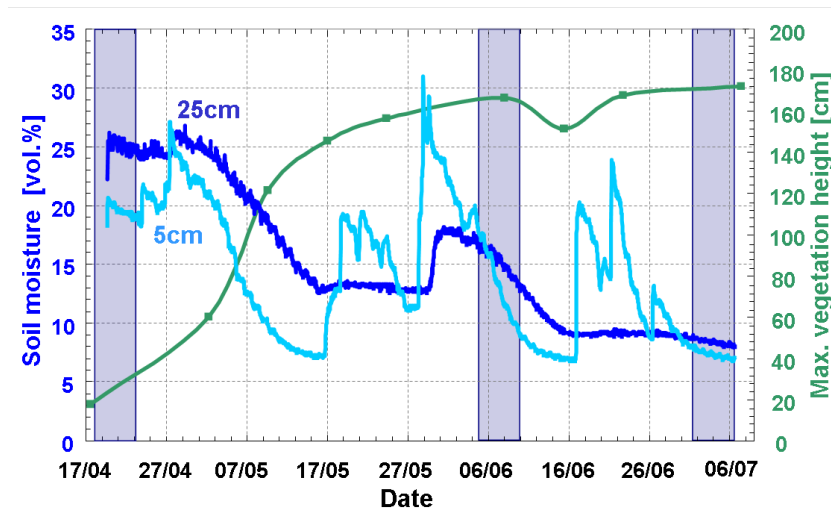


Figure 52: Data of a continuously recording soil moisture station deployed by LMU and covering the entire vegetation growth period from April to July 2006 of the AgriSAR campaign; A selection of dates with overflights is indicated by the blue bars. Soil moisture was measured horizontally for two different depth (5cm, 25cm) represented by the blue lines; The maximum vegetation height is displayed with a green line, [23].

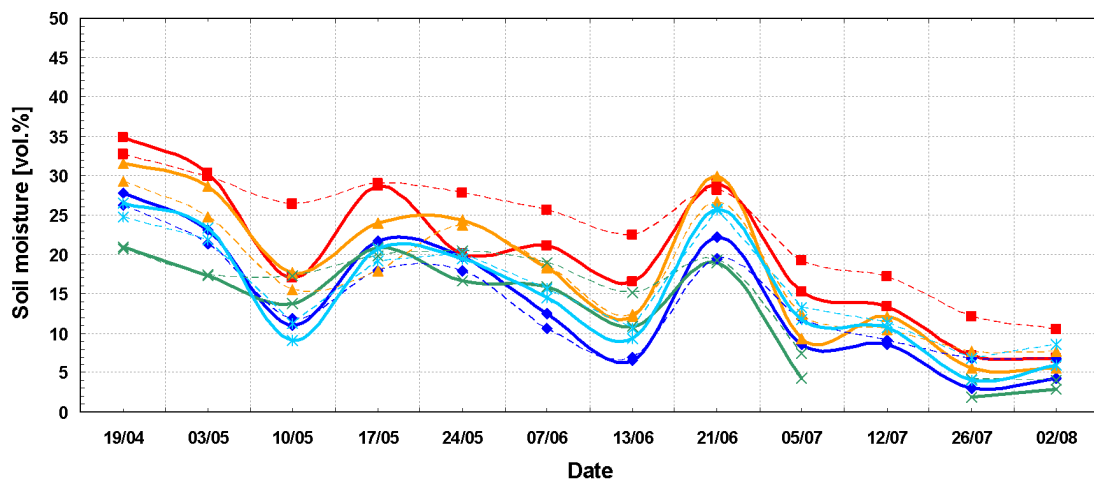


Figure 53: Weekly soil moisture measurements by ZALF/DLR covering the entire vegetation growth period from April to July 2006 of the AgriSAR campaign; Field mean values (measurement depth: 0-5cm (solid line), 5-10cm (dashed line)): Blue=winter barley, bright blue=winter rape, green=sugar beet, red=summer corn, orange=winter wheat [23].

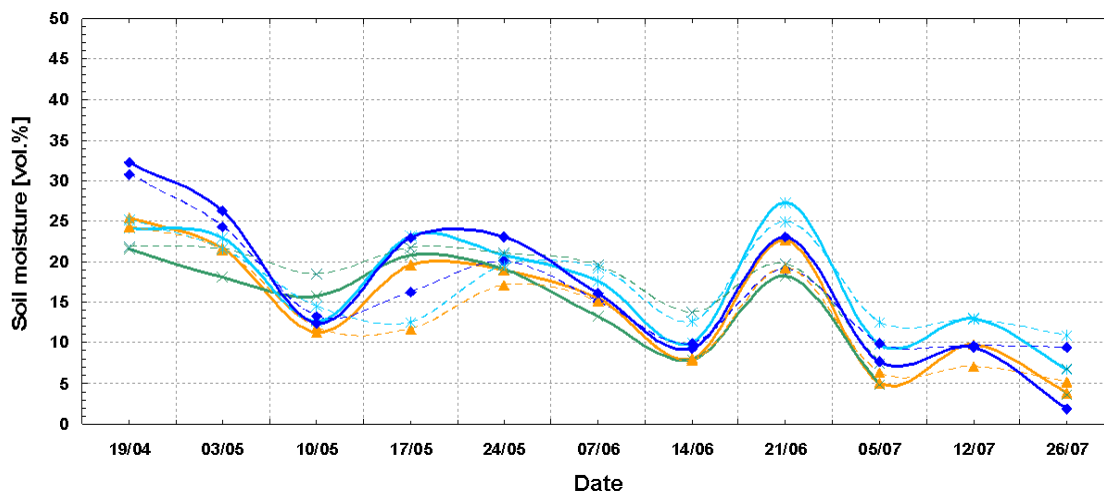


Figure 54: Weekly soil moisture measurements by CAU covering the entire vegetation growth period from April to July 2006 of the AgriSAR campaign; Field mean values (measurement depth: 0-5cm (solid line), 5-10cm (dashed line)): Blue=winter barley, bright blue=winter rape, green=sugar beet, orange=winter wheat [23].

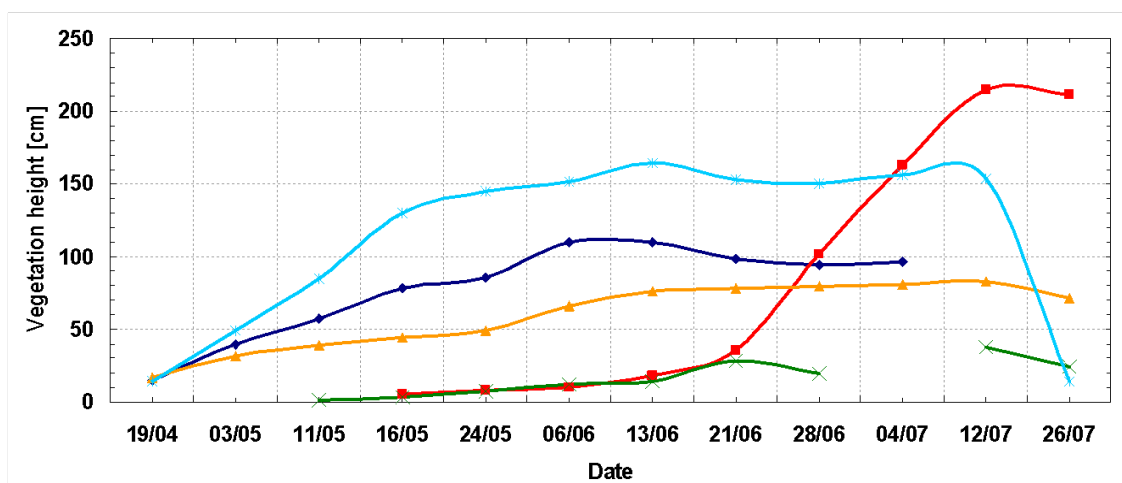


Figure 55: Vegetation height measurements of ZALF/DLR covering the entire vegetation growth period from April to July 2006 of the AgriSAR campaign; Field mean values: Blue=winter barley, bright blue=winter rape, green=sugar beet, red=summer corn, orange=winter wheat [23].

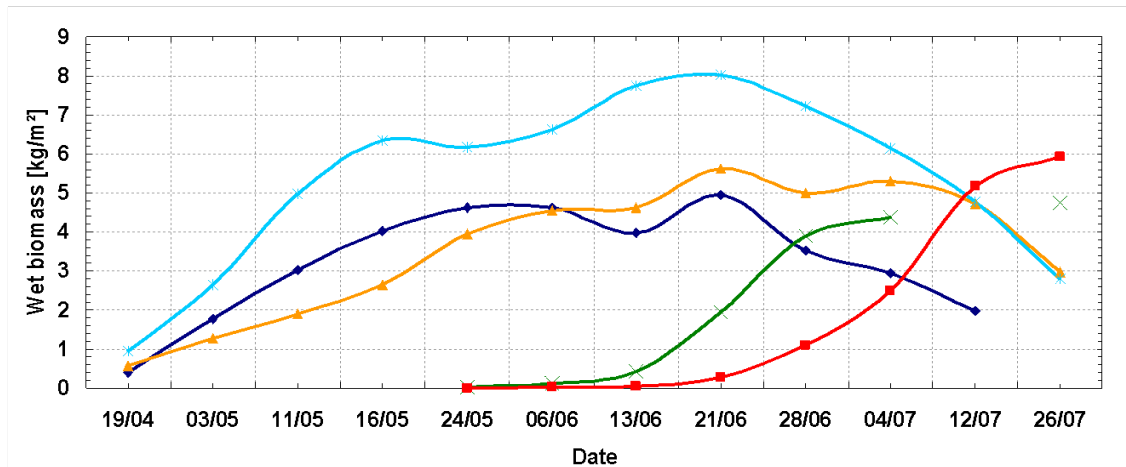


Figure 56: Wet biomass measurements of ZALF/DLR covering the entire vegetation growth period from April to July 2006 of the AgriSAR campaign; Field mean values: Blue=winter barley, bright blue=winter rape, green=sugar beet, red=summer corn, orange=winter wheat [23].



Figure 57: CESBIO-ESA LASER profiler with field campaign settings [23].

the AgriSAR campaign like in Figure 58. As LASER profiling is a two dimensional representation of a bi-directional entity, the roughness parameters vary due to profile length and direction of the profile compared to the overall roughness pattern (e.g. direction of furrows) on the field. In literature, a plurality of publications exists dealing with this issue of spatial variability of soil roughness [4, 44, 47, 46, 203, 80, 233, 14, 196]. In order to overcome the effect of directionality on the profiles, also stereo-photogrammetry was utilized for assessing the soil roughness. During the AgriSAR 2006 campaign the following measurement setup was used on each of the sampling locations of the CAU-team (cf. Figure 59 and [202]).

A calibrated *Rollei d7 metric* camera mounted on a metal rack acquired the stereo pair with 65% overlap [202]. The horizontal extend of the sampling area is limited

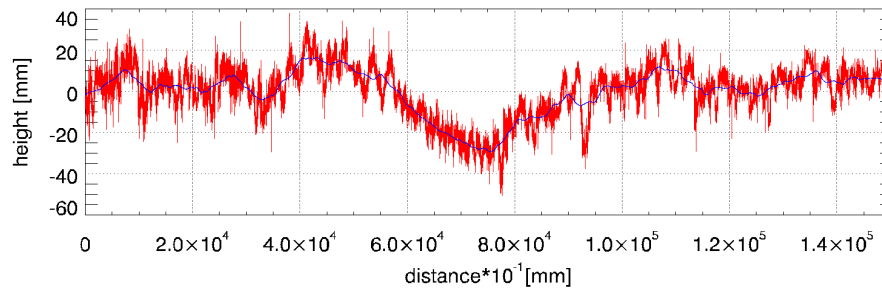


Figure 58: Exemplary roughness profile of a bare soil surface in April 2006 (field 102: Sugar beet) derived with CESBIO-ESA LASER profiler within the AgriSAR campaign; Red: Sampled values, blue: Moving average of 1000 sampled values.

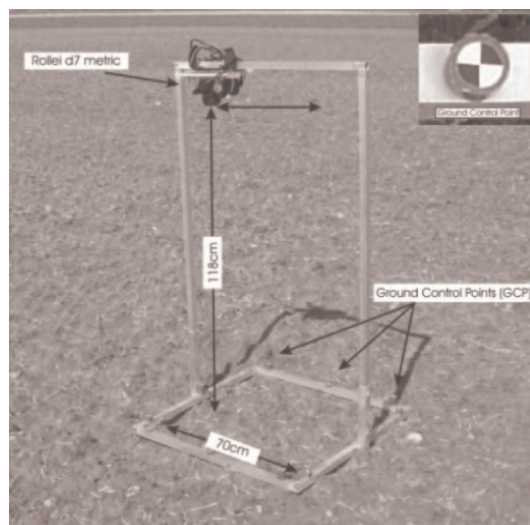


Figure 59: Measurement setup for soil roughness retrieval with a digital photogrammetric approach including camera, metal rack and GCPs [202].

to $70 \times 70 \text{cm}^2$ with a spatial resolution of 2mm [202]. For acquisitions on vegetated fields, the soil surface was completely cleared from plant parts without disturbing the soil surface. The Digital Surface Models DSM were generated using highly accurate GCPs for orientation [202]. The surface roughness measurements of the Ludwig Maximilians Universität München (LMU) were acquired using the same measurement technique, but different equipment. Details are given in [187], but an exemplary sample is shown in Figure 60.

In the end Figure 61 shows the temporal change of the RMS-height h_{rms} along the agricultural growth cycle, retrieved by CAU with the photogrammetric approach. A distinct variance in vertical roughness can be observed for the measurements, especially for the rough summer corn field compared to the smoother winter wheat fields. Furthermore, the variance of the RMS-height for the different dates from

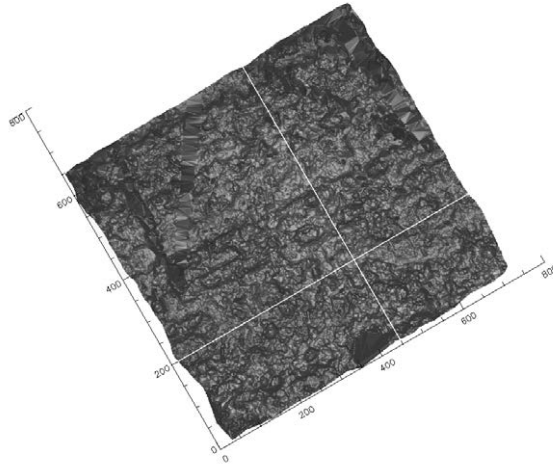


Figure 60: Bird view on three dimensional soil roughness measurement acquired by digital photogrammetry from the AgriSAR campaign; The white lines represent possible profiles for a two dimensional roughness representation.

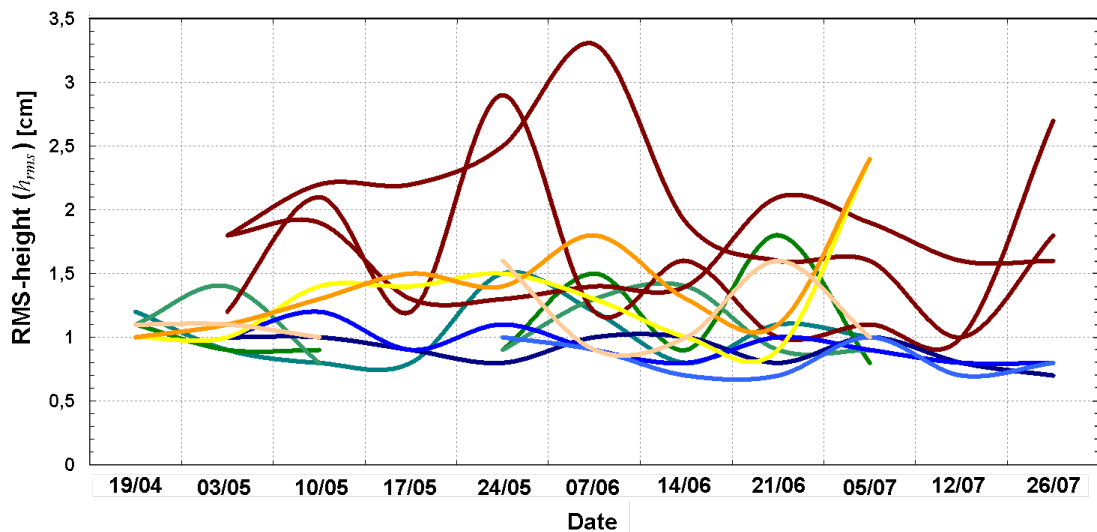


Figure 61: Time series of soil roughness measurements of the RMS-height, conducted by CAU, covering the entire vegetation growth period from April to July 2006 of the AgriSAR campaign with three measurement plots per test field; Blue=winter wheat (field: 250), green=sugar beet (field: 102), orange=sugar beet (field: 460), brown=summer corn (field: 222) [23].

April to July 2006 indicates that the assumption of a constant roughness level for the whole growth period is doubtful and a soil roughness estimation under vegetation cover is needed to update the soil roughness status along the growing cycle.

5.1.2. OPAQUE campaigns

OPAQUE stands for operational discharge and flooding predictions in head catchments. It represents a Federal Ministry of Education and Research (BMBF)-project to improve operational predictions of rainfall-runoff processes as well as enhancing the management of reservoirs and retention basins for an enhanced flood forecasting and an improved hazard warning.

The main objective in terms of soil parameter retrieval is the identification of critical catchment states caused by saturated top soil layers. Therefore two field campaigns were performed on the 31st of May 2007 and on the 8th of May 2008 by the Universities of Stuttgart and Potsdam, the German Research Centre for Geosciences (GFZ) and the German Aerospace Center (DLR) in the Weisseritz catchment area (50°40'-51°03' N, 13°31'-13°45' E) near Dresden, Germany (cf. Figure 49) [148, 149]. The study area is located within the Ore-Mountains range formed in the variscian time (Upper Karbon) with soils of sandy loam and loamy sand texture. It is deeply trenched by the river network of the Weisseritz running from South towards North. Therefore the topography changes rapidly between approximately 500-800m resulting in steep slopes along the river beds, where most of the forested areas are located (cf. Figure 62). But towards the North within the lower reaches of the river, the areas with agricultural cultivation dominate the landscape (cf. Figure 63). The mainly cultivated crop types are wheat, triticale,

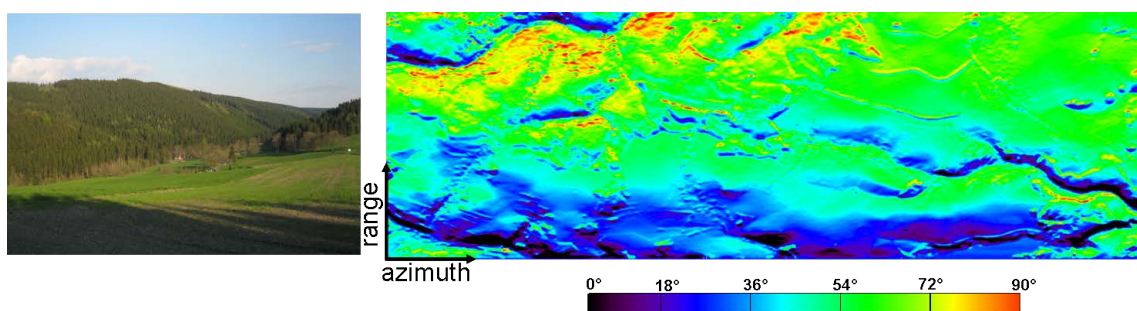


Figure 62: Exemplary image of a steep slope within the acquired scene (left) and local incidence angle (LIA) of the OPAQUE study area (right) exhibiting the strong topographical variations (cf. LIA variation for flat terrain: 25°-55°).

barley, rape, summer corn and grassland under a temperate climate with an annual mean temperature ranging from 4°C to 8.5°C and annual sum of precipitation varying between 700mm and 1000mm [39, 116, 45].

During the OPAQUE campaigns (single-, dual-, fully polarimetric and polarimetric interferometric) SAR data at X-, C-, L- and P-band were acquired by DLR's airborne E-SAR sensor. Figure 63 illustrates the location of the flight strip, the corner reflectors and the test fields of the OPAQUE 2007 campaign. During the campaign in 2007, a variety of agricultural crop types from winter triticale to summer corn were examined for vegetation and soil properties. An overview of the acquired soil moisture and vegetation measurements for the different crop types is provided in Table 3. The *in situ* measurements report a high soil moisture level in the

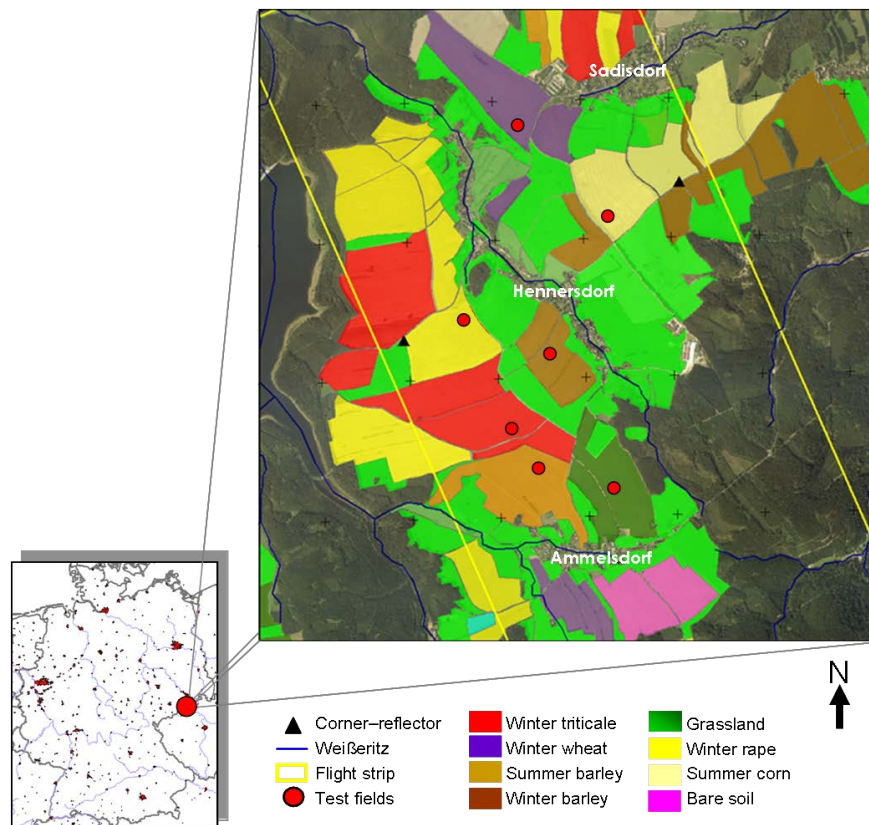


Figure 63: Overview of study area for the OPAQUE 2007 campaign including test fields, land use, flight strip and corner reflectors.

range of 25vol.% to 35vol.% and a distinct vegetation cover for the winter crops with more than 50cm vegetation height and 2.8kg/m² wet biomass.

In order to investigate the same study area under different hydrological and phenological conditions, a second OPAQUE campaign was carried out in 2008. As a specialty for the OPAQUE 2008 campaign, L-band data were recorded along three

5.1. STUDY AREAS

Table 3: *in situ* measurements of vegetation and soil moisture for May 2007 of the OPAQUE campaign as mean field values: Soil moisture (mv) and Standard Deviation (STDDEV) of mv (Δmv), vegetation height and wet biomass [148].

Fields	mv $\pm\Delta mv$ [vol.%]	Vegetation height [cm]	Wet biomass [kg/m ²]
Winter triticale	30.22 \pm 2.38	84.4	3.34
Winter barley	36.28 \pm 4.46	69.6	3.31
Winter rape	34.25 \pm 4.63	135.0	6.52
Winter wheat	31.79 \pm 2.61	54.6	2.85
Summer corn	27.96 \pm 5.33	16.4	0.10
Grassland	31.07 \pm 2.57	27.0	1.13
Summer barley	31.19 \pm 3.07	45.6	0.93

different flight headings to obtain a data set for multi-angular polarimetric analyses. In Figure 64 the three acquisitions are combined in a RGB-composite and are labeled as *master* (m), *opposite* (o) and *perpendicular* (p). The local incidence an-

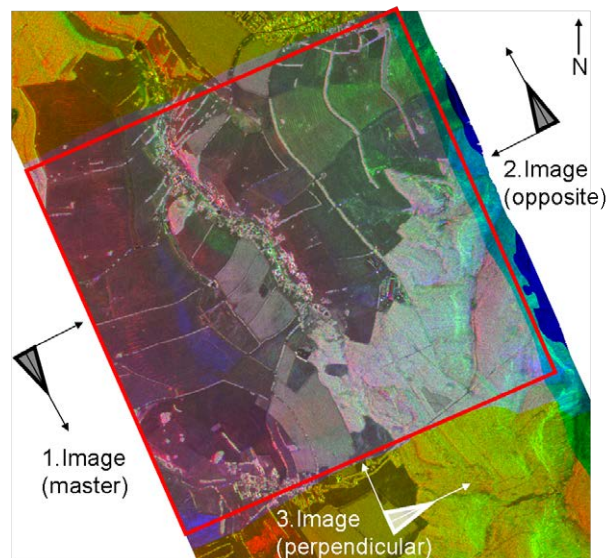


Figure 64: RGB-composite of the three flight headings in HH-polarization for L-band (R: *master*, G: *opposite*, B: *perpendicular*); Red frame indicates the overlapping area of the three flight strips [155].

gle (LIA) for each acquisition (*master*, *opposite* and *perpendicular*) is presented in Figure 65, whereas the different local incidence angles for each test field are listed in Table 4. The local incidence angle on the single test fields ranges from 23.4° to 58.6° and the absolute difference in local incidence between the respective scenes varies from 1.3° to 34.8°.

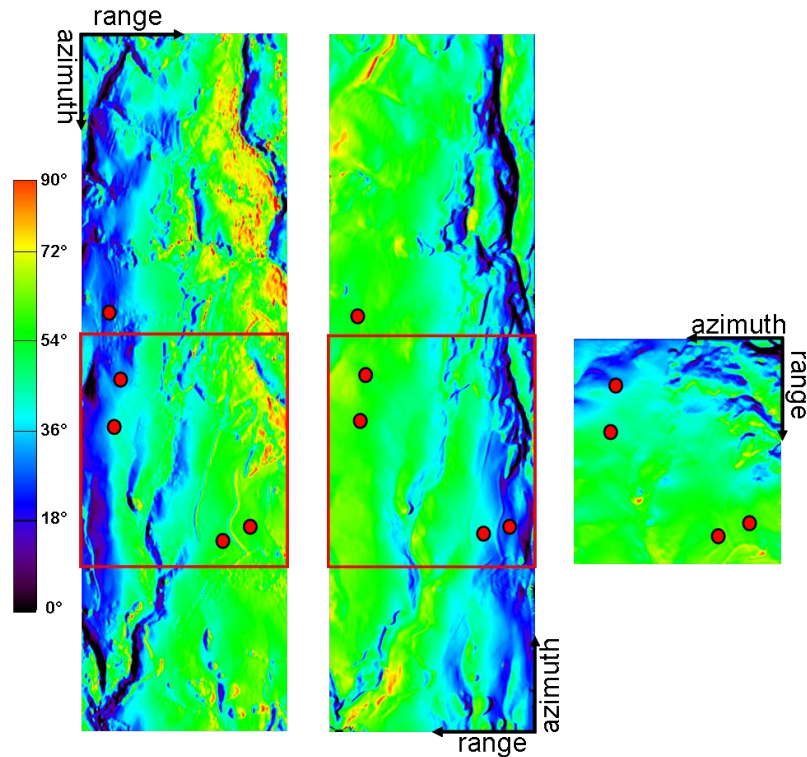


Figure 65: Local incidence angle of the multi-angular data set of the OPAQUE 2008 campaign (from left to right): *Master scene*, *opposite scene*, *perpendicular scene*; Red circles represent the test fields and the red frame indicates the overlapping area of all three acquisitions (cf. LIA variation for flat terrain: 25°-55°).

Table 4: Local incidence angle of different flight headings (*master*: θ_{l_m} , *opposite*: θ_{l_o} , *perpendicular*: θ_{l_p}) and absolute local incidence angle differences ($\Delta\theta_l |a-b| = |\theta_{l_a} - \theta_{l_b}|$) [155].

Fields	θ_{l_m} [°]	θ_{l_o} [°]	θ_{l_p} [°]	$\Delta\theta_l m-o $	$\Delta\theta_l m-p $	$\Delta\theta_l o-p $
Winter triticale	49.9	39.8	53.5	10.1	3.6	13.7
Winter barley	38.4	49.8	43.4	11.4	5.0	6.4
Winter rye	33.9	52.9	35.2	19.0	1.3	17.7
Winter wheat	58.6	26.6	55.5	32.0	3.1	28.9
Summer oat	23.4	58.2	-	34.8	-	-

Simultaneously to the airborne SAR acquisitions, soil and vegetation measurements were collected on these test fields covering different vegetation types for a later characterization of their influence on the SAR signal. A summary of the sampling locations and the measurements for the different test fields of the OPAQUE 2008 campaign is given in Table 5 and Figure 66.

Mobile FDR probes were used for near surface soil moisture measurements at 0-

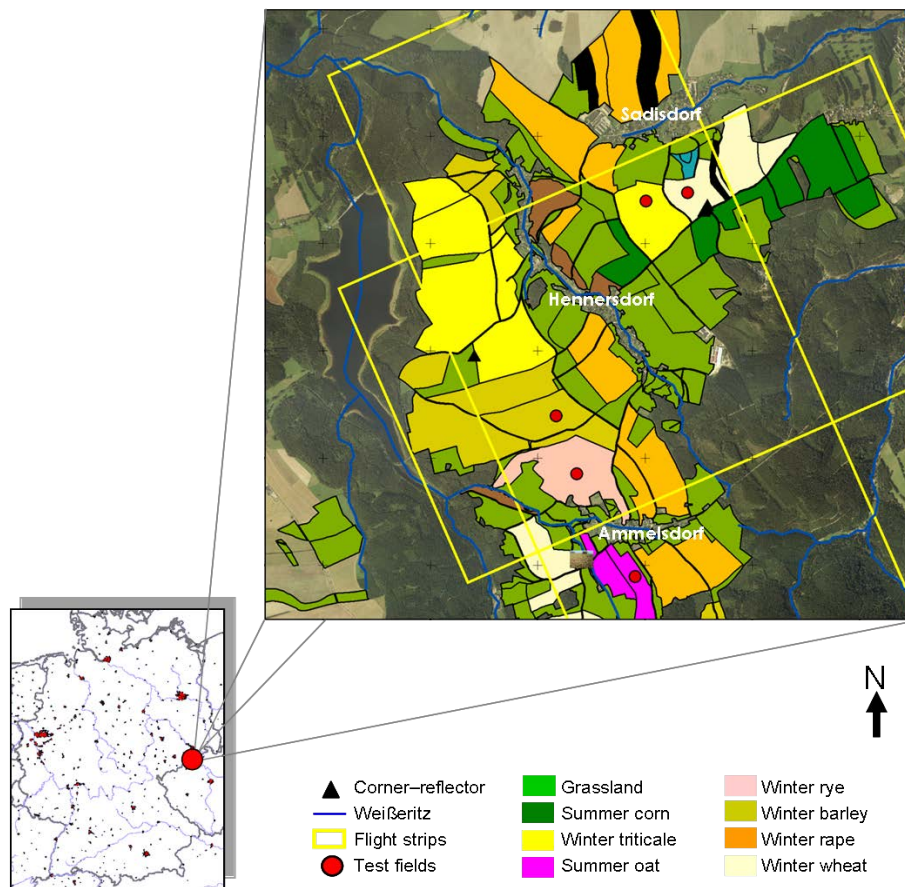


Figure 66: Overview of study area for the OPAQUE 2008 campaign including test fields, land use, perpendicular flight strips and corner reflectors.

5cm depth. Three individual measurements were averaged to obtain the measured soil moisture as reference for one measurement location. All the measurement locations of one field are processed to a mean field value (cf. Table 5). The Standard Deviation (STDDEV) of the measured soil moisture (Δmv) for each field varies about 12-25% compared to the measured mean soil moisture values [155]. This can not be allocated to topographic variations within the field parcels and can originate from the spatial intra-field variability of the soil moisture. Furthermore, the field measurements in Table 5 indicate a dry weather period, with soil moisture values from 11.8 vol.% to 22.7 vol.% for all test fields. In addition, the vegetation is emerging with a maximum height of 24cm, except for the summer oat field, which is almost bare.

Table 5: *in situ* measurements of soil moisture and vegetation for OPAQUE 2008 campaign as mean field values: Soil moisture (mv) and Standard Deviation (STDDEV) of mv (Δmv), vegetation height and wet biomass [155].

Fields	mv $\pm\Delta mv$ [vol.%]	Vegetation height [cm]	Wet biomass [kg/m ²]
Winter triticale	19.4 \pm 3.5	23.0	0.39
Winter barley	11.8 \pm 3.0	24.4	0.66
Winter rye	19.9 \pm 3.3	17.4	0.15
Winter wheat	16.9 \pm 2.7	14.0	0.24
Summer oat	22.7 \pm 2.8	6.75	-

- = no measurements

5.1.3. SARTEO campaign

The SARTEO-campaign was performed on the 27th of May 2008 within the Rur catchment in Western Germany by the Research Centre Jülich and DLR (cf. Figure 49). The SARTEO-project focus on the investigation of soil moisture under vegetation cover using fully polarimetric SAR data. For this reason DLR's airborne E-SAR sensor acquired these data in L-band following a triangular flight heading, which covers about 390km² of rural landscape for investigation [122].

Figure 67 illustrates the triangular flight configuration and highlights the scene around the town of Selhausen (50° 51' 50" N, 6° 26' 10" E), located near Cologne within the Lower Rhine Valley. The geologic development of this region was mostly influenced by the Quaternary. Thus the soil formation at this study area is dominated on one hand by aeolian deposits (loess) and on the other hand by the deposits of the Rur river [217]. On these soils of silty loam, the field measurements for soil moisture were conducted with FDR probes on selected test fields [86,163]. The highly productive soils are well suited for intensive agriculture covering the crop types: Winter wheat, winter barley and sugar beet within a temperate climate zone characterized by a variation of the annual mean temperature between 6°C and 9°C as well as an annual sum of precipitation varying between 700mm and 900mm [217]. The vegetation and soil moisture measurements of the field campaign are listed in Table 6 and relate to a soil moisture level of about 20vol.% under an emerging vegetation layer.

In addition, Figure 68 contains the local incidence angle (LIA), which varies mainly between 25° and 55°. As this agrees with the radar look angle of the E-SAR system (cf. Table 7), the similarity states the minor influence of topography for this

5.1. STUDY AREAS

Table 6: *in situ* measurements of soil moisture as mean field values and estimated vegetation height from photographs for May 2008 of the SARTEO campaign: Soil moisture (mv), Standard Deviation (STDDEV) of mv (Δmv) and vegetation height [122].

Fields	mv $\pm\Delta mv$ [vol.%]	Vegetation height ¹ [cm]
Winter barley	20.44 \pm 2.84	~ 70
Winter wheat	22.46 \pm 3.09	~ 30
Sugar beet	21.54 \pm 2.35	~ 10

¹ no direct measurements

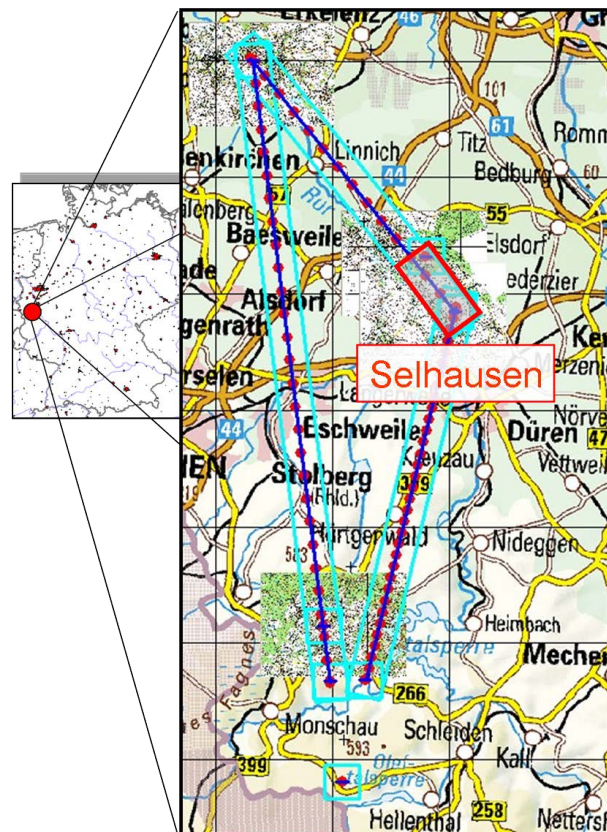


Figure 67: Flight tracks of the SARTEO campaign in the Rur catchment near Jülich; A triangular flight heading was chosen, where only the scene of Selhausen was considered for analysis due to available ground measurements [122].

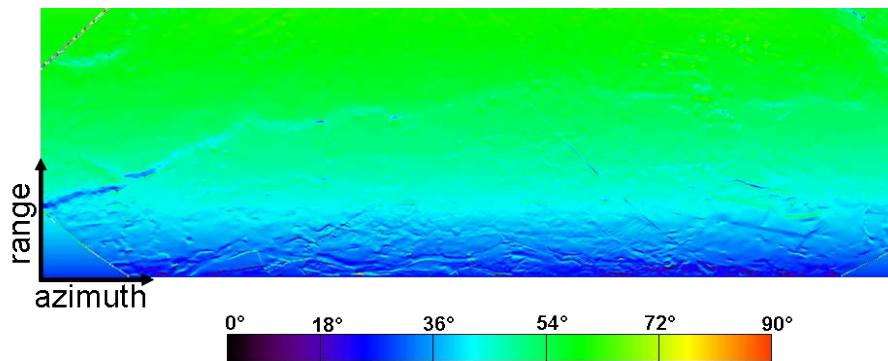


Figure 68: Local incidence angle for the SARTEO campaign in 2008 (radar look angle: 25°-55°).

flat study area. The topography follows the Rur river bed with a gentle decrease towards North-West from 125m in Düren to 83m in Jülich.

5.2. Polarimetric SAR data

As point-like *in situ* measurements are time consuming and personnel-intensive on larger scales, fully polarimetric airborne SAR data are investigated for soil parameter retrieval under vegetation cover.

5.2.1. Acquisition

The monostatic SAR data were acquired by DLR's airborne E-SAR system onboard a Dornier Do 228-212 aircraft. E-SAR features single pass across-track SAR interferometry capabilities at X-band (only VV polarization) for a later derivation of a Digital Surface Model (DSM) and fully polarimetric as well as interferometric data acquisition in C-(synthetic), L- and P-band for analysis of the Pol-InSAR or PolSAR observation space [135].

During the thesis studies different frequencies from X-band ($\lambda_c=3\text{cm}$) to P-band ($\lambda_c=86\text{cm}$) were analyzed for characterization of soil properties under agricultural vegetation [128, 158, 123, 124, 159, 150, 152, 153, 155, 200, 201]. For X- and C-band, it arises that at a certain stage (earlier at X-band, later at C-band) in the growth cycle, the backscattered signal from the mature vegetation is predominant and the soil information becomes negligible due to the low penetration. Moreover, P-band indicates a very low backscattering signal over agricultural areas due to the long wavelength, which degrades the significance of the extracted soil information due to the very low signal-to-noise ratio (SNR) [105]. Finally, L-band revealed as the most suitable frequency in terms of penetration and Signal to Noise



Figure 69: DLR's airborne E-SAR system on board a Dornier Do 228-212 aircraft [23].

Ratio (SNR) for sensing soil conditions under agricultural vegetation cover, aiming for an all-seasons monitoring strategy.

Technical specifications for L- and X-band antennas are shown in Table 7, as these frequencies are used for SAR processing (X-band) and for polarimetric SAR analyses (L-band) in Part 6. In addition, Table 7 includes the parameters for the ac-

Table 7: Technical specifications of the E-SAR instrument and parameters of the acquisition geometry, [135, 23, 148, 149].

Technical specifications	Symbol	X-band	L-band
Center frequency	f_0	9.6GHz	1.3GHz
Wavelength	λ_c	0.03m	0.23m
Transmit peak power	P_{Tmax}	2.5kW	400W
Receiver noise figure	nf_R	4.0dB	8.5dB
Antenna gain	G_t	17.5dB	15dB
Azimuth beamwidth	β_{az}	17°	18°
Elevation beamwidth	β_{el}	30°	35°
Antenna polarization		VV	HH,HV,VV,VH
Acquisition mode		single pol.	fully pol.
Max. signal bandwidth	B_{wmax}	100MHz	100MHz
Signal duration	τ	5 μ s	5 μ s
Pulse repetition frequency per channel	PRF	1000Hz	400Hz
Aircraft velocity	v_p	\sim 90m/s	\sim 90m/s
Radar look angle	θ	25°-55°	25°-55°
Swath width	l_s	\sim 3000m	\sim 3000m
Slant range resolution (no post processing)	δ_{rGSAR}	1.5m	1.5m
Azimuth resolution (no post processing)	$\delta_{az,SAR}$	0.72m	1.0m

quisition geometry, like the Radar Look Angle (RLA) ($\theta=25^\circ-55^\circ$) and the aircraft velocity ($v_p \simeq 90\text{m/s}$). The aircraft is equipped with a modern combined Differential Global Positioning System (DGPS)/Inertial Navigation System (INS) system for navigation and SAR motion compensation for precise SAR processing and geolocation. Moreover, during the campaigns corner reflectors were deployed at each study area in near and far range of the E-SAR flight headings (e.g. Figure 63). They were precisely adjusted to act as recoverable targets within the SAR acquisitions for later steps in the processing.

5.2.2. Processing

The general SAR processing work flow for E-SAR imagery is described in [23]. It includes operational modules for geocoding (WGS84, BESSEL) and DSM generation. The DSM is derived from the X-Band single pass SAR interferometry data and has a horizontal resolution of $5\text{m} \times 5\text{m}$ and an absolute vertical resolution of $\leq 1\text{m}$ [135]. The final specifications of the fully polarimetric E-SAR imagery products are listed in Table 8 verifying the very high quality of the airborne SAR product with a Noise Equivalent Sigma Zero (NESZ) of -30dB and a spatial resolution of $2\text{m} \times 2\text{m}$. Table 9 summarizes the selection of processed fully polarimetric

Table 8: Specifications of fully polarimetric E-SAR L-band data after processing and presuming of a factor two in *azimuth* direction, [135, 23, 148, 149].

Data specifications	Symbol	L-band
Noise Equivalent Sigma Zero (NESZ)		-30dB
Scene size		$\sim 3\text{km} \times 15\text{km}$
Absolute radiometric calibration		$\leq 3\text{dB}$
Relative radiometric calibration		$\leq 1\text{dB}$
Polarimetric calibration (cross talk)		$\leq -30\text{dB}$
Polarimetric calibration (phase)		$\leq 10^\circ$
Final <i>range</i> pixel spacing	Δ_{rg}	1.5m
Final <i>azimuth</i> pixel spacing	Δ_{az}	1.0m
Final slant <i>range</i> resolution	δ_{rg}	2.0m
Final <i>azimuth</i> resolution	$\delta_{az_{SAR}}$	2.0m

L-band acquisitions, which were retrieved from the three campaigns introduced in Chapter 5.1. and which are employed for experimental data analyses in the following Part 6. For a first scattering analysis, the processed L-band PolSAR data are displayed as normalized *Pauli* RGB-images in Figure 70. Even bounce (red), volume (green) and odd bounce (blue) scattering can be distinguished within the agricultural scenes. While volume scattering dominates mainly in the forested ar-

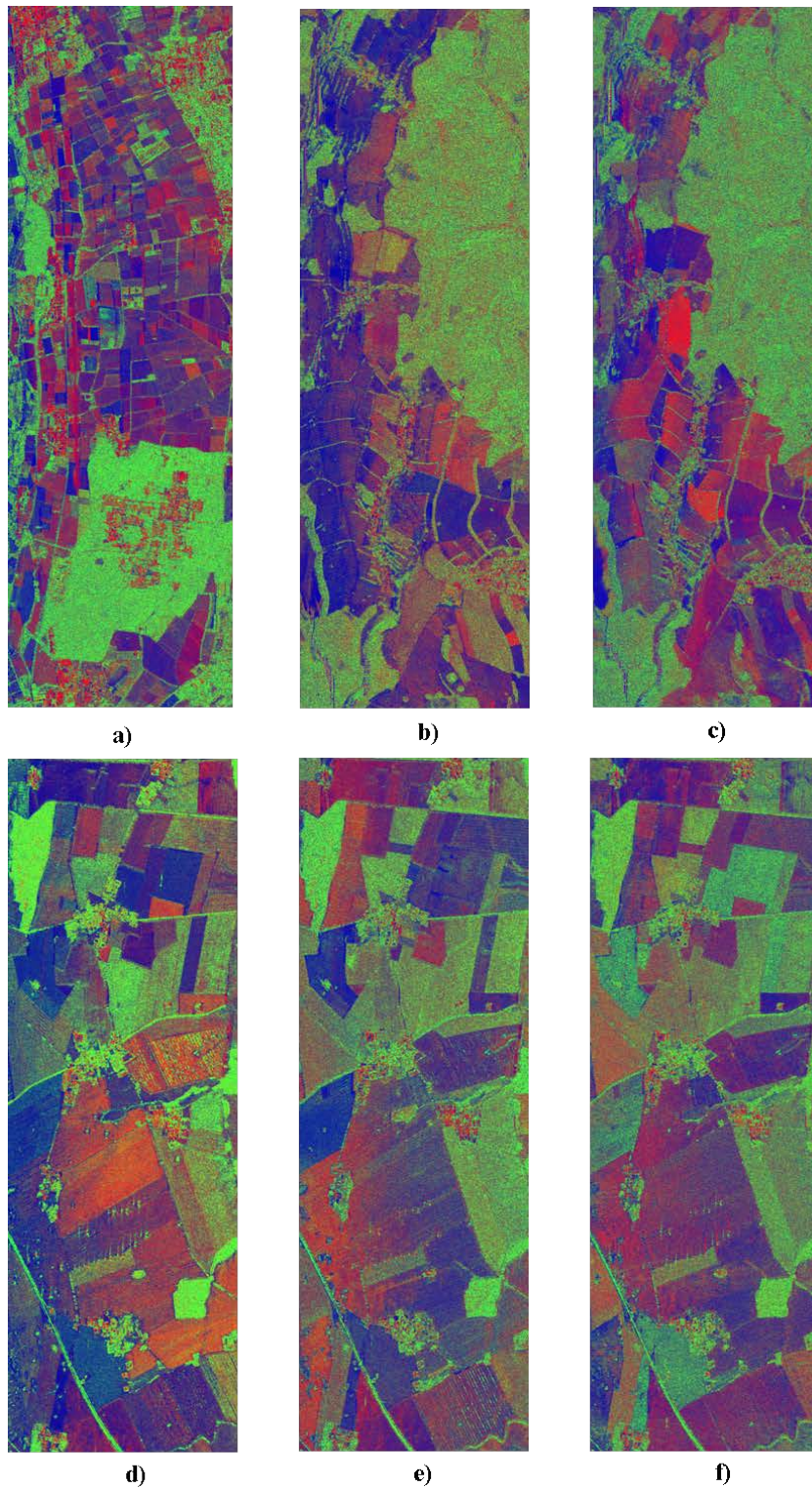


Figure 70: Normalized *Pauli* RGB-images (R: Even bounce scattering, G: Volume scattering B: Odd bounce scattering): a) SARTEO 2008, b) OPAQUE 2008, c) OPAQUE 2007, d) 19th of April, e) 7th of June, f) 5th of July of AgriSAR 2006 campaign.

eas and on strongly vegetated fields due to the presence of the vegetation layer, even bounce (like dihedral stalk-surface) and odd bounce (like surface) scattering occurs predominantly on vegetated and bare soil fields, respectively. This indicates already the applicability of L-band frequency for surface scattering analyses under vegetation cover in agricultural areas.

Table 9: Summary of selected fully polarimetric E-SAR L-Band acquisitions from the AgriSAR, OPAQUE and SARTEO campaigns for experimental data analyses, [23, 148, 149, 122].

Campaign	Test site	Date
AgriSAR	Görmin/E-W track	19.04.2006
	Görmin/N-S track	20.04.2006
	Görmin/E-W track	07.06.2006
	Görmin/N-S track	06.06.2006
	Görmin/E-W track	05.07.2006
	Görmin/N-S track	06.07.2006
OPAQUE	Weisseritz	31.05.2007
	Weisseritz/N-S track <i>master</i>	08.05.2008
	Weisseritz/S-N track <i>opposite</i>	08.05.2008
	Weisseritz/W-E track <i>perpendicular</i>	08.05.2008
SARTEO	Selhausen	27.05.2008

Part 6

Results and validation of soil parameter retrieval with experimental data

In this Chapter experimental L-band data acquired by the airborne E-SAR sensor are used to estimate soil moisture and soil roughness under agricultural vegetation cover. The retrieved soil information is validated with *in-situ* measurements, presented in Part 5, for a quality assessment. In addition, potentials and limitations of the proposed retrieval algorithms are discussed.

6.1. Results for soil moisture

In Part 4 a modular ‘tool box’ of polarimetric decomposition methods for retrieval of soil characteristics was introduced to provide a profound basis for representation of different natural scattering conditions. In summary, four different types of polarimetric decompositions are distinguished within this thesis using state-of-the-art techniques (cf. Chapter 4.1.4.) and newly developed methods (cf. Chapter 4.2.):

1. Eigen-based decomposition introduced in Chapter 3.2.4.1. and 4.1.4.
(e.g. soil moisture and soil roughness inversion over bare soils with the *X-Bragg* model like in [127])
2. Model-based decompositions introduced in Chapter 3.2.4.2. and 4.2.
(e.g. soil moisture and soil roughness inversion over bare and vegetated soils like in [124, 159, 150])
3. Hybrid decompositions representing a combination of eigen-based and model-based decompositions introduced in Chapter 4.2.6.
(e.g. soil moisture inversion over bare and vegetated soils like in [152, 153])
4. Multi-angular model-based decompositions introduced in Chapter 4.2.7.
(e.g. multi-angular soil moisture inversion over bare and vegetated soils like in [155, 151])

In this Chapter these different retrieval methods for soil moisture are applied to the fully polarimetric SAR data of the three study areas described in Part 5.

6.1.1. Results for soil moisture retrieval on bare soil

In Chapter 4.1. a variety of methods for moisture retrieval on bare soil is described covering empirical, semi-empirical and theoretical retrieval algorithms. In order to focus on theoretically-based polarimetric SAR approaches, the results using the inversion algorithm for the *X-Bragg* model are presented in this Chapter, starting with the processing scheme in Figure 71. The algorithm, established by

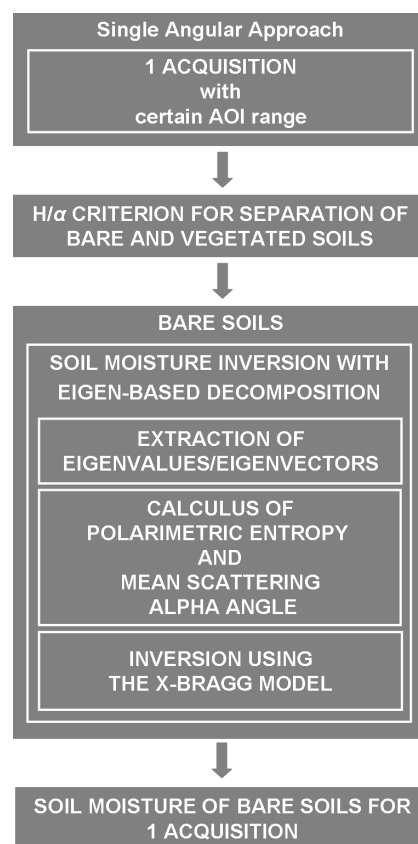


Figure 71: Processing scheme for soil moisture inversion on bare soils using the *X-Bragg* model approach [127].

Hajnsek et al., compares the polarimetric entropy H and the mean scattering alpha angle $\bar{\alpha}$ from the data with H and $\bar{\alpha}$ from the *X-Bragg* model for soil moisture inversion [127]. An $H/\bar{\alpha}$ -criterion is obtained from the *X-Bragg* model of [127] considering the respective local incidence angle θ_l and a maximum soil moisture of 50vol.% to determine the limiting polarimetric entropy and mean polarimetric scattering alpha values for dominant surface scattering. Figure 72 presents the comparison of the data values within the $H-\bar{\alpha}$ scattering plane (cf. Figure 12) with

these maximum boundaries of the modeled values (red frames) for different local incidence angles θ_l .

For all three campaigns in Figure 72, the entropy values of the data are predominantly larger than the boundaries (red boxes) of the modeled entropy values, especially for smaller local incidence angles ($\theta_l < 30^\circ$), which evidences the presence of depolarization that does not only come from soil roughness (considered by *X-Bragg*), but also from the growing vegetation cover (not considered by *X-Bragg*). Therefore, Figure 73 demonstrates that the influence of vegetation causes foremost an increase of entropy within the entropy- $\bar{\alpha}$ scattering plane, when moving from bare soil to forest scattering. In addition, the mean scattering alpha angle approaches 45° with increasing vegetation influence, indicating dipole-like scattering.

After inversion with the *X-Bragg* model, the results for soil moisture are shown in Figure 74 for the early dates in the growth cycle, when the vegetation contribution is assumed to be lower than in the mature stage (June, July). Only very few fields in the scenes are invertible due to the high polarimetric entropy and the medium to high scattering alpha angle $\bar{\alpha}$ of the data, which is especially evident in near range. This can be traced back to the scarcity of bare fields during the vegetation growth season, which is stated by the measured vegetation heights in Table 10. Entire fields can mostly be inverted in far range, as depicted in Figure 74 for the winter triticale field (frame 1) of the OPAQUE campaign in May 2008 and for the sugar beet field (frame 2) of the AgriSAR campaign in April 2006. In these regions the modeled entropy level of *X-Bragg* matches the entropy level of the data, while Table 11 includes the obtained inversion rates for the whole scene. However, the subsequent validation will disclose, if the high entropy can be explained by soil roughness or by the influence of vegetation.

The validation of the bare soil approach with *in situ* measurements is presented in Figure 76 for the AgriSAR, OPAQUE 2008 and SARTEO data. The results for the June and July acquisition of the AgriSAR campaign and the results of the OPAQUE 2007 campaign are not included, because in those cases the disturbance of the distinct vegetation canopy (cf. Figure 55 and Table 3) biases considerably the inversion with the bare soil approach resulting in a too strong overestimation.

For the retrieval of the estimated soil moistures, a 13x13 box around the sampling points leading to 169 looks was taken for comparison, regarding that only boxes with at least 5% invertible pixels were considered to avoid the influence of non-representative outliers (cf. Figure 75). Only some of the investigated fields indicate a very low vegetation cover approaching bare soil conditions (cf. Table

6.1. RESULTS FOR SOIL MOISTURE

Table 10: Inversion results (RMSE, STDDEV) of the *X-Bragg* bare soil approach and mean vegetation height for different crop types of the AgriSAR, OPAQUE and SARTEO campaign [149].

Campaign	Date	Crop type	RMSE	STDDEV ¹	Mean vegetation height [cm]
AgriSAR	19.4.2006	Winter wheat	/	/	18 ²
		Winter rape	/	/	16 ²
		Summer corn	/	/	0 ²
		Sugar beet	13.05	9.20	0
OPAQUE	08.5.2008	Winter triticale	19.91	7.00	23
		Summer oat	/	/	7
		Winter wheat	15.62	8.53	14
		Winter barley	/	/	24
SARTEO	27.5.2008	Winter rye	/	/	17
		Winter barley	/	/	~ 70 ³
		Winter wheat	/	/	~ 30 ³
		Sugar beet	15.18	7.49	~ 10 ³

¹mean of STDDEV of moisture estimates within the sampling boxes,

²combined CAU/ZALF/DLR measurements, ³no direct measurements,

/= too less invertible pixels

Table 11: Inversion rates of the *X-Bragg* bare soil approach for the AgriSAR, OPAQUE and SARTEO campaigns.

Campaign	Date	Inversion rate [%]
AgriSAR	19.4.2006	3.8
	07.6.2006	1.2
	05.7.2006	1.0
OPAQUE	31.5.2007	1.4
OPAQUE	08.5.2008	2.6
SARTEO	27.5.2008	1.3

10). Finally, the vegetation influence enlarges eminently the polarimetric entropy, leading to higher soil moisture values after inversion. The overestimation results in a fairly high Root Mean Square Error (RMSE) as depicted in Table 10. Due to the small rate of invertible pixels for the summer oat field of the OPAQUE 2008 campaign and for the summer corn field of the AgriSAR 2006 campaign (April) the RMSE was not calculated. In addition, the vegetated fields, like winter rape and winter wheat of the AgriSAR campaign (April), winter barley and winter rye of the OPAQUE 2008 campaign as well as winter wheat and winter barley of the

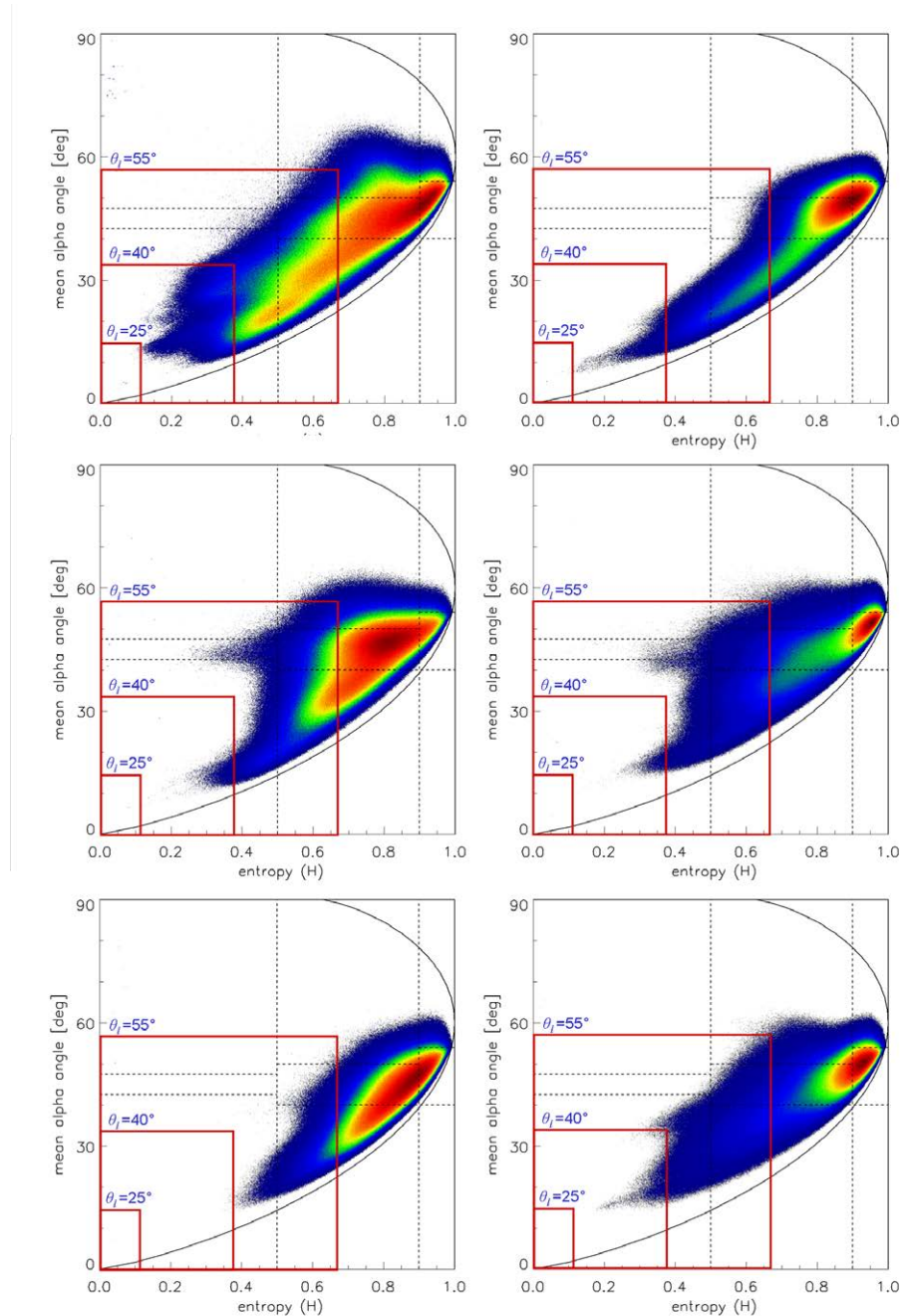


Figure 72: Two dimensional histograms of the $H-\bar{\alpha}$ scattering plane for 19th of April (top left), 7th of June (middle left), 5th of July (bottom left) of the AgriSAR campaign, for 8th of May of the OPAQUE 2008 campaign (top right), for 27th of May of the SARTEO 2008 campaign (middle right) and for 31st of May of the OPAQUE 2007 campaign (lower right) together with X -Bragg model boundaries for three different local incidence angles ($\theta_l = 25^\circ$, 40° and 55°). High counts refer to yellowish/reddish color, low counts to grayish/bluish color.

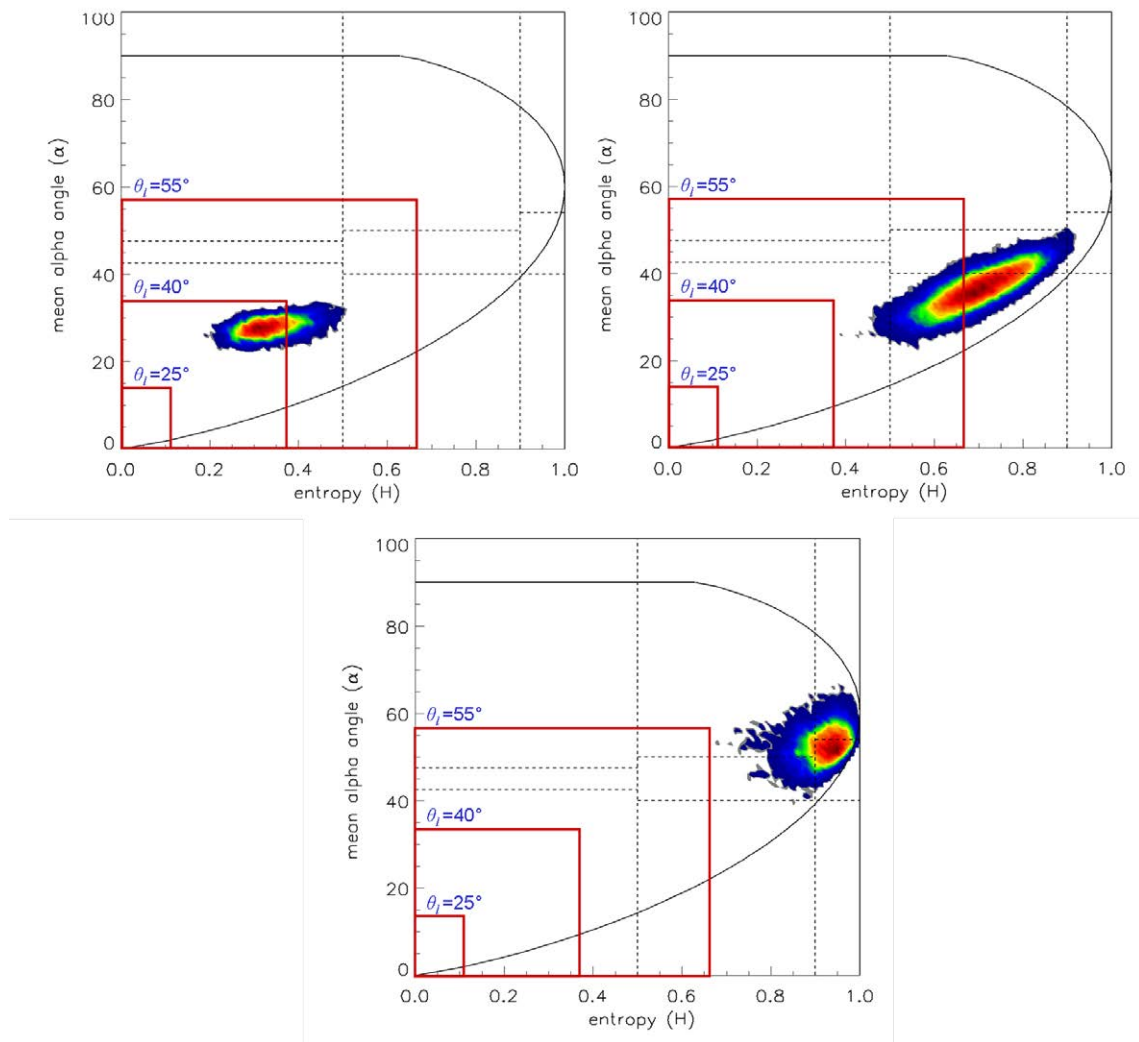


Figure 73: Two dimensional histograms of the $H-\bar{\alpha}$ scattering plane for different types of scatterers within the AgriSAR campaign on 19th of April 2006; Scattering types: Bare soil field 102 (top left), vegetated rape field 140 with 14cm height (top right) and a forest (bottom) together with X-Bragg model boundaries for three different local incidence angles ($\theta_l = 25^\circ, 40^\circ$ and 55°). High counts refer to yellowish/reddish color, low counts to grayish/bluish color.

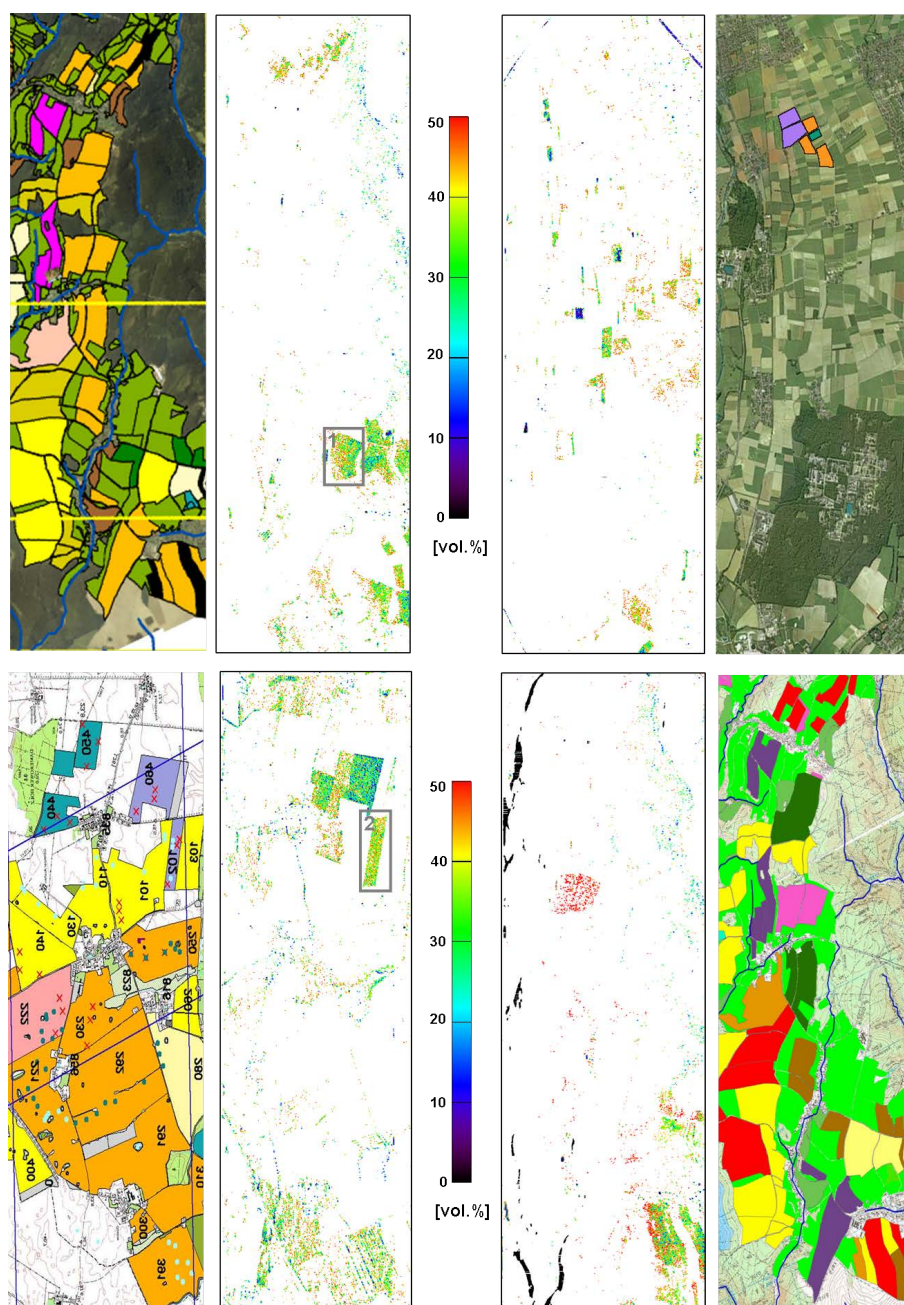


Figure 74: Results of soil moisture inversion using the *X-Bragg* model for the AgriSAR, OPAQUE and SARTEO campaign; (from left to right in 1st row) Land use map of OPAQUE 2008, soil moisture of OPAQUE 2008, soil moisture of SARTEO, land use map of SARTEO (© GoogleMaps), (2nd row) land use map of AgriSAR 2006, soil moisture for AgriSAR in April 2006, soil moisture of OPAQUE 2007, land use map of OPAQUE 2007 (Legend of land use maps: For AgriSAR 2006 in Figure 51, for OPAQUE 2007 in Figure 63, for OPAQUE 2008 in Figure 66, for SARTEO 2008: Green = winter barley, orange= winter wheat, purple = sugar beet. White color represents non-invertible pixels (image smooth: 4x4).

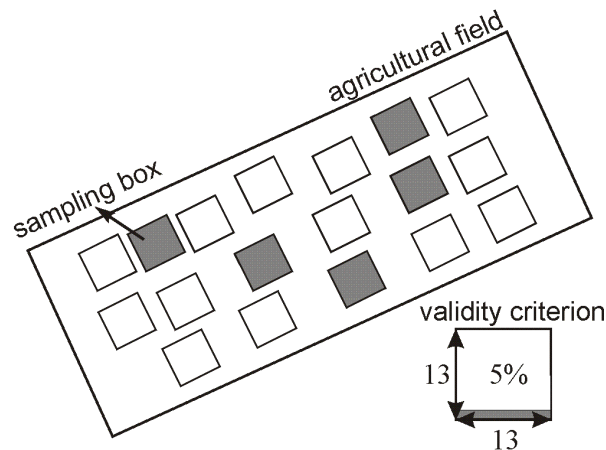


Figure 75: Sampling scheme on test fields for the bare soil inversion using the *X-Bragg* model: 13x13 pixels around each measurement location (squares) form a sampling box. Criteria for a valid sampling box of the validation: 1. Minimum 5% invertible pixels per box; 2. Minimum five valid sampling boxes per field (gray boxes); 3. For field data of the AgriSAR campaign, measured outliers with a deviation of three times the standard deviation of the mean value were excluded.

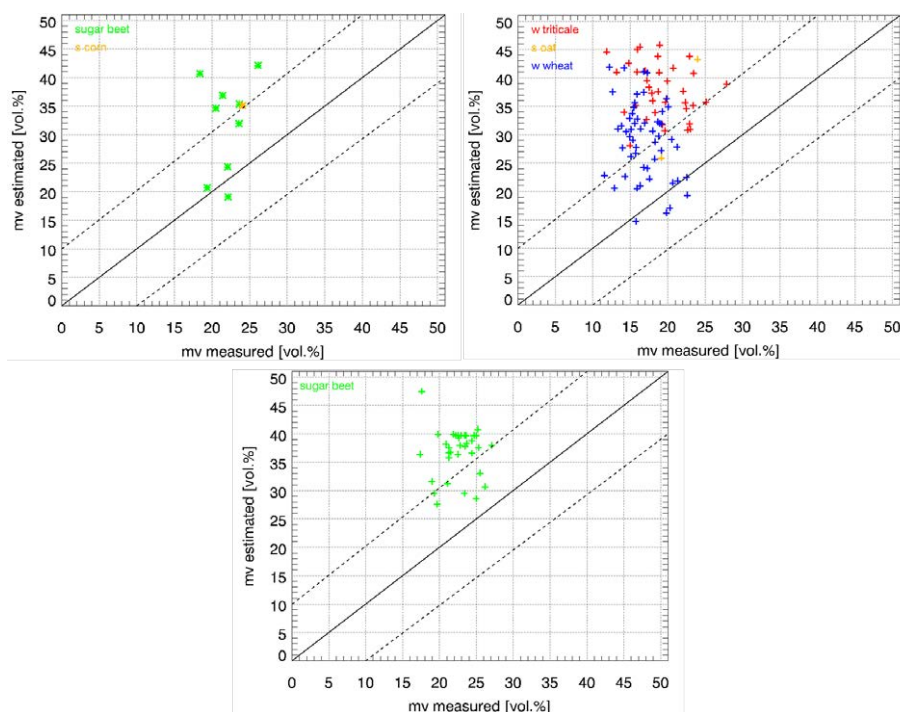


Figure 76: Validation of soil moisture inversion on bare soils using the *X-Bragg* model for AgriSAR data (left: April 2006), for OPAQUE 2008 data (middle) and for SARTEO data (right) compared with field measurements (validation box: 13x13 pixels; Dashed lines indicate the $\pm 10\%$ -interval).



Figure 77: A selection of test fields indicating the diversity of agricultural scattering scenarios along the growing cycle for soil moisture inversion under vegetation cover. From upper left to lower right: Winter barley (May, OPAQUE 2008), winter wheat (May, OPAQUE 2008), summer oat (May, OPAQUE 2008), winter barley (May, SARTEO), winter rape (July, AgriSAR), winter wheat (June, AgriSAR), winter rape (June, AgriSAR), sugar beet (July, AgriSAR), summer corn (July, AgriSAR).

SARTEO campaign, could not be inverted with the *X-Bragg* approach. Therefore the validation results and especially Figure 73 confirm the need of a decomposition for the mixed soil-vegetation PolSAR signature, before applying the *X-Bragg* surface scattering model for inversion of the soil component. In addition, Figure 77 reveals that a variety of agricultural scattering scenarios has to be taken into account along the vegetation growth period in order to invert soil moisture under vegetation cover.

6.1.2. Results for soil moisture retrieval under vegetation cover

In Chapter 4.2. several methods were introduced to decompose fully polarimetric SAR data and to estimate soil moisture under vegetation cover with PolSAR inversion techniques. In the following appropriate combinations of these different methods for each step of the decomposition and inversion algorithm are applied to the acquired PolSAR data.

6.1.2.1. Model-based decomposition

A model-based polarimetric decomposition is applied on the PolSAR data sets using single modules of Chapter 4.2. in a way that is described in the processing scheme of Figure 78 [159]. In a first step an eigen-based decomposition, intro-

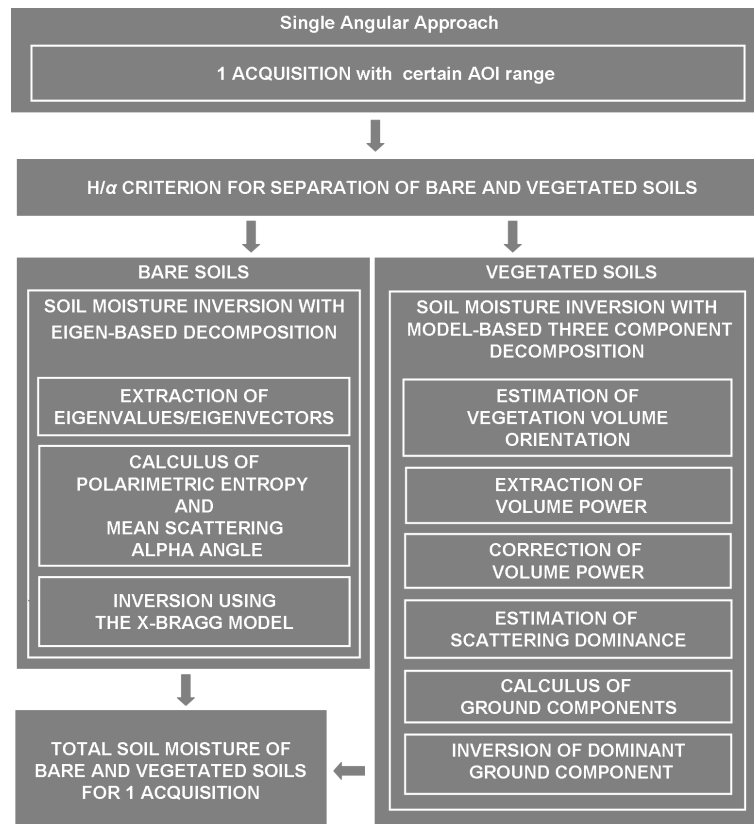


Figure 78: Scheme of model-based polarimetric decomposition technique and inversion algorithm for soil moisture [159].

duced in Chapter 3.2.4.1., is applied to the data in order to calculate the polarimetric entropy (H) and mean polarimetric scattering alpha ($\bar{\alpha}$) values [65]. The $H/\bar{\alpha}$ -criterion, introduced in the previous Chapter 6.1.1., is used to separate dominant surface scattering of bare soils from ground scattering of vegetated soils. Pixels matching this criterion are classified as non-vegetated bare soil pixels and are inverted for soil moisture via the *X-Bragg* inversion approach introduced in Chapter 4.1.4..

For pixels not matching the criterion, a more complicated scattering scenario consisting of ground and vegetation components is assumed, which is characterized

by Equation 219 and introduced in Chapter 4.2. [159].

$$\begin{aligned} \langle [T_{Data}] \rangle = & f_S \begin{bmatrix} 1 & \beta_S^* \text{sinc}(2\psi_1) & 0 \\ \beta_S \text{sinc}(2\psi_1) & \frac{1}{2} |\beta_S|^2 (1 + \text{sinc}(4\psi_1)) & 0 \\ 0 & 0 & \frac{1}{2} |\beta_S|^2 (1 - \text{sinc}(4\psi_1)) \end{bmatrix} + \\ & f_D \cdot m_{d_g}^2 \cdot m_{d_v}^2 \begin{bmatrix} |\alpha_D|^2 & \alpha_D & 0 \\ \alpha_D^* & 1 & 0 \\ 0 & 0 & 0 \end{bmatrix} + f_V \begin{bmatrix} V_{11} & V_{12} & 0 \\ V_{12} & V_{22} & 0 \\ 0 & 0 & V_{33} \end{bmatrix}. \end{aligned} \quad (219)$$

In order to select the orientation of an agricultural vegetation volume, the approach of *Yamaguchi et al.* is applied to model the orientation of the volume, where horizontally oriented, vertically oriented and randomly oriented vegetation components are distinguished [342]. Hence, the volume matrix with the variables $V_{11} - V_{33}$ can be filled with the matrix values of Equations 165 to 167.

After the estimation of the volume orientation and the volume matrix respectively, the volume power f_V is extracted by solving Equation 219 using the selected vegetation volume. As the three component decomposition can lead to negative eigenvalues of the ground components, the volume power f_V is corrected for the different volume orientation cases, as explained in Chapter 4.2.2., using the approach of [320].

After the subtraction of the corrected and selected volume component the ground components are used to estimate the scattering dominance by the criterion, defined in [343] and introduced in Chapter 4.2.3., to set the parameter α_D or β_S in the non-dominant case to zero for reasons of parameter reduction. For the dihedral component, the loss components m_{d_g} and m_{d_v} are incorporated according to Equations 135 and 136. For the surface component, the distribution width accounting for roughness induced depolarization ψ_l is fixed to the empirically defined value of $\pi/12$ to keep the linear system solvable. Focusing on the left image of Figure 79, the result of the polarimetric, model-based decomposition for the OPAQUE 2007 campaign is shown as a RGB-composite of the normalized power components, where the dihedral scattering power is set to red, the volume scattering power is set to green and the surface scattering power is set to blue. Comparing the RGB-composite with the land use map, the forested areas indicate a clear and homogeneous volume scattering signature, whereas on the agricultural fields surface or dihedral scattering are mainly dominant except for the winter rape fields (yellow color in land use map), which also illustrate a distinct volume scattering component due to a dense vegetation layer of approximately 100-120cm height. In addition, there exist also fields, which change their scattering dominance within

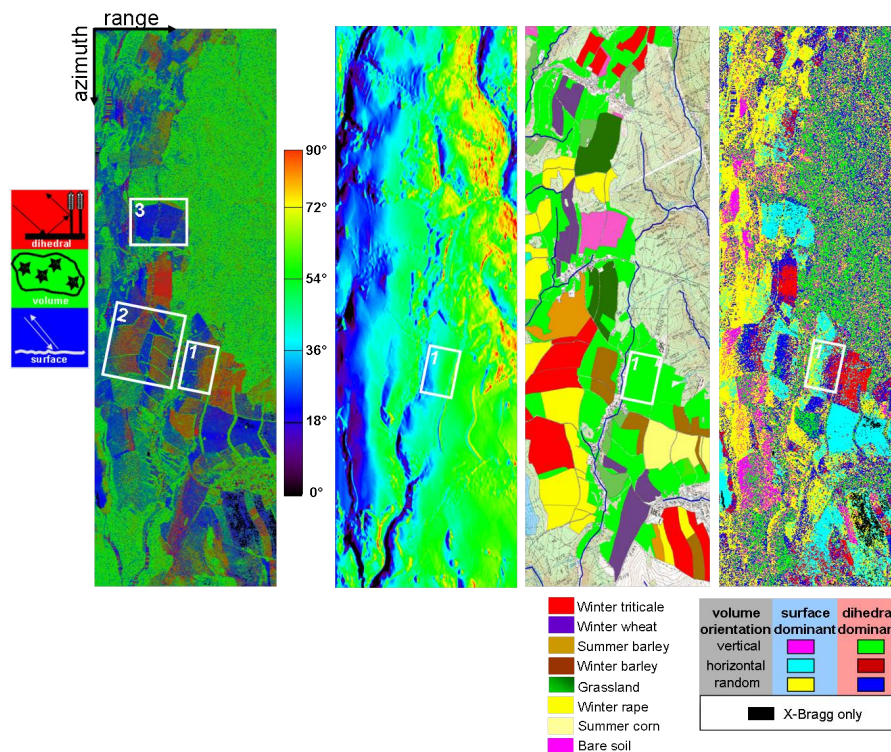


Figure 79: Results of the model-based polarimetric decomposition for the OPAQUE 2007 campaign, (from left to right) 1. RGB-composite of normalized decomposed powers (R: Dihedral, G: Volume, B: Surface), 2. Local incidence angle [$^{\circ}$], 3. Land use map, 4. Decomposition methods used for retrieval of soil characteristics [159].

the field parcel despite the presence of the same crop type. One example is given by a grassland area in the center of the image (frame 1), which changes in ascending range direction from surface to dihedral scattering. Hence, the local incidence angle θ_l in Figure 79 exhibits a clear gradient within the grassland area from steep angles of 25° to shallower angles of 55° , which constitutes the influence of topography on the scattering dominance.

For the OPAQUE 2007 campaign, the scene was acquired on the 31st of May 2007, when most of the agricultural areas were already fully covered by vegetation (Table 12 states more than 50cm vegetation height for the winter crops). Therefore the dihedral scattering (red color in RGB-image) is clearly visible, which can be detected on the winter triticale and winter barley fields in the middle of the image (frame 2). Furthermore, the bare soil fields show a clear surface dominance (frame 3), which states the logic correctness and the physical relevance of the model-based decomposition in agricultural areas.

In Figures 80 and 81 the decomposition results for the AgriSAR 2006, for the OPAQUE 2008 and for the SARTEO campaign are presented. For the analysis of

the AgriSAR data, a date in the beginning (April), in the middle (June) and in the end (July) of the vegetation growth period is selected to analyze the behavior of the model-based decomposition algorithm with growing vegetation cover. In general the volume component is constantly increasing along the growing period in Figure 80 due to the rising complexity of the plant scattering scenario, especially on the winter rape fields. The normalized decomposition powers (1st row)

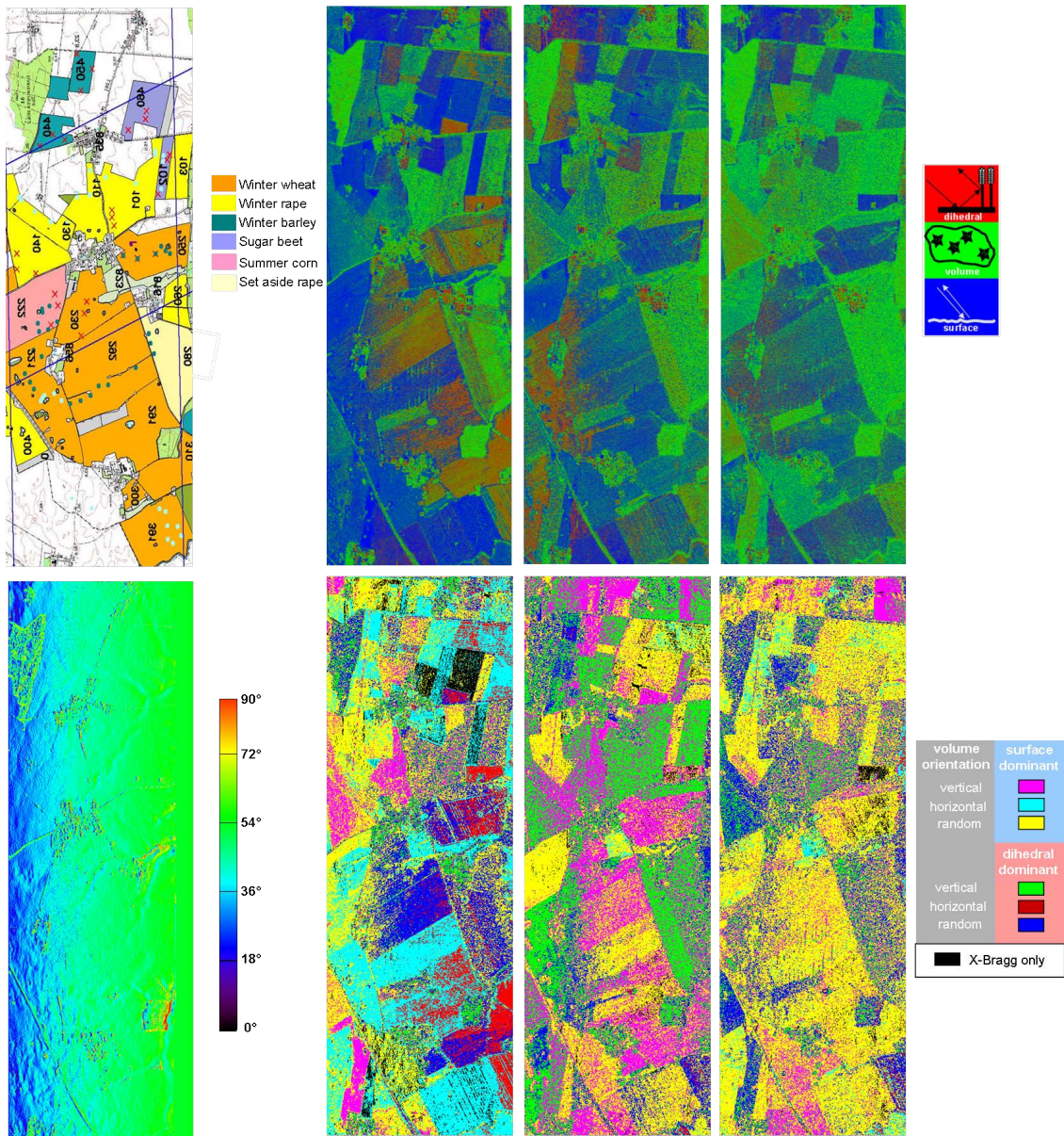


Figure 80: Results of the model-based polarimetric decomposition for the AgriSAR 2006 campaign (from left to right); 1st row: Land use map and RGB-composite of normalized decomposed powers (R: Dihedral, G: Volume, B: Surface) for 19th of April, for 7th of June and for 5th of July 2006; 2nd row: Local incidence angle and decomposition methods for 19th of April, 7th of June and 5th of July 2006.

6.1. RESULTS FOR SOIL MOISTURE

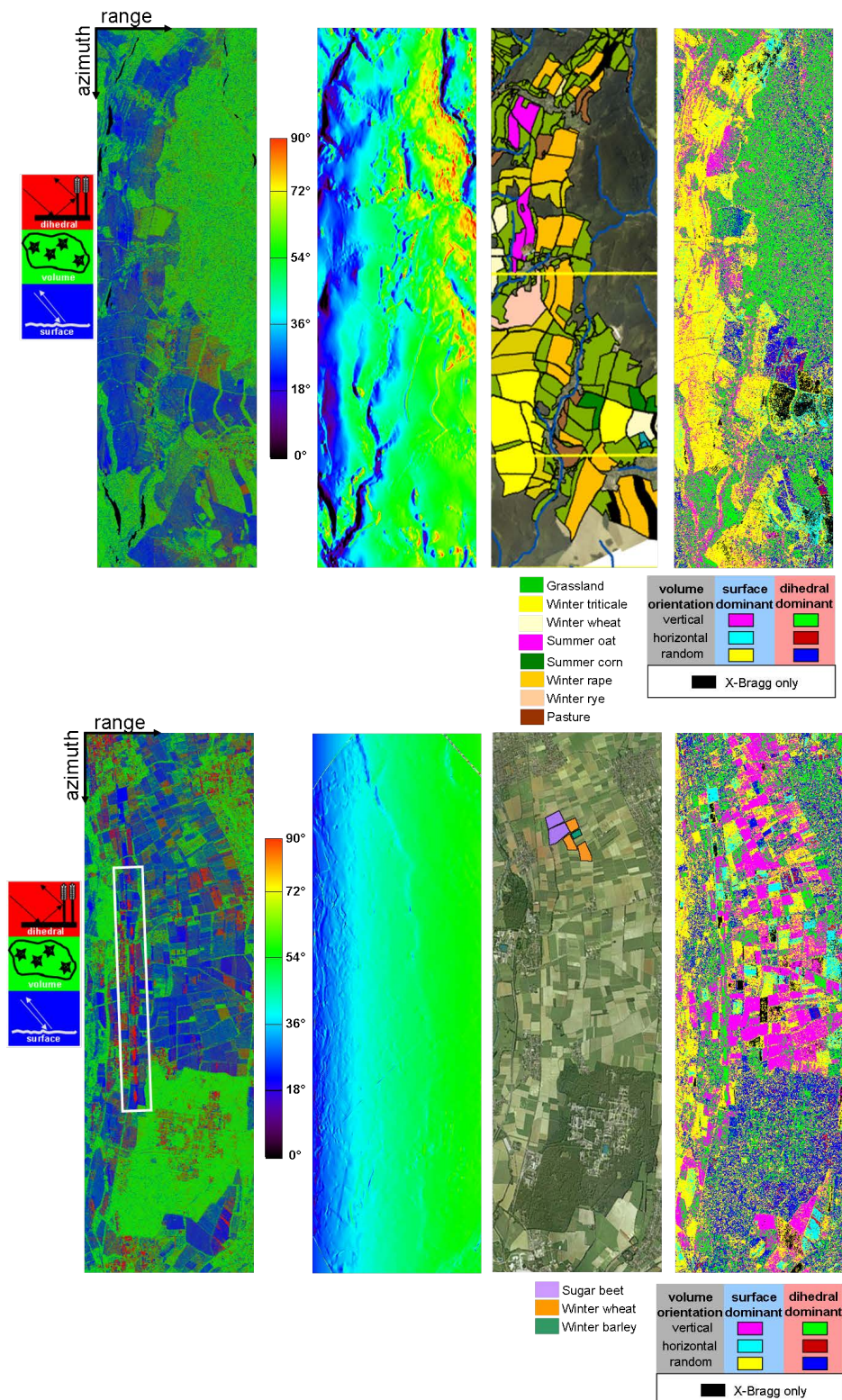


Figure 81: Results of the model-based decomposition for the OPAQUE 2008 (1st row) and SARTEO (2nd row) campaign (from left to right): RGB-composite of normalized decomposed powers (R: Dihedral, G: Volume, B: Surface), local incidence angle, land use map and decomposition methods.

and the decomposition methods (2nd row) justify a variety of scattering scenarios appearing along the growing season, which are reflected well by the model-based decomposition. Especially for the end of the growth period (5th of July) the winter wheat fields (orange color in land use map) appear as surface and not dihedral scatterers, which is not expected at a vegetation height of ~ 80 cm. The solution might be given by a dry weather period, where the last rain was recorded on the 26th of June (cf. Appendix D). The vegetation water content within the wheat plants decreased significantly to about 65% making the vegetation canopy more or less transparent for L-band waves. Therefore a distinct water content in the plant stalks is missing to induce a dihedral reflection with the soil and the vertical plant stalks.

For the OPAQUE 2008 data in Figure 81, the image of the normalized decomposition powers indicates an earlier growth status of the vegetation with mainly surface dominant scattering compared to the advanced phenological situation with a more closed vegetation canopy for the OPAQUE 2007 data (showing already dihedral scattering in Figure 79). This also reflects into the decomposition methods, where the majority of the agricultural areas are decomposed using a random vegetation volume accounting for a soil covering plant structure in the phenological stage of leaf development (cf. Figure 4 as well as Appendix B for phenology and Table 5 for vegetation height of the test fields within the OPAQUE 2008 campaign). Moreover, the acquisition of the SARTEO campaign in May 2008 indicates a medium to low vegetation cover, where surface scattering dominates on the agricultural fields (cf. Figure 81). The vegetation component is mostly characterized as randomly or vertically oriented pointing towards a phenological phase of stem elongation (cf. Figure 4 and Appendix B). Unfortunately, no direct vegetation measurements were taken during this campaign.

In the end, the decomposition results of all campaigns indicate a physically meaningful decomposition of the scattering signal in agricultural areas for a variety of crop types and phenological conditions along the growth season.

6.1.2.2. Inversion and validation of surface and dihedral components

Depending on the scattering dominance either the dihedral or the surface component is inverted for soil moisture, following the procedures explained in Chapter 4.2.5.. For the final result of the soil moisture retrieval, the estimated soil moistures from the bare soil areas with the *X-Bragg* approach and from the vegetated soil areas (surface and dihedral) with the ground components of the model-based decomposition are unified in one total soil moisture result. This unified result is

depicted in Figures 82 - 84 for the OPAQUE 2007, AgriSAR 2006, OPAQUE 2008 and SARTEO 2008 campaign, respectively. All displayed soil moisture images are scaled from 0vol.% to 50vol.%, in which the areas colored in white represent non-invertible regions.

Beginning with the analysis of Figure 82 for the OPAQUE 2007 campaign, the inversion of soil moisture from the *X-Bragg* approach reveals that the areas classified for this approach are relatively sparse and are mostly located in the far range region, as already stated in Chapter 6.1.1.. An exception are the black areas along azimuth direction which exhibit very steep incidence angles ($\theta_l < 5^\circ$), which can be considered as invalid due to the extremely low moisture value. The level of inverted soil moisture values is high, which can be explained by the relatively low values of polarimetric entropy and of mean scattering alpha angle modeled with the *X-Bragg* model compared to the high values of polarimetric entropy and of mean scattering alpha angles from the data, which is in accordance with the results in Chapter 6.1.1. (cf. Figure 72).

Soil moistures, retrieved from the surface and dihedral scattering components of the three component model-based decomposition, exhibit different densely inverted land use classes, which result from the scattering dominance specified in the model-based decomposition (cf. Figure 79). Hence, for the inversion from the surface component, the summer corn fields on the lower right of the image (frame 1), which were only sparsely vegetated at the acquisition date, demonstrate a spatially complete inversion result. In addition, the inversion from the dihedral component indicates a quite complete inversion for the winter triticale (frame 2) and the winter barley (frame 3) fields, which grew already to a vegetation height of more than 60cm causing a distinct dihedral scattering component.

The combined results of all inverted soil moisture approaches in Figures 82-84 exhibit that major parts of the forested areas show a sparse inversion due to restrictions of the polarimetric scattering models, which fit only for agricultural regions at L-band. In addition, a long stretched region in near range illustrates a lack of inversion for the two OPAQUE data sets, which might be explained by comparison with the local incidence angle within these regions of missing inversion (cf. Figures 79 and 82 for the OPAQUE 2007 campaign as well as Figures 81 and 84 for the OPAQUE 2008 campaign). The angles are below 20° local incidence, which reduces strongly the observable space of polarimetry and limits the inversion.

For the AgriSAR campaign the inverted soil moisture is depicted in Figure 83, including the three dates along the growing season together with the land use information. The inversion rates for the three dates along the growth cycle, which

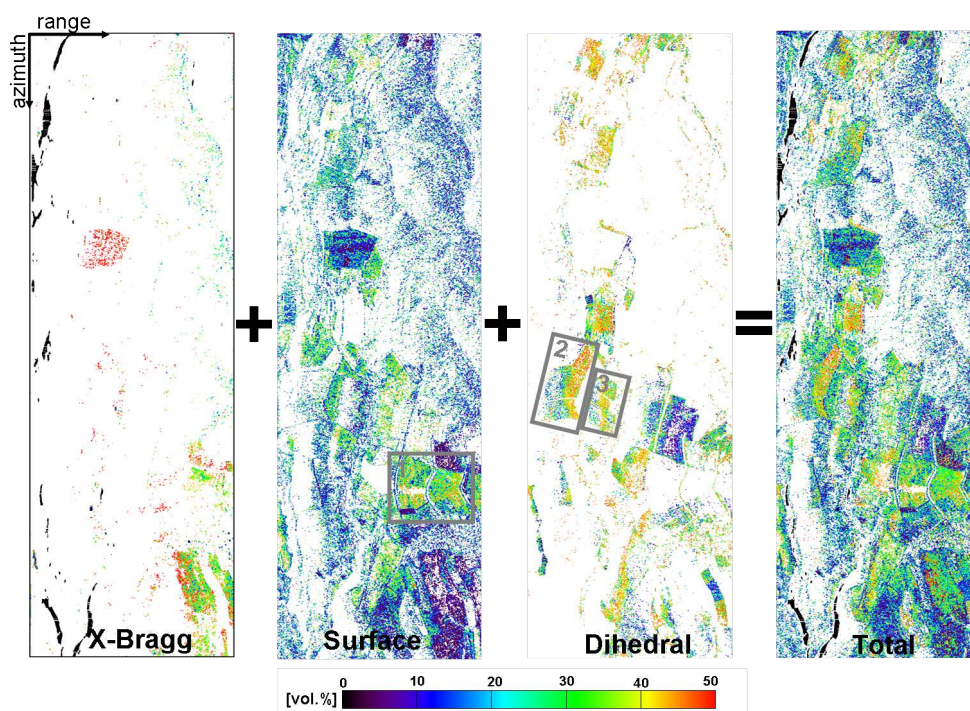


Figure 82: Estimated soil moisture of the *X-Bragg* approach (on bare soils), the surface and the dihedral component of the three component model-based decomposition (on vegetated soils) for the OPAQUE 2007 campaign. ‘Total’ presents the combined soil moisture result of all components. White color represents non-invertible pixels (image smooth: 4x4) [159].

range from 25% in June to 35% in April, are reported in Table 13. In Figure 83 the majority of non-invertible regions (white color) appear within the June acquisition, when the vegetation was almost fully grown for the winter crops (cf. Figures 55 and 56). This effect is explicitly pronounced for the winter rape fields with a vegetation height of about 150cm, whereas it is less noticeable for the other two acquisitions. Reasons might be on one hand the low vegetation height of less than 30cm for the April acquisition and on the other hand a distinct, but more dry and therefore transparent, vegetation canopy for the July acquisition. Hence, the used vegetation model within the applied model-based approach is not adapted sufficiently well to the different scattering scenarios along the crop cycle, which has the greatest impact on the winter rape fields with their complex plant geometry of a stalk and a bean layer (cf. Figure 77).

In addition, the inversion on the dihedral dominant scattering parts (cf. Figure 83 and decomposition methods in Figure 80) show a distinct overcompensation for the June and July acquisitions using the combined vegetation attenuation/roughness scattering loss $m_{d_g}^2 \cdot m_{d_v}^2$ (cf. Equation 219), which in particular

6.1. RESULTS FOR SOIL MOISTURE

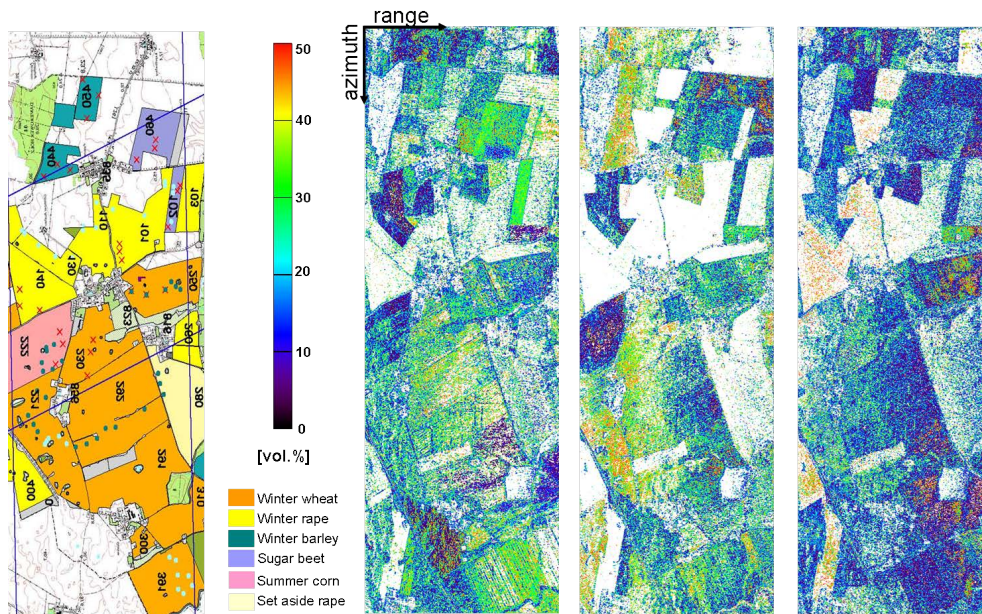


Figure 83: Land use map and estimated soil moisture of the *X-Bragg* approach (on bare soils), the surface and the dihedral component of the three component model-based decomposition (on vegetated soils) for 19th of April, for 7th of June and for 5th of July of the AgriSAR 2006 campaign. White color represents non-invertible pixels (image smooth: 4x4).

hampers the inversion of the winter rape fields of the AgriSAR campaign.

For the OPAQUE 2008 and the SARTEO campaign, the inverted soil moisture is presented in Figure 84. The regions of steep local incidence (near range) and the forested regions within the inversion result for both campaigns evince the known lack of inversion, for reasons already discussed with the OPAQUE 2007 data (cf. Figure 82). The inversion rates for the OPAQUE 2008 and the SARTEO campaign amount to 24% and to 25%, respectively (cf. Table 13). The agricultural regions reveal a more or less complete inversion on agricultural fields, which are classified as randomly oriented in Figure 81. This is mostly the case for the vegetation of the OPAQUE 2008 campaign, where only the winter rape fields exhibit a dihedral dominant scattering signal indicating a stalk-dominated vegetation geometry. The inversion failed for this crop type due to the aforementioned reason of an over-compensation in the dihedral scattering power caused by a too strong correction of the attenuation loss. Besides, the dihedral reflections of a power line (white frame) in Figure 81 for the SARTEO campaign lead to a linear feature in the soil moisture image, which is in this way not soil related and invertible, respectively. A second reason for low inversion rates on some fields of the SARTEO acquisition might be given by the different orientation cases found by the decomposition algorithm and depicted in Figure 81. As the selection of the volume orientation is

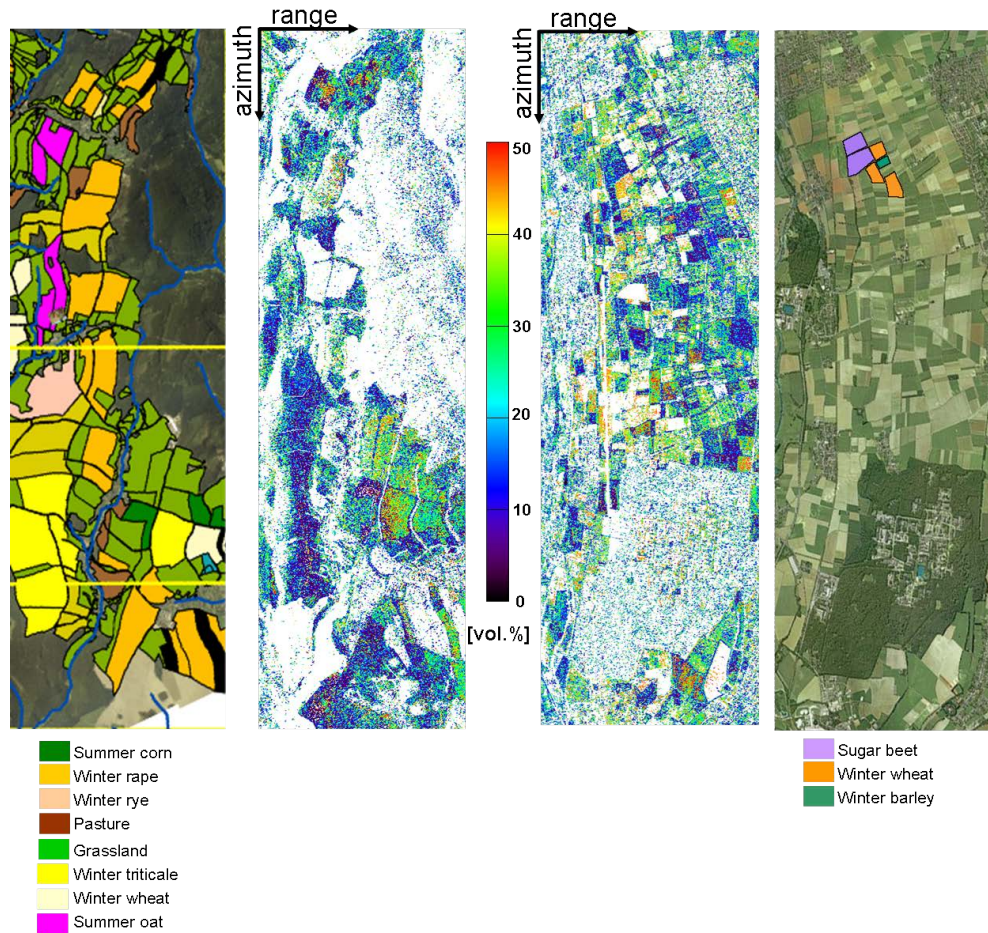


Figure 84: Land use map and estimated soil moisture of the *X-Bragg* approach (on bare soils), the surface and the dihedral component of the three component model-based decomposition (on vegetated soils) for the OPAQUE 2008 (left) and for the SARTEO (right) campaign. White color represents non-invertible pixels (image smooth: 4x4).

based on thresholds of a polarization power ratio (cf. Equation 164), the empirically set thresholds might not always lead to the optimum choice.

In a next step the estimated soil moisture values are validated for evaluation of the inversion performance starting with the OPAQUE 2007 campaign. The validation compares soil moisture values, averaged spatially from ground measurement points in 0-10cm depth (top soil layer), with the estimated soil moisture values from bare and vegetated soils. For the ground measurements within the OPAQUE 2007 campaign, mobile FDR-probes were used, whereas for the retrieval of the estimated soil moistures the same sampling strategy, introduced in Figure 75, is applied.

The seven different crop types winter wheat, winter triticale, winter barley, winter rape, summer corn, summer barley and grassland are used for analyses of

6.1. RESULTS FOR SOIL MOISTURE

soil moisture estimation under vegetation cover, where the vegetation characteristics are described in Table 12. In Figure 85 the comparison between measured and estimated soil moisture values for the seven different crop types is displayed together with the RMSE and the mean of the STDDEVs of the estimated soil moisture values within the sampling boxes. In Table 12 the RMSE of the estimated soil

Table 12: Vegetation characterization and inversion results (RMSE, STDDEV) on seven different test fields for the OPAQUE campaign in May 2007, [159].

Fields	Plant height [cm]	Row distance [cm]	Wet biomass [kg/m ²]	STDDEV ¹ [vol.%]	RMSE [vol.%]
Winter wheat	55	10	2.85	10.63	8.46
Winter barley	70	10	3.31	13.06	11.09
Winter triticale	85	10	3.34	10.70	9.98
Winter rape	135	18	6.52	11.43	20.16
Summer corn	16	75	0.1	11.44	7.32
Summer barley	45	23	0.93	13.08	9.37
Grassland	27	10	1.13	8.53	8.75

¹mean of STDDEV of moisture estimates within the sampling boxes

moistures from all investigated crop types exhibits an accuracy of 8.5-20.2vol.% for the OPAQUE 2007 data. Furthermore, a mean standard deviation of the estimated soil moistures of 8.5-13.1vol.% (OPAQUE 2007) indicates a broad range of inverted moisture values (cf. Table 12). Reasons for this might be on one side the complex and spatially highly varying scattering scenario inverted with a limited number of observables and on the other side the characteristics of soil moisture itself, which is also varying distinctly over one field parcel. A detailed, field-based analysis is given as follows:

The estimated soil moisture values on the winter wheat and summer corn fields show no significant trend and over- and underestimate the measured soil moisture in Figure 85. For the winter rape, the winter barley and the summer barley fields, an underestimation is visible in Figure 85, caused by the inverted soil moisture values of the surface component under a vegetation canopy from 45cm (summer barley) up to 135cm (winter rape). This can be linked to a β_S -parameter, that is too small after removal of the volume component. In conclusion, the modeling of the vegetation volume within this retrieval approach is still not satisfactory and has to be re-examined in the subsequent approaches.

On the other hand, soil moisture values from the winter triticale and the grassland field are mostly inverted from the dihedral scattering component and depict an overestimation, which is induced by the already suspected overcompensation of

the combined vegetation attenuation/roughness scattering loss ($m_{d_g}^2 \cdot m_{d_v}^2$), which is also directly retrieved from the PolSAR data itself. In this way, the parameter

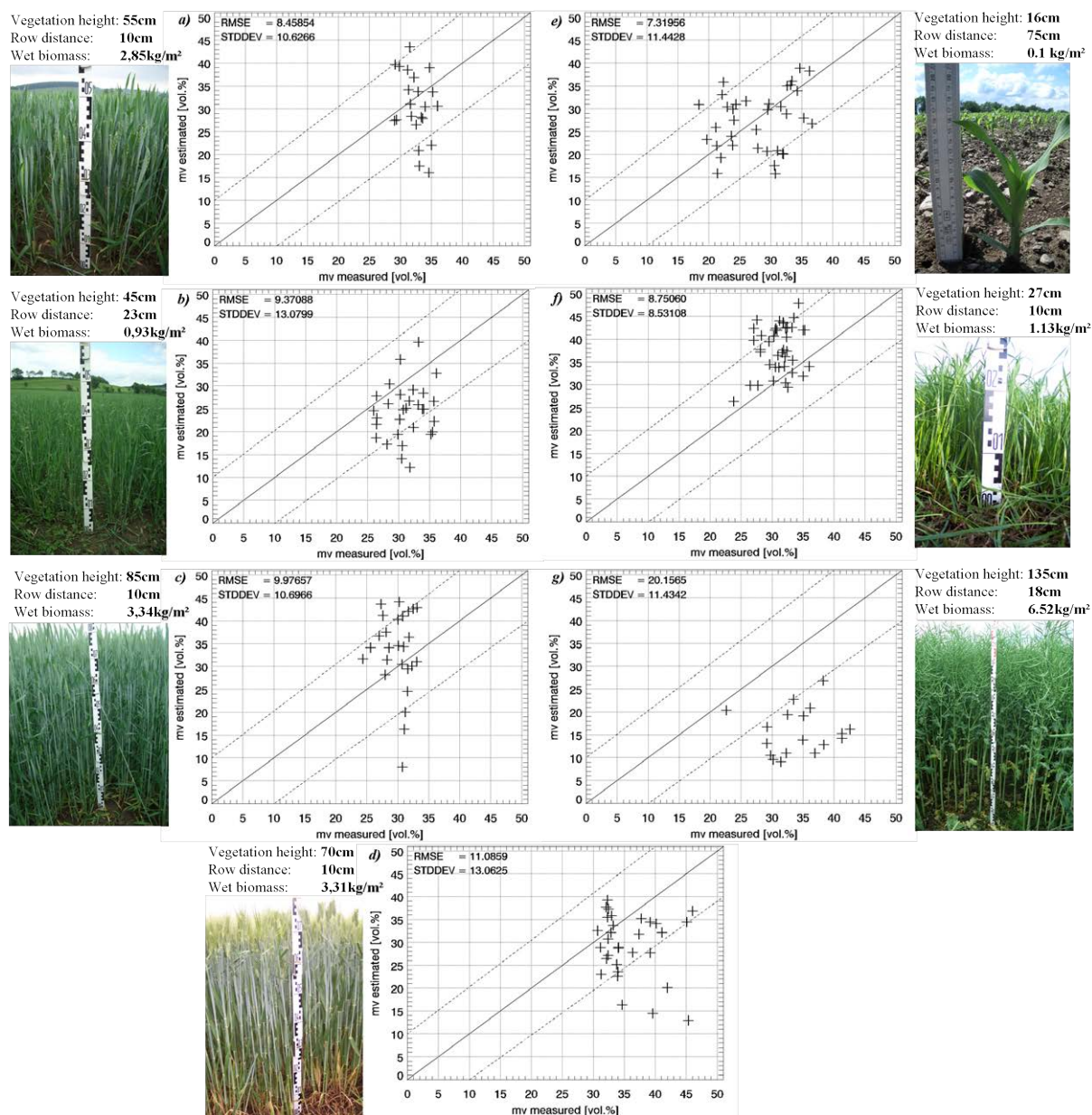


Figure 85: Comparison between measured and estimated soil moisture values from the model-based approach for winter wheat (a), summer barley (b), winter triticale (c), winter barley (d), summer corn (e), grassland (f), winter rape (g) of the OPAQUE 2007 campaign; RMSE = root mean square error of soil moisture inversion; STDDEV = mean of STDDEV of moisture estimates within the sampling boxes [159].

space is kept constant and analytically solvable, but the loss factor within the di-hedral component will be adapted for the following retrieval approaches.

Moreover, Figure 86 and Table 13 represent the validation of the model-based

6.1. RESULTS FOR SOIL MOISTURE

decomposition and soil moisture inversion approach of Chapter 6.1.2.1. for the AgriSAR, OPAQUE 2008 and SARTEO campaign. The validation was conducted in

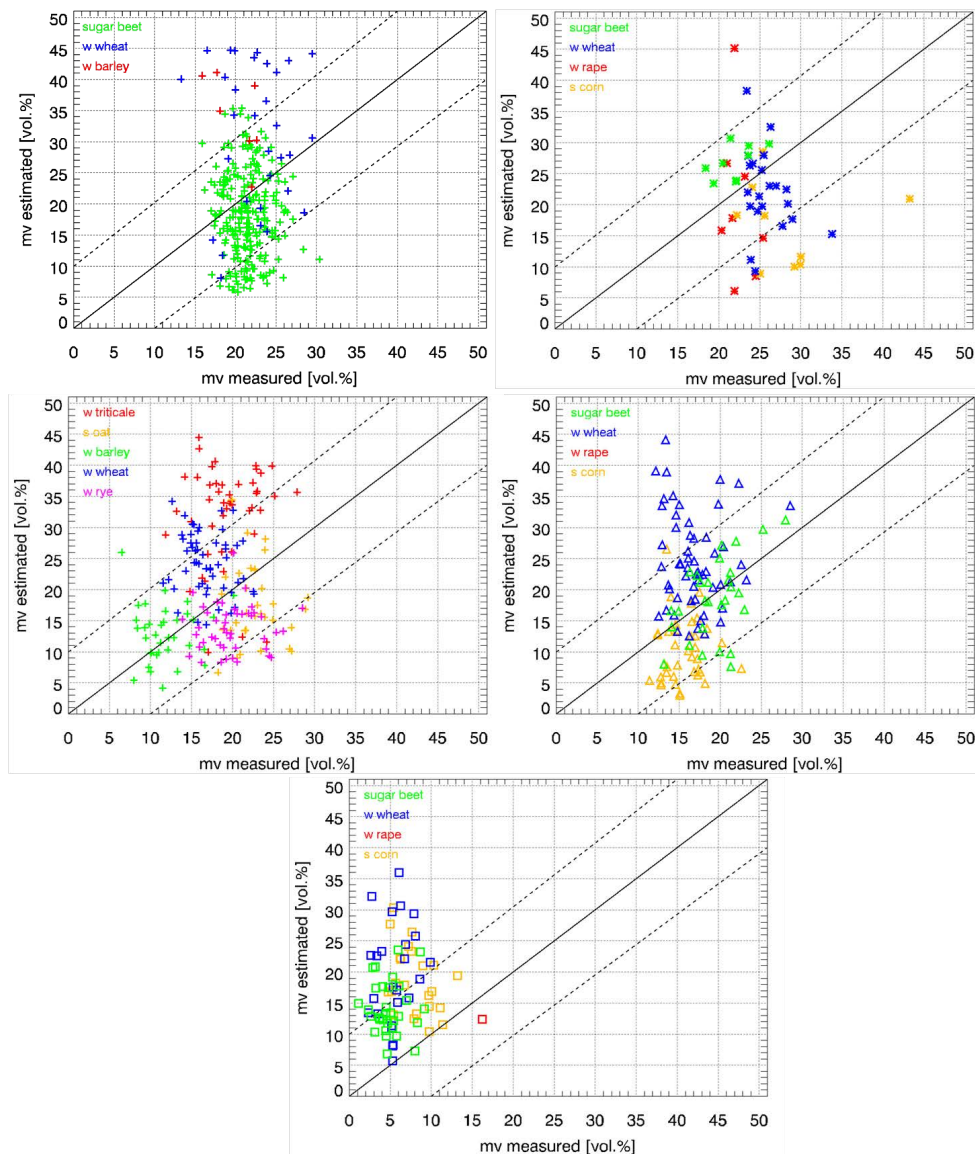


Figure 86: Comparison between measured and estimated soil moisture values from the model-based approach for different crop types of the SARTEO 2008 campaign (top left), of the OPAQUE 2008 campaign (middle left) and of the AgriSAR 2006 campaign (top right: 19th of April, middle right: 7th of June, bottom: 5th of July).

the same way as presented in Figure 75. Compared to the validation of the bare soil inversion algorithm using the *X-Bragg* model (cf. Figure 76), the results of the model-based decomposition and inversion approach for bare and vegetated soils evidences a distinctively lower level of RMSE and a significantly higher inversion rate in Figure 86 and Table 13. However, a detailed analysis of the different crop types reveals that the inverted soil moisture values of the summer crops are mostly

Table 13: Quality assessment of inversion results with the model-based approach including all investigated crop types for the AgriSAR 2006, OPAQUE 2008 and SARTEO 2008 campaign.

Date	RMSE [vol.%]	STDDEV ¹ [vol.%]	Inversion rate [%]
AgriSAR 19.4.2006	10.37	12.38	35
AgriSAR 07.6.2006	9.19	12.06	25
AgriSAR 05.7.2006	13.04	12.38	30
OPAQUE 08.5.2008	10.11	13.01	24
SARTEO 27.5.2008	8.59	10.31	25

¹mean of STDDEV for moisture estimates within the sampling boxes

inside the ± 10 vol.%-interval, whereas the soil moisture inversion of the winter crops with a more pronounced vegetation cover generates mostly an overestimation. This is caused by an insufficient vegetation volume characterization, by a deficit in the separation between vegetated and bare soils (e.g. overestimation for AgriSAR 5th of July acquisition and for the winter triticale field of OPAQUE 2008 acquisition) and by an inversion of the dihedral component, which used a vegetation attenuation/roughness scattering loss (e.g. overestimation for winter crops of the SARTEO acquisition). Moreover, the inversion for the 5th of July within the AgriSAR campaign revealed the strongest RMSE of 13.04vol.%, exhibiting a very low moisture level (1-12vol.%) together with the largest vegetation cover (vegetation height: ~ 70 -170cm). In the next chapters, further investigations are necessary to test additional approaches of modeling the volume disturbance and the dihedral loss component as well as to study the influence of topography on the inversion of soil moisture, in order to overcome the limits in soil moisture retrieval for regions with steep local incidence angle.

6.1.2.3. Inversion and validation of surface and dihedral components using *Pauli*-based ground-to-volume ratios

One of the major problems concluded from the last Chapter 6.1.2.2. is posed by the characterization of the vegetation volume scattering, which is mainly embodied in the cross-polarized scattering component S_{XX} . This component is characterized in agriculture by a mixed scattering response of the vegetation cover and the soil roughness. Normalized *Pauli*-based ground-to-volume scattering ratios Pa are derived directly from the polarimetric SAR data, as introduced in Equation 176, for splitting the cross-polarized component into a roughness and a vegetation contribution (cf. Figure 38). Figure 87 displays exemplarily the normalized surface

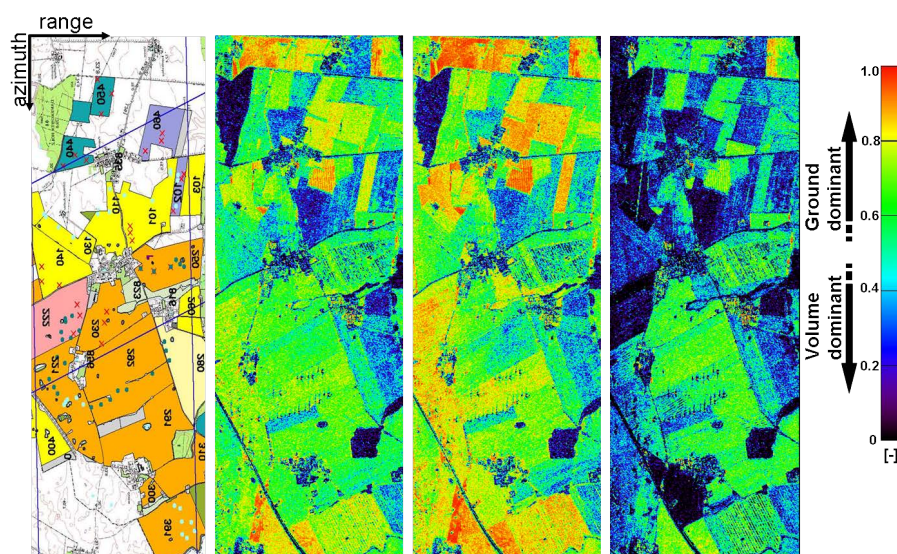


Figure 87: Normalized *Pauli*-based ground-to-volume ratios for 19th of April 2006 of the AgriSAR campaign (from left to right): Land use map of AgriSAR 2006 campaign, combined ground-to-volume ratio Pa_G , surface ground-to-volume ratio Pa_S and dihedral ground-to-volume ratio Pa_D [150].

and dihedral ground-to-volume ratios for the 19th of April 2006 of the AgriSAR campaign, where volume scattering indicates a normalized *Pauli*-based ground-to-volume ratio close to zero and pure ground scattering a ratio close to one. Due to reasons of space the normalized *Pauli*-based ground-to-volume ratios for all other acquisitions are presented in Appendix F.

For all campaigns soil moisture was estimated according to the method introduced in Chapter 4.2.5.3. and is shown in Figures 88 and 89, where the roughness depolarization parameter (ψ_l) and the soil roughness (ks) were acquired from Equations 217 and 218 as a pre-processing step and were incorporated in the soil moisture retrieval from the surface and the dihedral component (surface: ψ_l , dihedral: m_{d_g}). The soil moisture inversion results for all campaigns are scaled from 0vol.% to 50vol.% and non-invertible pixels are masked white. For the AgriSAR campaign, a distinct difference in soil moisture level is observed between the beginning of the growing season in spring (19th of April) compared to the end of the growing season in summer (5th of July), which can also be confirmed by analyses of the soil moisture measurements on the test fields (cf. Figures 52-54). Furthermore, in the inverted moisture results of Figure 88 the acquisition of the 19th of April exhibits a considerably reduced inversion rate on the winter wheat fields (orange color in land use map), which can be explained by the dihedral dominance, selected by the criterion of *Freeman and Durden* (cf. Table 2 and Figure 39). But in the early

stage of the vegetation growth period the stalks of the wheat plants were not developed yet. Thus the selected dihedral inversion led to non-physical results on these fields.

Moving to the OPAQUE and SARTEO campaigns, the soil moisture inversion results in a considerable increase in inversion rate (34% for OPAQUE 2007, 39% for SARTEO and 40% for OPAQUE 2008) compared to the previous approach of Chapter 6.1.2.2.. The inverted soil moisture for bare and vegetated soils is depicted in

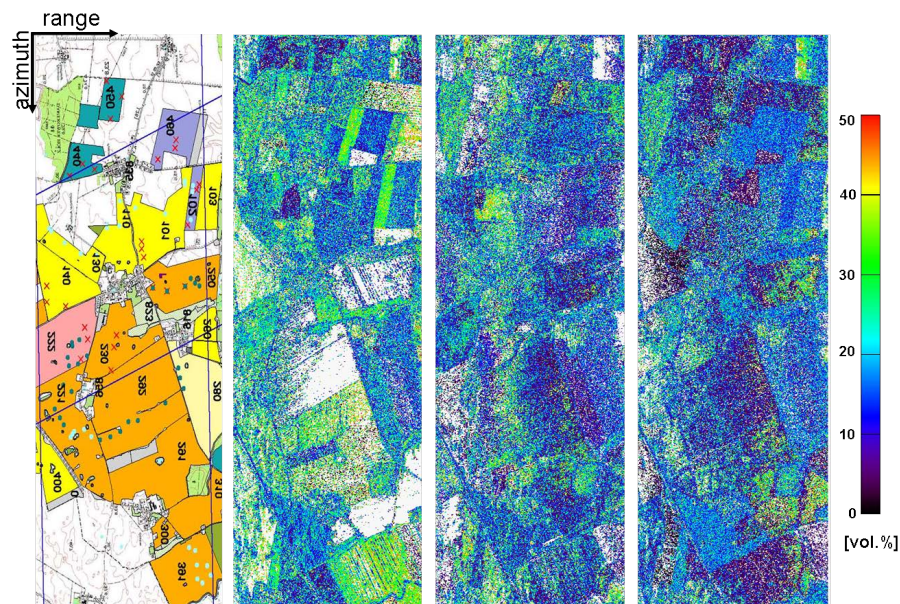


Figure 88: Inverted soil moisture for the AgriSAR 2006 campaign applying the model-based approach with normalized *Pauli*-based ground-to-volume ratios for the entire vegetation growth period (from left to right): Land use map of AgriSAR campaign, soil moisture for 19th of April, for 7th of June and for 5th of July 2006 (image smooth: 4x4) [150].

Figure 89 for the OPAQUE and SARTEO campaigns. In comparison with the results of Chapter 6.1.2.1., the largest increase of invertible pixels takes place in the forested areas and the winter rape fields (frame 1 in Figure 89). Hence, both represent land use classes with a strong volume component, which seem to be better separated including the normalized *Pauli*-based ground-to-volume ratios. Furthermore, the newly developed ratio of Equation 201, replacing the *X-Bragg* bare soil inversion approach, evinces a more homogeneous inversion (frame 2 in Figure 89) than for the former approach in Figure 84. In order to assess the inversion quality, the validation between measured and estimated soil moistures is shown in Figure 91 for the AgriSAR, the OPAQUE and the SARTEO campaigns including a variety of summer and winter crops. Moreover, the sampling strategy for the validation is explained in Figure 90. The RMSE between the measured and the estimated

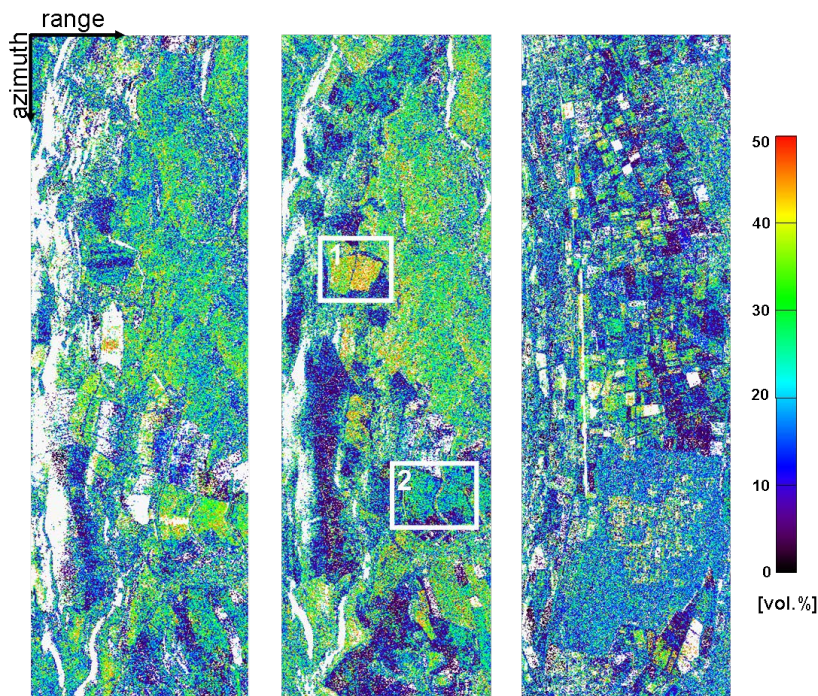


Figure 89: Inverted soil moisture for OPAQUE and SARTEO campaigns applying the model-based approach with normalized *Pauli*-based ground-to-volume ratios (from left to right): Soil moisture for OPAQUE 2007 (31st of May), OPAQUE 2008 (8th of May) and SARTEO 2008 (27th of May) campaigns (image smooth: 4x4).

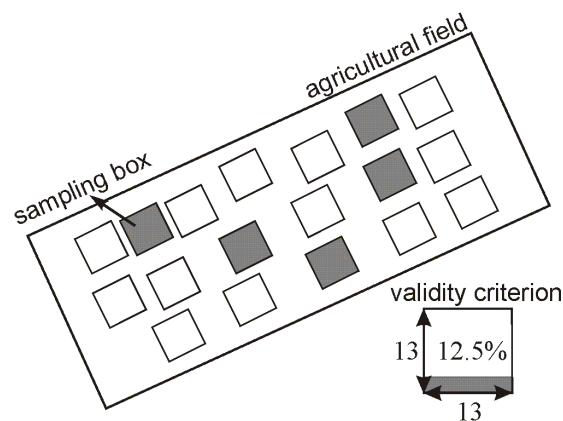


Figure 90: Sampling scheme on the test fields for the inversion approach incorporating normalized *Pauli*-based ground-to-volume ratios: 13x13 pixels around each measurement location (squares) form a sampling box. Criteria for a valid sampling box of the validation: 1. Minimum 12.5% invertible pixels per box; 2. Minimum five valid sampling boxes per field (gray boxes); 3. For field data of the AgriSAR campaign, measured outliers with a deviation of three times the standard deviation of the mean value were excluded.

moisture values of the six acquisitions varies from 6.80vol.% for the AgriSAR acquisition on the 7th of June until 13.20vol.% for the OPAQUE 2007 acquisition, while all RMSE values are reported in Table 14. Moreover, the uncertainty of the

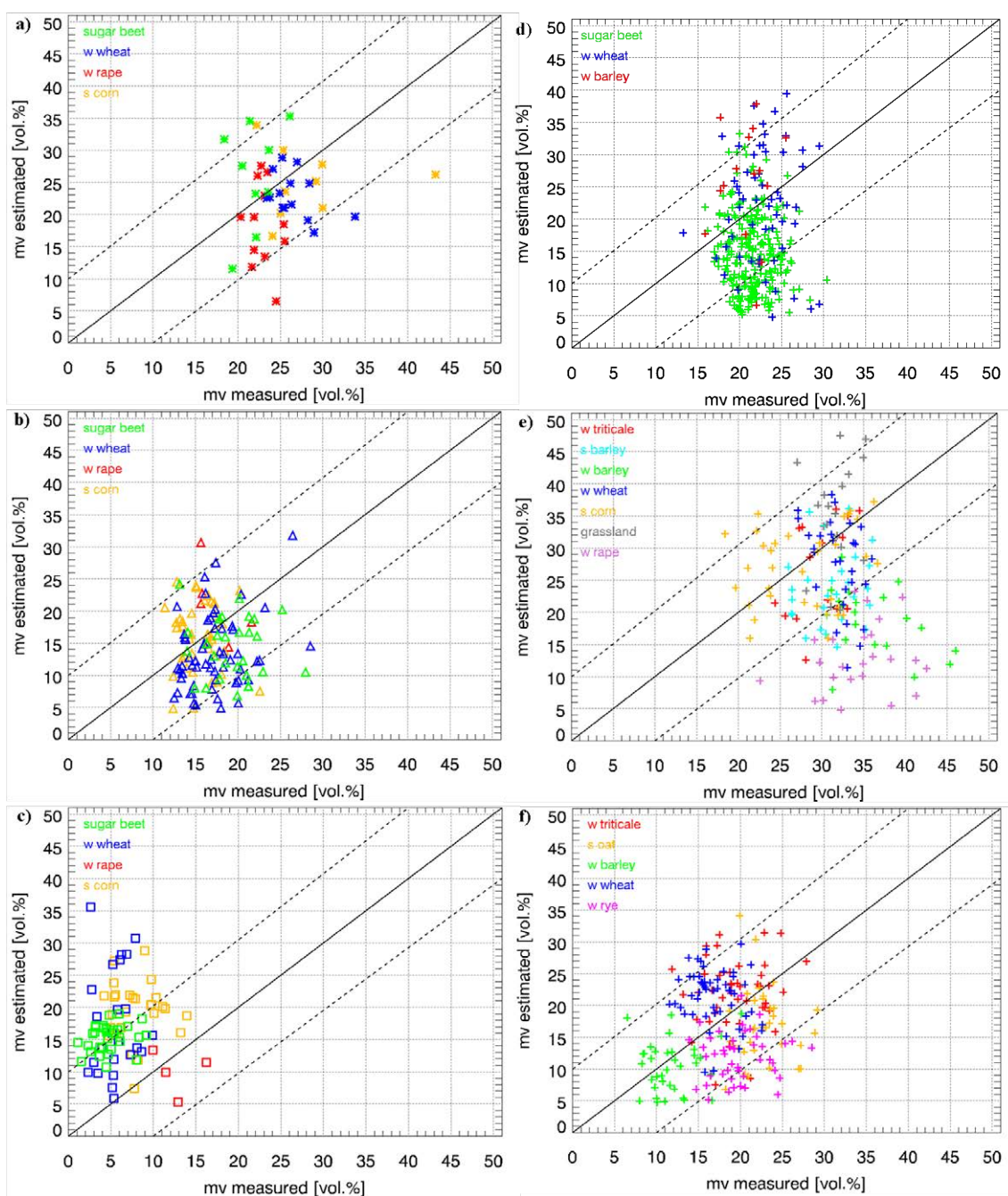


Figure 91: Comparison of measured and estimated soil moisture for the AgriSAR campaign on 19th of April (a), on 7th of June (b), on 5th of July (c), for the SARTEO campaign (d), for the OPAQUE 2007 campaign (e) and for the OPAQUE 2008 campaign (f) applying the model-based approach with normalized *Pauli*-based ground-to-volume ratios.

retrieval method is also indicated in Table 14 by the mean of the standard devi-

6.1. RESULTS FOR SOIL MOISTURE

ation for the estimated soil moisture within the sampling boxes, which indicates approximately the same or even higher levels than the RMSE values. This strong

Table 14: Quality assessment of inversion results including all crop types for the AgriSAR 2006, OPAQUE 2008 and SARTEO 2008 campaign applying the model-based approach with normalized *Pauli*-based ground-to-volume ratios.

Date	RMSE [vol.%]	STDDEV ¹ [vol.%]	Inversion rate [%]
AgriSAR 19.4.2006	7.70	11.97	43
AgriSAR 07.6.2006	6.80	11.19	43
AgriSAR 05.7.2006	12.39	12.59	42
OPAQUE 31.5.2007	13.20	10.87	34
OPAQUE 08.5.2008	11.10	10.55	40
SARTEO 27.5.2008	9.45	10.09	39

¹mean of STDDEV for moisture estimates within the sampling boxes

deviation can be explained by a certain insensitivity to capture the intra-field variability with the applied approach. The deviation is especially high for the July date (STDDEV=12.59vol.%) of the AgriSAR campaign in the end of the growth period, where the low soil moisture level of the measurements (1-12Vol.%) could not be obtained with the applied approach and the results show an overestimation with a RMSE of 12.39vol.%. But comparing all campaigns, the RMSE-level is only ~1-2vol.% lower (AgriSAR) or higher (OPAQUE, SARTEO) than for the algorithm presented before and in Chapter 6.1.2.1., which yields only a small improvement or a small deterioration of the RMSE.

However, the occurrence of distinct outliers (outside the ± 20 vol.%-interval) is strongly reduced for the model-based approach incorporating the ground-to-volume ratios due to a better cross-polarization separation (cf. Figure 91), except for the winter barley and the winter rape fields within the OPAQUE 2007 campaign. The distinct underestimation of these soil moisture estimates results from an inversion of the surface component under 70cm (winter barley) and 135cm (winter rape) of a closed vegetation canopy combined with a shallow incidence angle of around 50° (winter barley) and 45° (winter rape) and slopes facing away from the sensor. These conditions hamper the presence of dihedral scattering, which would have been desirable for inversion under such vegetation conditions (cf. Table 3).

6.1.2.4. Hybrid decomposition and inversion

The hybrid decomposition, which is introduced in Chapter 4.2.6., combines a model-based and an eigen-based decomposition in order to subtract an appro-

appropriate rank-3 volume contribution and to separate subsequently the ground components in a physically meaningful way. For reasons of performance validation, the AgriSAR, OPAQUE and SARTEO data sets were used for application of the algorithm in different scattering scenarios. As the performance is distinctively enhanced using the physically constrained volume component $f_{V_{ch}}$, all results will incorporate this particularly adapted volume scattering component. Finally, Figure 92 outlines the processing scheme of the hybrid three component decomposition for soil moisture estimation under vegetation.

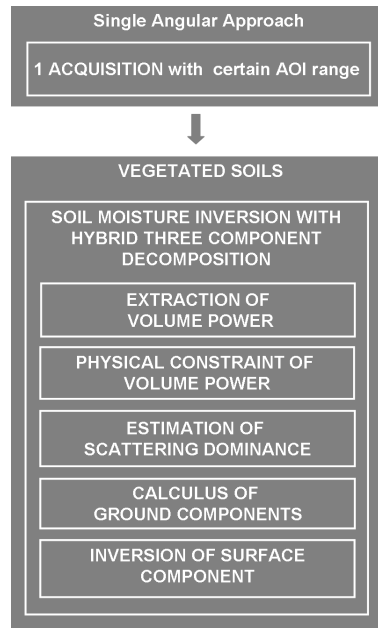


Figure 92: Scheme of the hybrid three component decomposition and inversion algorithm for soil moisture.

6.1.2.4.1. Hybrid decomposition using a physically constrained volume component

Figure 93 illustrates exemplarily the surface (α_s) and dihedral (α_d) scattering mechanisms for the 19th of April 2006 (AgriSAR campaign) retrieved by the hybrid decomposition described in Chapter 4.2.6., including a physically constrained volume intensity component $f_{V_{ch}}$ with $\epsilon_{est}=20$ (cf. Chapter 4.2.6.1.). Furthermore, the results for the surface and dihedral scattering mechanisms of the remaining acquisitions are added in Appendix G.

A smooth and transient change of the scattering mechanisms over the scenes in Figure 93 and Appendix G, which follows the incidence angle conditions, indicates the natural and physically correct separation of the two scattering mechanisms

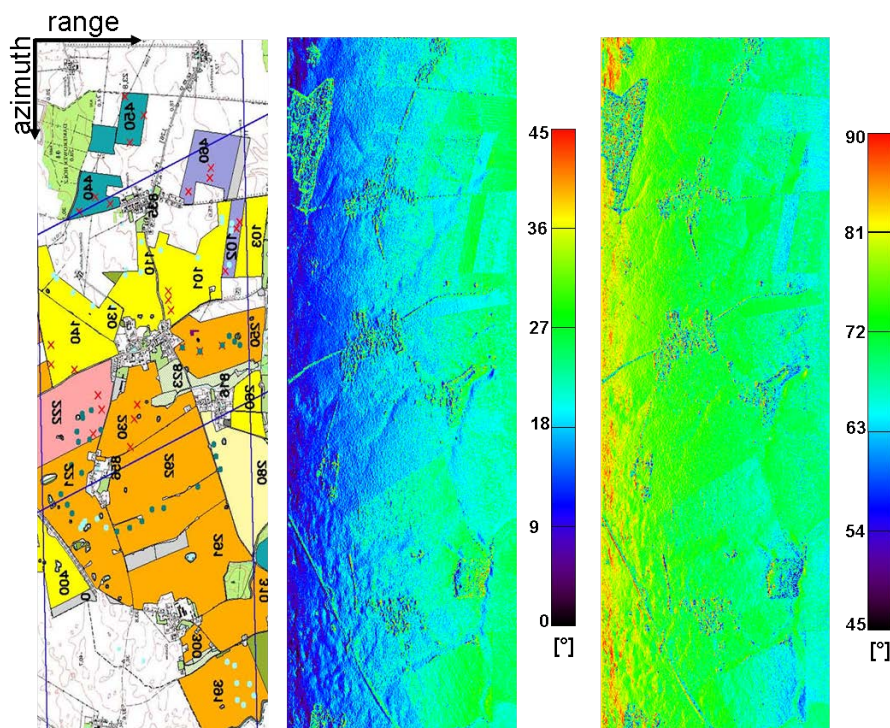


Figure 93: Land use map (left) as well as surface α_s (middle) and dihedral α_d (right) scattering mechanisms for 19th of April 2006 of the AgriSAR campaign using the hybrid decomposition with a physically constrained volume component $f_{V_{ch}}$ (ϵ_{est} -level=20) [156].

by the orthogonality condition, introduced in Chapter 4.2.6.. Therefore the hybrid decomposition exceeds the classical model-based decompositions of Chapter 6.1.2.1. and 6.1.2.5., because in the classical cases the non-dominant scattering mechanism has to be set to a pre-defined artificial value to keep the decomposition system analytically solvable [124, 159, 151].

The α_1 -criterion for the determination of the appropriate ϵ_{est} -level (Equation 212) revealed a clear minimum for the different campaign sites and acquisition dates stating a stable performance over a wide range of topography and over a diversity in vegetation phenology (cf. Table 15).

6.1.2.4.2. Inversion and validation of hybrid decomposition

After the retrieval of the appropriate surface and dihedral scattering mechanism (α_s , α_d), the soil moisture can be retrieved for both ground components. As the intensity of the volume component $f_{V_{ch}}$ is specifically adapted using the physically-based Bragg surface scattering model, the inversion rate of the dihedral component revealed to be negligible and the results are not shown. Figure 94 displays the soil

Table 15: Estimated dielectric level (ϵ_{est} -level) for each acquisition from the α_1 -criterion of Equation 212 (m=*master*-acquisition, o=*opposite*-acquisition) [156,153].

Date	ϵ_{est} -level [-]
AgriSAR 19.4.2006	20
AgriSAR 07.6.2006	10
AgriSAR 05.7.2006	8
OPAQUE 31.5.2007	30 ¹
OPAQUE 08.5.2008 (m)	18
OPAQUE 08.5.2008 (o)	18
SARTEO 27.5.2008	15

¹more stringent criterion: $\alpha_1 < 20^\circ$

moisture maps inverted for the AgriSAR, the OPAQUE, the SARTEO campaigns. The applied ϵ_{est} -level was obtained as shown in Chapter 4.2.6.1., while the appropriate level for the OPAQUE 2007 campaign was found by a more stringent α_1 -criterion of 20° . The ϵ_{est} -levels presented in Table 15 correspond well with the range of the soil moisture data from the measurement campaigns on the test sites. All inverted soil moisture images are scaled individually to enhance the contrast. White areas are masked due to non-physical results in the inversion process, while areas without DEM-coverage are masked gray.

In Table 16 the inversion rates are reported for the three campaigns. Compared to methods in Chapter 6.1.2.1. [124, 159] and Chapter 6.1.2.3. [150], an almost complete and continuous inversion can be achieved with an inversion rate of more than 97% for all acquisitions, including a wide range of local incidence angles and vegetation states (cf. Figure 94). This reflects a very favorable result for run off simulations and flood forecasting models, where a whole catchment needs to be monitored continuously in order to retrieve the spatial soil moisture distribution within the catchment.

With focus on the covering vegetation layer, the maximum vegetation height varied from 18cm maximum height for the 19th of April acquisition (AgriSAR) to 172cm for the 5th of July acquisition (AgriSAR) (cf. Figure 52). The OPAQUE and SARTEO campaigns exhibit intermediate vegetation heights, which are still of great interest, because not only the height also the phenology of agricultural plant alters distinctively along the growth cycle. The phenological conditions are illustrated exemplarily for different crop types in Figure 77. Therefore the physically constrained volume component seems to compensate the influence of the vegetation cover quite well, despite the diversity of different scattering scenarios

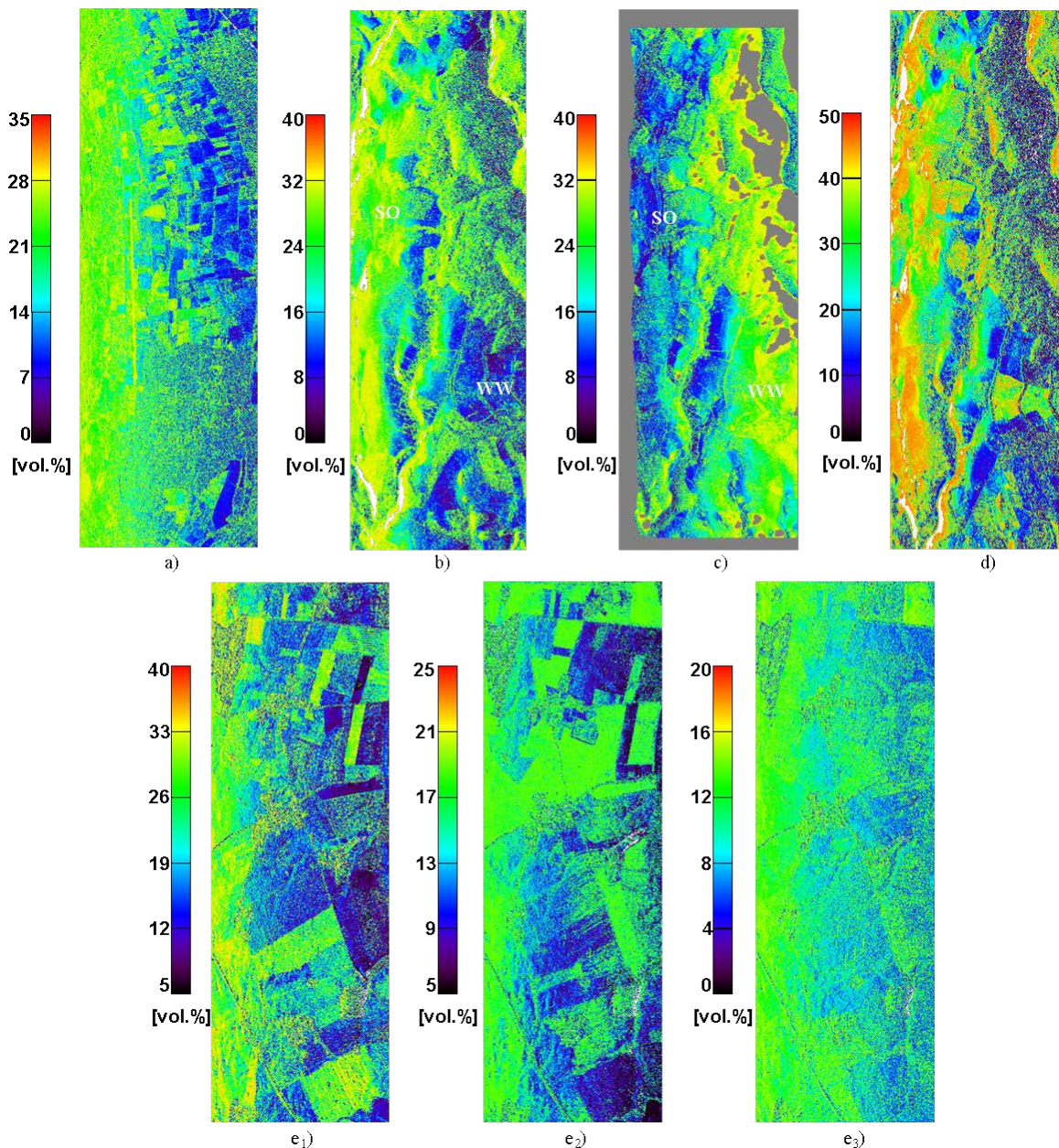


Figure 94: Results for soil moisture inversion under vegetation cover using a hybrid decomposition and inversion approach: a) SARTEO campaign (27th of May 2008 with $\epsilon_{est}=15$); b) OPAQUE campaign (8th of May 2008 with $\epsilon_{est}=18$) *master-scene*; c) OPAQUE campaign (8th of May 2008 with $\epsilon_{est}=18$) *opposite-scene*; d) OPAQUE campaign (31st of May 2007 with $\epsilon_{est}=30$); e) AgriSAR campaign e₁) 19th of April 2006 with $\epsilon_{est}=20$, e₂) 7th of June 2006 with $\epsilon_{est}=10$, e₃) 5th of July 2006 with $\epsilon_{est}=8$); Areas without DEM-coverage are masked gray; Non-invertible regions are masked white; Near to far range spreads from left to right edge of the images except for (c), where the situation is reversed; SO=summer oat, WW=winter wheat [153, 156].

in agriculture. This leads to the consistent and continuous inversion results for all scenes depicted in Figure 94.

Field measurements of soil moisture were taken with TDR, FDR and gravimetric probes during the three campaigns for a quantitative analysis of the inversion. Figure 95 provides the settings of the validation for the different test fields. The

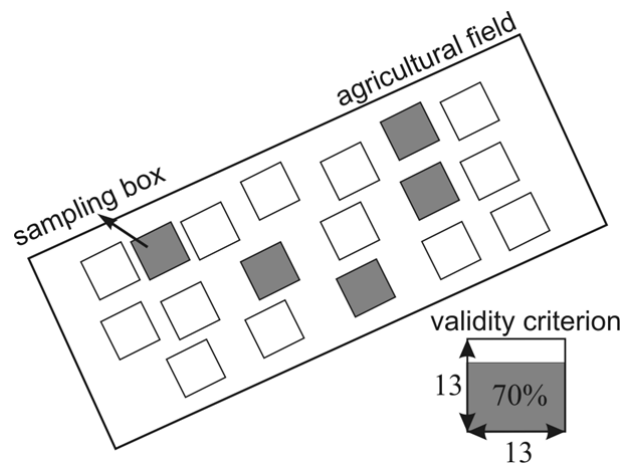


Figure 95: Sampling scheme on the test fields for validation of the hybrid decomposition and inversion algorithm: 13x13 pixels around each measurement location (squares) form a sampling box. Criteria for a valid sampling box of the validation: 1. Minimum 70% invertible pixels per box; 2. Minimum five valid sampling boxes per field (gray boxes) 3. For field data of the AgriSAR campaign, measured outliers with a deviation of three times the standard deviation of the mean value were excluded.

resulting scatter plots of measured soil moistures on ground compared with estimated soil moistures from the developed approach are presented in Figure 96 for all acquisitions covering the entire vegetation growth period as well as different incidence angle scenarios.

Comparing the seven acquisition dates, the different levels of measured soil moisture vary between 1vol.% and 46vol.%. The performance of the developed algorithm is constantly on a high level resulting in a root mean square error (RMSE) between 4.4vol.% and 11.0vol.%, as shown in Table 16, for all land uses, topographic variations and along the entire vegetation growth period.

An increased RMSE is given for the OPAQUE 2008 data, where an investigation for different local incidence angles was conducted. Therefore a *master*-scene (m) in descending mode and an *opposite*-scene (o) in ascending mode were processed for soil moisture inversion. The RMSE of the *opposite*-scene is significantly increased to 9.52vol.% compared to 7.49vol.% for the *master*-scene (cf. Figure 96 and Table 16). For the *opposite*-scene, the soil moisture inversion overestimates for the winter wheat field (WW) in near range and underestimates for the summer oat

6.1. RESULTS FOR SOIL MOISTURE

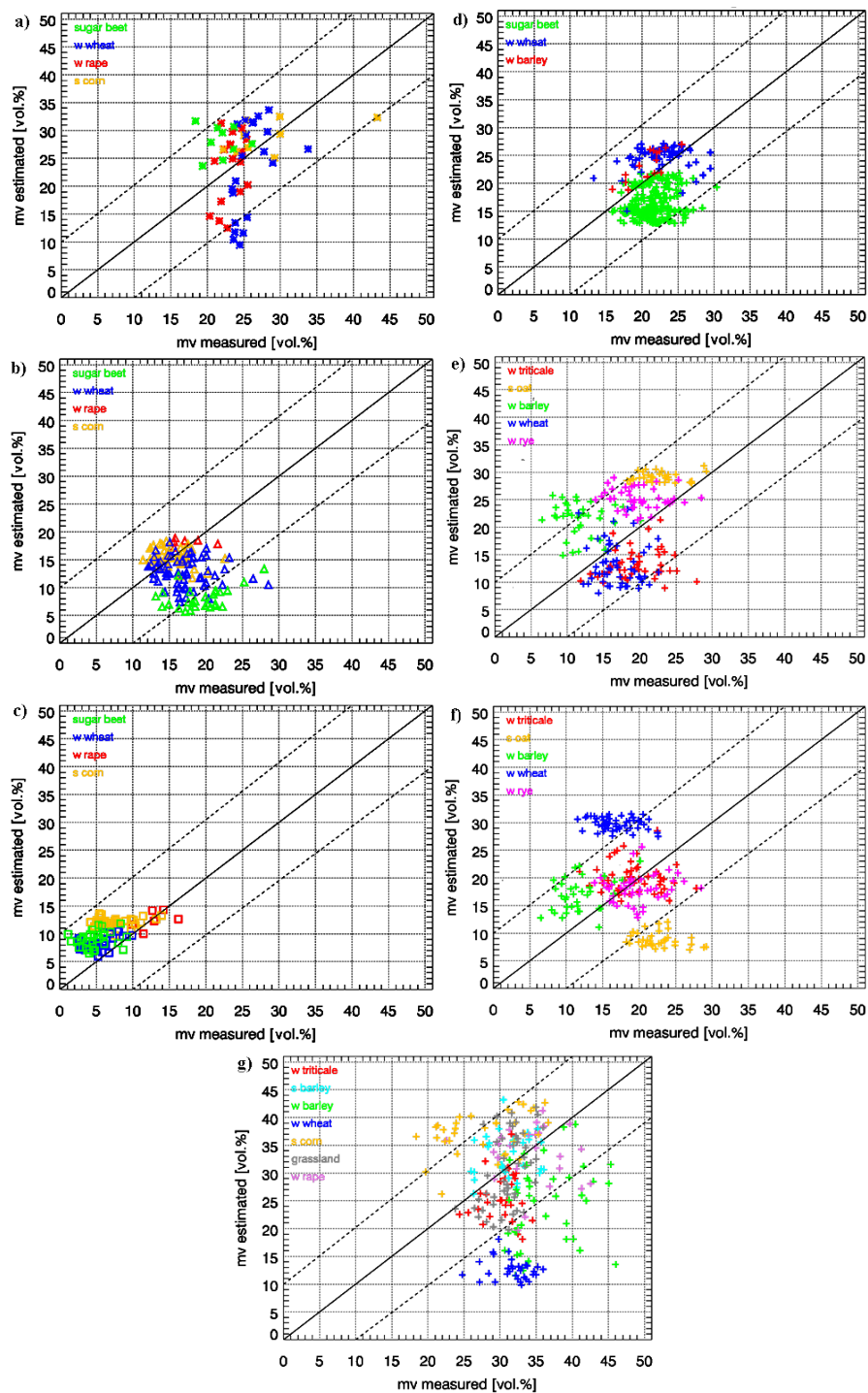


Figure 96: Scatter plots of measured soil moisture values from TDR, FDR and gravimetric probes against estimated soil moisture values using the hybrid decomposition and inversion algorithm for a variety of land use types. AgriSAR 2006 – Validation along the growth cycle: At the beginning of the vegetation growth period at 19th of April (a), in the middle of the growth period at 7th of June (b) and at the end of the vegetation growth period at 5th of July (c); SARTEO 2008 – Validation for emerging vegetation at 27th of May (d); OPAQUE 2008 – Validation for different local incidence angles under pronounced topography at 8th of May: *master-scene* (e) and *opposite-scene* (f). OPAQUE 2007 – Validation for mature winter crops at 31st of May (g) [153, 156].

field (SO) in far range (cf. Figure 94). The situation is reversed, but appears less pronounced, for the *master*-scene.

Hence, a certain dependency of the inversion on the local incidence angle is already visible on the images of Figure 94. The local incidence angle (θ_l) as main factor of the forward modeling of the surface component influences subsequently the soil moisture retrieval from the physical constraining of the volume intensity ($f_{V_{ch}}$) until the calculus of the surface scattering alpha (α_s) for the subsequent soil moisture inversion. Furthermore, the effect of incidence angle variability on soil

Table 16: Inversion rate, RMSE, STDDEV and maximum of vegetation height for the hybrid decomposition and inversion with physically constrained volume intensity $f_{V_{ch}}$ applied for all study areas covering a variety of crop types in different phenological stages (m=*master* acquisition, o=*opposite* acquisition) [153, 156].

Date	Inversion rate [%]	RMSE [vol.%]	STDDEV ² [vol.%]	Max. Vegetation height [cm]
AgriSAR 19.4.2006	99.77	6.75	3.72	18
AgriSAR 07.6.2006	99.79	6.98	2.37	167
AgriSAR 05.7.2006	99.69	4.43	2.21	172
OPAQUE 31.5.2007	97.89	11.02	5.19	85
OPAQUE 08.5.2008 (m)	98.17	7.49	3.74	82
OPAQUE 08.5.2008 (o)	98.38	9.52	3.16	82
SARTEO 27.5.2008	99.95	5.80	2.62	~ 70 ¹

²mean of STDDEV for moisture estimates within the sampling boxes,

¹no direct measurements

moisture inversion under vegetation cover is studied in [155].

Another effect raising the RMSE for oriented scattering scenarios is the confinement of this decomposition algorithm to random volumes. There is no orientation effect of the vegetation volume included in the current algorithm, which would cause a non-zero T_{12} -element in $[T_V]$. Thus, it can be explained, why fields like sugar beet in June (AgriSAR campaign) with mainly horizontally oriented broad leaves exhibit a pronounced underestimation. First attempts with the inclusion of a standard approach concerning vegetation orientation in this hybrid decomposition algorithm like in [124, 159, 151] (using the co-polarization power ratio of Equation 164 for separation in horizontally oriented, vertically oriented or randomly oriented vegetation volumes with fixed distribution widths and distribution means) resulted in a major loss of inversion rate and of inversion accuracy.

As the result with the highest RMSE of 11.02vol.%, the OPAQUE 2007 campaign data reveal a combination of the oriented vegetation and the incidence angle ef-

fect. Thus a considerable variability of the inverted soil moisture, guided by topography, can be noticed from Figure 96g. While the steep incidence angle regions can be assigned to high soil moisture values ($\sim 45\text{vol.}\%$), the shallow local incidence angle regions (cf. Figure 62) reveal a low soil moisture level ($\sim 15\text{vol.}\%$) in Figure 94d. But for some fields like winter wheat and winter barley having a favorable shallow local incidence (cf. Figures 65 and 66), the RMSE still rises above $10\text{vol.}\%$ owing to the strong vertical orientation of the vegetation (cf. images in Figure 85) causing an even stronger underestimation.

6.1.2.5. Multi-angular model-based decomposition and inversion

In order to overcome the incidence angle effect on the soil moisture inversion under vegetation cover, mentioned in previous Chapters, a novel multi-angular approach is introduced in the following. Figure 64 presents the three different flight headings acquired during the OPAQUE 2008 campaign to obtain a multi-angular set of acquisitions (cf. Chapter 5.1.2.). The different scenes are labeled as *master* (m), *opposite* (o) and *perpendicular* (p). In order to combine these scenes for a multi-angular model-based decomposition, a processing scheme shown in Figure 97 was developed. Similar to the single angular-approach of Chapter 6.1.2.1. an $H/\bar{\alpha}$ -criterion is applied for each scene individually, to separate regions of vegetated and non-vegetated soils. The non-vegetated soils are inverted by the *X-Bragg* surface scattering approach of Chapter 6.1.1., while the areas of vegetated soils are decomposed with a model-based three component polarimetric decomposition given as

$$\begin{aligned}
 \langle [T_{Data}] \rangle &= [T_{XB}] + [T_{AD}] + [T_{GV}] \\
 &= f_S \begin{bmatrix} 1 & \beta_S^* \text{sinc}(2\psi_1) & 0 \\ \beta_S \text{sinc}(2\psi_1) & \frac{1}{2} |\beta_S|^2 (1 + \text{sinc}(4\psi_1)) & 0 \\ 0 & 0 & \frac{1}{2} |\beta_S|^2 (1 - \text{sinc}(4\psi_1)) \end{bmatrix} + \\
 f_D \cdot m_{dv}^2 &\begin{bmatrix} |\alpha_D|^2 & \alpha_D & 0 \\ \alpha_D^* & 1 & 0 \\ 0 & 0 & 0 \end{bmatrix} + f_V \begin{bmatrix} V_{11} & V_{12} & 0 \\ V_{12} & V_{22} & 0 \\ 0 & 0 & V_{33} \end{bmatrix}. \tag{220}
 \end{aligned}$$

The coherency matrix $\langle [T_{Data}] \rangle$ is decomposed into a depolarizing (rank-3) surface scattering component $[T_{XB}]$, a deterministic (rank-1) dihedral scattering component $[T_{AD}]$ and a generalized (rank-3) volume scattering component $[T_{GV}]$. In order to obtain a determined and analytically solvable inversion problem, it is necessary to pre-determine the volume components V_{11} - V_{33} (as already presented in

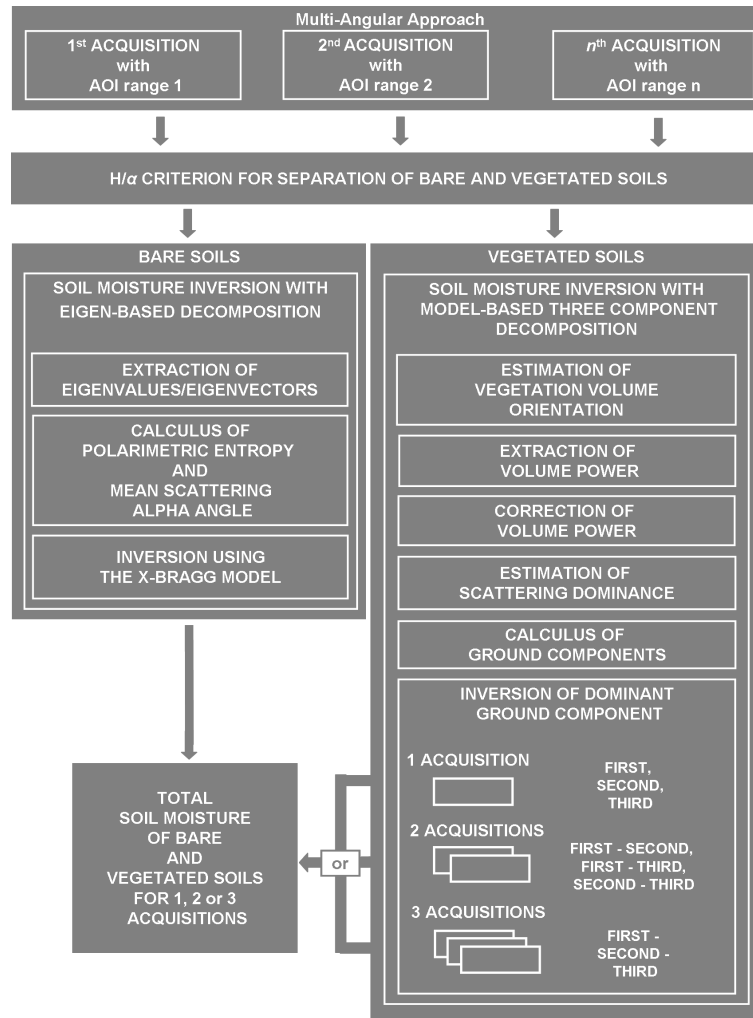


Figure 97: Processing scheme of the multi-angular polarimetric decomposition and inversion procedure for soil moisture form bare and vegetated soils [155].

Chapter 6.1.2.), the roughness depolarization (ψ_l) and the vegetation attenuation loss (m_{d_v}), which was introduced in Equation 136. The roughness-term (ψ_l) can be retrieved from the following relation incorporating the circular coherence (cf. Chapter 4.1.5. and [204]):

$$\psi_l = \frac{\pi}{2} \cdot (1 - |\gamma_{RLL}|). \quad (221)$$

The estimation of the volume orientation to allocate the volume components V_{11} - V_{33} , the extraction and correction of volume power, the estimation of the scattering dominance and the calculus of the ground component are already explained particularly in Chapter 6.1.2.1. and are applied separately for all the incorporated acquisitions. Afterwards the inversion is applied according to Chapter 4.2.7.1., where seven different inversion configurations are possible incorporating one, two

or three acquisitions from a single-angular to a tri-angular approach.

In Figure 98 the local incidence angle θ_l and the normalized power components of the model-based decomposition are depicted for each acquisition. The red frame indicates the overlapping region of all acquisitions. Due to the variability of the local topography, caused by the river morphology, the local incidence angle covers a wide range from almost perpendicular until grazing (1st column). The influence of the topography on the appearance of one of the three scattering mechanism can be seen by comparing the local incidence angle maps (1st column) with the model-based decomposition results (2nd column). In regions with steep local incidence the surface scattering mechanism (blue colored) dominates, while for shallower local incidence the dihedral scattering mechanism (red colored) emerges.

The results of the model-based decomposition (2nd column) compared against the land use information (5th column) appear plausible and physically meaningful, which is in accordance with the results in the previous chapters and with [124, 151, 158, 159].

6.1.2.5.1. Inversion and validation of the multi-angular model-based decomposition

The soil moisture results using the multi-angular decomposition and inversion procedure (cf. Figure 97) are visualized in Figure 98 for the OPAQUE 2008 data set. Focusing on the soil moisture inversion (3rd to 5th column) the results are displayed between 0vol.% and 50vol.%. Non-invertible pixels, e.g. for the forested area in the upper right corner of each image in Figure 98, are set to white. Especially the soil moisture inversions from one acquisition (3rd column) exhibit regions with a very low inversion rate at steep local incidence angles ($\theta_l < 25^\circ$). This effect confirms the insensitivity of the electromagnetic models at these steep incidence angles, as predicted from sensitivity analysis in Chapter 4.2.5.. Hence, the limitation of a single-angular approach with just one acquisition is obvious in the 3rd column of Figure 98.

The advantage of the multi-angular approach regarding the inversion rate becomes evident in the 4th and 5th column of Figure 98. An analysis of the inversion results for soil moisture on the overlapping area (red box) reveals a significant increase of inversion rate, when moving from simple single-angular to multi-angular approaches (cf. Table 17). For a single acquisition in a single-angular configuration, an inversion rate of about 30-50% is achieved, whereas for two acquisitions in a bi-angular configuration the rate rises to approximately 55-65%. Finally using all three acquisitions in a tri-angular configuration an inversion rate of about

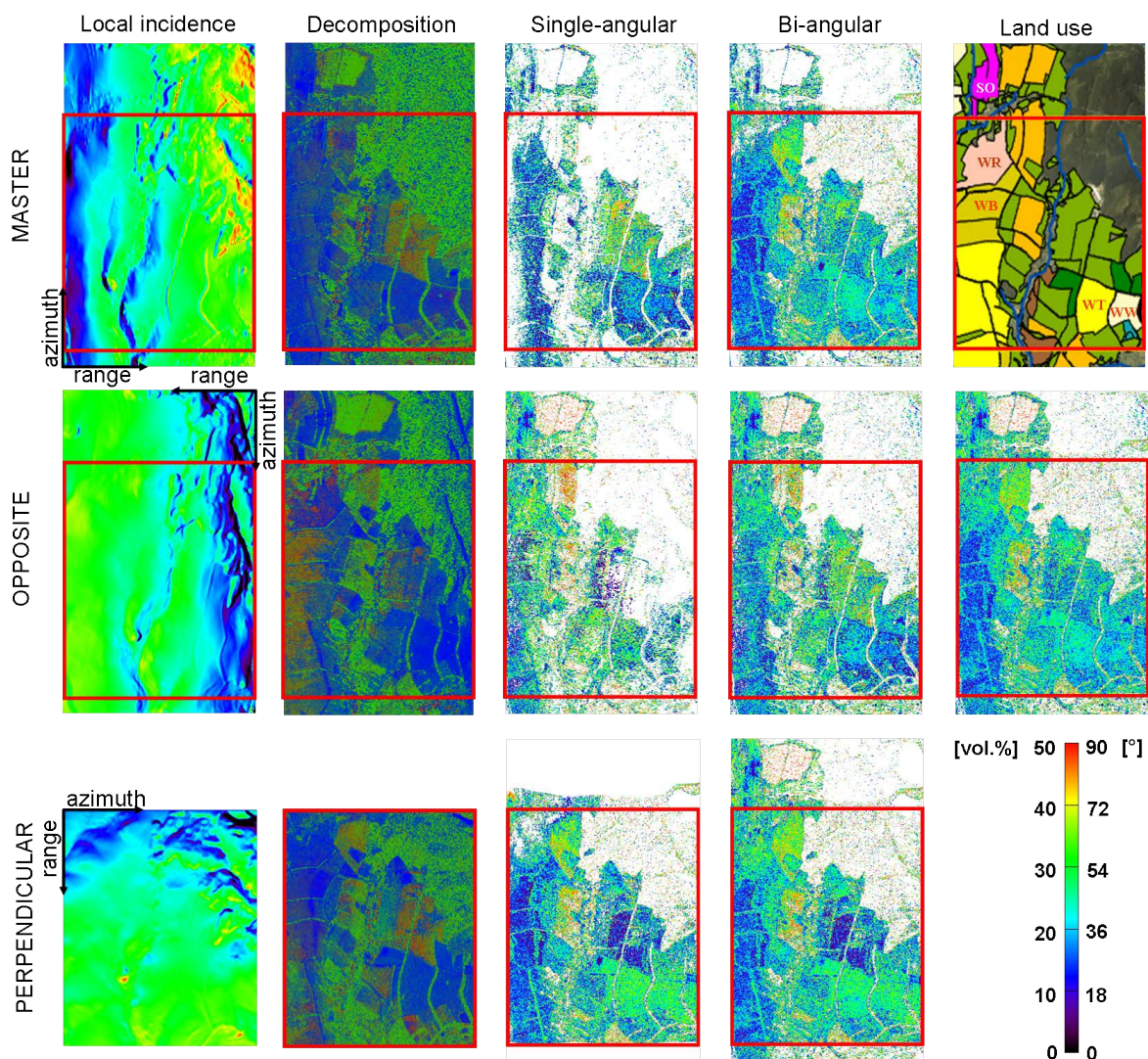


Figure 98: 1.column: Local incidence angle [$^{\circ}$] for each acquisition geometry: *Master* (1.row), *opposite* (2.row) and *perpendicular* (3.row); 2. column: RGB-composites of normalized power contributions of the three component model-based decomposition from the dihedral (red), volume (green) and surface (blue) scattering component for each acquisition geometry: *Master* (1.row), *opposite* (2.row) and *perpendicular* (3.row); 3. column: Single-angular soil moisture: *Master* (1.row), *opposite* (2.row) and *perpendicular* (3.row) in *master* acquisition geometry; 4. column: Bi-angular angular soil moisture: *Master-perpendicular* (1.row), *master-opposite* (2.row) and *opposite-perpendicular* (3.row) in *master* acquisition geometry; 5. column: Land use map (1.row, labels of the test fields are explained in Table 18 and green=grassland, dark green=summer corn, orange=winter rape, brown=pasture), Triangular soil moisture: *Master-opposite-perpendicular* (2.row) in *master* acquisition geometry; All soil moisture images are displayed with an averaging window 4x4. White color represents non-invertible pixels; The red frame indicates the overlapping zone of the three acquisitions [155].

70% is obtained. The inverted soil moisture results for each of the seven differ-

Table 17: Inversion rate of the different incidence angle configurations for multi-angular model-based decomposition on the OPAQUE 2008 data (m=*master*, o=*opposite*, p=*perpendicular* acquisition) on agricultural fields (forest, water and urban areas are not considered) within the red frame (see Figure 64) [151, 155].

Configurations	<i>master</i>	<i>opposite</i>	<i>perpendicular</i>
Single acquisition	40%	30%	49%
Two acquisitions	m-o 56%	m-p 63%	o-p 61%
Three acquisitions	m-o-p 71%		

ent incidence angle configurations are validated against the ground measurements introduced in Chapter 5.1.2.. The estimated soil moisture values have been averaged within a 13x13 box centered at the sampling points leading to 169 samples with a single sample resolution of 2x2m (cf. Figure 95 for sampling scheme). Only boxes with at least 70% invertible pixels have been considered to avoid non-representative outliers.

In Figure 99 scatter plots display the comparison of measured to estimated soil moisture for the different configurations. Additionally, the RMSE is summarized in Table 18 for all investigated fields and all configurations. The RMSE ranges from 4.41vol.% to 10.33vol.%, while a minimum of five pairs of measured and inverted soil moisture samples has been used. Fields with a low inversion rate (less than five valid samples), have been discarded and are indicated with the signature '<' in Tables 18 and 19. The winter wheat field for instance features a steep local incidence angle of 26.6° in the case of a single-angular inversion using the *opposite*-acquisition, which inhibits a soil moisture inversion. Therefore the entire set of test fields can not be validated for soil moisture retrieval with a single-angular configuration (*master*, *opposite* or *perpendicular*), as it is evident in Figure 98 and 99a-c.

The multi-angular configurations result in higher inversion rates and lead to more continuous soil moisture patterns, even for the high validation requirements of 70% box coverage for a valid inversion result. Considering the mean RMSE over all investigated fields the best performance and the highest inversion quality is obtained for the tri-angular configuration (m-o-p). A mean RMSE of 5.85vol.% and a mean STDDEV of 9.47vol.% have been obtained (cf. Figures 99d and 99h as well as Tables 18 and 19). For the bi-angular approaches the mean RMSE ranges

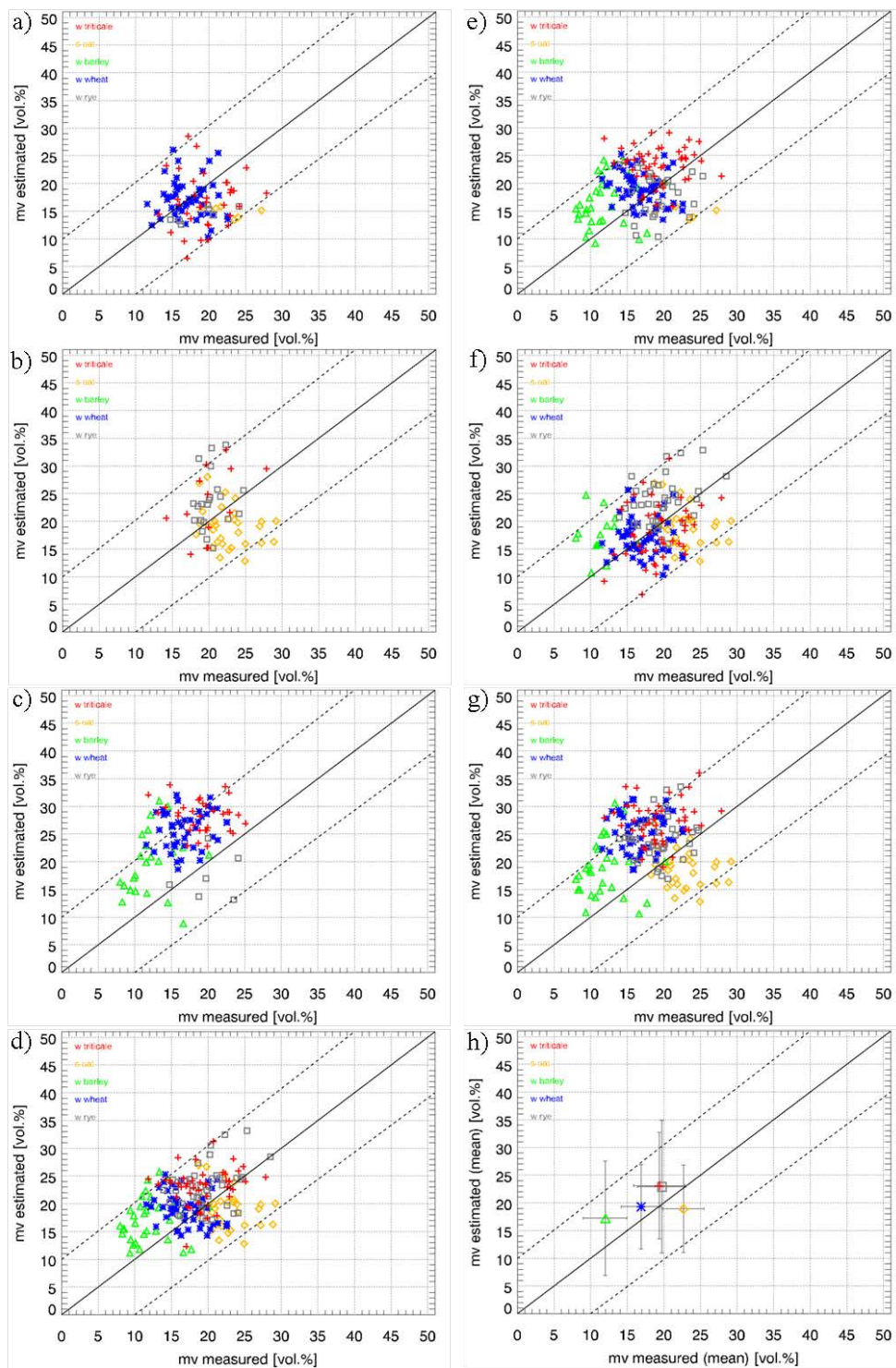


Figure 99: Scatter plots of measured against estimated soil moisture values for the different incidence angle configurations including all investigated fields (w=winter, s=summer). a) *master* (m) acquisition; b) *opposite* (o) acquisition; c) *perpendicular* (p) acquisition; d) m-o-p configuration; e) m-p configuration; f) m-o configuration; g) o-p configuration; h) field mean value of soil moisture for one field from m-o-p configuration (gray bars indicate the standard deviation of the estimates and the measurements) [155].

6.1. RESULTS FOR SOIL MOISTURE

Table 18: Root Mean Square Error (RMSE) in [vol.%] of the inversion for the different incidence angle configurations (m=*master*, o=*opposite*, p=*perpendicular*) for the investigated fields (WT=winter triticale, WB=winter barley, WR=winter rye, WW=winter wheat, SO=summer oat, - = out of scene, < = too less values for a valid analysis, Mean= mean of RMSE of all fields for one incidence angle configuration) [155].

Configuration	WT	WB	WR	WW	SO	Mean
m	6.34	<	5.25	4.52	8.55	6.17
o	6.34	<	6.11	<	6.43	6.29
p	10.33	9.75	5.86	9.79	-	8.93
m-o	5.42	7.76	5.81	4.41	6.35	5.95
m-p	6.27	6.85	4.89	5.04	8.55	6.32
o-p	9.46	8.78	6.42	9.54	6.43	8.13
m-o-p	5.72	6.94	5.27	4.98	6.35	5.85

between 5.95vol.% and 8.13vol.%, while for the single-angular approaches the mean-RMSE is in all cases higher than 6.17vol.%. The results confirm a stability of the mean-RMSE for the different approaches in the range of 6-8vol.% and a mean of STDDEV between 10-11vol.% that improves slightly for the case of the tri-angular inversion (mean RMSE<6vol.%, mean of STDDEV<10vol.%) (cf. Figure 99 as well as Tables 18 and 19). The results of the winter rye field indicate

Table 19: Mean field value of STDDEV of soil moisture within the sampling boxes in [vol.%] of the different incidence angle configurations (m=*master*, o=*opposite*, p=*perpendicular*) for the investigated fields (WT=winter triticale, WB=winter barley, WR=winter rye, WW=winter wheat, SO=summer oat, - = out of scene, < = too less values for a valid analysis, Mean = mean of STDDEV of all fields for one incidence angle configuration) [155].

Configuration	WT	WB	WR	WW	SO	Mean
m	11.17	<	11.83	9.01	11.36	10.84
o	12.21	<	10.77	<	8.04	10.34
p	10.97	10.08	12.19	9.86	-	10.78
m-o	11.33	12.77	12.19	9.13	7.86	10.66
m-p	10.52	10.27	12.65	7.64	11.36	10.49
o-p	10.67	10.80	11.77	9.96	8.04	10.25
m-o-p	9.61	10.34	11.94	7.60	7.86	9.47

the highest stability with a RMSE below 6.5vol.% for all configurations because of the moderate to shallow local incidence (cf. Table 4) in all acquisitions, which is favorable for soil moisture retrieval (cf. Chapter 4.2.5.). Also the winter wheat

field with 58.6° local incidence for the *master*-acquisition yields a favorable RMSE of 4.52vol.% due to an inversion dominated by the bare soil method (using the *X-Bragg* model) under predestinate shallow incidence angle conditions (cf. Chapter 4.2.5.). The summer oat field shows a RMSE of 8.55vol.% due to an underestimation of soil moisture for the *master*-acquisition, which originates from a very small local incidence angle of 23.4° . Even if the vegetation cover is very weak (6.5cm vegetation height), the bare soil inversion fails because of the steep local incidence angle, for which the corresponding small polarimetric entropy and mean scattering alpha angle of the *X-Bragg* model do not match the too large values of the data (cf. Chapter 6.1.1.).

The winter triticale and the winter wheat field are located in the far range region with 53.5° and 55.5° for the *perpendicular*-acquisition and exhibit the highest variability with an RMSE of more than 9.5vol.%. Actually, the local incidence angle range fits for soil moisture inversion, but for these fields the soil moisture retrieval with the *perpendicular*-acquisition results in an overestimation. One reason might be the low vegetation layer of 14-23cm which generates valid results for bare soil inversion on some parts of the fields confusing low vegetation with roughness. The same problem is occurring for the winter barley field with a local incidence angle of 43.4° and a vegetation height of 24.4cm causing an RMSE of 9.75vol.%.

A second reason might be the roughness estimation for the surface component of the model-based decomposition (from Equation 221), which indicates a very high roughness level for the winter triticale and the winter wheat field in the *perpendicular*-acquisition configuration, which might be caused by the shallow incidence together with the presence of a low vegetation layer and a specific orientation of the soil furrows.

Hence, neither the bare soil inversion nor the model-based inversion performs sufficiently well in this case. In addition, the angular diversity is not supportive for an inversion improvement. Therefore the assumptions of the different inputs in the decomposition procedures of the multi-angular algorithm (H- $\bar{\alpha}$ criterion, roughness estimation, volume estimation) and their consequences on an appropriate soil moisture inversion are crucial for the quality of the soil moisture inversion and express the need for a better parameterization and pre-estimation of the input variables. One way, approaching these needs, is presented by the single-layer approach of a hybrid decomposition with a physically constrained volume component for soil moisture inversion, as introduced in Chapters 4.2.6. and 6.1.2.4..

6.1.3. Best approach for soil moisture retrieval under vegetation cover

In the past Chapters several methods were described and applied to airborne fully

Table 20: RMSE, STDDEV and inversion rate of all applied decomposition and inversion algorithms for soil moisture retrieval including all study areas with all crop types.

Retrieval algorithm	RMSE [vol.%]	STDDEV ⁺ [vol.%]	Inversion rate [%]
AgriSAR 19.4.2006			
Bare soil <i>X-bragg</i>	13.05	9.20	4
Single angular model-based	10.37	12.38	35
Single angular model-based with ratio	7.70	11.97	43
Single angular hybrid	6.75	3.72	99
AgriSAR 7.6.2006			
Bare soil <i>X-bragg</i>	/	/	1
Single angular model-based	9.19	12.06	25
Single angular model-based with ratio	6.80	11.19	43
Single angular hybrid	6.98	2.37	99
AgriSAR 5.7.2006			
Bare soil <i>X-bragg</i>	/	/	1
Single angular model-based	13.04	12.38	30
Single angular model-based with ratio	12.39	12.59	42
Single angular hybrid	4.43	2.21	99
OPAQUE 31.5.2007			
Bare soil <i>X-bragg</i>	/	/	1
Single angular model-based	10.44	11.28	19
Single angular model-based with ratio	13.20	10.87	34
Single angular hybrid	11.02	5.19	98
OPAQUE 08.5.2008			
Bare soil <i>X-bragg</i>	16.84	7.77	3
Single angular model-based	10.11	13.01	24
Single angular model-based with ratio	11.10	10.55	40
Single angular hybrid	7.49	3.74	98
Tri-angular model-based	5.85	9.47	71
SARTEO 27.5.2008			
Bare soil <i>X-bragg</i>	15.18	7.49	1
Single angular model-based	8.59	10.31	25
Single angular model-based with ratio	9.45	10.09	39
Single angular hybrid	5.80	2.62	99

⁺ mean of STDDEV for moisture estimates within the sampling boxes,
/ = too less invertible pixels

polarimetric SAR data to extract the soil moisture information from the mixed (vegetation/soil) backscattering signature. In Table 20 the RMSE, the STDDEV and the inversion rate for the different retrieval methods are listed in order to identify subsequently the best approach in terms of estimation accuracy, inversion rate and applicability.

Firstly, the bare soil *X-Bragg* approach does not qualify as such approach, because it neglects completely the vegetation layer and leads obviously to the worst performance.

Secondly, the two single angular model-based decompositions show a quite comparable performance with a moderate RMSE of about 10vol.% and a medium inversion rate from 20% to 45% concerning all campaigns, presented in Table 20.

Finally, the single angular hybrid decomposition approach, using a physically constrained volume component, indicates the highest potential to retrieve soil moisture under agricultural vegetation cover with a RMSE between 5-11vol.% and an inversion rate of more than 97%. This retrieval approach requires only one single polarimetric SAR acquisition bypassing a more complex multi-angular acquisition scenario. Nonetheless, the tri-angular model-based algorithm obtains an even lower RMSE of 5.85vol.% than the single angular hybrid algorithm for the OPAQUE 2008 data set at the expenses of a higher acquisition complexity. Depending on the future design of fully polarimetric SAR missions, allowing quasi-simultaneously multi-angular or only single angular acquisitions, one of the two algorithms is more applicable.

6.2. Results for soil roughness

The retrieval of soil roughness is investigated for bare and vegetated soils using the methods introduced in Chapters 4.1.5. and 4.2.8., respectively. L-band fully polarimetric SAR data from DLR's E-SAR sensor acquired during the AgriSAR campaign are taken for analyses of the soil roughness. Unfortunately, roughness measurements were not available for all other campaigns.

6.2.1. Results for soil roughness retrieval on bare soil

As indicated in Chapter 4.1.5., the results for soil roughness retrieval on bare soils focus on inversion algorithms using SAR polarimetry. Figure 100 displays the roughness parameter k_s (cf. Equation 13) obtained from anisotropy A and circular coherence magnitude $|\gamma_{RRLL}|$, which represent the 'classical' roughness descriptors

for PolSAR data. In general, the roughness estimates from the anisotropy A show a

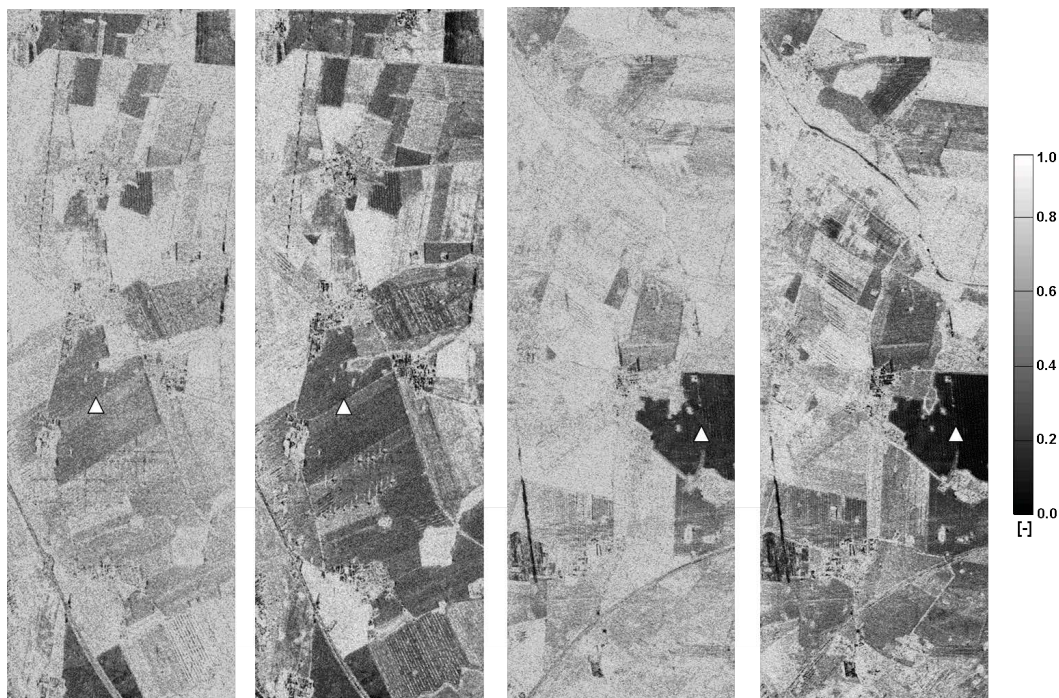


Figure 100: Roughness parameter k_s inverted from anisotropy and from circular coherence magnitude $|\gamma_{RLL}|$ for 19th/20th of April 2006 within the AgriSAR campaign; (from left to right): k_s of A for 'E-W' track, k_s of $|\gamma_{RLL}|$ for 'E-W' track, k_s of A for 'N-S' track, k_s of $|\gamma_{RLL}|$ for 'N-S' track. White triangular represents a winter wheat field.

higher roughness level than the roughness estimates from the $|\gamma_{RLL}|$ as discussed in Chapter 4.1.5. and [126,270]. This effect is clearly visible for both tracks ('E-W', 'N-S') in Figure 100. The different view angles of the two flight headings together with the orientation of the agricultural fields influence the estimated soil roughness values. This is especially visible on the very smooth winter wheat field in the 'N-S'-track (see white triangles in Figure 100) compared with the same field in the 'E-W'-track. In this way, the influence of preferential orientations on the fields, triggered by soil tillage, becomes evident for the estimation of soil roughness.

For a quality assessment the estimated soil roughness is compared with the measured soil roughness acquired by stereo-photogrammetry and by laser profiling for the 'E-W' and 'N-S'-track of the AgriSAR campaign on the 19th of April 2006 (cf. Chapter 5.1.1. for measurement techniques). At this time in spring the fields were still quite bare, while the vegetation parts, which already emerged from the soil, were removed before the roughness measurements on ground. The comparison with scenes later than April in the growth cycle does not provide deeper insights, because these 'classical' roughness descriptors do not account for the vegetation

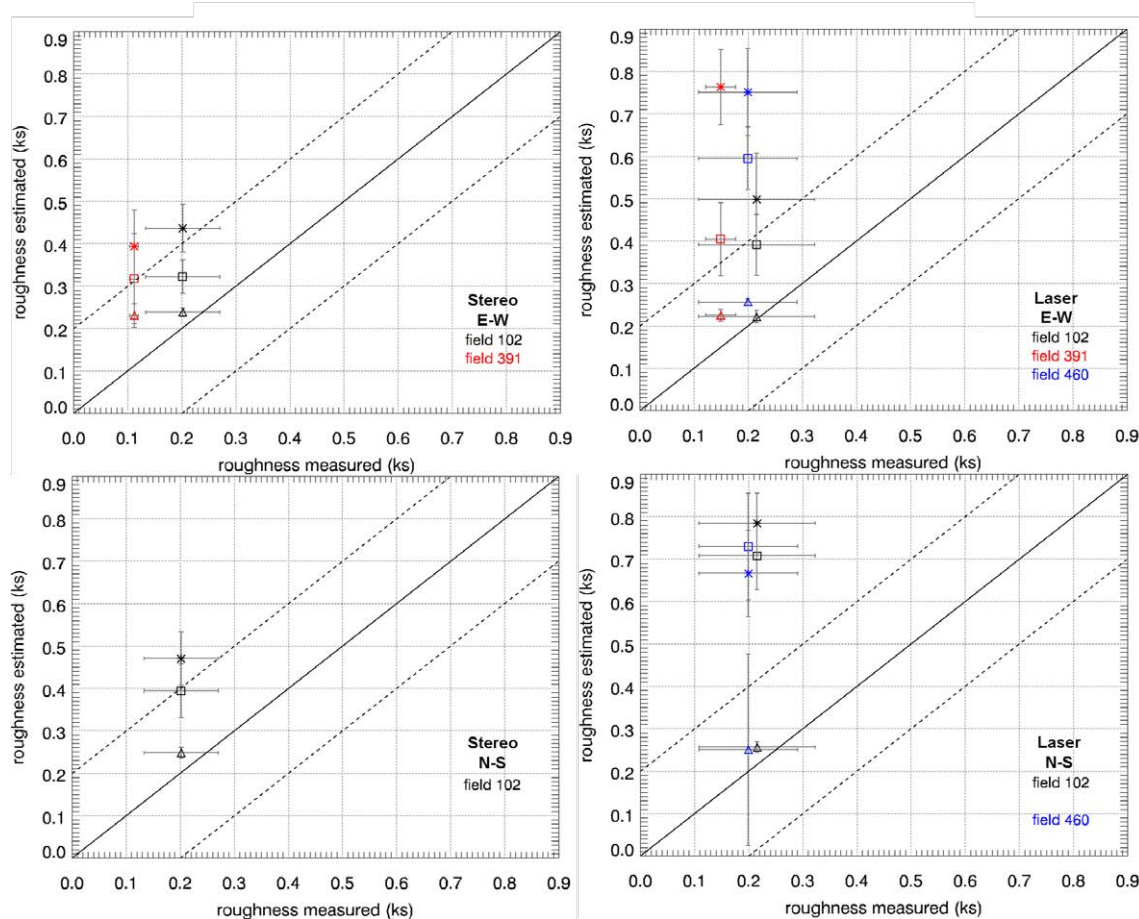


Figure 101: Validation of measured against estimated soil roughness values (ks) using anisotropy (stars), circular coherence magnitude (squares) and the modified X -Bragg ratio of Equation 218 (triangles) as methods for 'E-W'-track (top) and 'N-S'-track (bottom) of the AgriSAR campaign on 19th/20th of April 2006; Comparison with measurements from stereo-photogrammetry 'Stereo' (left) and with measurements from laser profiler 'Laser' (right) on sugar beet (102, 460) and winter wheat (391) fields; Gray bars indicate the standard deviation of the measurements and the estimates. A box of 9x9 pixels around each measurement location were taken for validation. [150].

disturbance and therefore are not applicable as soon as the vegetation layer covers the soil surface.

Focusing on the April data, illustrated in Figure 101, the roughness retrieved from the anisotropy A and the circular coherence magnitude $|\gamma_{RLL}|$ considerably overestimate the measured soil roughness values for both measurement techniques. In contrary, the results, applying the modified X -Bragg ratio of Equation 218, indicate the best agreement with the roughness measurement from stereo-photogrammetry as well as laser profiling.

6.2.2. Results for soil roughness retrieval under vegetation cover

Moving from bare to vegetated soils, the influence of the disturbing vegetation cover has to be considered within the soil roughness retrieval. Unfavorably, the vegetation is also generating a cross-polarized backscattering component, just like the soil roughness. In order to separate the two cross-polarized scattering contributions for a roughness retrieval under vegetation cover, the normalized *Pauli*-based ground-to-volume ratios are a possible option.

6.2.2.1. Inversion and validation of the modified X -Bragg ratio approach

The normalized *Pauli*-based ground-to-volume ratios were incorporated into an X -Bragg ratio, which proved its sensitivity to soil roughness on bare soils (cf. [127] and Chapter 4.2.8.1.). In this way only the part of the cross-polarized scattering component, which is caused by the soil roughness and not by the vegetation, is applied for the retrieval of soil roughness under vegetation cover.

Figure 102 presents the result for the soil roughness (ks) estimation under vegetation cover using the algorithm with normalized *Pauli*-based ground-to-volume ratios (cf. Chapter 4.2.8.1.) for the 19th/20th of April, the 6th/7th of June and the 5th/6th of July 2006. The level of the inverted soil roughness values appears quite similar for most of the fields on the three dates, despite the fact that the vegetation cover was significantly different (maximum vegetation height: 18cm in April, 172cm in July). The similarity of the results for the soil roughness estimates indicate the potential of soil roughness estimation under a growing vegetation cover using the approach outlined in Chapter 4.2.8., whereby no soil cultivation is assumed after plant emergence. A validation of the estimated soil roughness values compared with the measured soil roughness values from three dimensional stereo-photography, using mean of crop type values, is shown in Figure 103. A

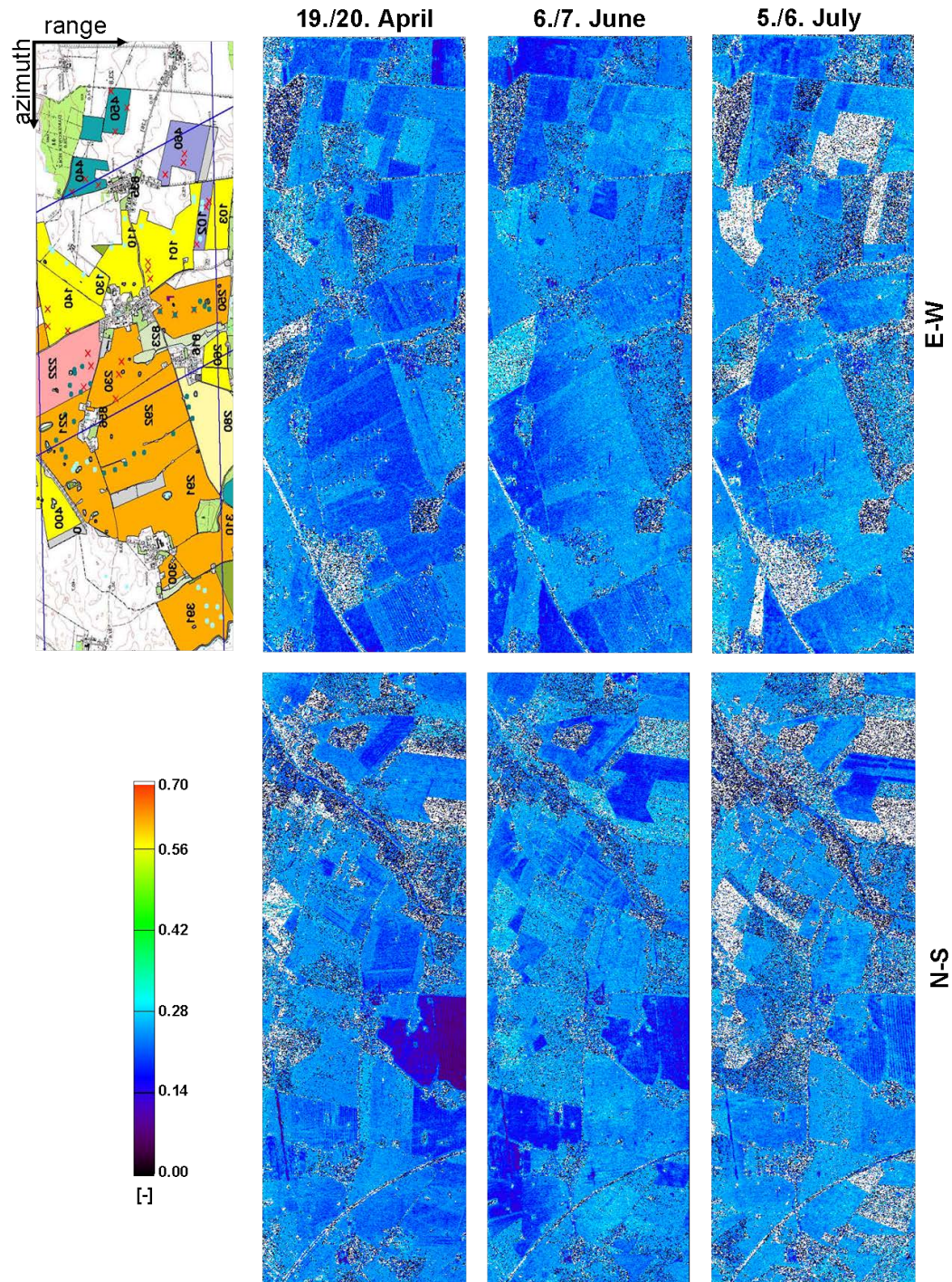


Figure 102: Estimated soil roughness (ks) using the modified *X-Bragg* ratio including the normalized *Pauli*-based ground-to-volume ratios for the AgriSAR 2006 campaign for the 'E-W'-track (top row) and the 'N-S'-track (bottom row) covering an entire vegetation growth period (from left to right): 19th/20th of April 2006, 6th/7th of June 2006 and 5th/6th of July 2006; Values range from 0 to 1, while areas with very rough soil conditions ($ks > 0.7$) are masked white [150].

6.2. RESULTS FOR SOIL ROUGHNESS

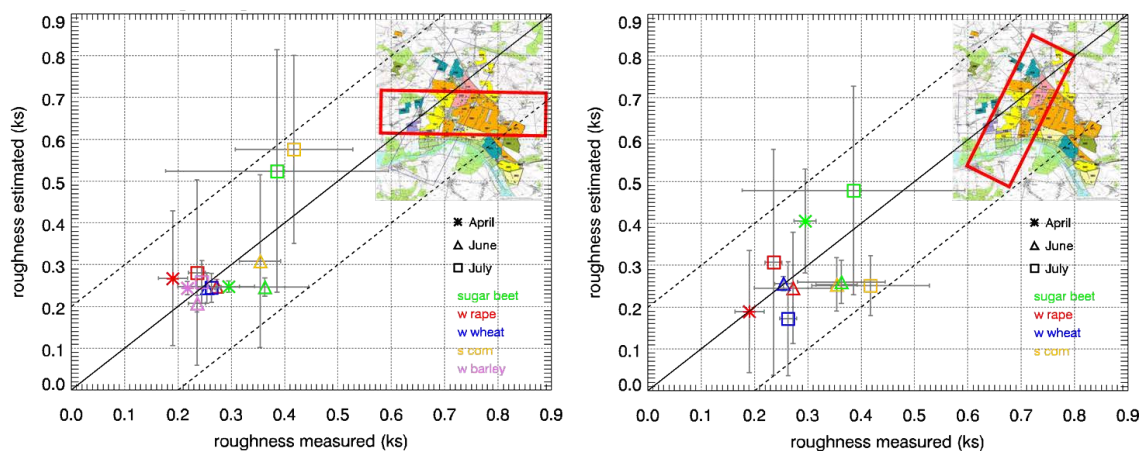


Figure 103: Validation of mean measured against mean estimated soil roughness (k_s) for the 'E-W'-track (left) and for the 'N-S'-track (right) of the AgriSAR 2006 campaign covering an entire vegetation growth period (April, June, July) and different crop types (s=summer, w=winter); Gray bars indicate the measured and the estimated standard deviation for each crop type and for each date [150].

box of 13x13 pixels was drawn around each measurement location to realize 169 looks for comparison. The standard deviations of the roughness measurements are calculated from the different sampling locations for each crop type. The standard deviations of the estimated roughness values are computed from the mean of the standard deviations retrieved from each sampling box around the measurement location.

The average RMSE of the roughness estimation for the 'E-W'-track and the 'N-S'-track over all crop types and all dates is 0.098 and 0.121 respectively, whereas a high standard deviation ($\Delta k_s > 0.2$) must be stated. This occurs mainly for the winter rape, the sugar beet and the summer corn fields in July owing a mature vegetation layer of about 45-170cm and 2-6kg/m² wet biomass. Moreover this denotes the uncertainty introduced in the retrieval by the distinct vegetation layer, which can only be eliminated to a certain extent by the presented approach. But despite the different headings ('E-W'-track, 'N-S'-track) the overall-RMSE stays in a comparable range, which indicates the low bias of the two dimensional roughness retrieval approach to different orientations of field furrows.

6.2.3. Best approach for soil roughness retrieval under vegetation cover

Reviewing the status of the retrieval studies presented in this thesis, only the algorithm incorporating the modified *X-Bragg* ratio is capable to deal with a soil

roughness retrieval under vegetation cover. Therefore only this algorithm applies. The best RMSE for the soil roughness estimation was achieved on the 'E-W'-track including all crop types and all dates with a soil roughness k_s equal to 0.098, which corresponds to a standard deviation of the vertical roughness s of 0.37cm.

Part 7

Summary and conclusions

In the following, the performance, achieved with the different retrieval algorithms for soil parameter estimation, is summarized, conclusions are drawn and a look into the future is attempted.

7.1. Summary

For reasons of soil heterogeneity, topography, but also of atmospheric forcing and plant dynamics, soil moisture varies distinctively in time and space [242]. One of the major challenges in hydrological sciences represents therefore the understanding and characterization of this variability as well as the establishment of a continuous monitoring system of the vadose zone properties [242]. Due to the high spatial resolution and the sensitivity for dielectric and geometric properties of scatterers, SAR systems can contribute significantly and thus qualify as crucial components in this monitoring system. Consequently, a soil parameter retrieval from field to catchment scale can be supported with a spatial resolution in the range of meters.

This thesis intends to contribute in understanding and assessing the role that SAR polarimetry at L-band can play in this context. Physically-based inversion models and algorithms, which exploit the PolSAR observation space, were developed for soil characterization under vegetation cover without the necessity of *a priori* knowledge. These (multi-angular) polarimetric decomposition and inversion methods were applied on L-band airborne PolSAR data of the AgriSAR 2006, OPAQUE 2007, OPAQUE 2008 and SARTEO 2008 campaigns, acquired by the E-SAR sensor of DLR. Subsequently, the inversion results were compared with ground measurements of soil moisture and soil roughness, covering the entire vegetation growth period and a variety of soil, crop type as well as terrain conditions. Four different types of polarimetric decomposition methods were applied on these data using state-of-the-art techniques (cf. Chapter 4.1.4.) and newly developed methods (cf. Chapter 4.2.):

- Eigen-based decompositions (cf. Chapter 3.2.4.1. and 4.1.4.)
These decompositions use the eigen-space, spare pre-defined/rigid scattering components, necessary in model-based decompositions, and are independent of

topographic variations along the *azimuth*. In contrary, depolarizing components of vegetation and/or ground scattering, can not be separated from polarized scattering components hampering a direct inversion of the latter.

- Model-based decompositions (cf. Chapter 3.2.4.2. and 4.2.)
Model-based decompositions enable the separation of vegetation- and/or roughness-induced depolarization from ground scattering components for a subsequent inversion. But the quality of inversion depends on the correctness and complexity of the applied volume/ground scattering models. Their parameterization is confined by the available observation space and leads to necessary, but crucial simplifications.
- Hybrid decomposition (cf. Chapter 4.2.6.)
The hybrid decomposition unifies the benefits of the first two decompositions resulting in a physically meaningful separation of volume and ground components as well as of the ground components themselves. Unfortunately, a certain performance loss for inversion of steep local incidence regions, which is inherent in all model-based decompositions due to model insensitivities, is still present in this case.
- Multi-angular model-based decomposition (cf. Chapter 4.2.7.)
The multi-angular inversion technique copes with the performance losses in regions with steep local incidence (distinct topography) due to the enlarged observation space, but still inherits the dependency of the model-based decompositions on the applied scattering models and their appropriate parameterization.

The performance achieved by the different soil parameter retrieval approaches have been presented and discussed in Part 6 and are summarized in Table 20. In the following the main results and conclusions are consolidated:

- Soil moisture inversion of bare soils (Chapter 6.1.1.) [159]:
The single component *X-Bragg* approach of [127] for soil moisture inversion on bare soils can only be applied on a very limited amount of non-vegetated or very sparsely vegetated fields and performs best in terms of inversion rate for regions of shallow local incidence angle ($\theta_l > 50^\circ$). For all acquisitions only very small inversion rates of less than 5% can be obtained. This result can be explained by the high polarimetric entropy of the PolSAR data mostly due to the presence of vegetation, which is only predicted by the *X-Bragg* model for regions of shallow local incidence and therefore leads to the distinct overestimation shown in the validation plots of Figure 76.

- Soil moisture inversion of bare and vegetated soil using single angular modified model-based decompositions (Chapters 6.1.2.1.-6.1.2.3.) [159, 150, 39]:

The results of the modified three component model-based polarimetric decompositions demonstrate their applicability on vegetated agricultural fields enabling a physically meaningful separation of scattering contributions, which is depicted in Figures 79-81. Moreover, both ground scattering components (surface, dihedral) have been used for the estimation of soil moisture. Useful inversion results have been achieved in the presence of 45cm vegetation height and 0.9kg/m² wet biomass (OPAQUE 2007, low vegetation scenario) as well as for 172cm vegetation height and 6.24kg/m² wet biomass (July, AgriSAR 2006, high vegetation scenario).

The retrieved soil moisture values are validated against ground measurements taken by TDR, FDR and gravimetric probes. Across all three campaign data sets, the RMSE of the estimated soil moistures from both scattering contributions (surface, dihedral), including all investigated crop types, exhibits an accuracy of 8.59-13.04vol.%. Nevertheless, a mean standard deviation of the estimated soil moistures of 10.31-13.01vol.% indicates a broad range of inverted soil moisture values.

Reasons for this outcome might be on one side the temporally and spatially highly varying scattering scenarios inverted with a limited number of PolSAR observables, using for instance a pre-defined dihedral loss factor, including the vegetation attenuation and the roughness scattering loss. On the other side, the characteristics of soil moisture itself might be a reason, which is also varying distinctly within one field parcel. Further investigations were necessary to gain a deeper understanding of the scattering volume disturbance and to improve its modeling as well as to study the influence of topography on the inversion of soil moisture.

For reasons of an improved disturbance handling within the vegetation volume, the normalized *Pauli*-based ground-to-volume ratios Pa were incorporated in the single angular model-based decomposition algorithm to improve the separation of the cross-polarized scattering component coming from both, the vegetation volume and the surface roughness (cf. Chapter 4.2.5.3.). The inverted results indicate a positive trend in terms of soil moisture inversion under a variety of vegetation cover. The inversion rate increased from around 25-35% for the model-based approach to about 35-45% for the approach including the normalized *Pauli*-based ground-to-volume ratios (cf. Tables 13 and 14). The largest increase of invertible pixels occurs for the land use classes with a

strong volume component, like winter rape, due to the better separation of the cross-polarization component. In comparison to the field measurements, the inverted soil moisture under vegetation cover is retrieved with an RMSE from 6.80vol.% (AgriSAR in April 2006) to 13.20vol.% (OPAQUE 2007) (cf. Table 14). But comparing all campaigns, the RMSE-level is only ~ 1 -2vol.% lower (AgriSAR) or higher (OPAQUE, SARTEO) than for the algorithm presented before in Chapter 6.1.2.1., which yields only a small improvement or a small deterioration of the RMSE. However, the occurrence of distinct outliers (outside the ± 20 vol.%-interval) is strongly reduced for the model-based approach incorporating the normalized *Pauli*-based ground-to-volume ratios due to a better cross-polarization separation (cf. Figures 83-84 with Figure 91). For the AgriSAR campaign, the measured vegetation canopy reached up to a maximum height of 172cm and a maximum wet biomass of 6.24kg/m² in July 2006. For this multi-temporal campaign, the inversion by the model-based decomposition approach incorporating the normalized *Pauli*-based ground-to-volume ratios results in a RMSE between 6.80vol.% and 12.39vol.% for the estimation of soil moisture covering the whole growth period (April-July 2006) as well as different soil moisture conditions. Despite the promising RMSE for the April and June date (RMSE < 7.8vol.%) of the AgriSAR campaign, the standard deviation of the inversion estimates (cf. Table 14) reports a significant uncertainty especially concerning the intra-field variability. This observation still claims for a more sophisticated separation of volume and ground contributions and of the ground contributions themselves. A possible solution are hybrid polarimetric decompositions.

- Soil moisture inversion of bare and vegetated soils using a single angular hybrid decomposition (Chapter 6.1.2.4.) [152, 153, 156]:

The hybrid polarimetric decomposition, using eigen-based as well as model-based decomposition techniques and incorporating a physically constrained volume intensity component $f_{V_{ch}}$, were introduced in Chapter 4.2.6.. The algorithm with a physically meaningful ground/vegetation separation was applied for inversion of soil moisture under vegetation cover. The approach is not depending on the volume particle shape α_v of the vegetation and results in a physically guided separation of surface and dihedral scattering mechanisms, using an orthogonality condition shown in Figure 93.

The α_1 -criterion for retrieval of the appropriate ϵ_{est} -level indicated a clear minimum for the different campaign sites and acquisition dates, stating a stable performance to separate volume and ground contributions (cf. Table 15) over

a wide range of topography (OPAQUE campaigns) and over a diversity in vegetation phenology (AgriSAR and SARTEO campaigns). A continuous and consistent inversion of the surface scattering component is achieved for all dates of the three campaigns, including diverse crop types in different phenological conditions (cf. Figure 94).

The inversion rate remains always higher than 97%, while the vegetation was significantly changing along the growing cycle from a maximum height of 18cm in April to a maximum height of 172cm in July (AgriSAR campaign). A quality assessment of the algorithm was carried out by validation with TDR, FDR and gravimetric measurements. For all scenes, including a variety of vegetation types in different phenological stages and different topographical conditions, the RMSE-level ranges between 4.4vol.% and 11.0vol.% and the mean of the STDDEV varies only between 2.1vol.% and 5.2vol.% compared to the previously presented algorithms (cf. Table 20). Due to the high inversion rate and the sufficient inversion accuracy a decreasing trend in soil moisture could be tracked for the AgriSAR campaign ranging from a level of ~ 25 vol.% in April (start of growth period) to a level of ~ 8 vol.% in July (end of growth period).

However, the vegetation volume component $[T_V]$ is only considered as a random volume, neglecting distinct orientations within the vegetation volume. Therefore strongly orientated vegetation and a shallow local incidence (long ray path through vegetation), like in the case of the winter wheat and winter barley fields (OPAQUE 2007 campaign with RMSE=11vol.%), affect the quality of the current decomposition procedure. In addition, a certain dependency of the inversion on the local incidence angle is still present in the results. Therefore a regionalization of the α_1 -criterion, leading to a spatially varying ε_{est} -level, might result in an improved inversion. Another solution is the implementation of a multi-angular polarimetric decomposition for soil moisture inversion.

- Soil moisture inversion of bare and vegetated soils using a multi-angular model-based decomposition (Chapter 6.1.2.5.) [151, 155]:

Within the developed algorithm, the polarimetric and the multi-angular observation space are unified for a combined multi-angular polarimetric decomposition and inversion of soil moisture under vegetation cover. The multi-angular polarimetric decomposition algorithm and the inversion procedure with minimum of absolute differences were applied to the data of the OPAQUE 2008 campaign, acquired in the Weisseritz catchment area. The results state a significant rise of inversion rate from 30% for one of the single-angular cases to 70% for the multi-angular case, including three acquisitions, in Chapter 6.1.2.5..

In addition, the results demonstrate, how topographic effects caused by steep slopes can be compensated for soil moisture inversion, if more than a single acquisition is used (cf. Figure 98). The estimated soil moisture values were validated against ground measurements from FDR probes for the OPAQUE 2008 test site including several different crop types.

The mean-RMSE of the soil moisture retrieval with the different incidence angle configurations indicates a stable inversion for the majority of methods resulting in an error level of approximately 6-8vol.% (level of mean-STDDEV within the boxes 10-11vol.%) with a slight improvement for the tri-angular approach incorporating three acquisitions (*master-opposite-perpendicular*) with a mean-RMSE of 5.9vol.% (mean-STDDEV within the sampling boxes of 9.5vol.%). The RMSE decreases not automatically as more acquisitions are included in the soil moisture retrieval.

This might be due to the following assumptions necessary to obtain an analytically solvable inversion problem with the limited observation space. The roughness term (ψ_l) and the volume component inside the model-based decomposition [T_{GV}] as well as the bare soil classification with the $H-\bar{\alpha}$ criterion are estimated for each acquisition separately. This can lead to a reduced quality of the results for certain ranges of local incidence angles on natural media due to model insensitivities (cf. Chapter 4.2.5.).

Hence, the quality of an inversion, using a combination of two, three or more acquisitions for a multi-angular approach, can be affected by insufficient assumptions on the single acquisitions. This explains, why the incorporation of more than one acquisition within the algorithm is not necessarily resulting in a distinct accuracy improvement of the soil moisture estimation. For example, the configuration using the *opposite-* and the *perpendicular-*acquisition in a bi-angular approach obtains a mean-RMSE of 8.15vol.%, which is distinctly higher than utilizing only the *master-*acquisition with 6.17vol.% of mean-RMSE (cf. Chapter 6.1.2.5.1.).

But it turns out that a configuration of ascending and descending acquisitions (like *master-opposite*) is more favorable than a configuration with *perpendicular* headings (like *opposite-perpendicular*), considering equivalent local incidence angle conditions for both configurations (cf. Table 4). This might be caused by preferential orientations of soil furrows and of agricultural vegetation.

Hence, the developed multi-angular approach combines for the first time polarimetric decomposition techniques with the concept of multi-angularity. This adds up to a major increase in inversion rate for soil moisture estimation and a stable

inversion quality over all investigated test fields for the majority of incidence angle configurations. The remaining uncertainties of the developed approach, rooted in some assumptions of the polarimetric decompositions, have to be addressed in future studies in order to better estimate the input parameters for the decomposition as well as to establish a more robust criterion for distinguishing bare and vegetated soils in the case of low vegetation scenarios.

- Soil roughness inversion of bare soils (Chapter 6.2.1.):

Soil roughness was estimated on bare soils using the anisotropy A , the circular coherence magnitude $|\gamma_{RRL}|$ and the modified X -Bragg ratio ζ . The estimated soil roughness values were compared with roughness measurements from laser profiling and from stereo-photogrammetry. The validation was carried out on sugar beet and winter wheat fields in April 2006 (beginning of vegetation growth period with no or little vegetation), where a distinct overestimation of the ‘classical’ roughness descriptors (A and $|\gamma_{RRL}|$) compared to ζ was observed for the ‘E-W’ and the ‘N-S’ track in Figure 101. Here, ζ benefits as an estimator that takes only the roughness induced part of the cross-polarized scattering component into account.

- Soil roughness inversion of vegetated soils (Chapter 6.2.2.) [150]:

The vegetation cover causes a necessary separation of the cross-polarized scattering component S_{XX} for a valid soil roughness inversion. Therefore normalized *Pauli*-based ground-to-volume ratios were included in the decomposition formalism to develop a modified X -Bragg ratio ζ , which uses only the roughness part included in the cross-polarized component. The results for the AgriSAR 2006 campaign indicate a high potential in terms of soil roughness estimation under a variety of vegetation cover conditions (maximum height: 172cm and maximum wet biomass: 6.24kg/m²) over the whole growth period (April-July) as well as under different soil moisture conditions. This results in an overall-RMSE in $ks|_s$ of less than 0.10|0.37cm (‘E-W’-track) and of less than 0.12|0.44cm (‘N-S’-track) for the estimation of soil roughness indicating a marginal dependence of the algorithm performance on the orientation of field furrows.

7.2. Contributions

The main goal of this thesis was the extension of soil parameter retrieval from bare to vegetated soils using fully polarimetric SAR data towards a continuous monitoring of soil moisture and soil roughness. The main scattering contributions from the soil and the vegetation have been accessed through polarimetric decomposition and inversion algorithms. The following innovative contributions can be recognized:

- Polarimetric model-based decompositions, foremost developed for forested areas, were adapted and applied to agricultural scattering scenarios.
- Single- and multi-angular, polarimetric decomposition algorithms have been developed and/or optimized to increase their flexibility to cover different soil and vegetation scattering scenarios.
- Generally valid and transferable (to different test sites) algorithms for soil parameter retrieval under vegetation cover using fully polarimetric SAR data were established.
- L-band was approved to be an ideal frequency for soil parameter retrieval under agricultural vegetation cover due to the adequate penetration of the vegetation canopy combined with an sufficient signal-to-noise ratio (SNR) on bare fields.
- Soil moisture and soil roughness estimation under agricultural vegetation cover was successfully applied with considerable inversion rates indicating the spatial distribution of both soil parameters.
- Monitoring (excluding frozen and snow-covered soils) of soil characteristics with a precision of 5-10vol.% in soil moisture (range of *in situ* values: 1-46vol.%) and 0.1|0.37cm-0.15|0.55cm in soil roughness $ks|s$ (range of *in situ* values: 0.14|0.5cm-1.09|4.0cm) within the catchment seems already possible with the developed fully polarimetric SAR algorithms.

Besides airborne SAR campaigns, also future space-borne, long wavelength SAR missions like ALOS-2 [160] and Tandem-L [171] can benefit from the developed techniques to estimate soil parameters and to separate soil from vegetation contributions using polarimetric SAR.

The joint occurrence of volume and ground scatterers appears further in different natural scattering scenarios (in terms of vegetation and soil surface, snow pack and soil surface, ice surface and glacier volume, sea ice volume and water

surface). Therefore the modular scattering components of the polarimetric SAR decomposition algorithms can also be adapted to non-agricultural volume and ground cases [273,248].

7.3. Outlook

The retrieval of soil parameters by means of SAR remote sensing received an innovative and vital impulse by the use of polarimetric decomposition algorithms developed on the basis of fully polarimetric acquisitions. The next logical step might be the integration of PolSAR-derived soil moisture into hydrological models using data assimilation techniques. In terms of inversion and modeling the next challenge is the extension of soil parameter estimation beyond the agricultural case. Both are discussed in the following.

Data assimilation and hydrological modeling

Concerning data assimilation in hydrological models, emphasis should be put on the combination of polarimetric SAR remote sensing with geophysical methods (e.g. Ground Penetrating Radar [137]), in order to obtain high-resolution soil moisture in both, horizontal and vertical dimension. In this way, also the total amount of water in the vadose zone, can be assessed, whereas microwave remote sensing approaches are only sensitive to the near surface soil moisture [260]. However, if no vertical soil moisture profiles are available, root zone moisture might also be retrieved by assimilation of remote sensing data into models [216], using for instance a particle filtering algorithm and the soil water model *HYDRUS*, ranging from the soil surface to the root zone (0-1m depth) [218]. The quality of such retrieval methods strongly depends on the knowledge of soil hydraulic properties [79] and on model initialization [332].

With respect to the horizontal dimension, the validity of upscaling and downscaling concepts for different soil moisture products and their ability to reflect the spatial variability of soil moisture should be further investigated for data assimilation purposes [16, 38]. This should allow an improved comparison of products from different sensors at different spatial scales [27] and subsequently lead to enhanced data assimilation concepts. The establishment of long-term terrestrial observatories is therefore essential for serving as multi-scale and multi-methodological sites for hydrological processes in the vadose zone [260, 39, 322, 335]. A novel probing technique for soil moisture, facilitating the monitoring in such observatories, is

Ground Albedo Neutron Sensing (GANS) [346] that bridges the ‘scale-gap’ [212] between intra-field (field scale) and inter-field variability (hillslope scale) [259]. Due to its spatial coverage beyond the field scale, it is particularly well suited for comparison with the SAR-derived soil moisture patterns.

In order to exploit the improved capabilities to monitor soil moisture variation in space and time, hydrological modeling of the vadose zone processes is crucial to improve the characterization and quantification of hydraulic parameters and hydrological fluxes within the soil. Therefore the retrieved spatial soil moisture patterns should be used to initialize/update hydrological (e.g. WaSim-ETH [271]) or Soil Vegetation Atmosphere Transfer (SVAT) models (e.g. PROMET-V [269]) based on data assimilation procedures [136, 332, 240, 333, 185, 220, 253]. A comprehensive review on existing assimilation methods is given in [322].

Hence, an upcoming need for distributed hydrological models exists. In the moment pedotransfer-functions or climatic proxi-data are often applied in models to characterize the soil conditions [39, 10]. In particular, the lateral flow through the soil macropores needs to be included to improve the process description of hydrological models by inclusion of a downslope subsurface flow [260, 344].

A restriction of remotely sensed soil moisture to support hydrological modeling for flood prediction, especially concerning flash floods with a very quick response to storm events, is given by the temporal resolution of actual space-borne SAR sensors [37]. A solution towards sufficient temporal and spatial coverage is expected from future, innovative, space-borne SAR mission concepts, as for example Tandem-L [171].

SAR Remote Sensing and soil parameter retrieval

The performance of polarimetric decompositions for soil moisture retrieval from PolSAR data raises hope for the application of these techniques beyond the work in this thesis and indicates the innovative potential of the decomposition approaches for soil characterization [209].

However, concerning the global applicability of PolSAR decomposition algorithms for soil parameter retrieval under vegetation, forested areas are still excluded due to the different scattering scenario. Some concepts already exist, how to retrieve soil moisture under forest using P-band [121, 157, 215] or VHF/UHF-band [214] polarimetric SAR remote sensing. The lower frequencies (compared to L-band) should provide enough penetration through the forest canopy, to obtain soil information from the underlying ground. But no concept has proven its applicability yet.

A missing component is also the soil moisture retrieval under snow cover and for frozen soils, which is not assessed by any polarimetric SAR approach at the moment [329] and gains importance in higher latitudes or during winter times in mid-latitudes.

Besides the case of snow-covered and forested regions, also the soil parameter retrieval under agricultural vegetation cover is still a challenging case despite the achievements presented and discussed. Several assumptions for the soil and vegetation layer had to be made to confine the observable space to enable inversion. For instance the soil was assumed as non-penetrable, which neglects possible volume scattering [65] and the presence of sub-surface layers [103, 173]. This becomes increasingly important for dry soils and longer wavelengths.

In addition, the PolSAR algorithms, applied in Part 6, assume a vegetation layer, characterized by one single volume of uniformly shaped particles with certain orientation distributions. Hence, the existence of a multi-layered volume including differently shaped plant constituents has not been considered. Even strongly oriented vegetation cases, causing differential propagation effects (cf. Equation 159), were not taken into account in the applied retrieval methods.

Concerning these remaining challenges, several other ways emerged to characterize or remove the disturbing vegetation layer and to extract the underlying soil information. Each domain is an innovative area of contemporary SAR research and involves a more complex acquisition method than solely (multi-angular) polarimetric SAR, leading to an increased observation space for inversion:

- Retrieval of vegetation height and vegetation extinction with Polarimetric Synthetic Aperture Radar Interferometry (Pol-InSAR) for agricultural areas [117, 191]. These Pol-InSAR-derived parameters can be included in PolSAR volume scattering models to account for propagation effects within the vegetation layer [65].
- Bistatic soil moisture retrieval using the non-reciprocity of the cross-polarized channels ($S_{HV} \neq S_{VH}$) and the bistatic angle to find the optimum configuration for soil moisture estimation [52, 247, 293].
- Decomposition of vegetation and ground scattering components by polarimetric SAR tomography using multiple acquisitions to vertically sample the vegetation covered soil, in order to retrieve the parts of the backscattered signature, which originate predominantly from the soil [290, 291].

Future upcoming, space-borne, fully polarimetric, long wavelength SAR missions, like ALOS-2 and Tandem-L, will benefit considerably from the applications, de-

veloped in the field of polarimetric SAR remote sensing [221]. In addition, also in the future, combined active-passive microwave missions, which merge a low resolution moisture product from the passive sensor with an high resolution one from the active sensor, will profit distinctively by incorporating an enhanced high resolution product from polarimetric SAR into their applications.

However, the performance of all space-borne, long wavelength retrieval methods will depend on the correction of the ionospheric effect on the polarimetric SAR signature [340, 21]. First promising results for a successful removal on ALOS-data are already demonstrated in [210].

Concludingly, this work is a step towards soil sensing under vegetation cover. But in order to put things in the right perspective, I would like to share a quote of *Žarko Petan*:

‘In the end always truth will win. But unfortunately we are just in the beginning’. In this sense: . . . Back to work, there is still a lot to do. . .

Bibliography

- [1] B.P. Ablitt. *Characterization of Particles and their Scattering Effects on Polarized Light*. PhD thesis, University of Nottingham, 2000.
- [2] B.P. Ablitt, K.I. Hopcraft, K.D. Turpin, P.C.Y. Chang, J.G. Walker, and E. Jakeman. Imaging and multiple scattering through media containing optically active particles. *Waves in Random and Complex Media*, 9:561–572, 1999.
- [3] S. Allain. *Caractérisation d'un sol nu à partir de données SAR polarimétriques Etude multi-fréquentielle et multi-résolutions*. PhD thesis, Université de Rennes 1, 2003.
- [4] J. Alvarez-Mozos, N.E.C. Verhoest, A. Larranaga, J. Casali, and M. Gonzalez-Audicana. Influence of surface roughness spatial variability and temporal dynamics on the retrieval of soil moisture from SAR observations. *Sensors*, 9:463–489, 2009.
- [5] T.P. Anguela, M. Zribi, N. Baghdadi, and C. Loumagne. Analysis of local variation of soil surface parameters with TerraSAR-X radar data over bare agricultural fields. *IEEE Transactions on Geoscience and Remote Sensing*, 48:874–881, 2010.
- [6] M. Ariei. *Retrieval of soil moisture under vegetation using polarimetric RADAR*. PhD thesis, California Institute of Technology, 2009.
- [7] M. Ariei, J.J. van Zyl, and Y. Kim. A general characterization for polarimetric scattering from vegetation canopies. *IEEE Transactions on Geoscience and Remote Sensing*, 48:3349–3357, 2010.
- [8] M. Ariei, J.J. van Zyl, and Y. Kim. Adaptive model-based decomposition of polarimetric SAR covariance matrices. *IEEE Transactions on Geoscience and Remote Sensing*, 49:1104–1113, 2011.
- [9] E. Attema and F.T. Ulaby. Vegetation modelled as a water cloud. *Radio Science*, 13:357–364, 1978.
- [10] N. Baghdadi, O. Cerdan, M. Zribi, V. Auzet, F. Darboux, M. El Hajj, and R.B. Kheir. Operational performance of current synthetic aperture radar sensors

- in mapping soil surface characteristics in agricultural environments: Application to hydrological and erosion modelling. *Hydrological Processes*, 22:9–20, 2008.
- [11] N. Baghdadi, S. Gaultier, and Ch. King. Retrieving surface roughness and soil moisture from SAR data using neural networks. In *Proc. of International Symposium on Retrieval of Bio- and Geophysical Parameters from SAR Data for Land Applications, Sheffield, U.K., September 11-14*, pages 315–319, 2001.
- [12] N. Baghdadi, N. Holah, and M. Zribi. Soil moisture estimation using multi-incidence and multi-polarization ASAR data. *International Journal of Remote Sensing*, 27:1907–1920, 2006.
- [13] N. Baghdadi, C. King, A. Chanzy, and J.P. Wigneron. An empirical calibration of the integral equation model based on SAR data, soil moisture and surface roughness measurements over bare soil. *International Journal of Remote Sensing*, 23:4325–4340, 2002.
- [14] N. Baghdadi, P. Paillou, M. Davidson, G. Grandjean, and P. Dubois. Relationship between profile length and roughness parameters for natural surfaces. *International Journal of Remote Sensing*, 21:3375–3381, 2000.
- [15] J.D. Ballester-Berman. *Retrieval of biophysical parameters of agricultural crops using polarimetric SAR interferometry*. PhD thesis, University of Alicante, 2007.
- [16] A. Bárdossy and W. Lehmann. Spatial distribution of soil moisture in a small catchment. Part 1: Geostatistical analysis. *Journal of Hydrology*, 206:1–15, 1998.
- [17] B.C. Bates, Z.W. Kundzewicz, S. Wu, and J.P. Palutikof. Climate change and water. Technical report, Intergovernmental Panel on Climate Change, IPCC Secretariat, Geneva, Switzerland, 2008.
- [18] A. Baumgartner and H.J. Liebscher. *Allgemeine Hydrologie, Quantitative Hydrologie*. Borntraeger Verlag, Berlin, Germany, 1996.
- [19] E. Baur, S. Buckreuss, W. Holpp, P. Honold, W. Keydel, H. Klausning, and A. Moreira. *Radar mit realer und synthetischer Apertur: Konzeption und Realisierung*. Oldenburg Verlag, Munich, Germany, 2000.

- [20] P. Beckmann and A. Spizzichino. *The Scattering of Electromagnetic Waves from Rough Surfaces*. Pergamon Press, Oxford, U.K., 1963.
- [21] D.P. Belcher. Theoretical limits on SAR imposed by the ionosphere. *IET Radar, Sonar and Navigation*, 2:435–448, 2008.
- [22] R. Bernard, Ph. Martin, J.L. Thony, M. Vauclin, and D. Vidal-Madjar. C-band radar for determining surface soil moisture. *Remote Sensing of Environment*, 12:189–200, 1982.
- [23] R. Bianchi, M. Davidson, I. Hajnsek, M. Wooding, and C. Wloczyk. AgriSAR 2006 - final report. Technical report, European Space Agency, 2006.
- [24] R. Bindlish, T.J. Jackson, and R. van der Velde. High resolution soil moisture mapping using AIRSAR observations during SMEX02. In *Proceedings of International Geoscience and Remote Sensing Symposium, Denver, USA, July 31 - August 4*, pages 2324 – 2327, 2006.
- [25] J.R. Birchak, C.G. Gardner, J.E. Hipp, and J.M. Victor. High dielectric constant microwave probes for sensing of soil moisture. *Proceedings of the IEEE*, 62:93–98, 1974.
- [26] X. Blaes and P. Defourny. Characterizing bidimensional roughness of agricultural soil surfaces for SAR modelling. *IEEE Transactions on Geoscience and Remote Sensing*, 46:4050–4061, 2008.
- [27] G. Blöschl and M. Sivapalan. Scale issues in hydrological modelling: A review. *Hydrological Processes*, 9:251–290, 1995.
- [28] T. Blume, E. Zehe, and A. Bronstert. Use of soil moisture dynamics and patterns at different spatio-temporal scales for the investigations of subsurface flow processes. *Hydrology and Earth System Sciences*, 13:1215–1234, 2009.
- [29] W.-M. Boerner, M.B. El-Arini, C.-Y. Chan, and P.M. Mastoris. Polarization dependence in electromagnetic inverse problems. *IEEE Transactions on Antennas and Propagation*, AP-29:262–271, 1981.
- [30] H.R. Bogaen, M. Herbst, J.A. Huisman, U. Rosenbaum, A. Weuthen, and H. Vereecken. Potential of wireless sensor networks for measuring soil water content variability. *Vadose Zone Journal*, 9:1002–1013, 2010.
- [31] C.F. Bohren and D.R. Huffman. *Absorption and Scattering of Light by Small Particles*. Wiley-VCH Verlag, Hoboken, USA, 2004.

- [32] M. Born and E. Wolf. *Principle of Optics: Electromagnetic Theory of Propagation, Interference and Diffraction of Light*. Cambridge University Press, Cambridge, U.K., 1999.
- [33] M. Bracaglia, P. Ferrazzoli, and L. Guerriero. A fully polarimetric multiple scattering model for crops. *Remote Sensing of Environment*, 54:170–179, 1995.
- [34] A. Brandelik and C. Hübner. Soil moisture determination - accurate, large and deep. *Physics and Chemistry of The Earth*, 21:157–160, 1996.
- [35] B. Brisco, M.A. Hares, and W.D. Zebchuk. Soil moisture measurements using portable dielectric probes and time domain reflectometry. *Water Resources Research*, 28:1339–1346, 1992.
- [36] L. Brocca, F. Melone, T. Moramarco, W. Wagner, V. Naeimi, Z. Bartalis, and S. Hasenauer. Improving runoff prediction through the assimilation of the ASCAT soil moisture product. *Hydrology and Earth System Sciences Discussions*, 7:4113–4144, 2010.
- [37] L. Brocca, R. Morbidelli, F. Melone, and T. Moramarco. Soil moisture spatial variability in experimental areas of central Italy. *Journal of Hydrology*, 333:356–373, 2007.
- [38] A. Bronstert and A. Bárdossy. The role of spatial variability of soil moisture for modelling surface runoff generation at the small catchment scale. *Hydrology and Earth System Sciences*, 3:505–516, 1999.
- [39] A. Bronstert, B. Creutzfeldt, T. Graeff, I. Hajnsek, M. Heistermann, S. Itzerott, T. Jagdhuber, D. Kneis, E. Lueck, D. Reusser, and E. Zehe. Potentials and constraints of different type of soil moisture observations for flood simulations in headwater catchments. *Natural Hazards*, 60:879–914, 2012.
- [40] A. Bronstert, D. Niehoff, and G. Bürger. Effects of climate and land-use change on storm runoff generation: Present knowledge and modelling capabilities. *Hydrological Processes*, 16:509–529, 2002.
- [41] C. Brosseau. *Fundamentals of polarized light: A statistical optics approach*. Wiley & Sons, Hoboken, USA, 1998.

- [42] S.C.M. Brown, S. Quegan, K. Morrison, J.C. Bennett, and G. Cookmartin. High-resolution measurements of scattering in wheat canopies - implications for crop parameter retrieval. *IEEE Transactions on Geoscience and Remote Sensing*, 41:1602–1610, 2003.
- [43] L. Bruckler, H. Witono, and P. Stengel. Near surface soil moisture estimation from microwave measurements. *Journal of Remote Sensing and Environment*, 26:101–121, 1988.
- [44] R. Bryant, M.S. Moran, P.D. Thomas, C.D. Holifield Collins, S. Skirvin, M. Rahman, K. Slocum, P. Starks, D. Bosch, and M.P. González Dugo. Measuring surface roughness height to parameterize radar backscatter models for retrieval of surface soil moisture. *Geoscience and Remote Sensing Letters*, 4:137–141, 2007.
- [45] Naturschutz und Reaktorsicherheit Bundesministerium für Umwelt. *Hydrologischer Atlas von Deutschland*. Bundesministerium für Umwelt, Naturschutz und Reaktorsicherheit, Berlin, Germany, 2000.
- [46] M. Callens and N.E.C. Verhoest. Analysis of soil roughness measurements using a 25m laser profiler and a 4m wide meshboard. In *Proc. of IEEE International Geoscience and Remote Sensing Symposium, Anchorage, USA, September 20-24*, pages 1653 – 1656, 2004.
- [47] M. Callens, N.E.C. Verhoest, and M.W.J. Davidson. Parametrization of tillage-induced single-scale soil roughness from 4-m profiles. *IEEE Transactions on Geoscience and Remote sensing*, 44:878–888, 2006.
- [48] W. L. Cameron, N.N. Youssef, and L.K. Leung. Simulated polarimetric signatures of primitive geometrical shapes. *IEEE Transactions on Geoscience and Remote Sensing*, 34:793–803, 1996.
- [49] Canadian Space Agency. RADARSAT-2: A new satellite, a new vision. Technical report, Government RADARSAT Data Services, Saint-Hubert, Canada, 2010.
- [50] R. Cardell-Oliver, M. Kranz, K. Smettem, and K. Mayer. A reactive soil moisture sensor network: Design and field evaluation. *International Journal of Distributed Sensor Networks*, 1:149–162, 2005.
- [51] W.G. Carrara. *Spotlight synthetic aperture radar: signal processing algorithms*. Artech House, Boston, USA, 1995.

- [52] E. Ceraldi, G. Franceschetti, A. Iodice, and D. Riccio. Estimating the soil dielectric constant via scattering measurements along the specular direction. *IEEE Transactions on Geoscience and Remote Sensing*, 43:295–304, 2005.
- [53] M.T. Chahine. The hydrological cycle and its influence on climate. *Nature*, 359:373–380, 1992.
- [54] D.S. Chanasyk and M.A. Naeth. Field measurement of soil moisture using neutron probes. *Canadian Journal of Soil Science*, 76:317–323, 1996.
- [55] S. Chandrasekhar. *Radiative Transfer*. Dover Press, Mineola, USA, 1960.
- [56] A. Chanzy. Basic soil surface characteristics from active microwave remote sensing. *Remote Sensing Reviews*, 7:303–319, 1993.
- [57] K.S. Chen, T.D. Wu, L. Tsang, Q. Li, J. Shi, and A.K. Fung. Emission of rough surfaces calculated by the integral equation method with comparison to three-dimensional moment method simulations. *IEEE Transactions on Geoscience and Remote Sensing*, 41:90–101, 2003.
- [58] T. Chiu and K. Sarabandi. Electromagnetic scattering from short branching vegetation. *IEEE Transactions on Geoscience and Remote Sensing*, 38:911–925, 2000.
- [59] H.T. Chuah, S.W. Kam, and Y.H. Chye. Microwave dielectric properties of rubber and oil palm leaf samples: Measurement and modelling. *International Journal of Remote Sensing*, 18:2623–2639, 1997.
- [60] S.R. Cloude. Group theory and polarisation algebra. *Optik*, 75:26–36, 1986.
- [61] S.R. Cloude. *Polarimetry: The Characterisation of Polarisation Effects in EM Scattering*. PhD thesis, Faculty of Engineering, University of Birmingham, 1987.
- [62] S.R. Cloude. Lie groups in electromagnetic wave propagation and scattering. *Journal of electromagnetic waves and applications*, 6:947–974, 1992.
- [63] S.R. Cloude. Concept of polarization entropy in optical scattering. *Optical engineering*, 34:1599–1610, 1995.
- [64] S.R. Cloude. Eigenvalue parameters for surface roughness studies. In *Proc. of SPIE Conference on Polarization: Measurement, Analysis and Remote Sensing II, Denver, USA, July 19*, pages 2–13, 1999.

- [65] S.R. Cloude. *Polarisation: Applications in remote sensing*. Oxford University Press, Oxford, U.K., 2010.
- [66] S.R. Cloude, D.G. Corr, and M.L. Williams. Target detection beneath foliage using polarimetric synthetic aperture radar interferometry. *Waves Random media*, 14:S393–S414, 2004.
- [67] S.R. Cloude, J. Fortuny, J.M. Lopez-Sanchez, and A.J. Sieber. Wide-band polarimetric radar inversion studies for vegetation layers. *IEEE Transactions on Geoscience and Remote Sensing*, 37:2430–2441, 1999.
- [68] S.R. Cloude and G.D. Lewis. Eigenvalue analysis of Mueller matrix for bead basted aluminium surfaces. In *Proc. of SPIE Conference on Polarisation: Polarisation Analysis and Measurements III*, vol. AM107, July-August, pages 10–23, 2000.
- [69] S.R. Cloude, K.P. Papathanassiou, and W.M. Boerner. The remote sensing of oriented volume scattering using polarimetric radar interferometry. In *Proc. of IEEE International Symposium on Antennas and Propagation, Fukuoka, Japan, August 21-25*, pages 1–4, 2000.
- [70] S.R. Cloude, K.P. Papathanassiou, and E. Pottier. Radar polarimetry and polarimetric interferometry. *IEICE Trans. Electron*, E84-C:1814–1822, 2001.
- [71] S.R. Cloude and E. Pottier. A review of target decomposition theorems in radar polarimetry. *IEEE Transactions on Geoscience and Remote Sensing*, 34:498–518, 1996.
- [72] S.R. Cloude and E. Pottier. An entropy based classification scheme for land applications of polarimetric SAR. *IEEE Transactions on Geoscience and Remote Sensing*, 35:68–78, 1997.
- [73] B.G. Colpitts. The Integral Equation Model and surface roughness signatures in soil moisture and tillage type determination. *IEEE Transactions on Geoscience and Remote Sensing*, 36:833–837, 1998.
- [74] G. Cookmartin, P. Saich, S. Quegan, R. Cordey, P. Burgess-Allen, and A. Sowter. Modeling microwave interactions with crops and comparison with ERS-2 SAR observations. *IEEE Transactions on Geoscience and Remote Sensing*, 38:658–670, 2000.
- [75] I.G. Cumming and F.H. Wong. *Digital processing of synthetic aperture radar data: Algorithms and implementation*. Artech House, Boston, USA, 2005.

- [76] J.C. Curlander and R.N. McDonough. *Synthetic aperture radar: Systems and signal processing*. Wiley & Sons, Hoboken, USA, 1991.
- [77] L.J. Cutrona. *Synthetic Aperture Radar*, chapter 21, pages 1011–1033. McGraw-Hill Publishing Company, New York, USA, 2. edition, 1990.
- [78] G. Daian, A. Taube, A. Birnboim, M. Daian, and Y. Shramkov. Modeling the dielectric properties of wood. *Wood Science and Technology*, 40:237–246, 2006.
- [79] N.N. Das and B.P. Mohanty. Root zone soil moisture assessment using remote sensing and vadose zone modeling. *Vadose Zone Journal*, 5:296–307, 2006.
- [80] M.W.J. Davidson, T. Le Toan, F. Mattia, G. Satalino, T. Manninen, and M. Borgeaud. On the characterization of agricultural soil roughness for radar remote sensing studies. *IEEE Transactions on geoscience and remote sensing*, 38:630–640, 2000.
- [81] G.J.M. De Lannoy, P.R. Houser, N.E.C. Verhoest, V.R.N. Pauwels, and T.J. Gish. Upscaling of point soil moisture measurements to field averages at the OPE3 test site. *Journal of Hydrology*, 343:1–11, 2007.
- [82] G.J.M. De Lannoy, N.E.C. Verhoest, P.R. Houser, T.J. Gish, and M. van Meirvenne. Spatial and temporal characteristics of soil moisture in an intensively monitored agricultural field (OPE3). *Journal of Hydrology*, 331:719–730, 2006.
- [83] G.P. de Loor. Dielectric properties of heterogeneous mixtures containing water. *The Journal of Microwave Power*, 3:67–73, 1968.
- [84] G.P. De Loor. The dielectric properties of wet materials. *IEEE Transactions on Geoscience and Remote Sensing*, GE-21:364–369, 1983.
- [85] Y.-L. Desnos, C. Buck, J. Guijaro, J.-L. Suchail, R. Torres, and E. Attema. ASAR-Envisat’s advanced synthetic aperture radar: Building on ERS achievements towards future earth watch missions. *ESA Bulletin*, 102:91–100, 2000.
- [86] W. Dinter. Naturräumliche Gliederung. In R. Wolff-Straub, D. Büscher, H. Diekjobst, P. Fasel, E. Foerster, R. Götte, A. Jagel, K. Kaplan, I. Koslowski, H. Kutzelnigg, U. Raabe, W. Schuhmacher, and C. Vanberg, editors, *Rote*

- Liste der gefährdeten Pflanzen und Tiere in Nordrhein-Westfalen*, volume 17, pages 29–36, Recklinghausen, Germany, 1999. LÖBF-reports.
- [87] M.I. Disney, P. Saich, and P. Lewis. Modelling the radiometric response of a dynamic 3D structural model of Scots pine in the optical and microwave domains. In *Proc. of IEEE International Symposium on Geoscience and Remote Sensing, Toulouse, France, July 21-25*, pages 3537 – 3539, 2003.
- [88] M.C. Dobson and F.T. Ulaby. Preliminary evaluation of the SIR-B response to soil moisture, surface roughness, and crop canopy cover. *IEEE Transactions on Geoscience and Remote Sensing*, GE-24:517–526, 1986.
- [89] M.C. Dobson and F.T. Ulaby. *Mapping soil moisture distribution with imaging radar*, chapter 8, pages 407–433. Wiley & Sons, Hoboken, USA, 1998.
- [90] M.C. Dobson, F.T. Ulaby, M.T. Hallikainen, and M.A. El-Rayes. Microwave dielectric behavior of wet soil-part II: dielectric mixing models. *IEEE Transactions on Geoscience and Remote Sensing*, GE-23:35–46, 1985.
- [91] W.A. Dorigo, K. Scipal, R.M. Parinussa, Y.Y. Liu, W. Wagner, R.A.M. de Jeu, and V. Naeimi. Error characterisation of global active and passive microwave soil moisture datasets. *Hydrology and Earth System Sciences*, 14:2605–2616, 2010.
- [92] P.C. Dubois, J. van Zyl, and T. Engman. Measuring soil moisture with imaging radars. *IEEE Transaction on Geoscience and Remote Sensing*, 33:915–926, 1995.
- [93] M.A. El-Rayes and F.T. Ulaby. Microwave dielectric spectrum of vegetation - Part I: Experimental observations. *IEEE Transactions on Geoscience and Remote Sensing*, GE-25:541–549, 1987.
- [94] Ch. Elachi. *Introduction to Physics and Techniques of Remote Sensing*. Wiley & Sons, Hoboken, USA, 1987.
- [95] Ch. Elachi. *Spaceborne radar remote sensing: applications and techniques*. IEEE Press, New York, USA, 1988.
- [96] T.M. Elfouhaily and C.-A. Guérin. A critical survey of approximate scattering wave theories from random rough surfaces. *Waves in random media*, 14:R1–R40, 2004.

- [97] D. Entekabi, E.G. Njoku, P.E. O'Neill, K.H. Kellogg, W.T. Crow, W.N. Edelstein, J.K. Entin, S.D. Goodman, T.J. Jackson, J. Johnson, J. Kimball, J.R. Piepmeier, R.D. Koster, M. Neil, K.C. McDonald, M. Moghaddam, S. Moran, R. Reichle, J.C. Shi, M.W. Spencer, S.W. Thurman, L. Tsang, and J. van Zyl. The soil moisture active passive (SMAP) mission. *Proceedings of the IEEE*, 98:704–716, 2010.
- [98] M.J. Escorihuela, P. de Rosnay, Y.H. Kerr, and J.-C. Calvet. Influence of bound-water relaxation frequency on soil moisture measurements. *IEEE Transactions on Geoscience and Remote Sensing*, 45:4067–4076, 2007.
- [99] P. Ferrazzoli and L. Guerriero. Radar sensitivity to tree geometry and woody volume: A model analysis. *IEEE Transactions on Geoscience and Remote Sensing*, 33:360–371, 1995.
- [100] L. Ferro-Famil. *téledétection multi-fréquentielle et multi-temporelle d'environnements naturels à partir de données SAR polarimétriques*. PhD thesis, Université de Nantes, 2000.
- [101] L. Ferro-Famil, A. Reigber, E. Pottier, and W.-M. Boerner. Scene characterization using subaperture polarimetric SAR data. *IEEE Transaction on Geoscience and Remote Sensing*, 41:2264–2276, 2003.
- [102] L.L. Foldy. The multiple scattering of waves. *Physical Review*, 67:107–119, 1945.
- [103] G. Franceschetti, P. Imperatore, A. Iodice, D. Riccio, and G. Ruello. Scattering from layered structures with one rough interface: A unified formulation of perturbative solutions. *IEEE Transactions on Geoscience and Remote Sensing*, 46:1634–1643, 2008.
- [104] G. Franceschetti and R. Lanari. *Synthetic aperture radar processing*. CRC Press, Boca Raton, USA, 2000.
- [105] A. Freeman. Fitting a two component scattering model to polarimetric SAR data from forests. *IEEE Transactions on Geoscience and Remote Sensing*, 45:2583–2592, 2007.
- [106] A. Freeman and S.L. Durden. A three-component scattering model for polarimetric SAR data. *IEEE Transactions on Geoscience and Remote Sensing*, 36:963–973, 1998.

- [107] A.K. Fung. *Microwave Scattering and Emission Models and Their Applications*. Artech House, Boston, USA, 1994.
- [108] A.K. Fung and K.S. Chen. An update of the IEM surface backscattering model. *IEEE Geoscience and Remote Sensing Letters*, 1:75–77, 2004.
- [109] R. Garcia Moreno, M.C. Diaz Alvarez, A. Tarquis Alonso, S. Barrington, and A. Saa Requejo. Tillage and soil type effects on soil surface roughness at semiarid climatic conditions. *Soil and Tillage Research*, 98:35–44, 2008.
- [110] W. H. Gardner. *Water content*, chapter Methods of soil analysis, part 1. Physical and mineralogical methods, pages 493–544. American Society of Agronomy, 1986.
- [111] R. Garica Moreno, M.C. Diaz Alvarez, A. Saa Requejo, J.L. Valencia Delfa, and A.M. Tarquis. Multiscaling analysis of soil roughness variability. *Geoderma*, 160:22–30, 2010.
- [112] A. Gatti, F. Mattia, C. D’Haese, N.E.C. Verhoest, M. Davidson, T. Le Toan, and M. Borgeaud. A comparison between laser, needle-like and meshboard technique for soil moisture roughness measurements. In *Proc. of International Symposium on Retrieval of Bio- and Geophysical Parameters from SAR Data for Land Applications, Sheffield, U.K., September 11-14*, pages 345–350, 2001.
- [113] H. Gerighausen, E. Borg, C. Wloczyk, B. Fichtelmann, A. Günther, H.-H. Vajen, M. Rosenberg, M. Schulz, and H.-G. Engler. DEMMIN- a test site for the validation of remote sensing data products. general description and application during AgriSAR 2006. Technical report, German Aerospace Center, German Remote Sensing Data Center, 2007.
- [114] I. Gherboudj, R. Magagi, A.A. Berg, and B. Toth. Soil moisture retrieval over agricultural fields from multi-polarized and multi-angular RADARSAT-2 SAR data. *Remote Sensing of Environment*, 115:33–43, 2011.
- [115] R.R. Gillies and T.N. Carlson. Thermal remote sensing of surface soil water content with partial vegetation cover for incorporation into climate models. *Journal of Applied Meteorology*, 34:745–756, 1995.
- [116] V. Goldberg, C. Frühauf, C. Bernhofer, O. Wienhaus, F. Zimmermann, and U. Seelig. Regional- und Lokalklima des Osterzgebirges. In *Untersuchung von Waldökosystemen im Erzgebirge als Grundlage für einen ökolo-*

- gisch begründeten Waldbau, *Forstwirtschaftliche Beiträge Tharandt*. TU Dresden, 1998.
- [117] J.L. Gomez-Dans, S. Quegan, and J.C. Bennett. Indoor C-band polarimetric interferometry observations of a mature wheat canopy. *IEEE Transactions on Geoscience and Remote Sensing*, 44:768–777, 2006.
- [118] J.W. Goodman. Some fundamental properties of speckle. *Journal of the Optical Society of America*, 66:1145–1150, 1976.
- [119] I. Hajnsek. *Inversion of Surface Parameters using Polarimetric SAR*. PhD thesis, Friedrich-Schiller-Universität Jena, 2001.
- [120] I. Hajnsek, R. Bianchi, M. Davidson, G. D’Urso, J. Gomez-Sanchez, A. Haushold, R. Horn, J. Howse, A. Löw, J. Lopez-Sanchez, R. Ludwig, J. Martinez-Lonzano, F. Mattia, J. Miguel, E. Moreno, v. Pauwels, T. Ruhtz, C. Schmullius, H. Skriver, J. Sobrino, W. Timmermans, C. Wloczyk, and M. Wooding. AgriSAR 2006 airborne SAR and optics campaigns for an improved monitoring of agricultural processes and practices. In *European Geosciences Union, General Assembly, Vienna, Austria, April 15-20, 2007*.
- [121] I. Hajnsek and T. Jagdhuber. Monitoring of soil moisture using orbital RADAR. Technical report, Microwaves and Radar Institute, German Aerospace Center, 2011. Contribution to secondary mission objectives for the BIOMASS study of ESA.
- [122] I. Hajnsek, T. Jagdhuber, and H. Schön. SARTEO - data analysis report. Technical Report DLR-HR-TR-SARTEO-002, German Aerospace Center - DLR, Microwaves and Radar Institute (HR), 2009.
- [123] I. Hajnsek, T. Jagdhuber, H. Schön, and K.P. Papathanassiou. Agricultural vegetation parameter estimation using Pol-SAR: Retrieval of soil moisture. In *Proc. of IEEE International Symposium on Geoscience and Remote Sensing, Boston, USA, July 6-11*, pages 323–326, 2008.
- [124] I. Hajnsek, T. Jagdhuber, H. Schön, and K.P. Papathanassiou. Potential of estimating soil moisture under vegetation cover by means of PolSAR. *IEEE Transactions on Geoscience and Remote Sensing*, 47:442–454, 2009.
- [125] I. Hajnsek, K.P. Papathanassiou, and S.R. Cloude. Removal of additive noise in polarimetric eigenvalue processing. In *Proc. of IEEE International Sympo-*

- sium on Geoscience and Remote Sensing, Sydney, Australia, July 9-13, pages 2778 – 2780, 2001.
- [126] I. Hajnsek, K.P. Papathanassiou, and S.R. Cloude. Surface parameter estimation using fully polarimetric L- and P-band RADAR data. In *Proc. of IEEE International Symposium on Retrieval of Bio- and Geophysical Parameters from SAR Data for Land Applications, Sheffield, U.K., September 11-14*, pages 159–164, 2001.
- [127] I. Hajnsek, E. Pottier, and S.R. Cloude. Inversion of surface parameters from polarimetric SAR. *IEEE Transactions on Geoscience and Remote Sensing*, 41:727–744, 2003.
- [128] I. Hajnsek, H. Schön, T. Jagdhuber, and K. Papathanassiou. Estimation of soil moisture under vegetation using PolSAR: A comparison of methods. In *Proceedings of AGRISAR final workshop, ESA-ESTEC, Noordwijk, The Netherlands, October 15-16*, pages 1–8, 2007.
- [129] I. Hajnsek, H. Schön, T. Jagdhuber, and K. Papathanassiou. Potentials and limitations of estimating soil moisture under vegetation cover by means of PolSAR. In *Proc. of IEEE International Symposium on Retrieval of Bio- and Geophysical Parameters from SAR Data for Land Applications, Bari, Italy, September 25-28*, pages 1–8, 2007.
- [130] M.T. Hallikainen, F.T. Ulaby, M.C. Dobson, M.A. El-Rayes, and L.-K. Wu. Microwave dielectric behavior of wet soil-part I: Empirical models and experimental observations. *IEEE Transactions on Geoscience and Remote Sensing*, VOL. GE-23:25–34, 1985.
- [131] K.H. Hartge and R. Horn. *Einführung in die Bodenphysik*. Enke Verlag, Stuttgart, Germany, 1999.
- [132] F.M. Henderson and A.J. Lewis. *Manual of Remote Sensing: Volume 2: Principles and Applications of Imaging Radar*. Wiley & Sons, Hoboken, USA, 1998.
- [133] W. Hoen. *A correlation-based approach to modeling interferometric RADAR observations of the Greenland ice sheet*. PhD thesis, Department of Applied Physics of Stanford University, 2001.

- [134] W.A. Holm and R.M. Barnes. On radar polarization mixed state decomposition theorems. In *Proc. of National Radar Conference, USA, April 20-21*, pages 248–254, 1988.
- [135] R. Horn. E-SAR: The experimental airborne SAR system of DLR. Technical report, DLR-HR, 2011.
- [136] P.R. Houser, W.J. Shuttleworth, J.S. Famiglietti, H.V. Gupta, K.H. Syed, and D.C. Goodrich. Integration of soil moisture remote sensing and hydrologic modeling using data assimilation. *Water Resources Research*, 34:3405–3420, 1998.
- [137] J.A. Huisman, J.J.J.C. Snepvangers, W. Bouten, and G.B.M. Heuvelink. Monitoring temporal development of spatial soil water content variation: Comparison of ground penetrating radar and time domain reflectometry. *Vadose Zone Journal*, 2:519–529, 2003.
- [138] T. Hurtig, F. Fukarek, and J. Stübs. *Physische Geographie von Mecklenburg*. VEB Deutscher Verlag der Wissenschaften, Berlin, GDR, 1957.
- [139] J.R. Huynen. *Phenomenological Theory of Radar Targets*. PhD thesis, Technical University of Delft, 1970.
- [140] M. Imhoff, M. Story, C. Vermillion, F. Khan, and F. Polcyn. Forest canopy characterization and vegetation penetration assessment with space-borne radar. *IEEE Transactions on Geoscience and Remote Sensing*, GE-24:535–542, 1986.
- [141] A. Inoue, T. Kurosu, H. Maeno, S. Uratsuka, T. Kozu, K. Dabrowska-Zielinska, and J. Qi. Season-long daily measurements of multifrequency (Ka, Ku, X, C, and L) and full-polarization backscatter signatures over paddy rice field and their relationship with biological variables. *Remote Sensing of Environment*, 81:194–204, 2002.
- [142] A. Iodice, A. Natale, and D. Riccio. Retrieval of soil surface parameters via a polarimetric two-scale model. *IEEE Transactions on Geoscience and Remote Sensing*, 49:2531–2547, 2011.
- [143] A. Ishimaru. *Wave propagation and scattering in random media*. IEEE Press and Oxford University Press, Oxford, U.K., 1997.
- [144] J.D. Jackson. *Classical electrodynamics*. Wiley & Sons, Hoboken, USA, 1999.

- [145] T.J. Jackson. Measuring surface soil moisture using passive microwave remote sensing. *Hydrological Processes*, 7:139–152, 1993.
- [146] S. Jacquemoud, C. Bacour, H. Poilve, and J.-P. Frangi. Comparison of four radiative transfer models to simulate plant canopies reflectance: Direct and inverse mode. *Remote Sensing of Environment*, 74:471–481, 2000.
- [147] T. Jagdhuber. Ableitung von Bodenfeuchteinformation aus multiskaligen ENVISAT ASAR Daten. Diploma thesis, Ludwig Maximilians Universität München, 2006.
- [148] T. Jagdhuber and I. Hajnsek. OPAQUE 2007: Kampagnen- und Prozessierungsbericht. Technical report, DLR, Oberpfaffenhofen, Germany, Report no. DLR-OPAQUE-2007, 2009.
- [149] T. Jagdhuber and I. Hajnsek. OPAQUE 2008: Kampagnen- und Prozessierungsbericht. Technical report, DLR, Oberpfaffenhofen, Germany, Report no. DLR-OPAQUE-2008, 2009.
- [150] T. Jagdhuber and I. Hajnsek. Model-based inversion of soil parameters under vegetation using ground-to-volume ratios. In *Proc. of European Conference on Synthetic Aperture Radar, Aachen, Germany, June 7-10*, pages 495–498, 2010.
- [151] T. Jagdhuber, I. Hajnsek, K.P. Papathanassiou, and A. Bronstert. Soil moisture estimation using a multi-angular modified three component decomposition. In *Proc. of IEEE International Symposium on Geoscience and Remote Sensing, Cape Town, South Africa, July 13-18*, pages 5–8, 2009.
- [152] T. Jagdhuber, I. Hajnsek, K.P. Papathanassiou, and A. Bronstert. Estimation of soil moisture under vegetation cover applying a hybrid decomposition on polarimetric SAR data. In *Proc. of European Conference on Moisture Measurement, Weimar, Germany, October 5-7*, pages 203–211, 2010.
- [153] T. Jagdhuber, I. Hajnsek, K.P. Papathanassiou, and A. Bronstert. A hybrid decomposition for soil moisture estimation under vegetation cover using polarimetric SAR. In *Proc. of International Workshop on Science and Applications of SAR Polarimetry and Polarimetric Interferometry, ESA-ESRIN, Frascati, Italy, January 24-28*, pages 1–6, 2011.
- [154] T. Jagdhuber, I. Hajnsek, K.P. Papathanassiou, and A. Bronstert. An approach to extended Fresnel scattering. unpublished, 2012.

- [155] T. Jagdhuber, I. Hajnsek, K.P. Papathanassiou, and A. Bronstert. Soil moisture estimation under vegetation cover using a multi-angular polarimetric decomposition. *IEEE Transactions on Geoscience and Remote Sensing*, 2012. in print.
- [156] T. Jagdhuber, I. Hajnsek, K.P. Papathanassiou, and A. Bronstert. Soil moisture retrieval under agricultural vegetation using fully polarimetric SAR. In *Proc. of IEEE International Symposium on Geoscience and Remote Sensing, Munich, Germany, July 22-27, 2012*. in print.
- [157] T. Jagdhuber, I. Hajnsek, S. Sauer, K.P. Papathanassiou, and A. Bronstert. Soil moisture retrieval under forest using polarimetric decomposition techniques at P-band. In *Proc. of European Conference on Synthetic Aperture Radar, Nuremberg, Germany, April 23-26, 2012*.
- [158] T. Jagdhuber, I. Hajnsek, H. Schön, and K.P. Papathanassiou. Pol-SAR time series for soil moisture estimation under vegetation. In *Proc. of European Conference on Synthetic Aperture Radar, Friedrichshafen, Germany, June 2-5, pages 181–184, 2008*.
- [159] T. Jagdhuber, H. Schön, I. Hajnsek, and K.P. Papathanassiou. Soil moisture estimation under vegetation applying polarimetric decomposition techniques. In *Proc. of International Workshop on Science and Applications of SAR Polarimetry and Polarimetric Interferometry, ESA-ESRIN, Frascati, Italy, January 26-30, pages 1–8, 2009*.
- [160] JAXA - Japanese Aerospace Exploration Agency. ALOS-2: The Advanced Land Observing Satellite-2. Technical report, 2010.
- [161] W. Jester and A. Klik. Soil surface roughness measurement - methods, applicability and surface representation. *Catena*, 64:174–192, 2005.
- [162] Y.-Q. Jin and S.R. Cloude. Numerical eigenanalysis of the coherency matrix for a layer of random nonspherical scatterers. *IEEE Transactions on Geoscience and Remote Sensing*, 32:1179–1185, 1994.
- [163] F. Jonard, L. Weihermueller, K.Z. Jadoon, M. Schwank, H. Vereecken, and S. Lambot. Mapping field-scale soil moisture with L-band radiometer and ground-penetrating radar over bare soil. *IEEE Transactions on Geoscience and Remote Sensing*, 49:2863–2875, 2011.

- [164] M.A. Karam, A.K. Fung, R.H. Lang, and N.S. Chauhan. A microwave scattering model for layered vegetation. *IEEE Transactions on Geoscience and Remote Sensing*, 30:767–784, 1992.
- [165] I. Katra, D.G. Blumberg, H. Lavee, and P. Sarah. A method for estimating the spatial distribution of soil moisture of arid microenvironments by close range thermal infrared imaging. *International Journal of Remote Sensing*, 27:2599–2611, 2006.
- [166] Y. Kerr, P. Waldteufel, J.-P. Wigneron, J.-M. Martinuzzi, J. Font, and M. Berger. Soil moisture retrieval from space: The soil moisture and ocean salinity (SMOS) mission. *IEEE Transactions on Geoscience and Remote Sensing*, 39:1729–1735, 2001.
- [167] A.B. Kostinski and W.-M. Boerner. On foundations of radar polarimetry. *IEEE Transactions on Geoscience and Remote Sensing*, AP-34:1395–1404, 1986.
- [168] C.N. Koyama and K. Schneider. Soil moisture retrieval under vegetation using polarized PALSAR data. In *Proc. of IEEE International Symposium on Geoscience and Remote Sensing, Vancouver, Canada, July 24-29*, pages 1059–1062, 2011.
- [169] W.F. Krajewski, M.C. Anderson, W.E. Eichinger, D. Entekhabi, B.K. Hornbuckle, P.R. Houser, G.G. Katul, W.P. Kustas, J.M. Norman, C. Peters-Lidard, and E.F. Wood. A remote sensing observatory for hydrologic sciences: A genesis for scaling to continental hydrology. *Water Resources Research*, 42, 2006.
- [170] A.W. Kraszewski, S. Trabelsi, and S.O. Nelson. Comparison of density-independent expressions for moisture content determination in wheat at microwave frequencies. *Journal of Agricultural Engineering Research*, 71:227–237, 1998.
- [171] G. Krieger, I. Hajnsek, K.P. Papathanassiou, M. Eineder, M. Younis, F. De Zan, P. Lopez-Dekker, S. Huber, M. Werner, P. Prats, H. Fiedler, A. Freeman, P. Rosen, S. Hensley, W. Johnson, L. Villeux, B. Grafmueller, R. Werninghaus, R. Bamler, and A. Moreira. Tandem-L: A Mission for Monitoring Earth System Dynamics with High Resolution SAR Interferometry. In *Proc. of European Conference on Synthetic Aperture Radar, Aachen, Germany, June 7-10*, pages 1–4, 2010.

- [172] E. Krogager. A new decomposition of the radar target scattering matrix. *Electronics Letter*, 26:1525–1526, 1990.
- [173] C. Kuo and M. Moghaddam. Electromagnetic scattering from multilayer rough surfaces with arbitrary dielectric profiles for remote sensing of sub-surface soil moisture. *IEEE Transaction on Geoscience and Remote Sensing*, 45:349–366, 2007.
- [174] R.H. Lang. Electromagnetic backscattering from a sparse distribution of lossy dielectric scatterers. *Radio Science*, 16:15–30, 1981.
- [175] R.H. Lang and J.S. Sidhu. Electromagnetic backscattering from a layer of vegetation: A discrete approach. *IEEE Transactions on Geoscience and Remote Sensing*, GE-21:62–71, 1983.
- [176] M. Lax. Multiple scattering of waves. *Review of Modern Physics*, 23:287–310, 1951.
- [177] S. Le Hegarat-Masclé, M. Zribi, F. Alem, A. Weisse, and C. Loumagne. Soil moisture estimation from ERS/SAR data: Toward an operational methodology. *IEEE Transactions on Geoscience and Remote Sensing*, 40:2647–2658, 2002.
- [178] B.J. Lee, V.P. Khuu, and Z.M. Zhang. Partially coherent spectral transmittance of dielectric thin films with roughness surfaces. *Journal of Thermophysics and Heat Transfer*, 19:360–366, 2005.
- [179] J.-S. Lee, M.R. Grunes, and G. De Grandi. Polarimetric SAR speckle filtering and its implication for classification. *IEEE Transactions on Geoscience and Remote Sensing*, 37:2363–2373, 1999.
- [180] J.-S. Lee, M.R. Grunes, and R. Kwok. Classification of multi-look polarimetric SAR imagery based on complex Wishart distribution. *International Journal of Remote Sensing*, 15:2299–2311, 1994.
- [181] J.-S. Lee and I. Jurkevich. Segmentation of SAR images. *IEEE Transactions on Geoscience and Remote Sensing*, 27:674–680, 1989.
- [182] J.-S. Lee and E. Pottier. *Polarimetric radar imaging: from basics to applications*. CRC Press, Boca Raton, USA, 2009.

- [183] G.A. Lehrs, F.D. Whisler, and M.J.M. Roemkens. Spatial variation of parameters describing soil surface roughness. *Journal of Soil Science Society of America*, 52:311–319, 1988.
- [184] S. Liang, A.H. Strahler, X. Jin, and Q. Zhu. Comparisons of radiative transfer models of vegetation canopies and laboratory measurements. *Remote Sensing of Environment*, 61:129–138, 1997.
- [185] D.-S. Lin, E.F. Wood, P.A. Troch, M. Mancini, and T.J. Jackson. Comparisons of remotely sensed and model-simulated soil moisture over a heterogeneous watershed. *Remote Sensing of Environment*, 48:159–171, 1994.
- [186] A. Loew. *Coupled modelling of land surface microwave interactions using ENVISAT ASAR data*. PhD thesis, Ludwig Maximilians Universität München, 2004.
- [187] A. Loew. Derivation of high resolution DTMs from stereoscopic photos of acre surfaces. Technical report, University of Munich, Department of Geography, 2006.
- [188] A. Loew, R. Ludwig, and W. Mauser. Derivation of surface soil moisture from ENVISAT ASAR wide swath and image mode data in agricultural areas. *IEEE Transactions on Geoscience and Remote Sensing*, 44:889–899, 2006.
- [189] J.M. Lopez-Sanchez. *Analysis and Estimation of Biophysical Parameters of Vegetation by Radar Polarimetry*. PhD thesis, University of Valencia, 1999.
- [190] J.M. Lopez-Sanchez, J.D. Ballester-Berman, and J. Fortunaty-Guasch. Indoor wide-band polarimetric measurements on maize plants: A study of the differential extinction coefficient. *IEEE Transactions on Geoscience and Remote Sensing*, 44:758–767, 2006.
- [191] J.M. Lopez-Sanchez, J.D. Ballester-Berman, and I. Hajnsek. First demonstration of agriculture height retrieval with PolInSAR airborne data. In *Proc. of International Workshop on Science and Applications of SAR Polarimetry and Polarimetric Interferometry, Frascati, Italy, January, 24-28*, pages 1–7, 2011.
- [192] J.M. Lopez-Sanchez, J.D. Ballester-Berman, and Y. Marquez-Moreno. Model limitations and parameter estimation methods for agricultural applications of polarimetric SAR interferometry. *IEEE Transactions on Geoscience and Remote Sensing*, 45:3481–3493, 2007.

- [193] S.-Y. Lu and R.A. Chipman. Homogeneous and inhomogeneous Jones matrices. *Journal of the Optical Society of America A*, 11:766–773, 1994.
- [194] M.A. Malicki, R. Plagge, and C.H. Roth. Improving the calibration of dielectric TDR soil moisture determination taking into account the solid soil. *European Journal of Soil Science*, 47:357–366, 1996.
- [195] M.A. Malicki and W.M. Skierucha. A manually controlled TDR soil moisture meter operating with 300ps rise-time needle pulse. *Irrigation Science*, 10:153–163, 1989.
- [196] A.T. Manninen. Multiscale surface roughness description for scattering modelling of bare soil. *Physica A*, 319:535–551, 2003.
- [197] F. Marliani, P. Simonetta, P. Pampaloni, and J.A. Kong. Simulating coherent backscattering from crops during the growing cycle. *IEEE Transactions on Geoscience and Remote Sensing*, 40:162–177, 2002.
- [198] T.J. Marshall, J.W. Holmes, and C.W. Rose. *Soil physics*. Cambridge University Press, Cambridge, U.K., 1996.
- [199] J.-M. Martinez, N. Floury, T. Le Toan, A. Beaudoin, M.T. Hallikainen, and M. Mäkynen. Measurements and modeling of vertical backscatter distribution in forest canopy. *IEEE Transactions on Geoscience and Remote Sensing*, 38:710–719, 2000.
- [200] M. Martone. Modified scattering decomposition for soil moisture estimation from polarimetric X-band data. Master’s thesis, University of Naples Federico Secondo, 2009.
- [201] M. Martone, T. Jagdhuber, I. Hajnsek, and A. Iodice. Modified scattering decomposition for soil moisture estimation from polarimetric X-band data. In *Proc. of IEEE GOLD Remote Sensing Conference, Livorno, Italy, April 20-30*, pages 1–3, 2010.
- [202] P. Marzahn and R. Ludwig. On the derivation of soil surface roughness from multi parametric PolSAR data and its potential for hydrological modeling. *Hydrology and Earth System Sciences*, 13:381–394, 2009.
- [203] F. Mattia, M.W.J. Davidson, T. Le Toan, C.M.F. D’Haese, N.E.C. Verhoest, A.M. Gatti, and M. Borgeaud. A comparison between soil roughness statistics used in surface scattering models derived from mechanical and laser

- profilers. *IEEE Transactions on Geoscience and Remote Sensing*, 41:1659–1671, 2003.
- [204] F. Mattia, T. Le Toan, J.-C. Souyris, G. De Carolis, N. Floury, F. Posa, and G. Pasquariello. The effect of surface roughness on multifrequency polarimetric SAR data. *IEEE Transactions on Geoscience and remote sensing*, 35:954–966, 1997.
- [205] H. Mc Nairn and B. Brisco. The application of C-band polarimetric SAR for agriculture: A review. *Canadian Journal of remote sensing*, 30:525–542, 2004.
- [206] G.A. Meehl, T.F. Stocker, W.D. Collins, P. Friedlingstein, A.T. Gaye, J.M. Gregory, A. Kitoh, R. Knutti, J.M. Murphy, A. Noda, S.C.B. Raper, I.G. Watterson, A.J. Weaver, and Z.-C. Zhao. Global climate projections. In *Climate Change 2007: The Physical Science Basis. Contribution of Working Group I to the Fourth Assessment Report of the Intergovernmental Panel on Climate Change*. Cambridge University Press, Cambridge, U.K., 2007.
- [207] U. Meier. Growth stages of mono- and dicotyledonous plants. Technical report, German Federal Biological Research Centre for Agriculture and Forestry, 2001.
- [208] B. Merz and E.J. Plate. An analysis of the effects of spatial variability of soil and soil moisture on runoff. *Water Resources Research*, 33:2909–2922, 1997.
- [209] A. Merzouki, H. McNairn, and A. Pacheco. Potential of mapping soil moisture by combining radar backscatter modeling and PolSAR decomposition. In *Proc. of IEEE International Symposium on Geoscience and Remote Sensing, Honolulu, Hawaii, July 25-30*, pages 4419–4422, 2010.
- [210] F.J. Meyer and J.B. Nicoll. Prediction, detection, and correction of Faraday rotation in full-polarimetric L-band SAR data. *IEEE Transactions on Geoscience and Remote Sensing*, 46:3076–3086, 2008.
- [211] J.D. Miller and G.J. Gaskin. ThetaProbe ML2x: principles of operation and applications, 2.edition. Technical report, Macaulay land use research institute and Delta-T Devices.

- [212] J. Minet, E. Laloy, S. Lambot, and M. Vanclooster. Effect of high-resolution spatial soil moisture variability on simulated runoff response using a distributed hydrologic model. *Hydrology and Earth System Sciences*, 15:1323–1338, 2011.
- [213] V.L. Mironov, M.C. Dobson, V.H. Kaupp, S.A. Komarov, and V.N. Kleshchenko. Generalized refractive mixing dielectric model for moist soils. *IEEE Transactions on Geoscience and Remote Sensing*, 42:773–785, 2004.
- [214] M. Moghaddam, Y. Rahmat-Samii, E. Rodriguez, D. Entekabi, J. Hoffman, D. Moller, L.E. Pierce, S. Saatchi, and M. Thomson. Microwave observatory of subcanopy and subsurface (MOSS): A mission concept for global deep soil moisture observations. *IEEE Transactions on Geoscience and Remote Sensing*, 45:2630–2643, 2007.
- [215] M. Moghaddam, S. Saatchi, and R.H. Cuenca. Estimating subcanopy soil moisture with radar. *Journal of Geophysical Research*, 105:14899–14911, 2000.
- [216] N. Montaldo, J.D. Albertson, M. Mancini, and G. Kiely. Robust simulation of root zone soil moisture with assimilation of surface soil moisture data. *Water Resources Research*, 37:2889–2900, 2001.
- [217] C. Montzka. *Assimilation of multispectral remotely sensed data in water balance and matter flux modelling in the Rur catchment basin*. PhD thesis, University of Bonn, 2007.
- [218] C. Montzka, H. Moradkhani, L. Weihermueller, H.-J. Hendricks Franssen, M. Canty, and H. Vereecken. Hydraulic parameter estimation by remotely-sensed top soil moisture observations with the particle filter. *Journal of Hydrology*, 399:410–421, 2011.
- [219] M.S. Moran, S. McElroy, J.M. Watts, and C.D. Peters-Lidard. *Radar Remote Sensing for Estimation of Surface Soil Moisture at the Watershed Scale*, chapter 7, pages 91–109. Texas A&M Press, 2005.
- [220] S.M. Moran, C.D. Peters-Lidard, J.M. Watts, and S. McElroy. Estimating soil moisture at the watershed scale with satellite-based radar and land surface models. *Canadian Journal of Remote Sensing*, 30:805–826, 2004.
- [221] A. Moreira, G. Krieger, M. Younis, I. Hajnsek, K. Papathanassiou, M. Eineder, and F. De Zan. TanDEM-L: A mission proposal for monitoring dynamic

- earth processes. In *Proc. of IEEE International Symposium on Geoscience and Remote Sensing, Vancouver, Canada, July 24-29*, pages 1385–1388, 2011.
- [222] D.C. Munson Jr. and R.L. Visentin. A signal processing view of strip-mapping synthetic aperture radar. *IEEE Transactions on Acoustics, Speech and Signal Processing*, 37:2131–2147, 1989.
- [223] M. Munzert and J. Frahm. *Pflanzliche Erzeugung: Grundlagen des Acker- und Pflanzenbaus, der guten fachlichen Praxis der Verfahrenstechnik, Produktions- und Verfahrenstechnik der Kulturpflanzen, Dauergrünland, Sonderkulturen, Nachwachsende Rohstoffe, ökologischer Landbau, Feldversuchswesen, Naturschutz und Landschaftspflege*. BLV Buchverlag GmbH & Co, Munich, Germany, 2006.
- [224] J.E. Nelson, K.D. Kephart, A. Bauer, and J.F. Connor. Growth staging of wheat, barley and wild oat. A strategic step to timing of field operations. *Montana State University Misc. Bulletin*, 4387:1–14, 1995.
- [225] M. Neumann. *Remote sensing of vegetation using multi-baseline polarimetric SAR interferometry: Theoretical modeling and physical parameter retrieval*. PhD thesis, University of Rennes 1, 2009.
- [226] M. Neumann, L. Ferro-Famil, and E. Pottier. A general model-based polarimetric decomposition scheme for vegetated areas. In *Proc. of International Workshop on Science and Applications of SAR Polarimetry and Polarimetric Interferometry, Frascati, Italy, January 26-30*, pages 1–8, 2009.
- [227] M. Neumann, L. Ferro-Famil, and A. Reigber. Estimation of forest structure, ground and canopy layer characteristics from multibaseline polarimetric interferometric SAR data. *IEEE Transactions on Geoscience and Remote Sensing*, 48:1086–1104, 2010.
- [228] D.J. Newman. Matrix mutual orthogonality and parameter independence. *Journal of Physics A: Mathematical and General*, 14:L429–L431, 1981.
- [229] S.V. Nghiem, S.H. Yueh, R. Kwok, and F.K. Li. Symmetry properties in polarimetric remote sensing. *Radio Science*, 27:693–711, 1992.
- [230] W. Ni, G. Sun, G. Zhifeng, and Y. Pang. Characterization of soil surface roughness from terrestrial laser scanner data. In *Proc. of IEEE International Symposium on Geoscience and Remote Sensing, Cape town, South Africa, July 13-18*, pages 428–431, 2009.

- [231] E.G. Njoku, T.J. Jackson, L. Venkataraman, T.K. Chan, and S.V. Nghiem. Soil moisture retrieval from AMSR-E. *IEEE Transactions on Geoscience and Remote Sensing*, 41:215–229, 2003.
- [232] Y. Oh. Quantitative retrieval of soil moisture content and surface roughness from mutlipolarized radar observations of bare soil surfaces. *IEEE Transactions on Geoscience and Remote Sensing*, 42:596–601, 2004.
- [233] Y. Oh and Y.C. Kay. Condition for precise measurement of soil surface roughness. *IEEE Transactions on Geoscience and Remote Sensing*, 36:691–696, 1998.
- [234] Y. Oh, K. Sarabandi, and F.T. Ulaby. An empirical model and an inversion technique for radar scattering from bare soil surfaces. *IEEE Transactions on Geoscience and Remote Sensing*, 30:370–381, 1992.
- [235] D. Or and J. Wraith. Temperature effects on soil bulk dielectric permittivity measured by time domain reflectometry. *Water Resources Research*, 35:371–383, 1999.
- [236] S.J. Orfanidis. *Electromagnetic Waves and Antennas*. Rutgers University, New Brunswick, USA, 2002.
- [237] J. Parjaka, V. Naeimi, G. Blöschl, and J. Komma. Matching ERS scatterometer based soil moisture patterns with simulations of a conceptual dual layer hydrologic model over Austria. *Hydrology and Earth System Sciences*, 13:259–271, 2009.
- [238] S.-E. Park and W.M. Moon. Inversion of soil moisture content from L- and P-band AIRSAR polarimetric SAR data. In *Proceedings of IEEE International Symposium on Geoscience and Remote Sensing, Barcelona, Spain, July 23-27*, pages 5194–5197, 2007.
- [239] S.-E. Park, W.M. Moon, and D.-J. Kim. Estimation of surface roughness parameter in intertidal mudflat using airborne polarimetric SAR data. *IEEE Transactions on Geoscience and Remote Sensing*, 47:1022–1031, 2009.
- [240] V.R.N. Pauwels, R. Hoeben, N.E.C. Verhoes, F.P. De Troch, and Troch P.A. Improvement of TOPLATS-based discharge predictions through assimilation of ERS-based remotely sensed soil moisture values. *Hydrological Processes*, 16:995–1013, 2002.

- [241] A. Paz, E. Thorin, and C. Topp. Dielectric mixing models for water content determination in woody biomass. *Wood Science and Technology*, pages 237–246, 2010.
- [242] D. Penna, M. Borga, D. Norbiato, and G. Dalla Fontana. Hillslope scale soil moisture variability in steep alpine terrain. *Journal of Hydrology*, 364:311–327, 2009.
- [243] N.R. Peplinski, F.T. Ulaby, and M.C. Dobson. Dielectric properties of soils in the 0.3-1.3 GHz range. *IEEE Transactions on Geoscience and Remote Sensing*, 33:803–807, 1995.
- [244] C. Perez-Gutierrez, J. Martinez-Fernandez, N. Sanchez, and J. Alvarez-Mozos. Modeling of soil roughness using terrestrial laser scanner for soil moisture retrieval. In *Proceedings of International Symposium on Geoscience and Remote Sensing, Barcelona, Spain, July 23-27*, pages 1877–1880, 2007.
- [245] G. Picard. *Modélisation radar des couverts végétaux. Applications à la télédétection de couverts forestiers et agricoles*. PhD thesis, University of Toulouse, 2002.
- [246] G. Picard, T. Le Toan, and F. Mattia. Understanding C-band radar backscatter from wheat canopy using a multiple-scattering coherent model. *IEEE Transactions on Geoscience and Remote Sensing*, 41:1583–1591, 2003.
- [247] N. Pierdicca, L. Pulvirenti, F. Ticconi, and M. Brogioni. Radar bistatic configurations for soil moisture retrieval: A simulation study. *IEEE Transactions on Geoscience and Remote Sensing*, 46:3252–3264, 2008.
- [248] I. Pisciotto, T. Jagdhuber, G. Parrella, and I. Hajnsek. First analysis on snow cover change using fully polarimetric TerraSAR-X data. In *Proc. of International Workshop on Science and Applications of SAR Polarimetry and Polarimetric Interferometry, ESA-ESRIN, Frascati, Italy, January 24-28*, 2011.
- [249] D. Polder and J.H. van Santen. The effective permeability of mixtures of solids. *Physica*, 12:257–271, 1945.
- [250] A. Quesney, S. le Hegarat-Masclé, O. Taconet, D. Vidal-Madjar, J.P. Wigneron, C. Loumagne, and M. Normand. Estimation of watershed soil moisture index from ERS/SAR data. *Remote Sensing of Environment*, 72:290–303, 2000.

- [251] M.M. Rahman, M.S. Moran, D.P. Thoma, R. Bryant, C.D. Holifield Collins, T. Jackson, B.J. Orr, and M. Tischler. Mapping surface roughness and soil moisture using multi-angle radar imagery without ancillary data. *Remote Sensing of Environment*, 112:391–402, 2008.
- [252] R.K. Raney, A. Freeman, R.W. Hawkins, and R. Bamler. A plea for Radar brightness. In *Proc. of IEEE International Symposium on Geoscience and Remote Sensing, Pasadena, USA, August 8-12*, pages 1090–1092, 1994.
- [253] R.H. Reichle, R.D. Koster, J. Dong, and A.A. Berg. Global soil moisture from satellite observations, land surface models, and ground data: Implications for data assimilation. *Journal of Hydrometeorology*, 5:430–442, 2004.
- [254] A. Reigber, R. Scheiber, M. Jäger, P. Prats, I. Hajnsek, T. Jagdhuber, K.P. Papathanassiou, M. Nannini, E. Aguilera, S. Baumgartner, and A. Moreira. Very high resolution airborne synthetic aperture radar imaging: Signal processing and applications. *Proceedings of the IEEE*, 2012. submitted.
- [255] S.O. Rice. Reflection of electromagnetic waves from slightly rough surfaces. *Communications on Pure and Applied Mathematics*, 4:351–378, 1951.
- [256] L.A. Richards. Capillary conduction of liquids through porous mediums. *Physics*, 1:318–333, 1931.
- [257] D. Rieke-Zapp and M.A. Nearing. Digital close range photogrammetry for measurement of soil erosion. *The Photogrammetric Record*, 20:69–87, 2005.
- [258] D. Rieke-Zapp, H. Wegmann, F. Santel, and M. Nearing. Digital photogrammetry for measuring soil surface roughness. In *Proc. of American Society of Photogrammetry and Remote Sensing, St. Louis, Missouri, April, 23-27*, pages 1–8, 2001.
- [259] C.A. Rivera Villarreyes, G. Baroni, and S.E. Oswald. Integral quantification of seasonal soil moisture changes in farmland by cosmic-ray neutrons. *Hydrology and Earth System Sciences*, 15:3843–3859, 2011.
- [260] D.A. Robinson, C.S. Campbell, J.W. Hopmans, B.K. Hornbuckle, S.B. Jones, R. Knight, F. Ogden, J. Selker, and O. Wendroth. Soil moisture measurement for ecological and hydrological watershed-scale observatories: A review. *Vadoze Zone Journal*, 7:358–389, 2008.

- [261] D.A. Robinson, S.B. Jones, J.M. Wraith, D. Or, and S.P. Friedman. A review of advances in dielectric and electrical conductivity measurement in soils using time domain reflectometry. *Vadose Zone Journal*, 2:444–475, 2003.
- [262] A. Rosenqvist, M. Shimada, N. Ito, and M. Watanabe. ALOS PALSAR: A pathfinder mission for global-scale monitoring of the environment. *IEEE Transactions on Geoscience and Remote Sensing*, 45:3307–3316, 2007.
- [263] K. Roth, R. Schulin, H. Fluehler, and W. Attinger. Calibration of time domain reflectometry for water content measurement using a composite dielectric approach. *Water Resources Research*, 26:2267–2273, 1990.
- [264] G.T. Ruck, D.E. Barrick, W. D. Stuart, and C.K. Krichbaum. *Radar Cross Section Handbook*. Plenum Press, New York, USA, 1970.
- [265] M. R. Sahebi and J. Angles. An inversion method based on multiangular approaches for estimating bare soil surface parameters from RADARSAT-1. *Hydrology and Earth System Sciences Discussions*, 6:207–241, 2009.
- [266] E.E. Sano, M.S. Moran, A.R. Huete, and T. Miura. C- and multiangle Ku-band synthetic aperture radar data for bare soil moisture estimation in agricultural areas. *Remote Sensing of Environment*, 64:77–90, 1998.
- [267] F. Scheffer and P. Schachtschabel. *Lehrbuch der Bodenkunde*. Enke Verlag, Stuttgart, Germany, 1992.
- [268] T.J. Schmugge, T.J. Jackson, and H.L. Mc Kim. Survey of methods for soil moisture determination. *Water Resources Research*, 16:961–979, 1980.
- [269] K. Schneider. Assimilating remote sensing data into a land-surface process model. *International Journal of Remote Sensing*, 24:2959–2980, 2003.
- [270] D.L. Schuler, J.-S. Lee, D. Kasilingam, and G. Nesti. Surface roughness and slope measurements using polarimetric SAR data. *IEEE Transactions on Geoscience and Remote Sensing*, 40:687–698, 2002.
- [271] J. Schulla. *Hydrologische Modellierung von Flusseinzugsgebieten zur Abschätzung der Folgen von Klimaveränderungen*. PhD thesis, ETH Zurich, 1997.
- [272] H.D. Scott. *Soil physics: Agricultural and environmental applications*. Iowa State University Press, Ames, USA, 2000.

- [273] J.J. Sharma, I. Hajnsek, K.P. Papathanassiou, and A. Moreira. Polarimetric decomposition over glacier ice using long-wavelength airborne PolSAR. *IEEE Transactions on Geoscience and Remote Sensing*, 49:519–535, 2011.
- [274] J. Shi, J. Wang, A.Y. Hsu, P.E. O’Neill, and E.T. Engman. Estimation of bare surface soil moisture and surface roughness parameter using L-band SAR image data. *IEEE Transactions on Geoscience and Remote Sensing*, 35:1254–1266, 1997.
- [275] O. Shishkova. Comparison of two statistical distributions inside the extended bragg model. Master’s thesis, Moscow Institute of Physics and Technology, Dolgoprudny, Russia, 2002.
- [276] B.L. Shrestha, H.C. Wood, and S. Sokhansanj. Prediction of moisture content of alfalfa using density-independent functions of microwave dielectric properties. *Measurement Science and Technology*, 16:1179–1185, 2005.
- [277] B.L. Shrestha, H.C. Wood, and S. Sokhansanj. Modelling of vegetation permittivity at microwave frequencies. *IEEE Transactions on Geoscience and Remote Sensing*, 45:342–348, 2007.
- [278] H. Skriver, M.T. Svendsen, and A.G. Thomsen. Multitemporal C- and L-band polarimetric signatures of crops. *IEEE Transactions on Geoscience and Remote Sensing*, 37:2413–2429, 1999.
- [279] R.E. Smith, J. Quinton, D.C. Goodrich, and M. Nearing. Soil-erosion models: Where do we really stand? *Earth surface processes and landforms*, 2010.
- [280] K.J. Song, X.B. Zhou, and Y. Fan. Retrieval of soil moisture content from microwave backscattering using a modified IEM model. *Progress in Electromagnetic Research B*, 26:383–399, 2010.
- [281] K.N. Srinivasa Rao. *The Rotation and Lorentz Groups and Their Representations for Physicists*. Wiley & Sons, Hoboken, USA, 1988.
- [282] H.S. Srivastava, P. Patel, M.L. Manchanda, and S. Adiga. Use of multiincidence angle RADARSAT-1 SAR data to incorporate the effect of surface roughness in soil moisture estimation. *IEEE Transactions on Geoscience and Remote Sensing*, 41:1638–1640, 2003.

- [283] H.S. Srivastava, P. Patel, Y. Sharma, and R.R. Navalgund. Large-area soil moisture estimation using multi-incidence-angle RADARSAT-1 SAR data. *IEEE Transactions on Geoscience and Remote Sensing*, 47:2528–2535, 2009.
- [284] R. Stenger, T. Wöhling, G.F. Barkle, and A. Wall. Relationship between dielectric permittivity and water content for vadose zone materials of volcanic origin. *Soil Research*, 45:299–309, 2007.
- [285] J.M. Stiles and K. Sarbandi. Electromagnetic scattering from grassland - part I: A fully phase-coherent scattering model. *Transactions on Geoscience and Remote Sensing*, 38:339–348, 2000.
- [286] M. Stojic, J. Chandler, P. Ashmore, and J. Luce. The assessment of sediment transport rates by automated digital photogrammetry. *Photogrammetric Engineering and Remote Sensing*, 64:387–395, 1998.
- [287] J.A. Stratton. *Electromagnetic Theory*. McGraw-Hill Publishing, New York, USA, 1941.
- [288] O. Taconet and V. Ciarletti. Estimating soil roughness indices on a ridge-and-furrow surface using stereo photogrammetry. *Soil and Tillage Research*, 93:64–76, 2007.
- [289] H.S. Tan. Microwave measurements and modelling of the permittivity of tropical vegetation samples. *Applied Physics*, 25:351–355, 1981.
- [290] S. Tebaldini. Algebraic synthesis of forest scenarios from multibaseline PolInSAR data. *IEEE Transactions on Geoscience and Remote Sensing*, 47:4132–4142, 2009.
- [291] S. Tebaldini. Single and multipolarimetric SAR tomography of forested areas: A parametric approach. *IEEE Transactions on Geoscience and Remote Sensing*, 48:2375–2387, 2010.
- [292] D.P. Thoma, M.S. Moran, R. Bryant, M. Rahman, C.D. Holifield-Collins, and S. Skirvin. Comparison of four models to determine surface soil moisture from C-band radar imagery in a sparsely vegetated semiarid landscape. *Water Resources Research*, 42:1–12, 2006.
- [293] F. Ticconi, N. Pierdicca, L. Pulvirenti, and M. Brogioni. A theoretical study of the sensitivity of spaceborne bistatic microwave systems to geophysical parameters of land surfaces. In *Proceedings of International Symposium on*

- Geoscience and Remote Sensing, Denver, Colorado, July 31 - August 4*, pages 1200–1203, 2006.
- [294] K. Tomiyasu. Tutorial review of synthetic-aperture radar (SAR) with applications to imaging of the ocean surface. *Proceedings of the IEEE*, 66:563–583, 1978.
- [295] G.C. Topp and J.L. Davis. Measurement of soil water content using time-domain reflectometry (TDR): A field evaluation. *Soil Science of America Journal*, 49:19–24, 1985.
- [296] G.C. Topp, J.L. Davis, and A.P. Annan. Electromagnetic determination of soil water content: Measurements in coaxial transmission lines. *Water Resources Research*, 16:574–582, 1980.
- [297] G.C. Topp, M. Yanuka, W.D. Zebchuk, and S. Zegelin. Determination of electrical conductivity using time domain reflectometry: Soil and water experiments in coaxial lines. *Water Resources Research*, 24:945–952, 1988.
- [298] A. Toure, K.P.B. Thomson, G. Edwards, R.J. Brown, and B.G. Brisco. Adaption of the MIMICS backscattering model to the agricultural context - wheat and canola at L- and C-bands. *IEEE Transactions on Geoscience and Remote Sensing*, 32:47–61, 1994.
- [299] R. Touzi and A. Lopes. Statistics of the Stokes parameters and of the complex coherence parameters in one-look and multilook speckle fields. *IEEE Transactions on geoscience and remote sensing*, 34:519–531, 1996.
- [300] S. Trabelsi, A.W. Kraszewski, and S.O. Nelson. Simultaneous determination of density and water content of particulate materials by microwave sensors. *Electronic Letters*, 33:874–876, 1997.
- [301] R.N. Treuhaft and S.R. Cloude. The structure of oriented vegetation from polarimetric interferometry. *IEEE Transactions on Geoscience and Remote Sensing*, 37:2620–2624, 1999.
- [302] R.N. Treuhaft, S.N. Madsen, M. Moghaddam, and J.J. van Zyl. Vegetation characteristics and underlying topography from interferometric radar. *Radio Science*, 31:1449–1485, 1996.
- [303] R.N. Treuhaft and P.R. Siqueira. Vertical structure of vegetated land surfaces from interferometric and polarimetric radar. *Radio Science*, 35:141–177, 2000.

- [304] L. Tsang, J.A. Kong, and K.-H. Ding. *Scattering of Electromagnetic Waves: Theory and Applications*. Wiley & Sons, Hoboken, USA, 2000.
- [305] L. Tsang, J.A. Kong, and R.T. Shin. *Theory of microwave remote sensing*. Wiley & Sons, Hoboken, USA, 1985.
- [306] E. Tuncer, S.M. Gubanski, and B. Nettelblad. Electrical properties of 4x4 binary dielectric mixtures. *Journal of Electrostatics*, 56:449–463, 2002.
- [307] F.T. Ulaby and M. A. El-Rayes. Microwave dielectric spectrum of vegetation: Part II: Dual dispersion model. *IEEE Transactions on Geoscience and Remote Sensing*, GE-25:550–557, 1987.
- [308] F.T. Ulaby and C. Elachi. *Radar Polarimetry for Geoscience Applications*. Artech House, Boston, USA, 1990.
- [309] F.T. Ulaby and R.P. Jedlicka. Microwave dielectric properties of plant materials. *IEEE Transactions on Geoscience and Remote Sensing*, GE-22:406–415, 1984.
- [310] F.T. Ulaby, F.K. Moore, and A.K. Fung. *Microwave Remote Sensing: Active and Passive: Volume III: From Theory to Applications*. Artech House, Boston, USA, 1986.
- [311] F.T. Ulaby, R.K. Moore, and A..K. Fung. *Microwave Remote Sensing: Active and Passive: Volume I: Fundamentals and Radiometry*. Artech House, Boston, USA, 1981.
- [312] F.T. Ulaby, R.K. Moore, and A.K. Fung. *Microwave and Remote Sensing: Active and Passive: Volume II: Radar Remote Sensing and Surface Scattering and Emission Theory*. Artech House, Boston, USA, 1982.
- [313] F.T. Ulaby, K. Sarabandi, K. Mc Donald, M. Whitt, and M.C. Dobson. Michigan microwave canopy scattering model. *International Journal of Remote Sensing*, 11:1223–1253, 1990.
- [314] F.T. Ulaby, A. Tavakoli, and T.B.A. Senior. Microwave propagation constant for a vegetation canopy with vertical stalks. *IEEE Transactions on Geoscience and remote sensing*, GE-25:714–725, 1987.
- [315] F.T. Ulaby and E.A. Wilson. Microwave attenuation properties of vegetation canopies. *IEEE Transactions on Geoscience and Remote Sensing*, GE-23:746–753, 1985.

- [316] G. R. Valenzuela. Depolarization of EM waves by slightly rough surfaces. *IEEE Transactions on Antennas and Propagation*, AP-15:552–557, 1967.
- [317] H.C. van de Hulst. *Light scattering by small particles*. Dover, Mineola, USA, 1981.
- [318] P.J. van Oevelen and D. H. Hoekman. Radar backscatter inversion techniques for estimation of surface soil moisture: EFEDA-spain and HAPEX-Sahel case studies. *IEEE Transactions on Geoscience and Remote Sensing*, 37:113–123, 1999.
- [319] J.J. van Zyl. Application of Cloude’s target decomposition theorem to polarimetric imaging radar data. In *SPIE-Radar Polarimetry Vol. 1748*, 1992.
- [320] J.J. van Zyl, M. Arii, and Y. Kim. Requirements for model-based polarimetric decompositions. In *Proc. of European Conference on Synthetic Aperture Radar, Friedrichshafen, Germany, June 2-5*, pages 41–44, 2008.
- [321] J.J. van Zyl, Y. Kim, and M. Arii. Requirements for model-based polarimetric decompositions. In *Proc. of IEEE International Symposium on Geoscience and Remote Sensing, Boston, USA, July 6-11*, pages 417–420, 2008.
- [322] H. Vereecken, J.A. Huisman, H. Bogaen, J. Vanderborght, J.A. Vrugt, and J.W. Hopmans. On the value of soil moisture measurements in vadose zone hydrology: A review. *Water Resources Research*, 44:1–21, 2008.
- [323] N.E.C. Verhoest, H. Lievens, W. Wagner, J. Alvarez-Mozos, M.S. Moran, and F. Mattia. On the soil roughness parameterization problem in soil moisture retrieval of bare surfaces from synthetic aperture radar. *Sensors*, 8:4213–4248, 2008.
- [324] A. Voronovich. Small-slope approximation for electromagnetic wave scattering at a rough interface of two dielectric half-spaces. *Waves in Random Media*, 4:337–367, 1994.
- [325] A.G. Voronovich. *Wave scattering from rough surfaces, Springer Series on Wave Phenomena*. Springer Verlag, Berlin, Germany, 1994.
- [326] N. Wagner, F. Bonitz, K. Emmerich, and K. Kupfer. Experimental investigations on the frequency and temperature dependent dielectric material properties of soil. *IEEE Transactions on Geoscience and Remote Sensing*, 2012. accepted.

- [327] N. Wagner, E. Trinks, and K. Kupfer. Determination of the spatial TDR-sensor characteristics in strong dispersive subsoil using 3D-FEM frequency domain simulations in combination with microwave dielectric spectroscopy. *Measurement Science and Technology*, 19:1137–1146, 2007.
- [328] W. Wagner. *Soil Moisture Retrieval from ERS Scatterometer Data*. PhD thesis, Vienna University of Technology, 1998.
- [329] W. Wagner, G. Blöschl, P. Pampaloni, J.-C. Clavet, B. Bizzarri, J.-P. Wigneron, and Y. Kerr. Operational readiness of microwave remote sensing of soil moisture for hydrologic applications. *Nordic Hydrology*, 38:1–20, 2007.
- [330] W. Wagner, C. Pathe, M. Doubkova, D. Sabel, A. Bartsch, S. Hasenauer, G. Blöschl, K. Scipal, J. Martinez-Fernandez, and A. Löw. Temporal stability of soil moisture and radar backscatter observed by the advanced synthetic aperture radar (ASAR). *Sensors*, 8:1174–1197, 2008.
- [331] W. Wagner and K. Scipal. Large-scale soil moisture mapping in Western Africa using the ERS scatterometer. *IEEE Transactions on Geoscience and Remote Sensing*, 38:1777–1782, 2000.
- [332] J.P. Walker and P.R. Houser. A methodology for initializing soil moisture in a global climate model: Assimilation of near-surface soil moisture observations. *Journal of Geophysical Research*, 106:761–774, 2001.
- [333] J.P. Walker and P.R. Houser. *Hydrologic Data Assimilation*, chapter 2, pages 1–30. Taylor & Francis, 2005.
- [334] S.G. Wang, X. Li, X.J. Han, and R. Jin. Estimation of surface soil moisture and roughness from multi-angular ASAR imagery in the Watershed Allied Telemetry Experimental Research (WATER). *Hydrology and Earth System Sciences*, 15:1415–1426, 2011.
- [335] A.W. Western, R.B. Grayson, and G. Blöschl. Scaling of soil moisture: A hydrologic perspective. *Annual Review of Earth and Planetary Sciences*, 30:149–180, 2002.
- [336] W.R. Whalley. Considerations on the use of time-domain reflectometry (TDR) for measuring soil water content. *Journal of Soil Science*, 44:1–9, 1993.

- [337] M.L. Williams and S. R. Cloude. Predictions of SAR polarimetry and InSAR coherence for a model wheat canopy. In *Proc. of IEEE International Symposium on Geoscience and Remote Sensing, Seoul, Korea, July 25-29*, pages 1383–1386, 2005.
- [338] T.D. Wu and K.S. Chen. A reappraisal of the validity of the IEM model for backscattering from rough surfaces. *IEEE Transactions on Geoscience and Remote Sensing*, 42:743–753, 2004.
- [339] F. Xu and Y.-Q. Jin. Multiparameter inversion of a layer of vegetation canopy over rough surface from the system response function based on the Mueller matrix solution of pulse echoes. *IEEE Transactions on Geoscience and Remote Sensing*, 44:2003–2015, 2006.
- [340] Z.-W. Xu, J. Wu, and Z.-S. Wu. A survey of ionospheric effects on space-based radar. *Waves in Random Media*, 14:189–273, 2004.
- [341] Y. Yamaguchi. *Radar Polarimetry from Basics to Application*. IEICE, 2007.
- [342] Y. Yamaguchi, T. Moriyama, M. Ishido, and Yamada H. Four-component scattering model for polarimetric SAR image decomposition. *Transactions on Geoscience and Remote Sensing*, 43:1699–1706, 2005.
- [343] Y. Yamaguchi, Y. Yajima, and H. Yamada. A four component decomposition of POLSAR images based on the coherency matrix. *IEEE Transactions on Geoscience and Remote Sensing Letters*, 3:292–296, 2006.
- [344] E. Zehe, H. Elsenbeer, F. Lindenmaier, K. Schulz, and A. Blöschl, G. Patterns of predictability in hydrological threshold systems. *Water Resources Research*, 43:12, 2007.
- [345] E. Zehe, T. Gräff, M. Morgner, A. Bauer, and A. Bronstert. Plot and field scale soil moisture dynamics and subsurface wetness control on runoff generation in a headwater in the ore mountains. *Hydrology and Earth System Sciences*, 14:873–889, 2010.
- [346] M. Zreda, D. Desilets, T.P.A. Ferre, and R.L. Scott. Measuring soil moisture content non-invasively at intermediate spatial scale using cosmic ray neutrons. *Geophysical Research Letters*, 35:1–5, 2008.

- [347] M. Zribi, N. Baghdadi, N. Holah, and O. Fafin. New methodology for soil surface moisture estimation and its application to ENVISAT-ASAR multi-incidence data inversion. *Remote Sensing of Environment*, 96:485–496, 2005.
- [348] M. Zribi, N. Baghdadi, N. Holah, O. Fafin, and C. Guerin. Evaluation of a rough soil surface description with ASAR-ENVISAT radar data. *Remote Sensing of Environment*, 95:67–76, 2005.
- [349] M. Zribi and M. Dechambre. A new empirical model to retrieve soil moisture and roughness from C-band radar data. *Remote Sensing of Environment*, 84:42–52, 2002.
- [350] M. Zribi, S. LeHegarat-Masclé, C. Otle, B. Kammoun, and C. Guerin. Surface soil moisture estimation from the synergistic use of the (multi-incidence and multi-resolution) active microwave ERS wind scatterometer and SAR data. *Remote Sensing of Environment*, 86:30–41, 2003.

Appendix

A Eigen-based noise correction

As the polarimetric coherency matrix $\langle [T_3] \rangle$ is defined as a hermitian, positive-semidefinite matrix, it can be diagonalized using a unitary transformation (cf. [71] and Chapter 3.2.4.1.).

$$\langle [T_3] \rangle = [E_3][\Sigma][E_3]^{-1} \quad (222)$$

If additive noise, modeled as zero-mean *Gaussian* white noise with noise power N , is present, the non-negative real eigenvalues $\lambda + N$ are overestimated as seen in Equation 223 [125].

$$[\Sigma] = \begin{bmatrix} \lambda_1 + N & 0 & 0 \\ 0 & \lambda_2 + N & 0 \\ 0 & 0 & \lambda_3 + N \end{bmatrix} \quad (223)$$

The idea behind the following noise filtering technique is funded on the correlation between the two cross-polarized channels (S_{HV}, S_{VH}) and the fact that for monostatic acquisition the reciprocity theorem holds in the absence of noise, which means complete correlation $S_{HV} = S_{VH}$. Therefore the decrease of correlation due to a present noise level allows an assessment using the eigen-analysis on the 4x4 coherency matrix of Equation 82. The diagonalization of the $\langle [T_4] \rangle$ results in the four dimensional diagonal matrix $[\Sigma_4]$.

$$[\Sigma_4] = \begin{bmatrix} \lambda_1 + N & 0 & 0 & 0 \\ 0 & \lambda_2 + N & 0 & 0 \\ 0 & 0 & \lambda_3 + N & 0 \\ 0 & 0 & 0 & N \end{bmatrix} \quad (224)$$

For a monostatic acquisition assuming the absence of noise, the $\langle [T_4] \rangle$ has actually rank 3 and the smallest eigenvalue should be zero. In the presence of noise the rank of $\langle [T_4] \rangle$ is increasing to four and the smallest (4.) eigenvalue represents the noise power ($\lambda_4 = N$ see Equation 224). Hence, the noise is filtered by subtracting the smallest eigenvalue λ_4 from the first three eigenvalues of $[\Sigma]$.

B Growth stages of plants

Figures 104-106 picture the phenological stages of rape, beet and maize after the BBCH-scale of *Meier* [207].

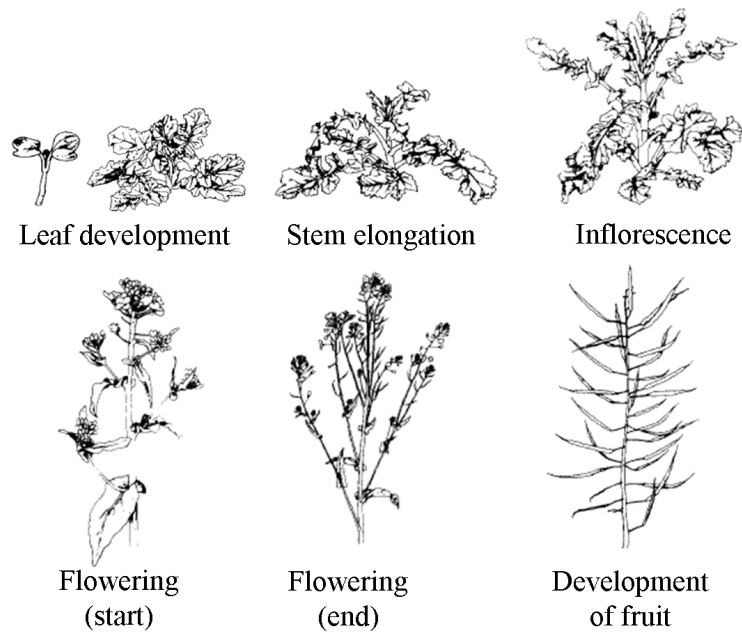


Figure 104: Phenology of rape plants [207]

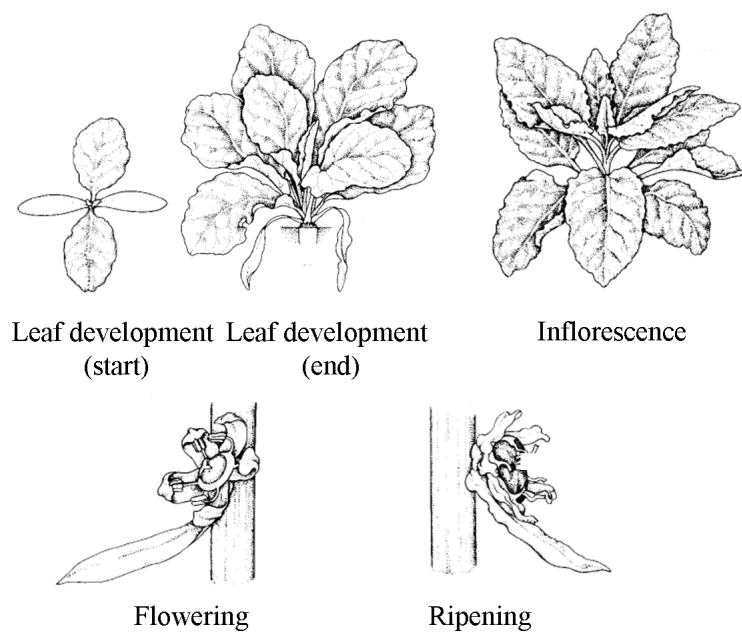


Figure 105: Phenology of beet plants [207]

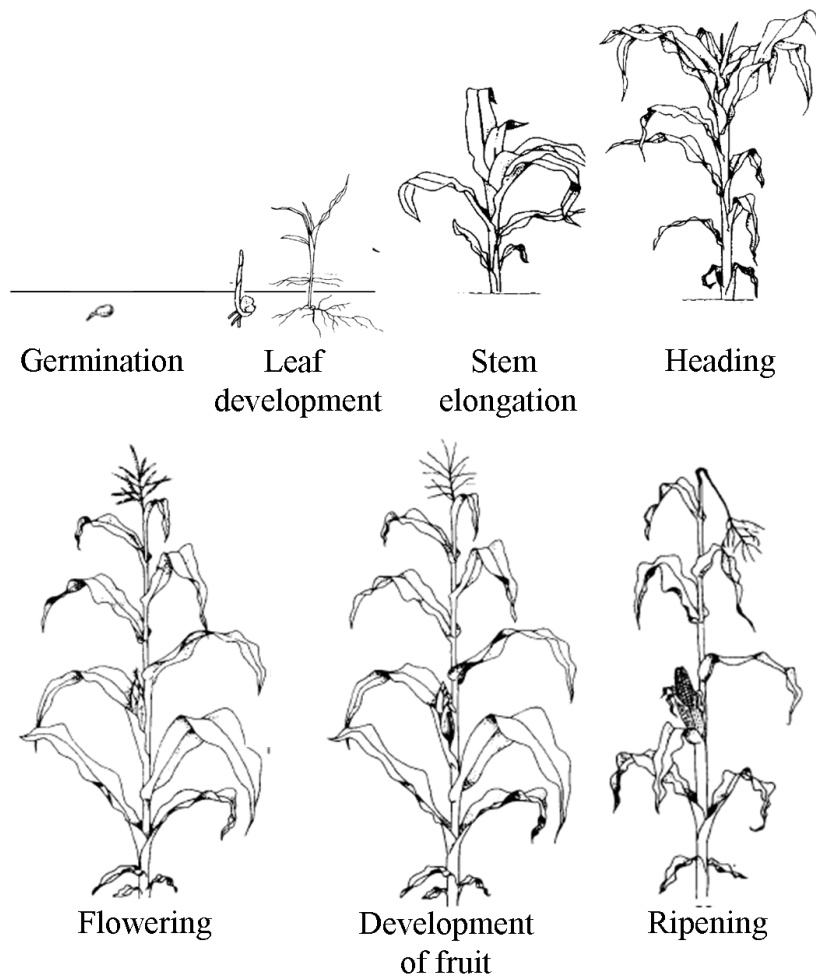


Figure 106: Phenology of maize plants [207]

C Volume modeling with spheroidal particles

The volume modeling with spheroidal particles allows a variation of the particle shape ($N = A_p - 1$), of the orientation angle PDFs ($pdf(\psi), pdf(\tau)$), of the mean orientation angles ($\bar{\psi}, \bar{\tau}$) and of the orientation angle widths ($\psi_w = 2\Delta\psi, \tau_w = 2\Delta\tau$). This enables the modeling of a variety of agricultural crops from thin stalk-dominated to broad leaf-dominated geometries with different orientation varieties. The representative volume coherency matrix $[T_{VG}]$ after element-wise integration is defined in Equation 155 for the respective case of mean orientation angles $\bar{\psi}$ and $\bar{\tau}$ and specified in the following:

$$[T_{VG}] = \frac{1}{480} \cdot \left[\begin{array}{l} 5N(16+5N)(1+2\cos(\Delta\tau))(2\cos(2\bar{\tau})-1)+3(10(32+N(24+5N))+N^2\cos(5\bar{\tau})\csc(\Delta\tau)\sec(\bar{\tau})\sin(5\Delta\tau)) \\ N\cos(2\bar{\psi})(5(8+5N)(1+2\cos(2\Delta\tau))(2\cos(2\bar{\tau})-1)+3(120+50N+N\cos(5\bar{\tau})\csc(\Delta\tau)\sec(\bar{\tau})\sin(5\Delta\tau)))\text{sinc}(2\Delta\psi) \\ N(5(8+5N)(1+2\cos(2\Delta\tau))(2\cos(2\bar{\tau})-1)+3(120+50N+N\cos(5\bar{\tau})\csc(\Delta\tau)\sec(\bar{\tau})\sin(5\Delta\tau)))\text{sin}(2\bar{\psi})\text{sinc}(2\Delta\psi) \\ \dots N\cos(2\bar{\psi})(5(8+5N)(1+2\cos(2\Delta\tau))(2\cos(2\bar{\tau})-1)+3(120+50N+N\cos(5\bar{\tau})\csc(\Delta\tau)\sec(\bar{\tau})\sin(5\Delta\tau)))\text{sinc}(2\Delta\psi) \\ \dots \frac{1}{2}N^2(150+\sec(\bar{\tau})+\csc(\Delta\tau)(25\cos(3\bar{\tau})\sin(3\Delta\tau)+3\cos(5\bar{\tau})\sin(5\Delta\tau)))(1+\cos(4\bar{\psi})\text{sinc}(4\Delta\psi)) \\ \dots \frac{1}{2}N^2(150+\sec(\bar{\tau})+\csc(\Delta\tau)(25\cos(3\bar{\tau})\sin(3\Delta\tau)+3\cos(5\bar{\tau})\sin(5\Delta\tau))\text{sin}(4\bar{\psi})\text{sinc}(4\Delta\psi) \\ \dots N(5(8+5N)(1+2\cos(2\Delta\tau))(2\cos(2\bar{\tau})-1)+3(120+50N+N\cos(5\bar{\tau})\csc(\Delta\tau)\sec(\bar{\tau})\sin(5\Delta\tau)))\text{sin}(2\bar{\psi})\text{sinc}(2\Delta\psi) \\ \dots \frac{1}{2}N^2(150+\sec(\bar{\tau})+\csc(\Delta\tau)(25\cos(3\bar{\tau})\sin(3\Delta\tau)+3\cos(5\bar{\tau})\sin(5\Delta\tau))\text{sin}(4\bar{\psi})\text{sinc}(4\Delta\psi) \\ \dots \frac{1}{2}N^2(150+\sec(\bar{\tau})+\csc(\Delta\tau)(25\cos(3\bar{\tau})\sin(3\Delta\tau)+3\cos(5\bar{\tau})\sin(5\Delta\tau))(1-\cos(4\bar{\psi})\text{sinc}(4\Delta\psi)) \end{array} \right]. \quad (225)$$

$\csc(x)$ and $\sec(x)$ represent the cosecant and the secant function.

The special case with mean orientation around zero $\bar{\psi} = 0$ and $\bar{\tau} = 0$ (horizontal mean orientation) is given in Equation 156 and in detail as follows:

$$[T_{VGH}] = \frac{1}{240} \cdot \left[\begin{array}{l} 480+N(400+89N)+4N(20+7N)*\cos(2\Delta\tau)+3N^2\cos(4\Delta\tau) \\ N(200+89N)+4(10+7N)\cos(2\Delta\tau)+3N\cos(4\Delta\tau)\text{sinc}(2\Delta\psi) \\ 0 \\ \dots N(200+89N)+4(10+7N)\cos(2\Delta\tau)+3N\cos(\Delta\tau)\text{sinc}(2\Delta\psi) \\ \dots N^2(89+28\cos(2\Delta\tau)+3\cos(4\Delta\tau))\frac{1}{2}(1+\text{sinc}(4\Delta\psi)) \\ \dots 0 \\ \dots 0 \\ \dots 0 \\ \dots N^2(89+28\cos(2\Delta\tau)+3\cos(4\Delta\tau))\frac{1}{2}(1-\text{sinc}(4\Delta\psi)) \end{array} \right]. \quad (226)$$

D Meteorological data from the AgriSAR campaign

The daily sum of the precipitation and the air temperature are presented for the whole growth period from April to July 2006 in Figures 107-110. The recording instruments were located at the Bowen Ratio station within the winter wheat field (nr. 250, cf. Figure 51) in the middle of the test site. The daily temperature variation rises from 0-20°C in April (spring) until 10-35°C in July (summer). Concerning the precipitation in spring, the data of April show several small rain events distributed over the whole month. In contrast, the data of May exhibit a dichotomy of a dry period in the first two weeks and a wet period in the last two weeks. Almost the same pattern can be recognized for June, but there are only two strong rain events on the 16th and 21st of June. In summer the precipitation data of July reveals a distinct dry period with only three smaller rain events (7th, 8th and 29th of July).

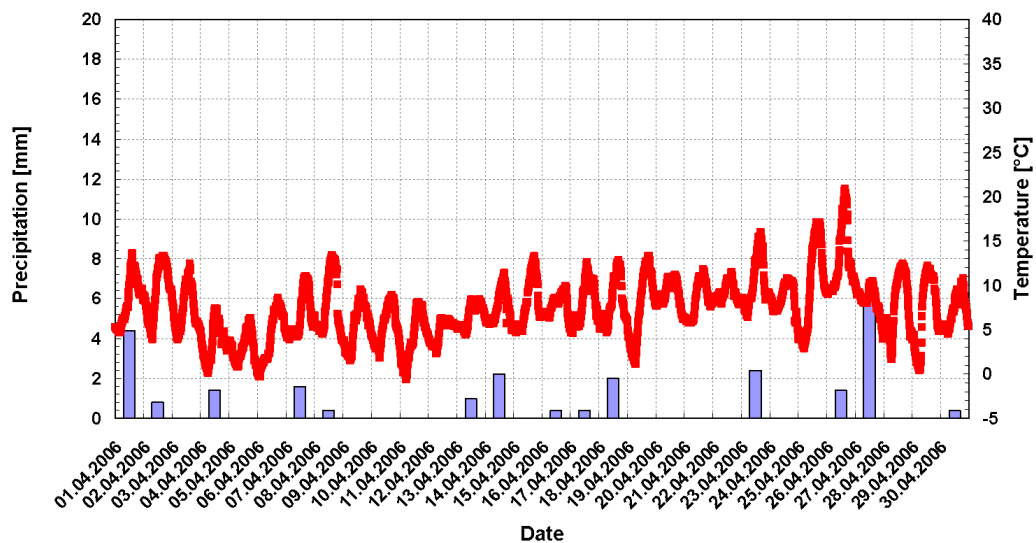


Figure 107: Meteorological measurements for April 2006 of the AgriSAR campaign; Red: Air temperature [°C], blue: Daily sum of precipitation [mm] (Sampling interval: 15 minutes) [23]

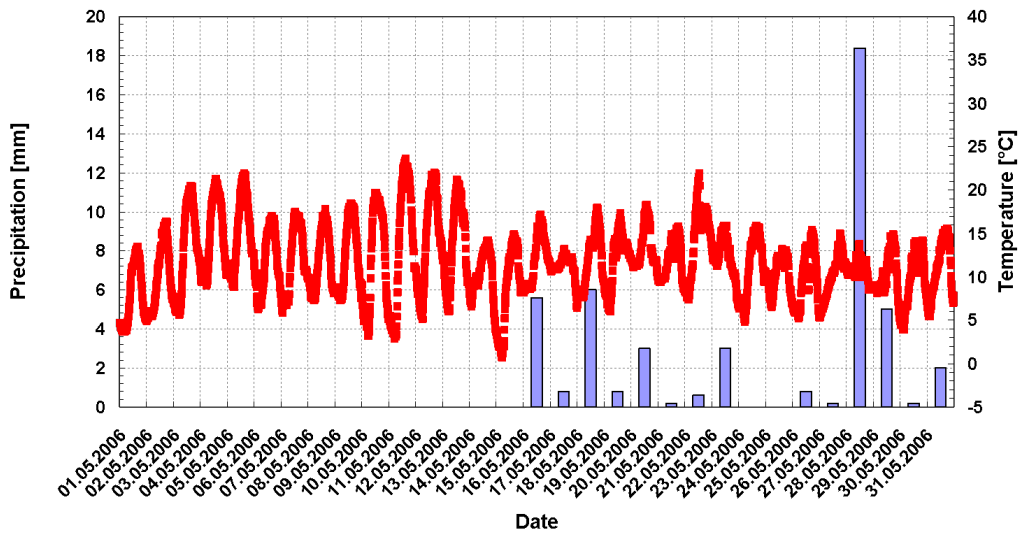


Figure 108: Meteorological measurements for May 2006 of the AgriSAR campaign; Red: Air temperature [°C], blue: Daily sum of precipitation [mm] (Sampling interval: 15 minutes) [23]

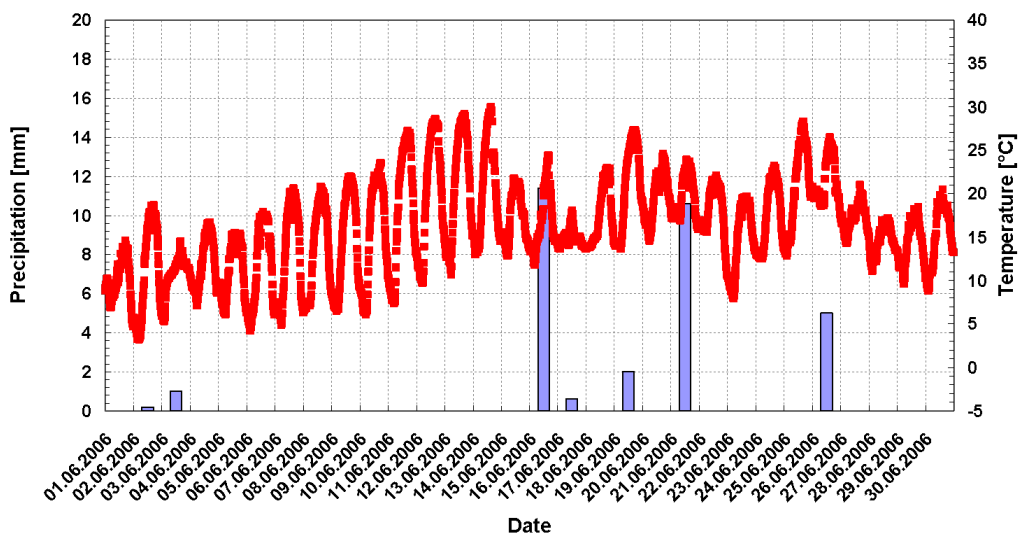


Figure 109: Meteorological measurements for June 2006 of the AgriSAR campaign; Red: Air temperature [°C], blue: Daily sum of precipitation [mm] (Sampling interval: 15 minutes) [23]

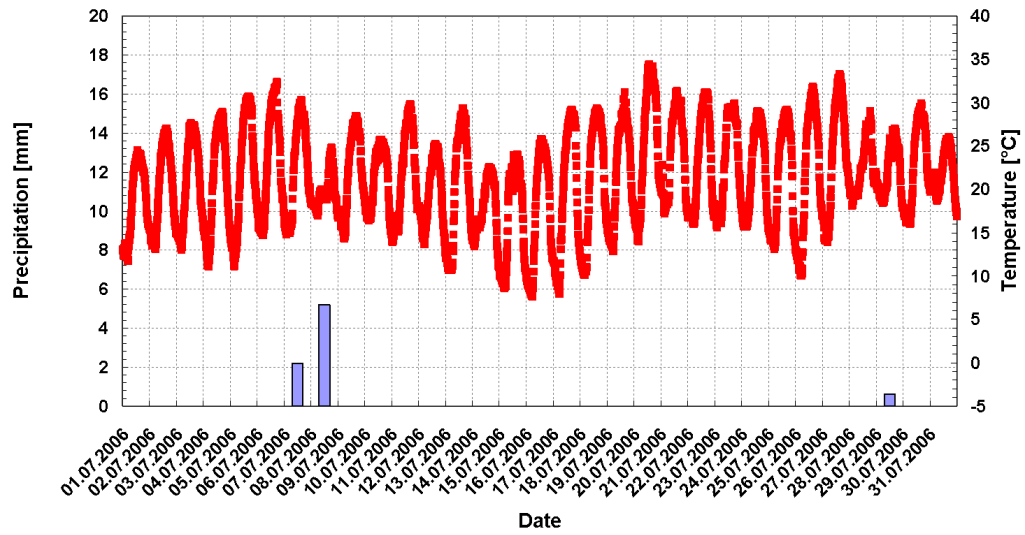


Figure 110: Meteorological measurements for July 2006 of the AgriSAR campaign; Red: Air temperature [°C], blue: Daily sum of precipitation [mm] (Sampling interval: 15 minutes) [23]

E Intensive measurement campaigns for soil moisture within AgriSAR campaign

During the AgriSAR campaign in 2006 three intensive measurement periods, so called ‘intensive campaigns’, were conducted in the beginning (19th/20th of April), in the middle (6th/7th of June) and in the end (5th/6th of July 2006) of the vegetation growth period. Table 21 shows the measured soil moisture values of the test fields selected for investigation, which were recorded by ISSIA and LMU using FDR, TDR and gravimetric probes [110].

Table 21: Intensive soil moisture measurements of the AgriSAR campaign as mean of field values: Soil moisture (mv) and standard deviation of mv (Δ mv); Field numbers are allocated in Figure 51 [23].

1. Intensive campaign: Measurements of ISSIA - 19 th /20 th of April 2006		
Field number	Crop type	mv $\pm\Delta$ mv [vol.%]
102	Sugar beet	22.96 \pm 2.6
230	Winter wheat	26.68 \pm 2.98
250	Winter wheat	26.01 \pm 1.4
1. Intensive campaign: Measurements of LMU - 19 th /20 th of April 2006		
101	Winter rape	21.98 \pm 1.93
102	Sugar beet	21.42 \pm 4.64
110	Winter rape	22.58 \pm 1.54
130	Winter rape	22.38 \pm 1.62
221	Winter wheat	27.39 \pm 3.03
222	Summer corn	25.66 \pm 3.28
250	Winter wheat	24.6 \pm 2.29
2. Intensive campaign: Measurements of LMU - 6 th /7 th of June 2006		
102	Sugar beet	19.36 \pm 4.25
222	Summer corn	15.95 \pm 4.15
230	Winter wheat	17.70 \pm 7.14
250	Winter wheat	16.95 \pm 3.69
3. Intensive campaign: Measurements of LMU - 5 th /6 th of July 2006		
222	Summer corn	7.13 \pm 3.35
250	Winter wheat	6.10 \pm 5.0
460	Sugar beet	4.39 \pm 1.65
3. Intensive campaign: Measurements of ISSIA - 5 th /6 th of July 2006		
102	Sugar beet	5.0 \pm 1.3
230	Winter Wheat	5.8 \pm 2.5

F Normalized *Pauli*-based ground-to-volume ratios

In Chapter 6.1.2.3. a model-based decomposition, including normalized *Pauli*-based ground-to-volume ratios for soil moisture inversion, was introduced. In the following, the normalized *Pauli*-based ground-to-volume ratios are shown for the AgriSAR, the OPAQUE and the SARTEO campaigns in Figures 111-115 to indicate the relation between ground and volume scattering, revealing the dominance of one scattering mechanism over the other. Volume scattering indicates a *Pauli*-based ground-to-volume ratio close to zero and pure ground scattering a ratio close to one.

The plausibility of the normalized *Pauli*-based ground-to-volume ratios to represent the relation between ground and volume scattering mechanisms can be assessed qualitatively by comparison with the normalized powers of the single angular model-based decomposition in Figures 79-81 and 84. In fact, the consistence between both parameters holds for all investigated acquisition, meaning that no surface or dihedral dominant region appears with a low value (close to zero) of the normalized *Pauli*-based ground-to-volume ratios. This underlines the potential of these ratios to support the physically meaningful separation of the cross-polarized component into a part from the vegetation volume and a part from the surface roughness.

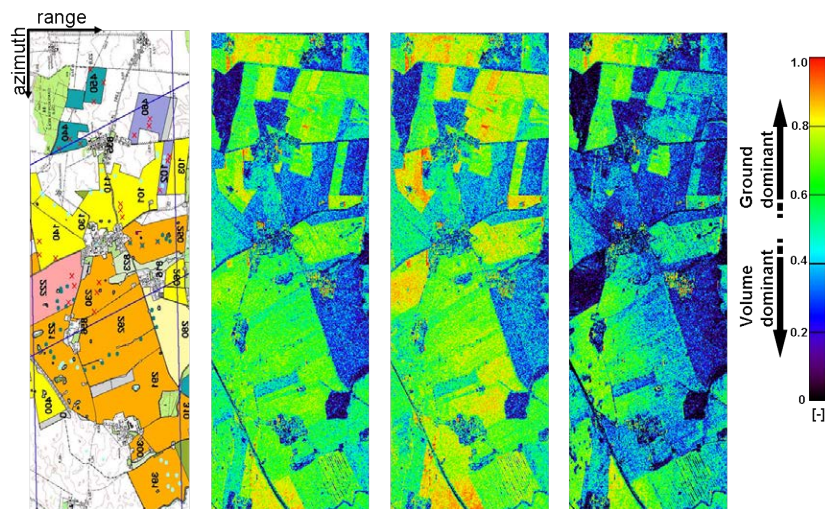


Figure 111: Normalized *Pauli*-based ground-to-volume ratios for the AgriSAR campaign on 7th of June 2006 (from left to right) land use of AgriSAR 2006 campaign, combined ground-to-volume ratio Pa_G , surface ground-to-volume ratio Pa_S and dihedral ground-to-volume ratio Pa_D).

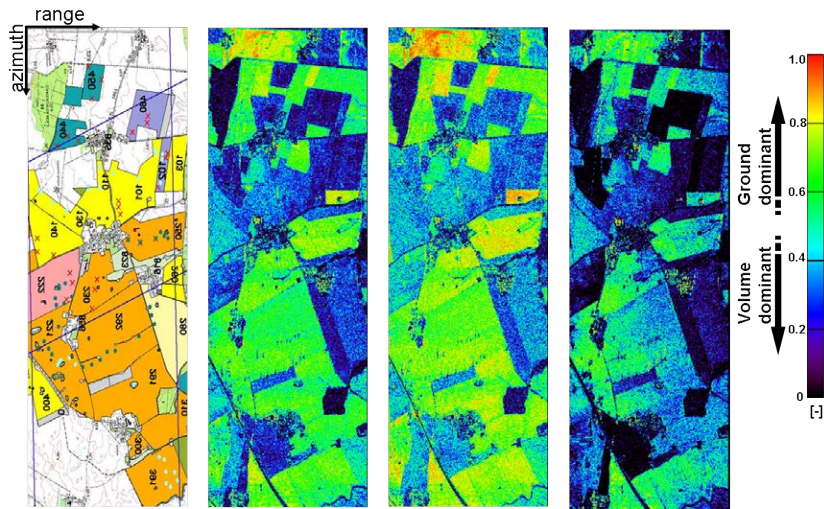


Figure 112: Normalized *Pauli*-based ground-to-volume ratios for the AgriSAR campaign on 5th of July 2006 (from left to right) land use of AgriSAR 2006 campaign, combined ground-to-volume ratio Pa_G , surface ground-to-volume ratio Pa_S and dihedral ground-to-volume ratio Pa_D).

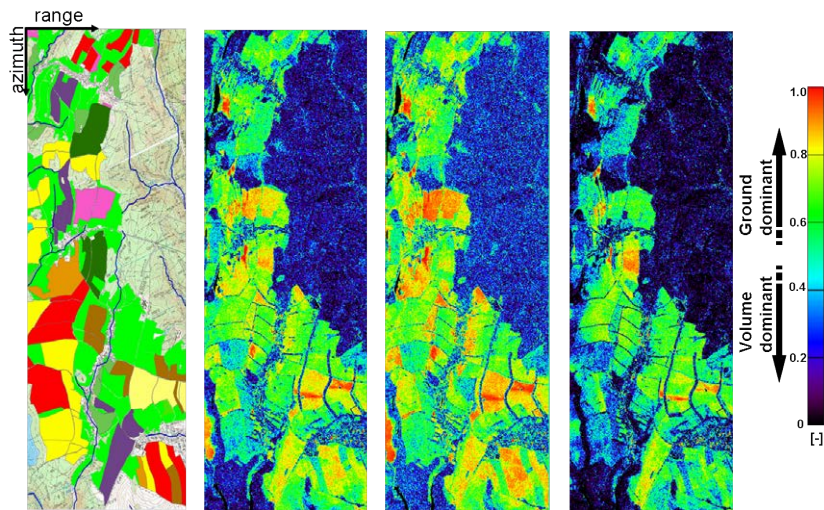


Figure 113: Normalized *Pauli*-based ground-to-volume ratios for the OPAQUE 2007 campaign on 31st of May (from left to right) land use of OPAQUE 2007 campaign, combined ground-to-volume ratio Pa_G , surface ground-to-volume ratio Pa_S and dihedral ground-to-volume ratio Pa_D).

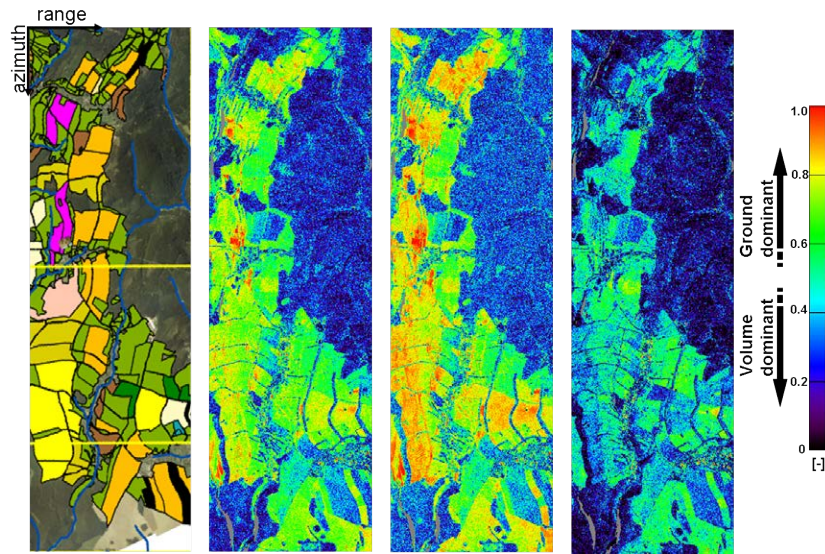


Figure 114: Normalized *Pauli*-based ground-to-volume ratios for the OPAQUE 2008 campaign on 8th of May (from left to right) land use of OPAQUE 2008 campaign, combined ground-to-volume ratio Pa_G , surface ground-to-volume ratio Pa_S and dihedral ground-to-volume ratio Pa_D).

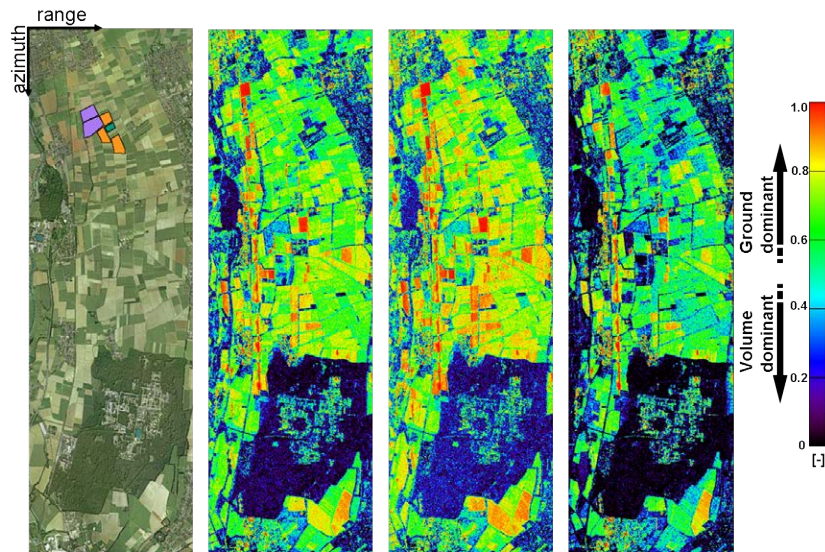


Figure 115: Normalized *Pauli*-based ground-to-volume ratios for the SARTEO 2008 campaign on 27th of May (from left to right) land use of SARTEO 2008 campaign, combined ground-to-volume ratio Pa_G , surface ground-to-volume ratio Pa_S and dihedral ground-to-volume ratio Pa_D).

G Surface and dihedral scattering mechanisms of the hybrid decomposition

In Chapter 6.1.2.4. the results of a hybrid decomposition for soil moisture inversion were presented. In Figures 116-120, the surface (α_s) and the dihedral (α_d) scattering mechanisms are depicted for the AgriSAR, the OPAQUE and the SARTEO campaign to indicate the valid separation of the ground scattering contributions (surface, dihedral) with the orthogonality relation introduced in Chapter 4.2.6..

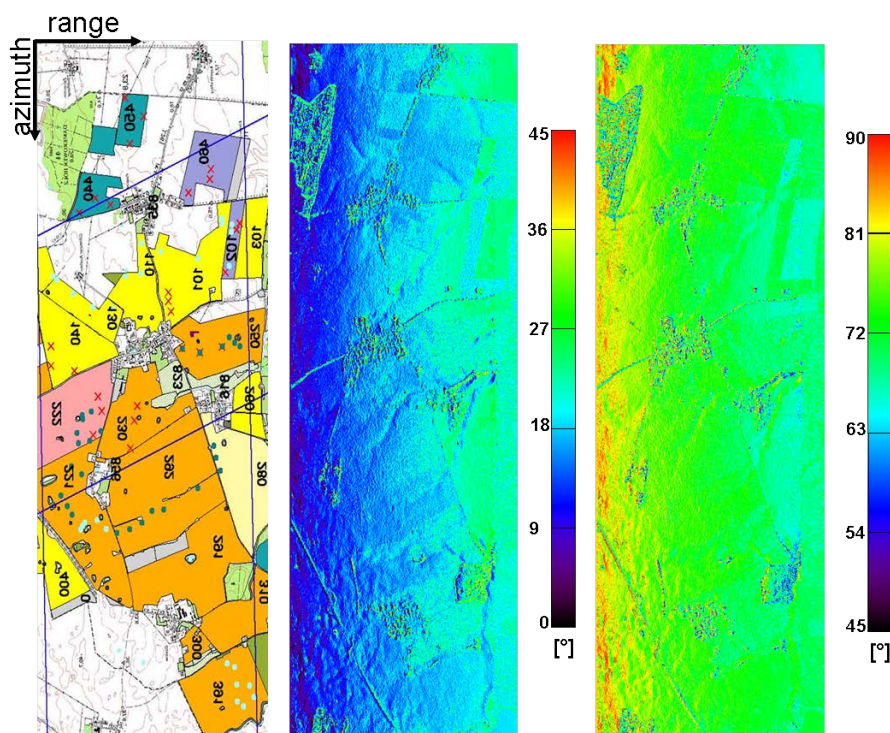


Figure 116: Land use (left) as well as alpha scattering angles of the surface (middle) and the dihedral (right) component for 7th of June 2006 of the AgriSAR campaign using the hybrid decomposition with a physically constrained volume component $f_{V_{Ch}}$ ($\epsilon_{est} - level = 10$).

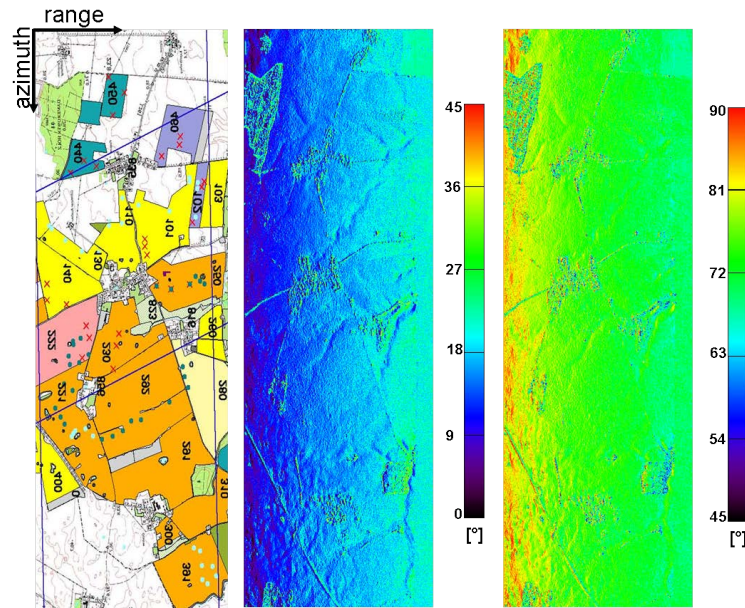


Figure 117: Land use (left) as well as alpha scattering angles of the surface (middle) and the dihedral (right) component for 5th of July 2006 of the AgriSAR campaign using the hybrid decomposition with a physically constrained volume component $f_{V_{ch}}$ ($\epsilon_{est} - level=8$).

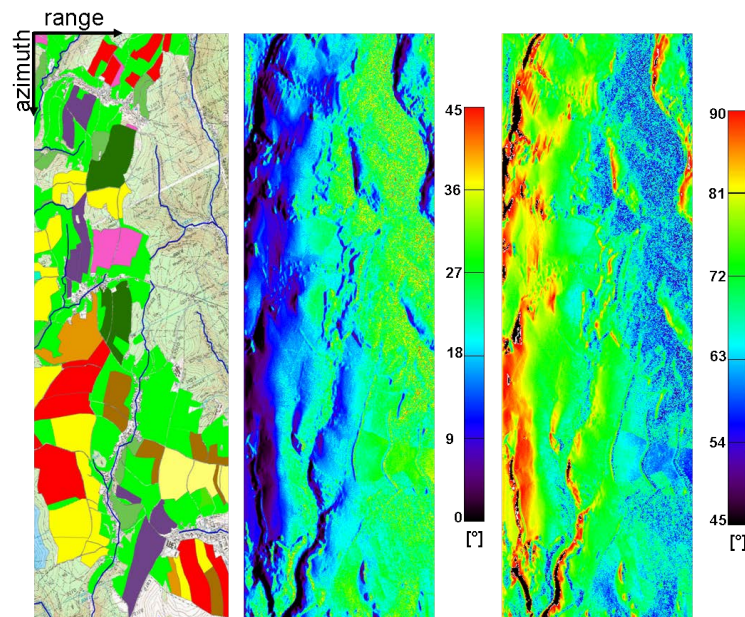


Figure 118: Land use (left) as well as alpha scattering angles of the surface (middle) and the dihedral (right) component for the OPAQUE 2007 campaign using the hybrid decomposition with a physically constrained volume component $f_{V_{ch}}$ ($\epsilon_{est} - level=30$).

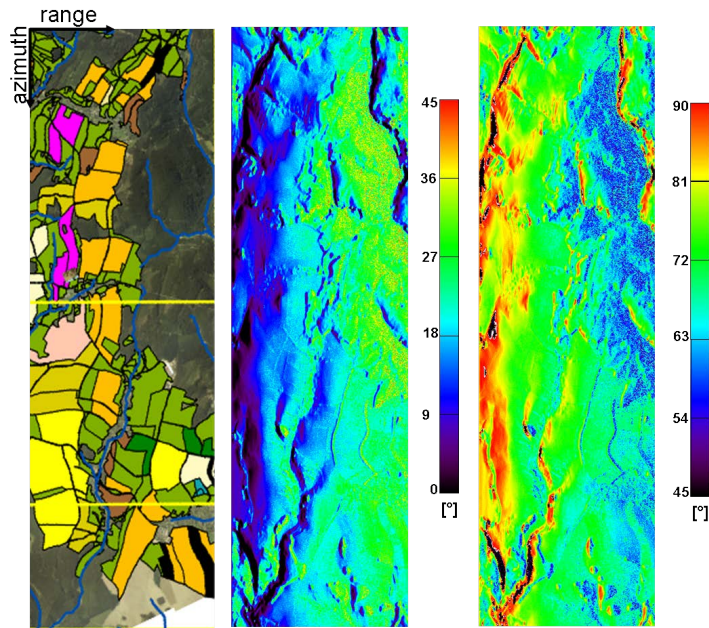


Figure 119: Land use (left) as well as alpha scattering angles of the surface (middle) and the dihedral (right) component for the OPAQUE 2008 campaign using the hybrid decomposition with a physically constrained volume component f_{VCh} ($\epsilon_{est} - level=18$) [153].

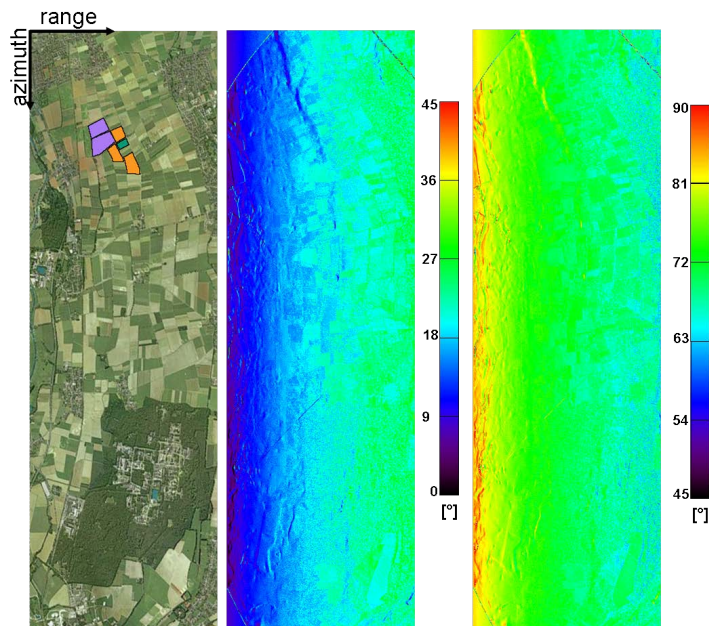


Figure 120: Land use (left) as well as alpha scattering angles of the surface (middle) and the dihedral (right) component for the SARTEO campaign using the hybrid decomposition with a physically constrained volume component f_{VCh} ($\epsilon_{est} - level=15$).